



ScuDo

Scuola di Dottorato ~ Doctoral School
WHAT YOU ARE, TAKES YOU FAR



Doctoral Dissertation
Doctoral Program in Energy Engineering (32nd Cycle)

Experimental analysis of an early diesel PCCI concept and strategies to limit its application constraints

Alessandro Mancarella

* * * * *

Supervisor

Prof. Stefano d'Ambrosio

Doctoral Examination Committee:

Prof. Jan Macek, Czech Technical University in Prague

Prof. Vincenzo Mulone, Università degli Studi di Roma Tor Vergata

Prof. Ivan Arsie, Università degli Studi di Napoli Parthenope

Prof. Nicolò Cavina, Università degli Studi di Bologna

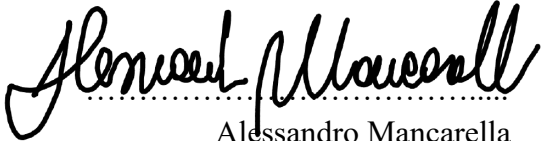
Prof. Ezio Spessa, Politecnico di Torino

Politecnico di Torino

July 27th, 2020

This thesis is licensed under a Creative Commons License, Attribution - Noncommercial - NoDerivative Works 4.0 International: see www.creativecommons.org. The text may be reproduced for non-commercial purposes, provided that credit is given to the original author.

I hereby declare that, the contents and organisation of this dissertation constitute my own original work and does not compromise in any way the rights of third parties, including those relating to the security of personal data.

A handwritten signature in black ink, reading "Alessandro Mancarella". The signature is written in a cursive style with a dotted line underneath it.

Alessandro Mancarella
Turin, 2020

Abstract

An experimental investigation was carried out with the aim to highlight the main benefits achievable by the implementation of an early Premixed Charge Compression Ignition (PCCI) diesel combustion concept, determining at the same time which are the constraints imposed on operating such a highly premixed strategy and which could be viable methods to possibly counteract them.

At first, the potentialities of an early single-injection PCCI concept were evaluated on a 3.0 l, four-cylinder, four-stroke Euro VI production diesel engine (F1C Euro VI) provided by FPT Industrial, equipped with a short-route (high-pressure) cooled exhaust gas recirculation (EGR) circuit, with a high-pressure Common Rail fuel injection system featuring solenoid injectors, and with a variable geometry turbine (VGT). With this engine, specifically designed to run under conventional diesel combustion (CDC) operations, experimental results showed that early PCCI operations (achieved by exploiting high levels of cooled EGR and retaining the control over combustion through highly advanced injection timings) were possible only with a very low maximum reachable brake mean effective pressure (*bmep*), around 2÷3 bar. Simultaneous engine-out soot and NO_x reductions (of up to 99% and 95%, respectively, compared to their CDC levels) could be achieved, getting rid of their well-known trade-off typical of the CDC mode, but with several penalties associated. In this regard, the increased emission of incomplete combustion products (unburned hydrocarbons, HC, and carbon monoxide), the intense combustion noise (CN), the higher fuel consumption and the worse combustion stability were the most challenging.

Then, to further investigate the early PCCI concept, enlarging its operating range, a modified engine (referred to as F1C PCCI), specifically designed to run under PCCI combustion mode, was derived from the conventional F1C Euro VI engine. Proper hardware modifications were designed by means of 3D CFD combustion simulations based on the preliminary PCCI tests carried out on the

conventional F1C Euro VI engine. The final hardware modifications included reduced compression ratio (from 17.5:1 to 14.6:1), modified piston shape, different fuel injectors with reduced cone angles, a higher volume EGR cooler and a smaller turbo-group. Compared to its corresponding standard version, the prototype engine (featuring a single fuel injection calibration) allowed to perform a suitable steady-state calibration in PCCI conditions up to 8.5 bar of *bmep*. Strong reductions of engine-out NO_x and soot emissions were still possible, but tailpipe HC and CO emissions at low load, intense CN and fuel consumption penalties ranging from about 3% to 11% (if compared to the corresponding values obtained with CDC operations with the baseline F1C Euro VI engine) still remained major issues. Nevertheless, it should be considered that the fuel consumption penalty induced by PCCI may be partially mitigated, since its potential to simultaneously reduce soot and NO_x engine-out emissions may lead to minimize the after-treatment requirements and the related costs, i.e. reducing the fuel penalties for active DPF (diesel particulate filter) regeneration and the costs for urea-based additives.

With the aim to address the increase in tailpipe HC and CO emissions, especially for low load and speed operations, a hot (uncooled) EGR strategy was tested at the lowest load engine operating conditions (up to *bmep* = 3 bar). Uncooled EGR, i.e. exhaust gas recirculated into the engine without passing through the EGR cooler (by-passing it), proved to be beneficial when the exhaust gas temperatures were so low that the oxidation catalyst did not exploit its full effectiveness, helping the catalyst to reach its operating temperature over a wider area of the engine map.

Multi-pulse (i.e., double and triple) fuel injection strategies were tested and compared to the baseline single-pulse PCCI combustion operations. Splitting the fuel injection pattern turned out to have the potential of reducing engine-out HC and CO emissions, optimizing the spray penetration and reducing the occurrence of over-mixing and wall impingement phenomena, with minor penalties in terms of soot and NO_x. Multi-pulse injection strategies also allowed to effectively dampen excessive CN levels, while slightly improving fuel economy.

Being EGR one of the crucial parameters involved in early PCCI combustion, its rate should be optimized inside a narrow interval to achieve a reasonable compromise in terms of engine-out pollutant emissions, fuel consumption and CN level. Therefore, a “zero-dimensional” (0D) model for the estimation of the EGR flowrate was built and analysed, highlighting how this could be potentially suitable for real-time control applications if implemented on-board the ECU.

Combustion instability may occur due to the high EGR level and its possible uneven distribution among the different cylinders. As combustion phasing is one of the most important parameters affecting diesel combustion, MFB50 (crank angle at

which 50% of the injected fuel has burnt) has been exploited as a controlled parameter to implement real-time combustion control techniques. A pressure-based and a model-based combustion controllers, able to control in real-time the MFB50 by properly shifting the start of injection (SOI) of the main fuel injection, have been developed and experimentally tested on the F1C Euro VI engine, in both steady-state and transient conditions, under CDC mode, to prove their robustness. Moreover, steady-state tests have been performed under PCCI operations, highlighting benefits in terms of reduced cylinder-to-cylinder and cycle-to-cycle variability of the combustion process.

As a further step, a preliminary assessment of the potentialities of single- and multiple-injection PCCI, intended to be calibrated inside a dedicated low-to-medium load and speed portion of the engine map and combined with a conventional diesel combustion calibration outside of it (simulating a dual-mode operation strategy engine), was performed along simulated NEDC and WHTC cycles. The simulation exploited interpolation of steady-state map measurements in terms of exhaust pollutant emissions, fuel and urea consumptions, giving an estimation of the possible benefits/penalties compared to a reference CDC case, even if not intended to be an accurate evaluation of real transient operations carried out in real driving conditions.

Finally, the detrimental effect of the progressive EGR cooler fouling on performance and emissions is presented and discussed. The increased pressure drop across a fouled EGR cooler results in a progressively reducing amount of EGR, thus revealing to be one of the major constraints to the applicability of the PCCI concepts.

Contents

1. Introduction.....	1
1.1 Overview	1
1.2 Pollutant and GHG emissions background.....	2
1.3 Advanced diesel combustion concepts	4
1.4 Possible technologies to enable LTC operations.....	9
1.4.1 Real-time combustion control techniques.....	9
1.4.2 Dual-loop EGR system	11
1.4.3 Variable intake valve closing (IVC) mechanisms.....	12
1.4.4 Advanced fuel injection systems.....	12
1.5 Practical implementation of LTC concepts	13
1.6 Outline of the Thesis	14
2. PCCI combustion potentialities in a conventional diesel engine.....	15
2.1 Preliminary experimental tests on PCCI concept.....	15
2.1.1 Experimental setup.....	15
2.1.2 Early single injection PCCI at low speed and low load	16
2.2 Model-based optimization methodology	26
2.2.1 Design of Experiments (DoE) setup	26
2.2.2 Statistical modeling.....	27
2.2.3 Optimization procedure.....	28
3. PCCI combustion in an optimized engine hardware	31
3.1 Engine hardware modifications	31
3.2 Low load PCCI: comparison between standard (F1C Euro VI) and prototype (F1C PCCI) engines	32
3.3 PCCI application on the prototype (F1C PCCI) engine	36
3.4 “Uncooled” EGR strategy at low load.....	46
3.4.1 “Hot” and “cold” EGR system layout configurations.....	47
3.4.2 Experimental comparison between hot and cold EGR system layouts	48
4. Noise and emissions reduction by multiple injection PCCI strategies	56

4.1 Double fuel injection PCCI strategy.....	56
4.1.1 Results and discussion	56
4.2 Triple fuel injection PCCI strategy.....	78
4.2.1 Results and discussion.....	78
5. Control-oriented models for EGR and MFB50 estimation.....	83
5.1 EGR mass flowrate estimation	83
5.1.1 Setting up the models	83
5.1.2 Assessment and validation of the models	92
5.2 Real-time combustion control techniques.....	96
5.2.1 Real-time combustion controls for the MFB50 monitoring.....	98
5.2.2 Experimental tests: results and discussion	102
6. Preliminary assessment of a dual-mode operation strategy.....	114
6.1 Dual-mode operation strategy	114
6.2 Preliminary assessment of the performance of a simulated dual-mode operation engine along NEDC and WHTC cycles.....	115
7. EGR cooler fouling.....	131
7.1 Experimental outcomes about the EGR cooler fouling.....	131
7.2 PCCI performance with the new and aged EGR coolers.....	138
Conclusions.....	142
Abbreviations and acronyms	145
References.....	149

List of Tables

Table 2.1. Main technical specifications of the tested engine	16
Table 2.2. Boundary values for the input parameters.	26
Table 2.3. Summary statistics for each response model.	28
Table 2.4. PCCI optimization parameters, at 1800×1.....	29
Table 3.1.. Comparison of the main technical specifications of the conventional F1C Euro VI diesel engine and of the PCCI version of the engine.	32
Table 3.2. PCCI optimization parameters, at 1800×1 (F1C PCCI).	33
Table 3.3. Euro VI emission standards for heavy-duty diesel engines for the World Harmonized Stationary Cycle (WHSC).....	38
Table 3.4. Relevant engine parameters for the “optimal” calibrations, with cold and hot EGR configurations.	48
Table 5.1. Test conditions for the EGR sweep tests under PCCI combustion mode.	107
Table 5.2. Main properties of Jet A1 and diesel EN590 fuels.	109
Table 6.1. Main technical specifications of the reference light-duty commercial vehicle.....	118
Table 6.2. Effect of active regeneration strategies of the DPF on fuel penalties from PCCI, along the NEDC.	129
Table 6.3. Effect of active regeneration strategies of the DPF on fuel penalties from PCCI, along the WHTC.	129
Table 6.4. Total fluid cost penalties from PCCI, along the NEDC.	130
Table 6.5. Total fluid cost penalties from PCCI, along the WHTC.	130

List of Figures

Figure 1.1. Contribution of the transport sector to total emissions of the main air pollutants, in the European Union [EEA, 2018a].	3
Figure 1.2. Share of transport GHG emissions, in Europe [EEA, 2018b].	3
Figure 1.3. Historical and target (forecast) CO ₂ regulations for new light-duty vehicles in different countries [Tietge, 2018].	4
Figure 1.4. Comparison of diesel combustion modes in a local equivalence ratio (ϕ) and local flame temperature (T) diagram [DieselNet, 2019].	6
Figure 2.1. NO _x (a) and soot (b) emissions as a function of X_{EGR} , at 1800×1.	18
Figure 2.2. Soot-NO _x trends, at 1800×1.	19
Figure 2.3. CO (a) and HC (b) emissions as a function of X_{EGR} , at 1800×1.	20
Figure 2.4. <i>bsfc</i> (a) and CO ₂ emissions (b) as a function of X_{EGR} , at 1800×1.	21
Figure 2.5. In-cylinder pressure and HRR traces for different X_{EGR} values. (a) SOI = 16 °CA bTDC;	23
Figure 2.6. Mean in-cylinder temperature and HRR traces for similar X_{EGR} values (65%), at SOI = 16 °CA bTDC, 24 °CA bTDC and 30 °CA bTDC.	24
Figure 2.7. CN as a function of X_{EGR} , at 1800×1.	25
Figure 2.8. PFP (a) and MFB50 (b) values as a function of X_{EGR} , at 1800×1.	25
Figure 2.9. <i>bsfc</i> model: predicted vs. experimental values, at 1800×1.	28
Figure 2.10. NO _x (a) and soot (b): comparison between the baseline and the optimized PCCI calibrations.	29
Figure 2.11. CO (a) and HC (b): comparison between the baseline and the optimized PCCI calibrations.	30
Figure 2.12. <i>bsfc</i> (a) and CN (b): comparison between the baseline and the optimized PCCI calibrations.	30

Figure 3.1. Section view of the piston bowl and injector spray edge of the F1C Euro VI and the F1C PCCI engines.	31
Figure 3.2. NO _x (a) and soot (b): comparison between the baseline CDC and the optimized PCCI calibrations for the two engine configurations (F1C Euro VI and F1C PCCI).	34
Figure 3.3. CO (a) and HC (b): comparison between the baseline CDC and the optimized PCCI calibrations for the two engine configurations (F1C Euro VI and F1C PCCI).	34
Figure 3.4. <i>bsfc</i> (a) and MFB50 (b): comparison between the baseline CDC and the optimized PCCI calibrations for the two engine configurations (F1C Euro VI and F1C PCCI).	35
Figure 3.5. CN comparison between the baseline CDC and the optimized PCCI calibrations for the two engine configurations (F1C Euro VI and F1C PCCI).	35
Figure 3.6. NO _x , soot and <i>bsfc</i> as a function of λ at 2000 \times 5, for different values of the input variables.	37
Figure 3.7. Air-fuel ratio (λ) for the F1C PCCI engine.	38
Figure 3.8. Percentage variations in engine-out NO _x (a) and soot (b) emissions between the F1C PCCI and the corresponding CDC values on the F1C Euro VI engine.	40
Figure 3.9. Percentage variations in engine-out CO (a) and HC (b) emissions between the F1C PCCI and the corresponding CDC values on the F1C Euro VI engine.	41
Figure 3.10. Percentage variations of tailpipe CO (a) and HC (b) emissions between the F1C PCCI engine and the WHSC limit.	42
Figure 3.11. Percentage variations of <i>bsfc</i> between the F1C PCCI and the corresponding CDC values on the F1C Euro VI engine.	43
Figure 3.12. Mass fraction burned x_b (a - left axis), HRR (a - right axis), in-cylinder pressure (b - left axis), and its derivative (b - right axis) versus crank angle position at the 2000 \times 2.3 point for both the F1C PCCI (blue dotted line) and the corresponding CDC calibration on the F1C Euro VI engine (red solid line).	44
Figure 3.13. Mass fraction burned x_b (a - left axis), HRR (a - right axis), in-cylinder pressure (b - left axis), and its derivative (b - right axis) versus crank angle position at the 2000 \times 7.5 point for both the F1C PCCI (blue dotted line) and the corresponding CDC calibration on the F1C Euro VI engine (red solid line).	44
Figure 3.14. Differences of the maximum in-cylinder pressure derivative between the F1C PCCI and the corresponding CDC values on the F1C Euro VI engine.	45

Figure 3.15. Increment of CN levels (in dBA) between the F1C PCCI and the corresponding CDC values on the F1C Euro VI engine.....	46
Figure 3.16. Comparison of engine-out HC emissions, with cold (a) and hot (b) EGR strategies.	49
Figure 3.17. Comparison of engine-out CO emissions, with cold (a) and hot (b) EGR strategies.	50
Figure 3.18 Comparison of the exh. gas temp. upstream the DOC, with cold (a) and hot (b) EGR strategies.	51
Figure 3.19 Comparison of the intake gas temperature, with cold (a) and hot (b) EGR strategies.	52
Figure 3.20 Comparison of tailpipe HC emissions, with cold (a) and hot (b) EGR strategies.	53
Figure 3.21 Comparison of tailpipe CO emissions, with cold (a) and hot (b) EGR strategies.	53
Figure 3.22 Comparison of exhaust NO _x emissions, with cold (a) and hot (b) EGR strategies.	54
Figure 3.23 Comparison of exhaust soot emissions, with cold (a) and hot (b) EGR strategies.	54
Figure 3.24 Comparison of <i>bsfc</i> , with cold (a) and hot (b) EGR strategies.....	55
Figure 4.1. Example of 2 nd injection timing sweeps: fuel injection rate and current profiles for a 75%-25% (a) and 50%-50% (b) fuel split.....	58
Figure 4.2. Results of a 2 nd injection timing sweep at 1400×1, for a 75%-25% (light green and triangular symbols) and 50%-50% (dark green and square symbols) fuel split. Comparison with the PCCI single injection (red solid line) and the CDC baseline (violet dashed line) calibrations.	59
Figure 4.3. Comparison of the HRR traces at 1400×1, between the PCCI single injection (a) and the 50%-50% (b) and 75%-25% (c) fuel split with double injection (2 nd injection timing sweep).....	61
Figure 4.4. One-third octave frequency bands at 1400×1, for the 75%-25% fuel split with double injection strategies (2 nd injection timing sweep, with low, medium and high DT values).....	63
Figure 4.5. Results of a 2 nd injection timing sweep at 1000×4, for a 75%-25% (light green and triangular symbols) and 50%-50% (dark green and square symbols) fuel split. Comparison with the PCCI single injection (red solid line) and the CDC baseline (violet dashed line) calibrations.	64
Figure 4.6. Results of a 2 nd injection timing sweep at 2000×5, for a 75%-25% (light green and triangular symbols) and 50%-50% (dark green and square symbols)	

fuel split. Comparison with the PCCI single injection (red solid line) and the CDC baseline (violet dashed line) calibrations.	65
Figure 4.7. Comparison of the HRR traces at 2000×5, between the PCCI single injection (a) and the 50%-50% (b) and 75%-25% (c) fuel split with double injection (2 nd injection timing sweep).....	66
Figure 4.8. Results of a 2 nd injection timing sweep at 2000×6.5, for a 75%-25% (light green and triangular symbols) and 50%-50% (dark green and square symbols) fuel split. Comparison with the PCCI single injection (red solid line) and the CDC baseline (violet dashed line) calibrations.....	68
Figure 4.9. Results of a 2 nd injection timing sweep at 2000×8.5, for a 75%-25% (light green and triangular symbols) and 50%-50% (dark green and square symbols) fuel split. Comparison with the PCCI single injection (red solid line) and the CDC baseline (violet dashed line) calibrations.....	69
Figure 4.10 1 st injection timing sweeps: fuel injection rate and current profiles for a 75%-25% (a) and 50%-50% (b) fuel split, at 2000×5.	71
Figure 4.11. Comparison of the HRR traces at 2000×5, between the PCCI single injection (a) and the 50%-50% (b) and 75%-25% (c) fuel split with double injection (1 st injection timing sweep).	72
Figure 4.12. Results of a 1 st injection timing sweep at 2000×5, for a 75%-25% (light blue and triangular symbols) and 50%-50% (dark blue and square symbols) fuel split. Comparison with the PCCI single injection (red solid line) and the CDC baseline (violet dashed line) calibrations.	73
Figure 4.13. Soot emissions comparison of 1 st (light and dark blue) and 2 nd (light and dark green) injection timing sweeps at 2000×5, for a 75%-25% (a) and 50%-50% (b) fuel split. Comparison with the PCCI single injection (red solid line) and the CDC baseline (violet dashed line) calibrations.	75
Figure 4.14. CN comparison of 1 st (light and dark blue) and 2 nd (light and dark green) injection timing sweeps at 2000×5, for a 75%-25% (a) and 50%-50% (b) fuel split. Comparison with the PCCI single injection (red solid line) and the CDC baseline (violet dashed line) calibrations.....	75
Figure 4.15. CO emissions comparison of 1 st (light and dark blue) and 2 nd (light and dark green) injection timing sweeps at 2000×5, for a 75%-25% (a) and 50%-50% (b) fuel split. Comparison with the PCCI single injection (red solid line) and the CDC baseline (violet dashed line) calibrations.....	76
Figure 4.16. HC emissions comparison of 1 st (light and dark blue) and 2 nd (light and dark green) injection timing sweeps at 2000×5, for a 75%-25% (a) and 50%-50% (b) fuel split. Comparison with the PCCI single injection (red solid line) and the CDC baseline (violet dashed line) calibrations.....	76

Figure 4.17. NO _x emissions comparison of 1 st (light and dark blue) and 2 nd (light and dark green) injection timing sweeps at 2000×5, for a 75%-25% (a) and 50%-50% (b) fuel split. Comparison with the PCCI single injection (red solid line) and the CDC baseline (violet dashed line) calibrations.	77
Figure 4.18. <i>bsfc</i> comparison of 1 st (light and dark blue) and 2 nd (light and dark green) injection timing sweeps at 2000×5, for a 75%-25% (a) and 50%-50% (b) fuel split. Comparison with the PCCI single injection (red solid line) and the CDC baseline (violet dashed line) calibrations.	77
Figure 4.19. Fuel injection rate and current profiles for the single (a), double (b) and triple (c) PCCI injection patterns, at 1400×1.	78
Figure 4.20. Fuel injection rate and current profiles for the single (a), double (b) and triple (c) PCCI injection patterns, at 2000×5.	79
Figure 4.21. Results of an EGR sweep at 1400×1. Comparison between PCCI single (red line), double (green line), triple (blue line) injections and the CDC baseline (violet dashed lines) calibration.	80
Figure 4.22. Results of an EGR sweep at 2000×5. Comparison between PCCI single (red line), double (green line), triple (blue line) injections and the CDC baseline (violet dashed lines) calibration.	81
Figure 5.1. Geometric profiles of the EGR poppet valve and of its seat.	85
Figure 5.2. Geometric passage area at different poppet valve lifts l_v : 2 mm (a), 5 mm (b) and 8 mm (c).	86
Figure 5.3. EGR valve geometric passage area (a) and electric duty-cycle (b) as function of the lift.	87
Figure 5.4. Effective EGR flow area and geometric flow area (a) and flow coefficient (b) as a function of the valve lift.	88
Figure 5.5. CFD flow velocity fields for three different l_v values: 2 mm (a), 5 mm (b) and 8 mm (c).	89
Figure 5.6. Predicted vs. experimental correlation for p_{exh} (a) and T_{exh} (b).	90
Figure 5.7. Discharge coefficients comparison for the fluid-dynamics and the semi-physical model.	91
Figure 5.8. Engine operating points carried out at the test bench on the F1C Euro VI engine (red circles: Engine map; green circles: Trade-off validation tests; blue triangles: PCCI validation tests).	92
Figure 5.9. Validation of the models for the prediction of mEGR on the replicated engine map dataset.	93
Figure 5.10. Validation of the models for the prediction of mEGR on the air quantity sweeps dataset.	93

Figure 5.11. Validation of the models for the prediction of mEGR on the PCCI dataset.	95
Figure 5.12. Engine operating points carried out at the test bench on the F1C Euro VI engine under CDC mode (red circles: Engine map; green circles: EGR sweeps).	100
Figure 5.13. Schematics of the RP setup for the pressure-based (a) and model-based (b) MFB50 controls	101
Figure 5.14. Engine operating points selected for the engine map (red circles), for the SOI/MFB50 sweeps (green circles) and for the EGR sweep under PCCI mode (blue triangle).....	103
Figure 5.15. Coefficient of variation of the peak firing pressure evaluated for the whole engine $CoV_{PFP,eng}$ (a, b and c) and amplitude of the dispersion range of the MFB50 (d) on engine mapping tests: comparison between the map-based, the pressure-based and the model-based controls. $CoV_{PFP,eng}$ is shown on tests for various engine loads at three different engine speeds: a) 850 rpm; b) 2000 rpm; c) 3000 rpm. The dispersion of the MFB50 (d) is reported at 2000 rpm for various engine loads.	104
Figure 5.16. Amplitude of the dispersion range of the CN (a) and NO_x and soot emissions (b) vs. b_{mep} at 2000 rpm: comparison between the map-based, the pressure-based and the model-based controls. The values are reported in adimensional units, referring all the values to those measured at $b_{mep} = 1$ bar for the map-based control	105
Figure 5.17. Engine-out soot and NO_x emissions vs. SOI at 1400 rpm \times 104 Nm (a) and 3000 rpm \times full load (b): comparison between the map-based and the pressure-based controls during SOI sweeps. The values are reported in adimensional units, referring all the values to those measured with the baseline SOI (the lowest value in the x-axes) for the map-based control.....	106
Figure 5.18. Coefficient of variation of the peak firing pressure evaluated for the whole engine $CoV_{PFP,eng}$ vs SOI on the SOI/MFB50 sweep tests, at 1400 \times 104 and 3000 \times FL: comparison between the map-based and the pressure-based controls.	106
Figure 5.19. Coefficient of variation of the peak firing pressure $CoV_{PFP,eng}$ (a) and of the indicated mean effective pressure $CoV_{imep,eng}$ (b) evaluated for the whole engine, and amplitude of the dispersion range of the CN (c) on the EGR sweep tests under PCCI combustion mode: comparison between the map-based and the pressure-based controls.....	108
Figure 5.20. Engine operating points during the WHTC (blue markers) and the load ramps (red markers). The black solid line represents the full load curve.....	109

Figure 5.21. MFB50 values, averaged between the four cylinders, as a function of engine speed and <i>b_{mep}</i> on the engine map tests.....	110
Figure 5.22. Portion of the reference load variation transient profile, at 1400 rpm.	110
Figure 5.23. Transient load variation profile at 1400 rpm - MFB50 and SOI _{main} values: comparison between the map-based (a, without SOI correction), the pressure-based (b) and the model-based (c) controls.	111
Figure 5.24. Amplitude of the variation range of the MFB50 and related mean MFB50 variations during transient operations: comparison between the map-based (a, without SOI correction) and the pressure-based (b) controls.	112
Figure 6.1. Combination of CDC and PCCI calibration for the simulation of a dual-mode operation strategy.....	115
Figure 6.2. Engine speed and torque sequence over the WHTC cycle.....	117
Figure 6.3. Vehicle speed and gear sequence over the NEDC cycle.....	118
Figure 6.4. Engine speed and torque sequence over the NEDC cycle.....	120
Figure 6.5. Cumulated NO _x (a and b) and Soot (c and d) emissions over the simulated NEDC (a and c) and WHTC (b and d) cycles, with CDC (blue lines), single-injection PCCI (red lines) and multiple-injection PCCI (green lines). The black dashed horizontal lines represent reference Euro 5/Euro VI limits.	121
Figure 6.6. Engine-out NO _x (a and b) and Soot (c and d) maps for the simulated PCCI engine. The second-by-second engine operating points over the simulated NEDC (a and c) and WHTC (b and d) cycles are overlapped as blue stars.	122
Figure 6.7. Urea consumption maps for the simulated PCCI engine. The second-by-second engine operating points over the simulated NEDC (a) and WHTC (b) cycles are overlapped as blue stars. Urea consumption inside the PCCI area is null.	124
Figure 6.8. Cumulated urea consumption over the simulated NEDC (a) and WHTC (b) cycles, with CDC (blue lines) and single-injection PCCI (red lines).	124
Figure 6.9. Cumulated CO (a and b) and HC (c and d) emissions over the simulated NEDC (a and c) and WHTC (b and d) cycles, with CDC (blue lines), single-injection PCCI (red lines) and multiple-injection PCCI (green lines). The black dashed horizontal lines represent reference Euro 5/Euro VI limits.	125
Figure 6.10. Engine-out CO (a and b) and HC (c and d) maps for the simulated PCCI engine. The second-by-second engine operating points over the simulated NEDC (a and c) and WHTC (b and d) cycles are overlapped as blue stars.	126

Figure 6.11. Tailpipe CO (a and b) and HC (c and d) maps for the simulated PCCI engine. The second-by-second engine operating points over the simulated NEDC (a and c) and WHTC (b and d) cycles are overlapped as red stars...	127
Figure 6.12. Cumulated fuel consumption over the simulated NEDC (a) and WHTC (b) cycles, with CDC (blue lines), single-injection PCCI (red lines) and multiple-injection PCCI (green lines).....	128
Figure 6.13. Fuel consumption maps for the simulated PCCI engine. The second-by-second engine operating points over the simulated NEDC (a) and WHTC (b) cycles are overlapped as blue stars.	128
Figure 7.1. Differential pressure across the EGR cooler as a function of the working time in the F1C PCCI engine (repetition of a 2000×5 test over time).....	133
Figure 7.2. EGR cooler effectiveness as a function of the working time in the F1C PCCI engine (repetition of a 2000×5 test over time).....	133
Figure 7.3. Air (a) and EGR (b) mass flowrates as a function of the working time in the F1C PCCI engine (repetition of a 2000×5 test over time).....	135
Figure 7.4. Lambda (λ) values as a function of the working time in the F1C PCCI engine (repetition of a 2000×5 test over time).....	135
Figure 7.5. PFP (a) and MFB50 (b) values as a function of the working time in the F1C PCCI engine (repetition of a 2000×5 test over time).....	136
Figure 7.6. CN (a) and NO _x (b) as a function of the working time in the F1C PCCI engine (repetition of a 2000×5 test over time).....	136
Figure 7.7. Mass fraction burned x_b (a – left axis), HRR (a - right axis), in-cylinder pressure (b – left axis), and its derivative (b - right axis) versus crank angle position for different working times of the EGR cooler (3 repetitions of a 2000×5 test over time).....	137
Figure 7.8. Pressure drop across the EGR cooler for the F1C PCCI engine during DoE test plans at 2000×5, with clean (blue) and fouled (red) heat exchanger. The color-filled symbols refer to the central points of the test plans.	139
Figure 7.9. EGR rate for the F1C PCCI engine during DoE test plans at 2000×5, with clean (blue) and fouled (red) heat exchanger. The color-filled symbols refer to the central points of the test plans.	139
Figure 7.10. MFB50 values for the F1C PCCI engine during DoE test plans at 2000×5, with clean (blue) and fouled (red) heat exchanger. The color-filled symbols refer to the central points of the test plans.....	140
Figure 7.11. <i>bsfc</i> values for the F1C PCCI engine during DoE test plans at 2000×5, with clean (blue) and fouled (red) heat exchanger. The color-filled symbols refer to the central points of the test plans.	140

Figure 7.12. NO_x emissions vs. λ for the F1C PCCI engine during DoE test plans at 2000×5, with clean (blue) and fouled (red) heat exchanger. The color-filled symbols refer to the central points of the test plans..... 141

Chapter 1

1. Introduction

1.1 Overview

Over the past decades, the major concerns and regulations about air pollution and anthropogenic climate change have been driving the transport sector (as one of the most important contributors to these issues) towards the development of new technologies for clean and efficient vehicles. In fact, besides a common misperception in modern society is that no further developments are attainable in internal combustion engines (ICEs), mainly due to the overly advertised electrification process, research on this topic is still carried out extensively.

For the foreseeable future (i.e., over a short-to-medium-term scenario), the ICE will remain the dominant technology for the vast majority of the road vehicles, although a gradual increase in powertrain electrification is likely to be expected during this period [Midttun & Witoszek, 2016]. However, a transition to a clean and low carbon mode of transport is necessary, over a long-term scenario. At present, electric vehicles (EVs), when compared to an efficient ICE on a well-to-wheel analysis, provide few benefits in terms of CO₂ mitigation (and this will be likely true until 2030), while predicted CO₂ savings under different EV uptake scenarios will likely diverge between 2030 and 2050 [Hill, et al., 2019]. Nevertheless, this unavoidable transition process would be certainly easier as long as a cleaner and more efficient transport system is developed in the meantime.

In this context, increasing interest has been put in diesel engines, due to their superior fuel conversion efficiency if compared to their gasoline counterparts. However, diesel engines tend to suffer from higher emissions of nitrogen oxides (NO_x) and particulate matter (PM), and for this reason modern diesel vehicles are commercialized with complex and expensive after-treatment systems (ATS), which partially degrade their gain in fuel economy (since they require periodic regeneration strategies) and increase their costs (due to their precious metal contents and/or the need of catalytic reduction additives) [Ye, et al., 2012]. Therefore, a

deeper research and development is required to gain more insight about in-cylinder combustion characteristics, possibly exploiting new concepts to be applied on engines to accomplish the goal of reducing directly in-cylinder emissions.

The subject of this dissertation would like to fit into this background, dealing with the Premixed Charge Compression Ignition (PCCI) combustion concept for compression ignition engines, which holds the potential to simultaneously reduce soot and NO_x engine-out emissions, getting rid of their well-known trade-off, typical of the conventional diesel combustion (CDC) mode. Unfortunately, although a great deal of efforts has been put by engine researchers in the past years, PCCI remains a challenging concept towards a practical implementation in real vehicle applications, due to a number of issues including intense combustion noise (CN), combustion instability, worse fuel consumption, high unburned hydrocarbon (HC) and carbon monoxide emissions.

The experimental investigation presented in this Thesis is therefore aimed at further investigating the viability of early, high-EGR (exhaust gas recirculation) PCCI concept. Additional information and adequate comprehension of the phenomena involved will be provided, as well as contributions to improve techniques and methods to suitably implement PCCI to a real diesel engine platform rather than to research single-cylinder engines, dealt with by a vast part of the literature on the topic [Doosje, et al., 2012]. Firstly, the application of an early-PCCI concept to a 3.0-liter mass production diesel engine will highlight how far benefits may be achieved by using standard engine hardware and components, which feature a number of intrinsic challenges for PCCI, when injecting the fuel early [Leermakers, et al., 2011]. Then, the analysis will point out the results attained by introducing purposely designed engine hardware modifications (adapted to overcome the intrinsic PCCI limitation to low load) and introducing a proper PCCI calibration across the whole low-to-medium speed and load portion of the engine map. A focus will be held on the potentialities of the PCCI approach and on viable solutions to overcome its well-known drawbacks, such as real-time combustion control algorithms, uncooled exhaust gas recirculation strategies and split fuel injection patterns, while attention will be put on critical issues not sufficiently pointed out in the literature, such as the EGR cooler fouling mechanisms.

1.2 Pollutant and GHG emissions background

Air pollution and anthropogenic climate change are two of the main environmental threats human society has to face, over the long term.

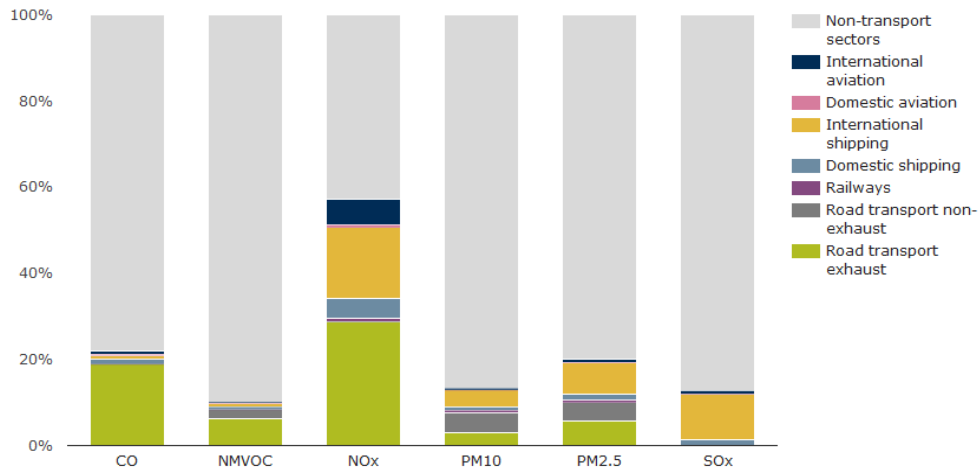


Figure 1.1. Contribution of the transport sector to total emissions of the main air pollutants, in the European Union [EEA, 2018a].

Poor air quality, especially in densely populated urban areas, is a serious health and environmental problem. This is due to the emission, by different sources and at levels that harm human health and the environment, of certain harmful ‘primary’ air pollutants, such as PM, NO_x, CO, HC and sulfur oxides (SO_x). Nearly all of them can undergo chemical transformations in the atmosphere, once emitted, creating ‘secondary’ pollutants, such as acid rain and photochemical smog. Transport, industry, power plants, agriculture and households all contribute to air pollution. Focusing on road transport sector, despite, in absolute terms, its pollutant emissions may not be as great as those from other sources (cf. Figure 1.1) [EEA, 2018a], the contribution due to circulating road vehicles is one of the most threatening. Indeed, population exposure to the pollutants released by this sector tends to be the most relevant, as they are generally emitted in densely populated areas where people live and work [EEA, 2016].

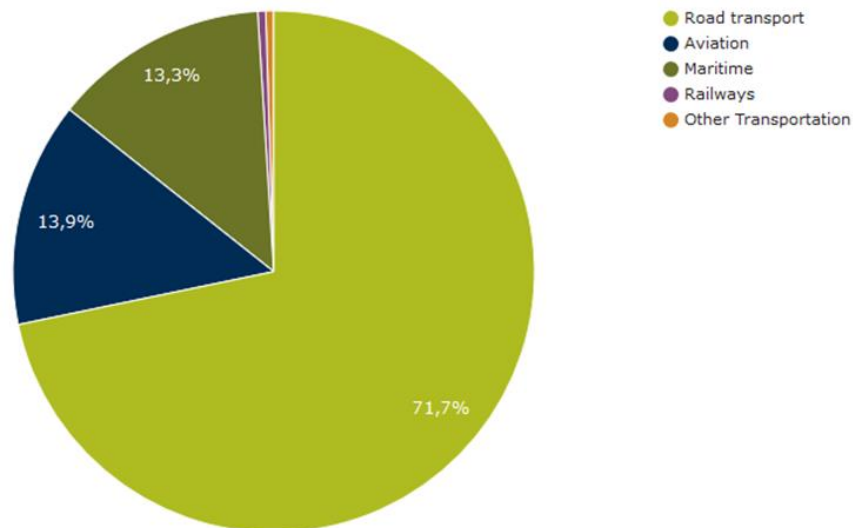


Figure 1.2. Share of transport GHG emissions, in Europe [EEA, 2018b].

Road transport is also one of the greatest sources of greenhouse gas (GHG) emissions, especially carbon dioxide (CO₂), accounting for more than 70% of the

transport GHG emissions (cf. Figure 1.2) and for around one fifth of the European Union's total [EEA, 2018b].

Policymakers are addressing these problems with increasingly stringent legislative control measures, to help minimize air pollutants and GHG emissions from different power sources, including the automotive sector.

Since the introduction of the Euro 1 regulation in 1993 for Light Duty Vehicles (LDVs), Euro standards have become progressively tighter and extended to include also Heavy Duty Vehicles (HDVs) [DieselNet, 2019]. These successive Euro standards have reached important reductions of the regulated pollutant emissions. At the same time, the European Union (EU) represents a leader also in terms of legislation for CO₂ emission targets for the transport sector (cf. Figure 1.3). New cars sold in the EU in 2017 have reached an average CO₂ emissions of 119 g CO₂/km [Tietge, 2018], although they are slowing down their CO₂ reduction rate compared to the previous years, highlighting challenges to meet future targets.

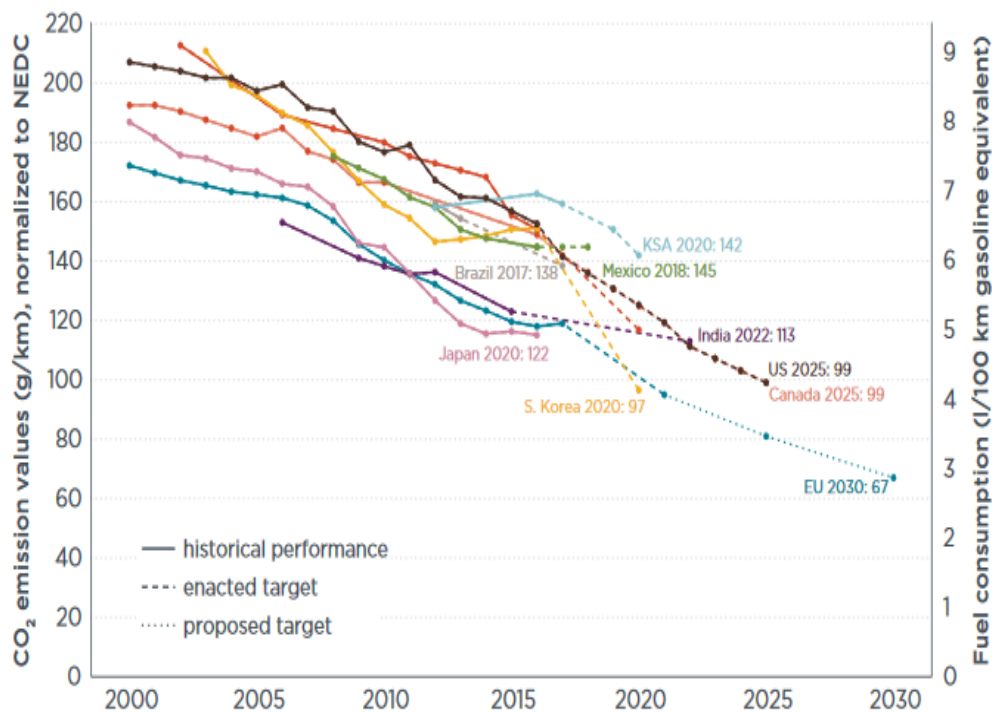


Figure 1.3. Historical and target (forecast) CO₂ regulations for new light-duty vehicles in different countries [Tietge, 2018].

1.3 Advanced diesel combustion concepts

In response to all these emission regulations and to the increasingly demand for highly efficient and cost effective vehicles, intensive research has been conducted to develop technologies aimed at reducing fuel consumption and pollutant emissions from ICES, in the past decades.

Due to their superior thermal efficiency, meaning lower fuel consumption and, thus, lower CO₂ emissions than their gasoline counterparts, in the past years diesel engines have played a crucial role for car manufacturers (especially in Europe) to meet the CO₂ targets on their entire vehicle fleet. Moreover, being the current

market penetration of Battery Electric Vehicles (BEVs) and Plug-in Hybrid Electric Vehicles (PHEVs) still limited, diesel engines represent a competitive solution for the short-to-medium-term future.

On the other hand, severe threats are related to the higher PM and NO_x emissions diesel engines are prone to emit. The current Euro 6/Euro VI regulations set very low levels of NO_x and PM for each new vehicle sold in the EU. For this reason, there have been upsurges in diesel engine technology research aimed at developing modern and efficient solutions, such as advanced fuel injection equipment, EGR systems, improved air handling and advanced turbocharger technology [Charlton, 2005; Taylor, 2008; Abdul Karim & Anwar Bin Sulaiman, 2018]. However, despite these efforts, further improvements in conventional diesel combustion technology are no longer sufficient in themselves to meet the stringent emission targets. Therefore, modern diesel vehicles are commercialized with ever more complex and expensive after-treatment systems (ATS), which partially degrade their gain in fuel efficiency [EEA,2016; Hooftman, et al., 2018]. Diesel Particulate Filter (DPF) technology, to abate PM, and Selective Catalytic Reduction (SCR) or Lean NO_x Trap (LNT) catalysts, to control NO_x, are the most commonly installed, in addition to the Diesel Oxidation Catalyst (DOC) systems to manage HC/CO emissions.

When dealing with possible strategies to improve diesel combustion and reduce its related harmful engine-out pollutants, possibly minimizing the after-treatment requirements and the related costs [Singh, et al., 2009], Low Temperature Combustion (LTC) modes, including Homogeneous and Premixed Charge Compression Ignition (HCCI/PCCI) concepts, represent some of the most attractive solutions.

In 1988 Kamimoto and Bae [Kamimoto & Bae, 1988] published a local equivalence ratio (ϕ) – local flame temperature (T) diagram that has been the reference for many studies on LTC concepts, being extensively discussed by Pickett et al. [Pickett & Siebers, 2004], Akihama et al. [Akihama, et al., 2001], and other researchers. The diagram shows the concentration of soot and NO_x emission formations as contour plots. A soot formation peninsula appears at ϕ greater than 2 and with peak flame temperatures between 1600 and 2500 K, whilst NO_x formation mainly occurs at temperatures above 2200 K and ϕ below 2. A version of the Kamimoto-Bae diagram is reproduced from [DieselNet, 2019] in Figure 1.4, to point out the different PCCI, HCCI and CDC operating paths.

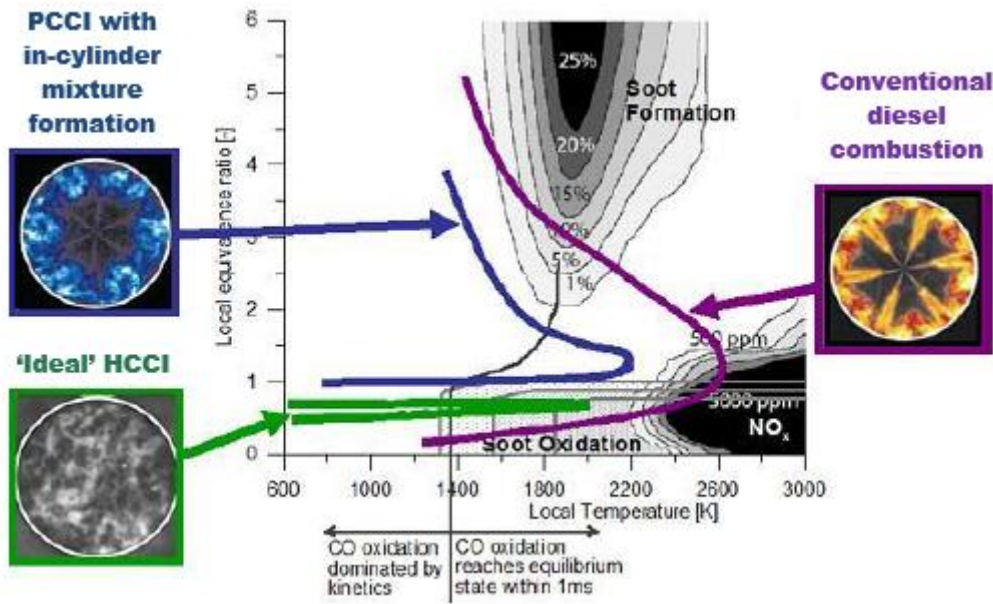


Figure 1.4. Comparison of diesel combustion modes in a local equivalence ratio (ϕ) and local flame temperature (T) diagram [DieselNet, 2019].

Conventional diesel combustion generally shows both “premixed” and “mixing-controlled” (or “diffusion”) phases, with their respective burned fractions depending, in part, on the engine load: the higher the engine operating conditions, the larger the burn fraction under mixing-controlled combustion [Pickett & Siebers, 2004]. The fuel injection, at high pressure, occurs during the last part of the compression stroke, i.e., just before the TDC. The fuel spray then atomizes, evaporates and forms a partially premixed mixture with the in-cylinder inducted charge, made up of fresh air and exhaust gases (coming from residuals and EGR). When the fuel auto-ignition conditions are reached, a portion of this mixture burns under premixed combustion, yielding to a sharp rise in the in-cylinder pressure. The fuel that does not take part to this premixed combustion burns later, under diffusive combustion. The combination of premixed and diffusive combustion stages tend to generate high levels of NO_x (especially when very high diffusion flame temperatures are established, exceeding 2500 K [Dec & Canaan, 1998]) and soot (generated inside the fuel-rich core of the diffusion flame envelope and only partially oxidized during the latest stages of combustion [Pickett & Siebers, 2006]), thus encompassing both the NO_x and the soot formation isles in Figure 1.4 (violet path).

An alternative combustion path, able to circumvent both soot and NO_x formation zones in the $\phi - T$ plot, is represented by HCCI combustion mode (cf. the green path in Figure 1.4). Its main characteristic is the creation of a homogeneous air-fuel mixture prior to the start of combustion (SOC) [Bendu & Murugan, 2014], with the fuel delivery occurring either externally, in the intake ports, or directly inside the cylinders, during the intake stroke or very early during the compression one, in proximity to the bottom dead center (BDC) [Musculus, et al., 2013]. In this way, the combustion temperatures are significantly lower than in the CDC regime, due to the enhanced premixed combustion, with the result of a hindered NO_x

formation, while the homogeneity of the mixture avoids the formation of fuel-rich regions, resulting in very low soot emissions as well [Stanglmaier & Roberts, 1999].

Another possibility is represented by PCCI combustion. This is achieved by injecting the fuel directly into the cylinders (but with shorter mixture preparation times than needed by HCCI) and using heavy amounts of EGR [d'Ambrosio, et al., 2016]. Such a solution brings to a loss of part of the homogeneity typical of HCCI, revealing to be a middle path between CDC and HCCI combustion modes (cf. blue path in Figure 1.4). The possible fuel injection strategies to reach PCCI mode lead to a further division of the PCCI concept into two subcategories, usually referred to as, respectively, “early-PCCI” (when the injection timing occurs earlier than in CDC regime) and “late-PCCI” (when the injection timing occurs later than in CDC regime). Focusing on the “early-PCCI” concept, the fuel is injected during the middle-to-late compression stroke, albeit well before the top dead center (TDC) location, into relatively low density gases which, in combination with the ignition-delaying effect of the EGR [Musculus, et al., 2013; d'Ambrosio & Ferrari, 2015a], effectively slow down the pre-ignition chemistry and provide large time for the air-fuel pre-combustion mixing. Therefore, the combustion process takes place at generally high premixed-to-diffusion ratios, resulting in local peak equivalence ratios low enough to circumvent the soot formation isle and in combustion temperatures mild enough to hinder, in turn, the evolution of polycyclic aromatic hydrocarbons (PAH) into soot particles [Akihama, et al., 2001]. Furthermore, the potential of the EGR to reduce the peak flame combustion temperatures below the threshold that gives rise to NO_x formation mechanisms is intensively exploited. This potential depends on three main effects, widely investigated in literature [Laddomatos, et al., 1997; Maiboom, et al., 2008; Park & Bae, 2014]: the dilution, the thermal and the chemical effects, even if the dilution effect has been demonstrated to be the predominant one [Laddomatos, et al., 1998].

The dilution effect is ascribed to the decrease in the oxygen concentration inside the intake charge, due to the recirculation of exhaust gases which partially replace fresh air. The main consequence is the deceleration of the mixing process between oxygen and fuel, resulting in a spatial extension of the flame region. Hence, the gas quantity that absorbs the heat release by combustion is larger, resulting in lower flame temperatures. Moreover, another consequence of the dilution effect is the reduction of the oxygen partial pressure, that has an effect on chemical kinetics of the elementary NO formation reactions.

The thermal effect is ascribed to the increase in the heat capacity of the intake charge, due to higher specific heat capacity of recirculated chemical species such as CO_2 and H_2O (triatomic molecules) compared with fresh air, which mainly consists of O_2 and N_2 (diatomic molecules). This results in lower gas temperatures during combustion, and particularly in lower flame temperatures.

The chemical effect is ascribed to the tendency of the recirculated CO_2 and H_2O molecules to dissociate during combustion. As the dissociation of these molecules is an endothermic chemical reaction, this results in a decrease in the flame combustion temperature.

Although LTC strategies seem to be very attractive for NO_x and soot mitigation, they share some challenges to be overcome towards possible mass production implementations. Increased incomplete combustion species emissions, high combustion noise, combustion instability and limited load range applicability are some of these common limitations.

The higher degree of premixed combustion typical of all LTC strategies is generally coupled with high HC and CO emissions, which can stem from either “under-mixing” of fuel or “over-mixing” phenomena [Musculus, et al., 2007]. “Under-mixing” can occur in PCCI applications when local mixture pockets suffer from local lack of oxygen, due to high EGR rates or insufficient mixing times. “Over-mixing” phenomena, instead, are commonly related to excessively lean mixture formations, which can go outside the fuel flammability limits. In addition, early fuel impingement on the cylinder walls or on the piston surface can be a major source of HC formation and emission [d’Ambrosio & Ferrari, 2015a], resulting in deterioration of fuel consumption, but also in lubricant oil dilution and higher risk of cylinder-ring sticking [Shibata, et al., 2016].

Combustion noise (CN) is another common limitation for LTC concepts. The highly premixed combustion process is able to produce a sudden and sharp charge pressure rise, due to the high rate of heat released during a short period of time, which induces strong engine block vibrations and subsequent noise emission [Torregrossa, et al., 2013]. For instance, especially when the highest possible loads in PCCI operations are reached, in-cylinder pressure (p_{cyl}) derivative values can hit values up to 15-20 bar/°CA [d’Ambrosio, et al., 2018], while acceptable pressure rise limits are generally around 8 bar/°CA [Dec & Sjöberg, 2007].

With regards to high load operation of LTC concepts, excessive increase in the in-cylinder pressure rates is one of the main constraints. Furthermore, difficulties are reported in achieving adequate control of the EGR-air-fuel premixing levels with growing loads, which in turn may negatively influence soot emissions [Beatrice, et al., 2008]. Indeed, EGR can only be used up until the oxygen availability limits are reached, i.e. up to the point for which further increases in the fuel injection quantity are ineffective because of the unavailability of oxygen [Saxena & Beyoda, 2013]. Rising loads also cause higher heat release, thus creating difficulties in keeping the cylinder temperature and pressure conditions low enough to mitigate NO_x formation mechanisms.

However, with specific regard to HCCI operations, the major challenge is represented by the hard control of ignition timing, which influences power and efficiency of the engine [Bendu & Murugan, 2014]. In fact, the homogeneous mixture preparation is essentially decoupled from auto-ignition process (this latter being affected by a number of different factors, including intake charge temperature, wall temperature, fuel chemistry, thermodynamic properties, etc. [Dec & Sjöberg, 2004]). Thus, the absence of a direct-ignition trigger (either a spark plug, like in gasoline engines, or the high thermodynamic conditions at SOI, like in CDC applications) makes the HCCI combustion control over a wide range of engine operating conditions an extremely difficult task. On the contrary, for PCCI operations the combustion phasing can be still partially coupled with the fuel

injection timing [Kook, et al., 2005], hence revealing much more practical than the HCCI concept.

In general, LTC regimes are reported to be highly sensitive to minor variations in the operating conditions [Cong, et al., 2011]. In particular, the sensitivity of the combustion process to the EGR level is extremely high and affects both engine performance and pollutant emissions. Therefore, combustion instability (arising in torque oscillations, up to the occurrence of misfiring events) may occur due to uneven EGR distribution among cycles and/or cylinders. This problem is expected to become even worse during fast engine dynamics, because of the different time constants characterizing the response of air- and fuel-paths [Carlucci, et al., 2014].

Finally, the large cooled EGR rates featured by PCCI modes are reported to increase the SOF (Soluble Organic Fraction) of the particulate matter [Hong, et al., 2011]. Even if SOF can be potentially treated by a DOC, it may still be harmful since it is the main agent, together with soot particles, responsible for EGR cooler fouling phenomena, which consist in the progressive sticking of exhaust gas particles on the surface of the heat exchanger, building up an insulating layer [Abarham, et al., 2013]. The creation of such a layer on the walls of the EGR cooler degrades its heat transfer efficiency and causes a progressively increasing pressure drop, up to severe clogging, hindering the correct gas flow through the EGR system [Kim, et al., 2008]. This could be a major reliability issue when PCCI concepts are dealt with, since the EGR quantity is one of the most important operating parameters.

1.4 Possible technologies to enable LTC operations

To support the enablement of diesel combustion systems towards such a more premixed combustion mode, several technologies have been studied and need to be further developed, such as real-time combustion controls, dual-loop EGR systems, variable intake valve closing (IVC) mechanisms, advanced fuel injection systems, etc. [National Research Council, 2011].

1.4.1 Real-time combustion control techniques

The growing computational efficiency of modern engine control units (ECUs) is providing the chance to implement more and more complex techniques for real-time combustion control in diesel engines. In particular, the adoption of real-time combustion algorithms are thought to be an almost mandatory technology to enable PCCI operation in real vehicles [Catania, et al., 2011; Carlucci, et al., 2014; Finesso, et al., 2015; Spessa, et al., 2017], since LTC combustion modes are extremely sensitive to the boundary conditions of their oxidation process (such as intake charge temperature, boost level, oxygen concentration, etc.), making the achievement of a stable combustion in every operating condition a tough task [Kimura, et al., 2002]. This issue is expected to become even more difficult during engine transient operations, which might lead to mismatches between fuel and air system setpoints, usually calibrated in steady-state at the engine test bench

[Guzzella & Onder, 2010], resulting in lower combustion stability (i.e., torque oscillations, misfiring events) and louder combustion noise that directly affect the driving comfort of the vehicle [Carlucci, et al., 2014].

Several types of combustion controls may be implemented, distinguished by the proper combustion metrics and/or exhaust pollutant emissions selected to be monitored in real-time. Moreover, these controls may be roughly categorized into two major types: closed-loop and feed-forward (or model-based).

Closed-loop methods are often based on direct measurements of the selected observed parameters. For example, as long as a combustion metric related to the combustion phasing is selected, in-cylinder pressure signal measurements may be performed [Wlodarczyk, 2006; Willems, et al., 2010; Carlucci, et al., 2014]. The derived signal, suitably post-processed, directly provides information about the combustion development, on both a cycle-to-cycle and cylinder-to-cylinder basis. Therefore, it can be exploited to control the selected combustion metric by correcting in real-time proper engine calibration parameters [Schten, et al., 2007].

Model-based (also referred to as “feed-forward”) approaches, instead, rely on the estimations performed by means of purposely built models, rather than to direct measurements performed by dedicated sensors such as in-cylinder pressure transducers (which may also represent an additional cost) to adapt the main engine calibration parameters in real-time [Finesso, et al., 2017]. In particular, the task of engine combustion modeling can be accomplished with different degrees of detail and, consequently, computational effort.

The highest degree of detail to predict the in-cylinder combustion process is achieved by 3D-CFD models [Cipolla, et al., 2007; Jemni, et al., 2011; Fontanesi & Giacopini, 2012], which provide the potential to reproduce quite reliably the whole physical and chemical process taking place inside the combustion chamber, but require an outstanding computational time. Therefore, their application as real-time combustion control algorithms is unrealistic.

A lower degree of detail may be attained by multi-zone modeling approaches [Hiroyasu, et al., 1983; Jung & Assanis, 2001], which generally include a fuel spray model coupled with a thermodynamic combustion model that is based on the discretization of the in-cylinder charge into multiple zones, each considered as homogeneous. In this way, multi-zone models are able to estimate in-cylinder gradients of temperature and chemical composition, revealing to be suitable for a coupling with pollutant formation sub-models. Unfortunately, at least as long as the computational performance of modern ECUs are considered, the computational time required to run them is still not feasible with real-time combustion control applications [Finesso, et al., 2017].

To decrease the computational time in comparison to the previously cited approaches, while still keeping satisfactory predictive capabilities (both in steady-state and transient engine operations), the so-called “zero-dimensional” (0D) models may be a viable solution [Rakopoulos & Giakoumis, 2006]. They are relatively simple models, with no spatial resolution, that exploit only lumped parameters variables [Guardiola, et al., 2012] and, thanks to their low computational effort required, reveal to be particularly suitable for on-board ECU applications.

Moreover, they are physically consistent, so that they do not require a high calibration effort, and at the same time their accuracy is still acceptable outside the calibration range [Finesso, et al., 2015].

Another category of models, often used in the field of automotive engine and combustion control, includes artificial intelligence systems, such as genetic algorithms (GAs), support vector machines (SVMs) and artificial neural networks (ANNs) [Asik, et al., 1997; Uzun, 2012; Finesso, et al., 2017]. They have the potential to capture complex non-linear behaviors by means of relatively simple mathematical operations, without the need of any detailed physical knowledge of the process (in fact, they are also referred to as “black box” approaches). Their computational time is generally small, so that they are appropriate candidates for feed-forward control algorithms to be implemented in the vehicle ECUs. Amongst the drawbacks, the “calibration training” of such a type of models usually requires a massive number of experimental tests. Moreover, their predictive capability is usually not reliable outside their calibration range.

1.4.2 Dual-loop EGR system

The use of increased EGR levels, during PCCI operations, to suppress the formation of both NO_x and soot, creates two non-trivial difficulties in addition to the previously commented remarks. First, when running at the lowest loads, the engine requires EGR rates up to 60÷70% [Li, et al., 2008], meaning that with a standard high-pressure (short-route) EGR system, only 30÷40% of the gas flowrate streams through the turbocharger, since the remainder is recirculated back into the intake manifold. As a result, the turbine generates less torque, hampering the ability of the turbocompressor to boost the intake pressure. This leads to less in-cylinder intake charge mass, richer mixtures and increased soot formation, as well as lower oxygen availability, which may prevent an adequate post-combustion oxidation of both soot and HC/CO molecules. Secondly, such large EGR fractions mean that the EGR cooling requirements increase, i.e. larger-volume and more effective EGR coolers are needed. Not only do these larger EGR coolers lead to packaging issues (in already crowded engine compartments), but they are also subject to fouling mechanisms (as previously pointed out), through the condensation of heavy HC present in the EGR flow, which form deposits on the EGR cooler walls decreasing their cooling efficiency [Styles, et al., 2008].

At this regard, a low-pressure (long-route) EGR may provide better mixing of air and EGR and, since it increases the gas flow through the turbocharger, it may shift its operating point to higher efficiency values [Doosje, et al., 2012]. Moreover, since the EGR stream is forced to flow through the ATS system, it is cleaned from the majority of soot and HC content before being recirculated through the EGR cooler, possibly reducing fouling issues. As a drawback, increased turbocharger lag may be detected during transient operations, due to the enlarged length of the EGR circuit, resulting in soot emission spikes due to the instantaneous lack of air and delay of boost pressure [Hagena, et al., 2006].

To exploit all the benefits of both the EGR circuit configurations, achieving high flexibility, dual-loop EGR systems has shown outstanding potentialities. For example, Yan and Wang [Yan & Wang., 2009] explored the possibility of using a VGT and a dual-loop EGR system to enable LTC operations. They have shown how such a solution may achieve a decoupled control of the in-cylinder oxygen amount, inert gas amount and intake gas temperature simultaneously.

1.4.3 Variable intake valve closing (IVC) mechanisms

Late intake valve closing (LIVC) timing may play a significant role to enhance LTC performance towards efficient and clean combustion. For this purpose, variable intake valve-closing devices, such as VVT (variable valve timing) or VVA (variable valve actuation), may be used to lower the in-cylinder temperatures by reducing the effective compression ratio by closing the intake valve later in the compression stroke [Nevin, et al., 2007]. Yutaka Murata et al. [Murata, et al., 2008] showed how a Miller-PCCI Combustion mode may be achieved by prolonging the ignition delay (ID) of the injected fuel through an effective compression ratio reduction with LIVC, while keeping the expansion ratio unchanged.

As long as the IVC timing is delayed, the boost pressure should be raised as well, to keep the required intake gas flowrate into the cylinders, since cylinder gases tend to be expelled out of the intake valve while the piston is moving upwards from the BDC, due to the extended valve-open period [Zhou, et al., 2018]. Furthermore, due to the lower in-cylinder temperatures, it is conjectured that less EGR will be needed to decrease NO_x and soot emissions, which may be also important to extend the LTC load range applicability.

1.4.4 Advanced fuel injection systems

Significant improvements in electronically controlled, high-pressure, Common-Rail fuel injection systems have contributed to accelerate the development of diesel-fueled PCCI combustion strategies, since mixture preparation for PCCI usually occurs through the direct injection of the fuel into the cylinder [Kimura, et al., 2001; Walter & Gatellier, 2002].

The approach of relatively early fuel injection timings to achieve PCCI mode, as said, leads typically to large ID values, due to the low in-cylinder gas temperatures and pressures, which do not facilitate fuel vaporization. As a matter of fact, complete vaporization is often not possible [Kim, et al., 2008], resulting in impingement of liquid fuel on the cylinder liner (wall-wetting) and/or piston surface (piston-wetting) and leading to worsened fuel consumption, lubricant oil dilution and high emissions of incomplete combustion species [Boot, et al., 2010].

Some of the strategies to reduce fuel-wall impingement from PCCI include late direct injection or the use of narrow spray cone angle injectors, as long as early direct injections are used [Manimaran, et al., 2013]. For example, the alternative of using narrow spray cone angle fuel injector nozzles (i.e., less than 100-degree cone angle) to avoid spray-wall interaction at early injection timings was explored by

Walter and Gatellier in [Walter & Gatellier, 2002]. A narrow spray cone angle concept might also be exploited in conjunction with multiple injection PCCI patterns and smaller diameter injector holes, to limit too high liquid fuel penetration [Lechner, et al., 2005].

1.5 Practical implementation of LTC concepts

The previous paragraph has pointed out features, benefits and challenges towards the implementation of HCCI/PCCI combustion modes. However, although several studies have been carried out on these various aspects of LTC concepts, only few practical implementations have been demonstrated in real engines. Some of them are listed hereinafter.

The UNiform BULky combustion System (UNIBUS) was proposed by Toyota [Yanagihara, 1996; Yanagihara, 2001] and involves an early injection timing (around 40÷50 °CA bTDC, forming a highly premixed mixture) followed by a delayed fuel injection after the TDC to trigger the combustion. Remarkably low NO_x emissions and simultaneous near zero smoke have been reported. The UNIBUS operation technique is able to cover half the speed and load engine map [Hasegawa & Yanagihara, 2003], but may be ineffective as long as inappropriate compression ratios and/or intake temperatures are dealt with, since this strategy is effective only if the second trigger injection takes place far enough before auto-ignition [Hardy & Reitz, 2006].

The Modulated Kinetics (MK) concept was developed by Nissan [Kimura, et al., 2001; Kimura, et al., 2002] and is a promising concept that relies on high EGR rates, increased fuel injection pressure, enhanced swirl levels and single late (i.e., close to or after the TDC) fuel injection event, to limit the formation of NO_x and soot. The late injection of diesel may avoid most of the issues associated with fuel-wall impingement [Lachaux, et al., 2008], but the relatively short ID of diesel fuel limits this approach only to low engine loads. Indeed, since the ID should be kept longer than the injection duration, in order to allow an appropriate pre-mixing process, an upper limit sets up on the fuel quantity deliverable at realistic rail pressures. Therefore, to ensure that the ID keeps longer than the injection duration, high rail pressures, reduced compression ratio and enhanced EGR gas cooling should be applied for advanced MK engines [Kawamoto, et al., 2004].

Narrow Angle Direct Injection (NADI) technique, developed by the Institut Français Du Pétrole (IFP), realizes the HCCI combustion concept by exploiting narrower injector spray cone angles to let the fuel being sprayed in proximity of the center of the piston head, preventing fuel impingement on the cylinder walls and consequently reducing the emissions of incomplete combustion species [Walter & Gatellier, 2002]. This is coupled with an amended combustion chamber (and piston bowl) design, suitable for the narrow-angle injection and able to enhance the creation of a homogeneous mixture as well as to facilitate multiple-stage injection strategies. However, higher load limitations are still present, thus requiring a shift to CDC when the engine load increases. Moreover, even if the narrow cone angles

may prove remarkably suitable at low load LTC conditions, they may inhibit good performance at high load, when CDC is required [Lechner, et al., 2005].

1.6 Outline of the Thesis

At first, in Chapter 2, the potentialities of an early-PCCI concept will be evaluated on a 3.0 l, 4-cylinder, Euro VI production diesel engine (F1C Euro VI) provided by FPT Industrial and designed to run under CDC mode, limiting the PCCI range applicability to a low speed/low load working area of the engine map.

Experimental tests, carried out on a modified engine (referred to as F1C PCCI), derived from the conventional F1C Euro VI engine but specifically designed to run under PCCI combustion mode, will be discussed starting from Chapter 3, highlighting how the hardware amendments have enlarged the PCCI operating range. With the aim to address the increase in tailpipe HC and CO emissions due to PCCI application, especially at low load and speed, the possible benefits deriving from a “hot” EGR strategy (i.e. featuring uncooled exhaust gas recirculated into the engine without passing through the EGR cooler, bypassing it) will be analyzed, too.

The effects of multi-pulse (i.e., double and triple) fuel injection strategies will be compared in Chapter 4 to those pertaining to a baseline single-pulse PCCI combustion calibration, to highlight their potential of reducing engine-out HC and CO emissions while dampening excessive CN levels and, possibly, fuel consumption.

Then, a “zero-dimensional” (0D) model for the estimation of the EGR flowrate will be presented and discussed in Chapter 5, highlighting how this could be potentially suitable for real-time control applications if implemented on-board the ECU. Moreover, the implementation of a pressure-based and a model-based combustion algorithms, able to control in real-time the MFB50 by properly shifting the start of injection (SOI) of the main pulse, will be discussed on the basis of experimental tests carried out on the F1C Euro VI engine.

Chapter 6 will be dedicated to a preliminary assessment of the potentialities of single- and multiple-injection PCCI along simulated NEDC and WHTC cycles. Interpolation of steady-state maps of exhaust pollutant emissions, fuel and urea consumptions will give an estimation of possible benefits/penalties compared to a reference CDC case.

Finally, the detrimental effect of the progressive EGR cooler fouling on performance and emissions will be presented and discussed in Chapter 7.

Chapter 2

2. PCCI combustion potentialities in a conventional diesel engine

2.1 Preliminary experimental tests on PCCI concept¹

A preliminary experimental investigation on the PCCI combustion concept has been carried out in a conventional diesel engine apparatus, applying an early single fuel injection strategy. The aim was to highlight the most important parameters affecting such a type of combustion concept and to study their influence on engine performance and engine-out pollutant emissions. Furthermore, this investigation has allowed the evaluation of the applicability range of the PCCI combustion mode in terms of speed and load on a conventional engine.

2.1.1 Experimental setup

The research facility for this part of the work was based on a fully instrumented 3.0 l, four-cylinder, four-stroke Euro VI² production diesel engine (F1C Euro VI) by FPT Industrial. Its main technical specifications are listed in Table 2.1. It is equipped with a short-route (high-pressure) cooled EGR circuit, featuring the EGR poppet valve placed upstream the EGR cooler. The EGR flow is driven back into the intake manifold by the positive pressure differential established between the exhaust and the intake lines. Should not it be enough, an exhaust flap is placed downstream the turbine to create exhaust backpressure, increasing the EGR flowrate. The engine is also equipped with a high-pressure Common Rail fuel injection system, endowed with solenoid injectors, and a variable geometry turbine (VGT).

During the installation of the engine at the testbed, low-frequency pressure transducers and thermocouples were placed in several positions along the engine circuit (such as upstream and downstream the turbocompressor, the intercooler and

¹ Most of the contents of this Section have been previously published in [d'Ambrosio, S., Iemmolo, D., Mancarella, A., & Vitolo, R. (2016). "Preliminary optimization of the PCCI combustion mode in a diesel engine through a design of experiments". *Energy Procedia*, 909-916. doi:10.1016/j.egypro.2016.11.115].

² European emission standards for new Heavy-Duty diesel engines are commonly referred to as Euro I ... VI, while Arabic numerals are used (Euro 1 ... 6) for Light-Duty vehicle standards. The considered engine application features a EURO VI Heavy-Duty homologation, therefore all of the research topics carried out hereinafter will deal with the engine only, since it is equipped to reference vehicles with technically permissible maximum laden mass over 3.5 tons.

the turbine, in the intake and exhaust manifold, etc.) to measure their pressure and temperature. Four high-frequency piezoelectric pressure transducers (Kistler 6058A) were also fitted to the glow-plug seats of each cylinder to measure the p_{cyl} time-histories, referenced on the basis of the measurement of the intake manifold absolute pressure provided by a high-frequency piezoresistive pressure transducer (Kistler 4007C).

Table 2.1. Main technical specifications of the tested engine

Engine type	3.0 l Euro VI 16V
Displacement	2998 cm ³
Bore / stroke	95.8 mm / 104 mm
Connecting rod	158 mm
Compression ratio	17.5
Valves per cylinder	4

The dynamic test bed where all the experimental tests were carried out is at the Internal Combustion Engines Advanced Laboratory of the Politecnico di Torino. Its equipment includes a cradle-mounted AVL APA 100 dynamometer, an AVL KMA 4000 system (for continuous fuel consumption measurement), an AVL AMA i60 system (for the raw gaseous emissions measurement), an AVL 415S smokemeter (for steady-state tests) or an AVL 439 opacimeter (for transient tests). The AVL AMA i60 system allows the simultaneous measurement of HC, NO_x/NO, CO/CO₂ and O₂ by means of two complete analyzer trains, giving the possibility to measure these gaseous concentrations both at the intake and the exhaust. All of the abovementioned measurement devices are controlled by PUMA Open 1.3.2 and Indicom automation systems. The CAMEO software can be used when automatic tests (for instance, related to DoE analysis) are required.

2.1.2 Early single injection PCCI at low speed and low load

A preliminary analysis of an early single injection PCCI application has been carried out and will be shown hereinafter. The investigation has been limited inside a narrow area of the F1C Euro VI engine map, bounded at low load and low-to-medium speed (i.e., up to $b_{mep} = 2$ bar and speed $n = 2000$ rpm). This is because the tested engine, designed for type-approval homologation to run under CDC mode, exhibited a large number of constraints when trying to achieve higher speed and load conditions under PCCI combustion mode (while keeping a stable, low NO_x and low soot combustion performance). These constraints include demanding EGR cooling requirements, troublesome fuel injection targeting (due to early timings requested), too high compression ratio (CR). In particular, when the engine load was increased, the recirculated EGR mass flowrates became progressively hotter, and the EGR cooler turned out to be inadequate to cope with the increasingly higher cooling performance required. The larger fuel injection quantities at higher loads were troublesome to be faced, too. This is because the fuel spray targeting angle from the injectors was not optimized for early-PCCI injection timings. This contributed to incomplete exploitation of all the in-cylinder oxygen present in the

bowl and in the squish areas, causing remarkably steep rise of soot, HC and CO emissions when increasing the load and, consequently, progressively advancing the injection pattern. Moreover, the high CR, suitable for CDC applications, led to excessive peak combustion pressure and temperature conditions, with consequent quickly rising noise and NO_x levels when rising the engine load.

The results of the analysis will be discussed with reference to a single engine operating point, namely 1800×1 (expressed in terms of speed n [rpm] × $bmeP$ [bar]), representative of the low load and low-to-medium speed area of the engine map investigated.

Many parameters, including (but not limited to) fuel injection pressure, number of injections, timing of the injection pattern, boost pressure and EGR rate, are known to greatly affect PCCI combustion outcomes [Kook, et al., 2005; Kook, et al., 2008; Jayashankara & Ganesan, 2010]. The EGR is the main driver for NO_x emission abatement, thanks to its previously described dilution, thermal and chemical effects, all able to reduce flame combustion temperatures. Accordingly, enhancing the premixed combustion stage by advancing the fuel injection timing (i.e., the SOI) has the potential to simultaneously decrease also soot emissions. In order to highlight these effects, Figures 2.1-2.7 show several EGR sweeps at different SOI levels, ranging between 16 and 30° bTCD. A single fuel injection strategy was chosen, at this preliminary stage of the analysis. To perform the tests, the EGR valve was kept wide open, while the EGR rate was modulated by varying the throttling position of the exhaust flap. The VGT rack was set to the maximum closure position in order to obtain the maximum achievable value of boost pressure (actually very limited, due to the low engine load conditions), while the rail pressure was kept constant at 580 bar (equal to its setpoint in the baseline Euro VI calibration of the engine).

The engine-out pollutants (soot, NO_x, HC and CO) were considered in terms of brake specific emissions (expressed in g/kWh) and evaluated as the ratio between each pollutant flowrate and the brake power of the engine. The EGR rate (X_{EGR}), used as abscissa value in the following Figures 2.1-2.4 and 2.6-2.7, is defined in Eq. (1) as the ratio between the recirculated exhaust gas mass flowrate and the total mass flowrate inducted in the cylinders:

$$X_{EGR} = \frac{\dot{m}_{EGR}}{\dot{m}_{EGR} + \dot{m}_a} \quad (1)$$

where \dot{m}_{EGR} and \dot{m}_a represent the EGR and fresh air mass flowrates, respectively. In the present investigation, the calculation of X_{EGR} was performed considering the accurate methodology developed in [d'Ambrosio et al., 2011], which requires the measurement of the volumetric concentrations of all the species at the engine exhaust as well as the knowledge of the composition of the inlet charge.

Specific emissions and fuel consumption

Figure 2.1 shows the effect of various EGR rates and SOI values on NO_x (Figure 2.1(a)) and soot (Figure 2.1(b)) emissions at the analyzed engine point 1800×1.

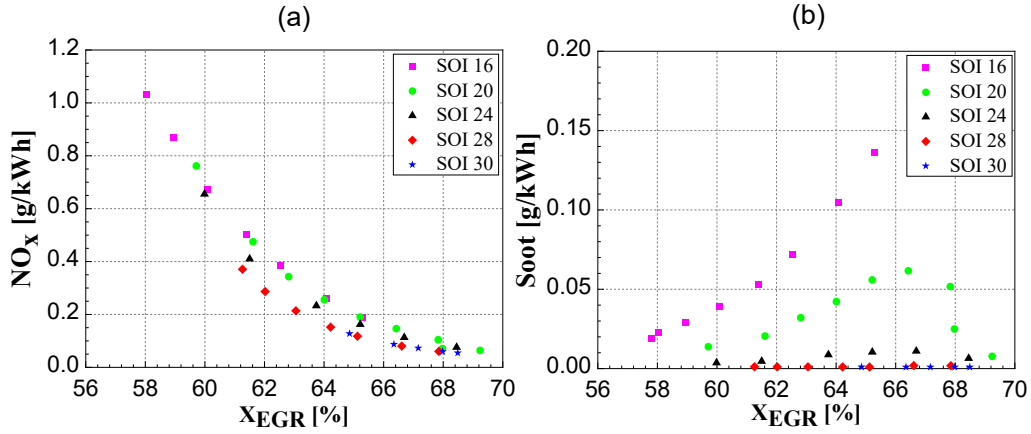


Figure 2.1. NO_x (a) and soot (b) emissions as a function of X_{EGR} , at 1800x1.

As previously stated, EGR may be effectively used to decrease the flame combustion temperatures, hence hindering NO_x formation mechanisms and, consequently, the related emission. This is particularly evident from Figure 2.1(a): increasing the EGR rate (from 58% to nearly 70%) gives the possibility to monotonically decrease NO_x levels, with minor influence of the particular SOI value implemented. This decreasing non-linear trend is quite steep (from 1 to 0.2 g/kWh) when passing from X_{EGR} values of 58% to around 64-65%. However, once these X_{EGR} values are reached, an extra 5% increase in the EGR rate would be required for a relatively small further reduction of NO_x (from 0.2 to 0.1 g/kWh). This may result in poor returns of cost-benefits, as will be highlighted in the following Figures considering all the other outcomes under analysis.

The use of EGR, of course, greatly affects also soot emissions, as Figure 2.1(b) highlights, and, unlike in the case of NO_x emissions, a non-trivial influence of SOI values on X_{EGR} -soot trends can be observed. Engine-out soot emission is the result of the balance of two competing mechanisms, i.e. soot formation and oxidation. Inducting more EGR into the cylinders leads to both lower combustion temperatures and reduced oxygen concentration, and both the soot formation and oxidation rates are highly dependent on these parameters, as already shown in Figure 1.4. For CDC applications, it is generally found in literature [Angrill, et al., 2000] that soot oxidation is affected more than soot formation by the lower in-cylinder temperatures and oxygen concentration brought by the charge dilution of the EGR. Conversely, when very high EGR levels are used in LTC applications, both the combustion temperatures may be reduced and the charge premixing, due to the long ID, may be increased so much, that the combustion is prevented from operating encompassing ϕ -T areas where soot formation can occur [Akihama, et al., 2001].

As a matter of fact, when the lowest SOI value is implemented (SOI = 16° bTDC, cf. the violet squares in Figure 2.1(b)), the engine-out soot emissions monotonically increase when more EGR is introduced. The in-cylinder soot formed in these conditions may either increase, if lack of oxygen prevails, or decrease, if lower temperatures prevail. In this case, the dominant consequence of increasing

EGR at SOI = 16° bTDC seems to be a less effective soot oxidation, resulting in the experienced increasing trend of engine-out soot.

When further advancing the fuel injection timing (SOI = 20° bTDC, cf. the green circles in Figure 2.1(b)), engine-out soot emissions are found to rise first, up to 0.06 g/kWh when passing from X_{EGR} values of 58% to around 66%. However, when an EGR rate of approximately 66% is reached, engine-out soot is found to suddenly drop with further X_{EGR} increments, up to 0.01 g/kWh when the EGR rate reaches nearly 70%. Since soot oxidation rates are expected to decrease with charge dilution, the drop of engine-out soot at the highest EGR rates has to be ascribed to the reduced formation rates.

Earlier fuel injection timings than 20° bTDC (cf. the black triangles, red diamonds and blue stars in Figure 2.1(b)) show the potential to cut engine-out soot emissions to very low levels, regardless of the particular X_{EGR} implemented. In these conditions, the ID values are high enough to allow a suitable premixing of the fuel with the inducted charge. This is able to avoid the formation, within the cylinders, of locally fuel-rich mixture pockets (with $\phi \geq 2$), which are known to be the main cause of soot generation [d'Ambrosio & Ferrari, 2015a] and, at the same time, the very high levels of charge dilution should limit the flame temperature to levels at which the soot formation rate is extremely low.

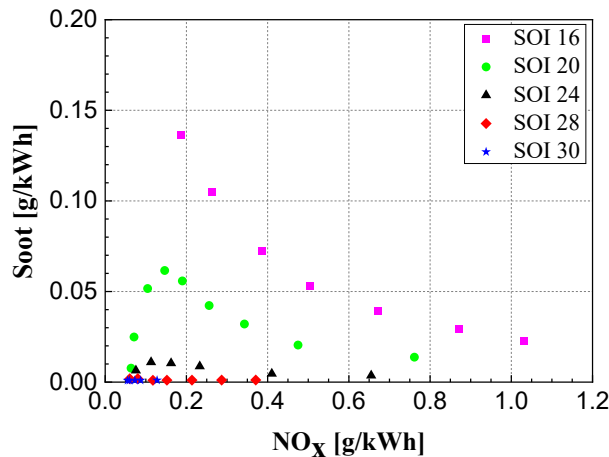


Figure 2.2. Soot-NO_x trends, at 1800×1.

The evidence of what observed from Figure 2.1 suggests that, during the the tests, the engine switched from CDC-like mode to a high-EGR low-sooting PCCI strategy, when SOI ≥ 20° bTDC were implemented. This is even more evident if Figure 2.2, which combines engine-out soot in the y-axis and NO_x in the x-axis, is observed. With a SOI = 16° bTDC (cf. the violet squares), a clear soot-NO_x trade-off, typical of CDC, is present: as long as EGR dilution is increased, lower flame temperatures reduce NO_x production but decrease soot oxidation, ultimately leading to higher engine-out soot emissions. A simultaneous reduction of both engine-out soot and NO_x is achievable only if SOI values ≥ 24° bTDC are applied, or if the highest EGR rates are implemented with SOI = 20° bTDC.

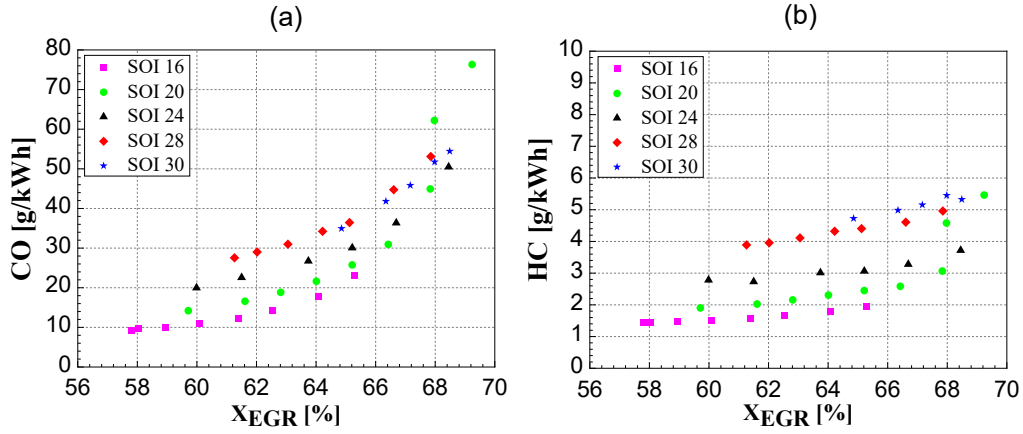


Figure 2.3. CO (a) and HC (b) emissions as a function of X_{EGR} , at 1800×1 .

Both CO and HC emissions are typically small for conventional, high temperature diesel combustion modes. Although large amounts of incomplete combustion species can be generated inside fuel-rich regions, mostly as a consequence of “under-mixing” mechanisms, the high combustion temperatures reached throughout the CDC process make CO and HC molecules to be easily oxidized in the latest combustion stages [Adomeit, et al., 2004]. On the contrary, when PCCI strategies are implemented, significant levels of both engine-out CO and HC emissions are generally observed, especially at high EGR dilution. This is confirmed by Figure 2.3, which reports engine-out CO (Figure 2.3(a)) and HC (Figure 2.3(b)) emissions as a function of X_{EGR} for the EGR sweep tests at different SOI values, for the analyzed engine point 1800×1 .

Expectedly, the lowest emissions of incomplete combustion species are observed with the lowest combination of SOI (16° bTDC, cf. violet squares in Figure 2.3) and X_{EGR} , which sets up a CDC-like combustion mode. Nevertheless, starting from these conditions, either advancing the fuel injection timing or increasing the EGR rate (i.e., approaching PCCI combustion modes) leads to worsened emissions of both CO and HC. As previously explained, the enlarged ID values obtained in these ways allow larger and larger amounts of fuel to be highly premixed with the inducted charge. This creates lower ϕ mixture pockets which burn at lower temperatures, hindering a complete combustion process. Moreover, advancing the SOI values also tends to intensify the risk of wall wetting phenomena, due to the injection event occurring in lower and lower gas density environments, while growing levels of EGR dilution induce lower combustion temperatures, which mean that the abundant HC and CO molecules that are generated will last less time above the temperature thresholds (around 1500 K for CO and 1200 K for HC [Kim, et al., 2009]) needed to undergo a complete oxidation processes in engine time scales. Therefore, CO and HC formation rates are increased and, simultaneously, their oxidation rates slowed down, justifying the trends observed in Figure 2.3.

Figure 2.4 shows the effect of EGR rates and SOI values on $bsfc$ and CO_2 emissions. Although a linear dependence exists between the emission of carbon dioxide and fuel consumption, in CDC applications [Mickūnaitis, et al., 2007],

comparing the trends of $bsfc$ and CO_2 emissions in Figure 2.4 highlights how this correlation can be lost during PCCI operation. This is particularly evident when the highest SOI and X_{EGR} values are implemented, because their combination brings to the worst increase in HC and CO engine-out emissions and does not accomplish the complete oxidation of the fuel into CO_2 . The equivalent GHG emission from the engine ought to be calculated assuming the following atmospheric oxidation of CO, though.

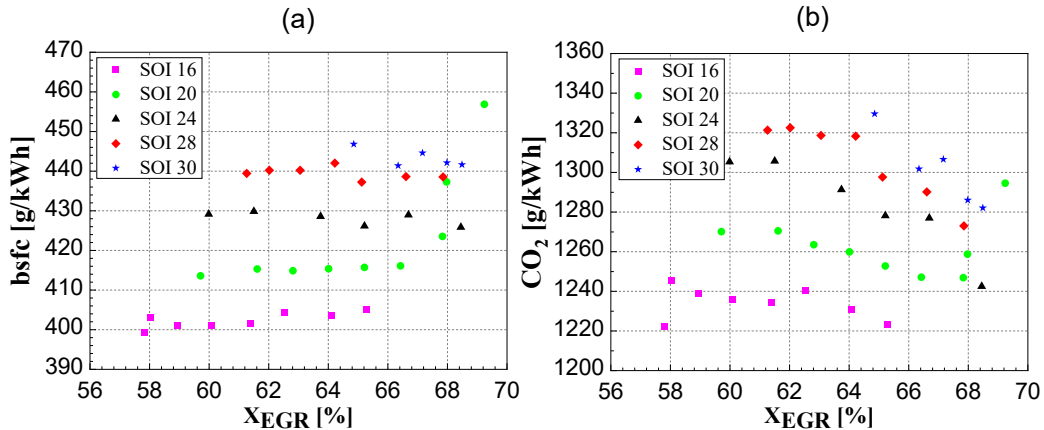


Figure 2.4. $bsfc$ (a) and CO_2 emissions (b) as a function of X_{EGR} , at 1800×1 .

In Figure 2.4(a), the influence of advanced SOI values on $bsfc$ is clearly visible. Advancing the fuel injection timing from 16° bTDC to 30° bTDC brings to nearly +10% fuel consumption penalty (from around 400 g/kWh to 440 g/kWh). This is due to three fundamental reasons. First, more advanced fuel injection timings brings the fuel to impinge more on the piston surface and/or on the cylinder walls, giving rise to increased HC and CO emissions and worse fuel consumption (i.e., lower combustion efficiency η_c , defined as the ratio between the total heat released from chemical reactions and the total energy of the fuel). Secondly, advancing the fuel injection timings (at fixed dilution level) makes the heat release take place earlier during the compression stroke, hence exacerbating the negative work on the piston moving towards the TDC [Park & Bae, 2011] (i.e., lower work conversion efficiency η_{wc} , defined as the efficiency with which the total apparent heat release is converted to indicated work). Lastly, advanced SOI values tend to increase the peak flame temperatures (which likely increase both convective and radiation heat transfer losses, even if forced convection from the bulk gases to the combustion chamber walls is the dominant heat transfer mechanism in a PCCI engine, whilst the radiation effect may be negligible [Soyhan, et al., 2009]) as well as to provide more time for the heat transfer to occur, with hot combustion gases generated near the TDC, when combustion chamber surface-area-to-volume ratios are high (i.e., lower heat-loss efficiency η_{hl} , related to the fraction of the total chemical heat release lost by heat transfer) [Kook, et al., 2005].

On the contrary, with the exception of the curve pertaining to $SOI = 20^\circ$ bTDC, for which the steep rise of incomplete combustion species (when the largest EGR fractions are implemented) induces a remarkably worsened fuel consumption, all the other $bsfc$ trends in function of X_{EGR} (at constant SOI) reveal to be only slightly

influenced by EGR. This is due to the presence of three competing effects. While η_c still tends to worsen as long as the EGR fraction is enlarged, the same larger EGR rate may promote both a better η_{wc} , through its retarding effect on combustion, and a better η_{hl} , through the mitigation of the peak flame combustion temperatures.

Heat release rate and combustion noise

In-cylinder pressure traces and heat release rate (HRR) are powerful tools to deeper investigate the engine combustion characteristics under PCCI combustion mode. As previously described in the “Experimental Setup” Section, four in-cylinder pressure histories (one for each cylinder) were acquired by means of high-frequency piezoelectric pressure transducers. Data post-elaboration was performed with AVL CONCERTO 5 software, in particular to calculate the HRR and mean temperature traces as well as the values of CN, MFB50 and peak firing pressure (PFP) which are reported in the following Figures 2.5-2.8. To reduce the influence of cycle-to-cycle combustion variability, average data sets of 100 consecutive engine cycles were used for the combustion analysis. Furthermore, a low-pass filter with a cut-off frequency of 5 kHz was implemented to the in-cylinder pressure signals, to avoid excessively noisy traces, due to pressure oscillation in the cavity of the glow-plug adapter in which the transducer is installed and which are not present in the combustion chamber pressure development.

Figure 2.5 shows the variations (as a function of X_{EGR}) of p_{cyl} and HRR traces for different SOI timings (16, 24 and 30 °bTDC). When moving from SOI = 16° bTDC to 30° bTDC, thus increasing the premixed combustion tendency, a peculiar “two-stage” heat release combustion becomes increasingly evident. The first “stage”, i.e. the low-temperature heat release (LTHR), is associated with low temperature oxidation reactions (“cool flame region”), while the second “stage”, i.e. the high-temperature heat release (HTHR), involves high temperature oxidation reactions (“hot flame region”) [Saxena & Beyoda, 2013]. In the middle, the negative temperature coefficient (NTC) regime develops [Curran, et al., 1998].

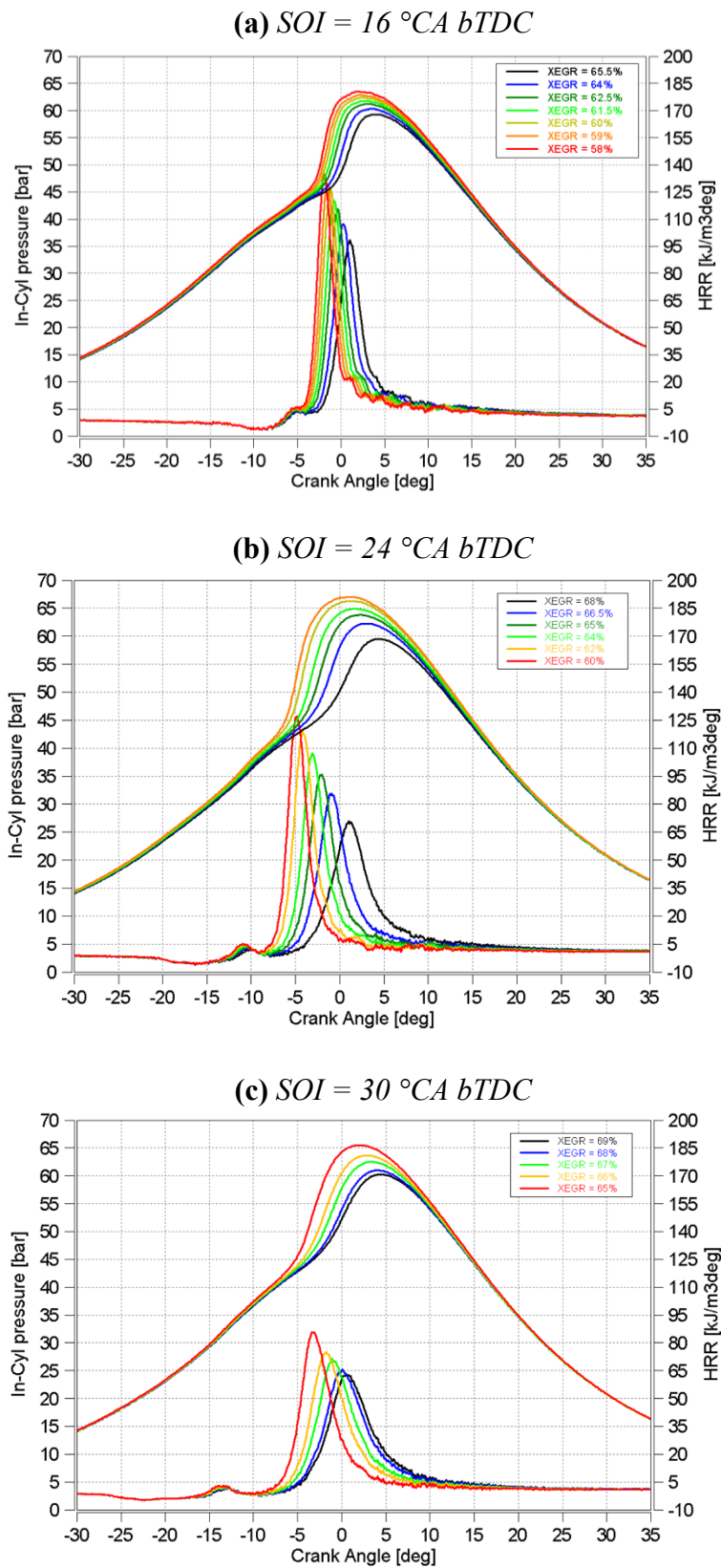


Figure 2.5. In-cylinder pressure and HRR traces for different X_{EGR} values. (a) $SOI = 16^\circ CA$ bTDC; (b) $SOI = 24^\circ CA$ bTDC; (c) $SOI = 30^\circ CA$ bTDC .

The LTHR curve observation is mainly related to the fuel and to the engine operating conditions. In general, fuels with lower octane numbers (like n-heptane, diesel and dimethyl ether) tend to display two-stage ignition processes, whereas fuels with higher octane numbers (like ethanol or iso-octane) typically display single-stage ignition processes [Saxena & Beyoda, 2013]. In the low temperature oxidation reactions, alkyl radicals R add to molecular oxygen to produce alkylperoxy radicals RO_2 , which initiate a series of elementary reactions that lead ultimately to chain branching. A small amount of heat release is generated, at temperatures below about 900 K. As the reaction temperature increases above about 900 K (cf. Figure 2.6), the RO_2 thermally decomposes, shutting off the low-temperature chain branching reaction path and reducing the overall reaction rate [Curran, et al., 1998].

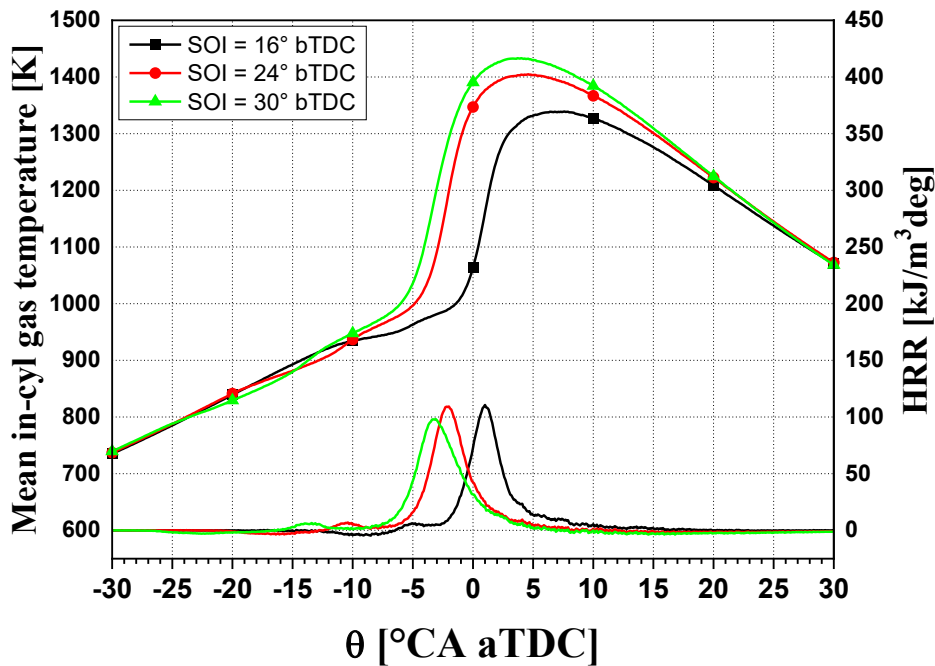


Figure 2.6. Mean in-cylinder temperature and HRR traces for similar X_{EGR} values (65%), at SOI = 16 °CA bTDC, 24 °CA bTDC and 30 °CA bTDC.

After the LTHR, the NTC regime develops, and lasts until further increases in pressure and temperature conditions lead to the high-temperature chain branching reaction path. The duration of NTC is not constant: Figures 2.5 and 2.6 show how it enlarges when advancing the fuel injection timing from 16 °bTDC to 30 °bTDC or when increasing X_{EGR} . As a matter of fact, either advancing the SOI or increasing the EGR rate brings to lower in-cylinder pressure and cool flame temperature, and this agrees with what found in [Dae & Chang, 2005], which pointed out that the duration of the NTC period enlarges when in-cylinder pressure and cool flame temperature are decreased, because this slows down the onset of the hot flame region. Moreover, different concentrations of formaldehyde (HCHO), one of the typical intermediate products out of low-temperature oxidation of hydrocarbon fuels, up to the following high-temperature ignition, may have opposite effects at different in-cylinder temperatures. In particular, experiments shown in [Kuwahara, et al., 2005] demonstrated how, when LTHR begins at temperatures above 900 K (it is the case of SOI = 16 °CA bTDC, in Figure 2.6),

HCHO tends to advance autoignition through the conversion of HCHO to H_2O_2 , whose subsequent breakdown serves as OH radical generator, advancing the process. However, when temperatures at the LTHR onset are below 900 K (it is the case of SOI = 24 and 30 °CA bTDC, in Figure 2.6), HCHO itself is reported to have a remarkable delaying effect, acting as an OH radical scavenger against the cool flame reactions.

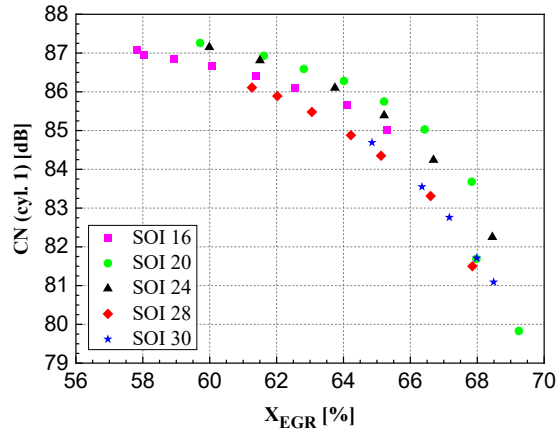


Figure 2.7. CN as a function of X_{EGR} , at 1800×1 .

The following high temperature oxidation reactions rapidly consume intermediates such as olefins and alkyl radicals (which are produced by thermal decomposition reactions including the chain breaking of C–C bonds in the fuel molecules), exploiting the significant concentration of radicals such as H, CH and OH. Once high temperature oxidation reactions take place locally, nearly instant autoignition is triggered throughout the combustion chamber (apart from the quench layers) [Saxena & Beyoda, 2013]. A steep p_{cyl} rise is then generated, and this creates severe CN, typical of highly premixed combustion modes. Clearly, the p_{cyl} gradient (strongly related to the CN levels) tends to be dampened when more exhaust gases are recirculated (cf. the CN trends in Figure 2.7).

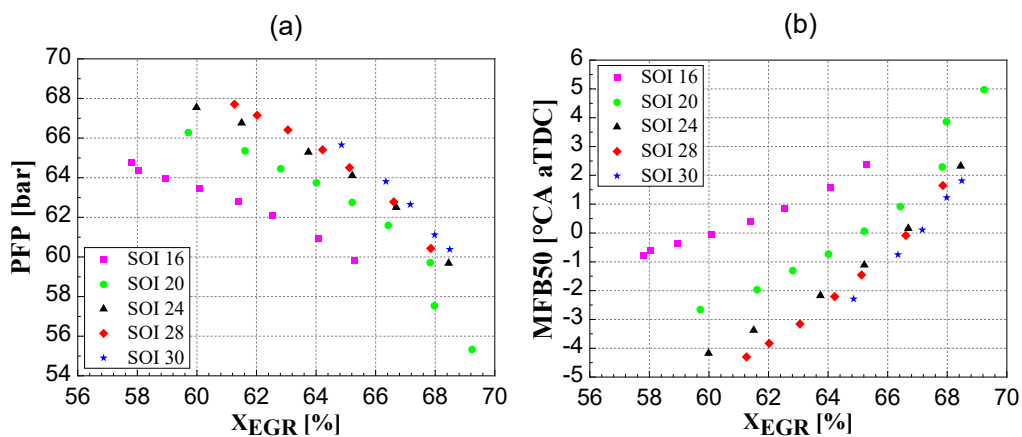


Figure 2.8. PFP (a) and MFB50 (b) values as a function of X_{EGR} , at 1800×1 .

Regardless of the particular SOI value, the traces shown in Figure 2.5 highlight that the PFP (also reported in function of X_{EGR} , in Figure 2.8(a)), as well as the peak HRR values, monotonically decrease with increasing X_{EGR} . This is because the inert

species present in the recirculated exhaust gases (such as CO₂, water vapor, etc.) absorb part of the heat generated by the combustion process, thus giving rise to lower PFP and HRR peaks, as well as to more retarded combustion phasing (cf. the MFB50 values reported in Figure 2.8(b)). As previously stated, this is also the reason of the lower NO_x formation at higher EGR rates.

2.2 Model-based optimization methodology

The phenomena involved in diesel engine technology, including PCCI applications, are complex and makes the task of optimal calibration a demanding procedure, in terms of both time and costs. As a consequence, model-based calibration approaches, which employ modern Design of Experiments (DoE) techniques, statistical modeling and optimization algorithms, may be adopted to simplify and efficiently produce high quality calibrations [Brooks, et al., 2005].

Starting from the preliminary outcomes of the analysis above reported, a model-based optimization methodology has been set up. The aim was to further explore the potentialities of the application of the early single injection PCCI strategy on the considered conventional diesel engine apparatus. As previously done, the results will be discussed with reference to the same engine operating point (1800×1), representative of the low-load and low-to-medium speed area of the F1C Euro VI engine map investigated.

2.2.1 Design of Experiments (DoE) setup

. DoE techniques, as a mean to properly set up experiment designs, can significantly limit the burden of experimental data collection at the test bench. Each planned experiment (i.e., each test point) is a combination of several “factors”, which are the independent input variables whose variations affect the dependent parameters, known as “responses” [Simpson, et al., 2001]. Based on the physical knowledge of the system under investigation, the most influent factors have to be selected, associated to specific values, or “levels”, in order to determine a “level-combination” for each experimental test which has to be carried out at the test bench. In this way, a matrix is built up, where each row represents an experimental test and each column gives a particular factor level [Montgomery, 2000]. In our case, experimental evidence suggested SOI, EGR rate and rail pressure as suitable input “factors”, while engine-out brake specific emissions (NO_x, soot, HC and CO), *bsfc* and CN were chosen as output “responses”.

Table 2.2. Boundary values for the input parameters.

Input	Lower limit	Upper limit
Exhaust Flap position [%]	85	95
SOI [°CA bTDC]	18	30
Rail pressure	500	700

Table 2.2 reports the maximum and minimum values within which the specific “levels” were established for the input parameters. The position of the backpressure

exhaust flap was used to regulate the EGR rate, since the EGR poppet valve was kept fully open in all the PCCI working conditions. The upper EGR rate limit (i.e., 95% throttled position of the exhaust flap) was established considering two phenomena. First, the high combustion instability (in terms of both cycle-to-cycle and cylinder-to-cylinder variations) occurring when too large exhaust gas quantity was recirculated. Secondly, the deterioration of the engine combustion efficiency arising beyond certain EGR rates, up to the occurrence of misfiring events (due to the increased difficulties in managing the inlet and outlet gas flows from the cylinders because of the rising engine backpressure caused by the exhaust flap). The higher limit for SOI (i.e., 30 °CA bTDC) was then set to limit the excessive increase in HC and CO emissions. Conversely, the corresponding EGR and SOI lower bounds were set in order to achieve a sufficient degree of premixed combustion in all the investigated “level-combinations”. Lastly, the rail pressure was bounded between 500 and 700 bar, i.e. an interval around the value considered during the preliminary analysis at 1800×1.

In the design of experiments for estimating statistical models, different types of DoE plans can be chosen, for instance classical (including full factorials, central composite designs, etc.), space-filling or computer-generated optimal designs [Montgomery, 2000]. Given the limit values listed in Table 2.2, and provided a suitable number of levels for each input parameter, a “V-optimal” design, which minimizes the values of the predicted error variance in the test plan, was chosen and set up by means of the Matlab software tool “MBC model”.

2.2.2 Statistical modeling

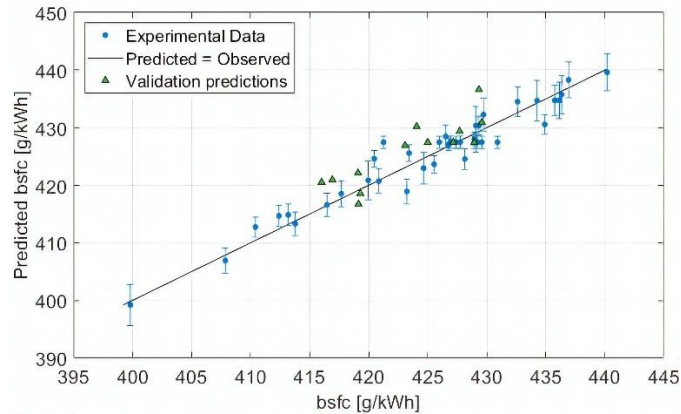
Once the test plan had been selected and prepared, the required experimental campaign was carried out at the test bench. The empirical data, gathered in this way, provided the data to build statistical models to relate the experimental input factors (exhaust flap position, SOI and rail pressure) to the measured response outcomes (engine-out brake specific emissions, *bsfc* and CN). The following steps were to choose which type of approximating models and fitting methods to be adopted. Many alternatives exist, but probably the best compromise between accuracy and simplicity is represented by the Response Surface Methodology (RSM), with the use of second-order polynomial functions as response approximating models and of the least squares regression analysis as fitting methods [Simpson, et al., 2001].

For each built response model, the Box-Cox transformation [Box & Cox, 1964] was applied if necessary, in order to normalize the distribution of the residuals. Moreover, the “stepwise regression” method [Montgomery, 2000] was used to eliminate from each model those regressors which have a negligible effect on the considered output.

Table 2.3. Summary statistics for each response model.

Response model	Number of param.	Box-Cox λ	R^2	R^2 adjusted	PRESS R^2	PRESS RMSE	RMSE	Validation RMSE
HC [g/kWh]	8	1	0.960	0.951	0.933	0.161	0.140	0.184
NOx [g/kWh]	8	0.5	0.994	0.992	0.989	0.346	0.268	0.282
CO [g/kWh]	8	-0.5	0.983	0.980	0.973	1.071	0.879	0.633
Soot [g/kWh]	10	1	0.880	0.837	0.749	0.002	0.001	0.001
<i>bsfc</i> [g/kWh]	8	1	0.938	0.925	0.913	2.537	2.392	3.616
CN [dB]	7	1	0.977	0.973	0.957	0.132	0.106	0.095

Table 2.3 reports some summary statistics for the built models. Looking at the reported statistical indexes, the models exhibit a satisfactory correlation with the experimental input values. The validation root mean square error (RMSE), which is obtained from the comparison of some validation tests with the response models, is reported in Table 2.3, and shows very similar values if compared to the model RMSE. As an example, Figure 2.9 depicts the predicted vs. experimental values for the *bsfc* modeling.

**Figure 2.9.** *bsfc* model: predicted vs. experimental values, at 1800×1 .

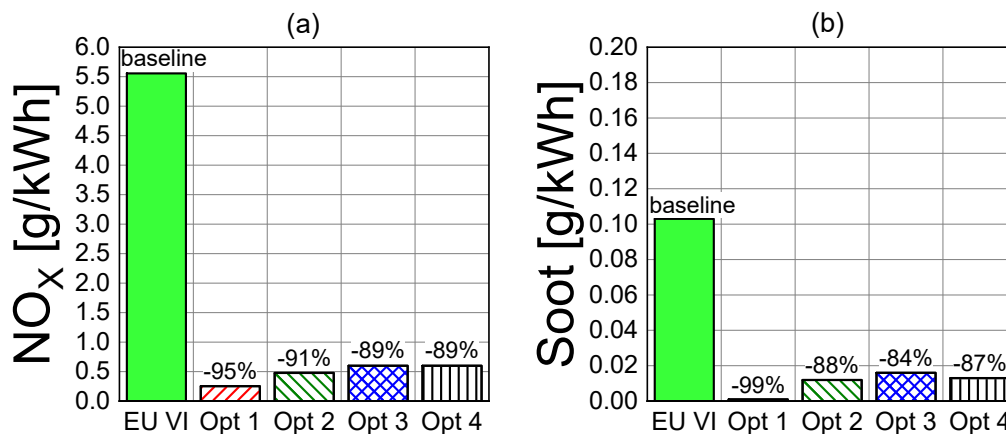
2.2.3 Optimization procedure

The response models showed a good fit, so they were used to generate the optimal PCCI calibration at 1800×1 , applying optimization techniques able to find which input values are needed to obtain certain optimal outcomes within a feasible area, bounded by properly setting some constraints.

Different optimization strategies have been tested for comparison. In particular, the focus was set on the minimization of the NO_x emissions and/or of the *bsfc*, meanwhile setting some upper boundaries to other output parameters. A “conjugated gradient optimization” method was adopted in the case of single-objective optimizations, while multi-objective optimizations have been computed employing a “Normal Boundaries Intersection” (NBI) algorithm. Details on the settings used for the various optimizations are reported in Table 2.4.

Table 2.4. PCCI optimization parameters, at 1800×1.

Point	Exh. flap [%]	SOI [°CA bTDC]	Rail pressure [bar]	Minimization parameters	Constraints (-)
Opt #1	95.0	30	700	NO _x	none
Opt #2	95.0	18	600	NO _x	<i>bsfc</i> < 425 g/kWh CO < 20 g/kWh HC < 2.0 g/kWh
Opt #3	94.6	18	500	<i>bsfc</i>	NO _x < 0.6 g/kWh CO < 15 g/kWh HC < 1.7 g/kWh
Opt #4	95.0	20	500	NO _x <i>bsfc</i>	Soot < 0.02 g/kWh CO < 20 g/kWh HC < 2.0 g/kWh

**Figure 2.10.** NO_x (a) and soot (b): comparison between the baseline and the optimized PCCI calibrations.

Figures 2.10-2.12 show a comparison of the main outcomes between the baseline engine calibration (featuring a CDC mode) and the four different optimizations featuring the early single injection PCCI mode. The first and second optimizations (Opt #1 and Opt #2), reported in Table 2.4, have the goal to minimize NO_x emissions, which are reduced of more than 90% with respect to the baseline engine calibration (cf. Figure 10(a)). In particular, Opt #1 gives the greatest reduction of NO_x (-95%) and a nearly smokeless combustion, setting a very advanced fuel injection timing (30° bTDC) in combination with the highest EGR rate (more than 60%), but without imposing any constraint on other outcomes. Thus, CO and HC emissions increase of 920% and 240%, respectively, while *bsfc* increases of more than 13% of the reference.

To limit the excessive fuel consumption and emission of engine-out incomplete combustion species, Opt #2 tried to minimize NO_x while setting proper constraints on *bsfc*, CO and HC (cf. last column of Table 2.4). The result is a slightly lower benefit as regards NO_x (-91%, against the -95% of Opt #1) and soot (-88%, against the -99% of Opt #1) abatement, compensated by valuable drop in CO (from +920% to +400%) and HC (from +240% to +45%) emissions as well as in *bsfc* (from +13.9% to +10.9%). Unfortunately, these penalties, especially those related to fuel consumption (higher than 10% of the baseline CDC value), still represent an issue.

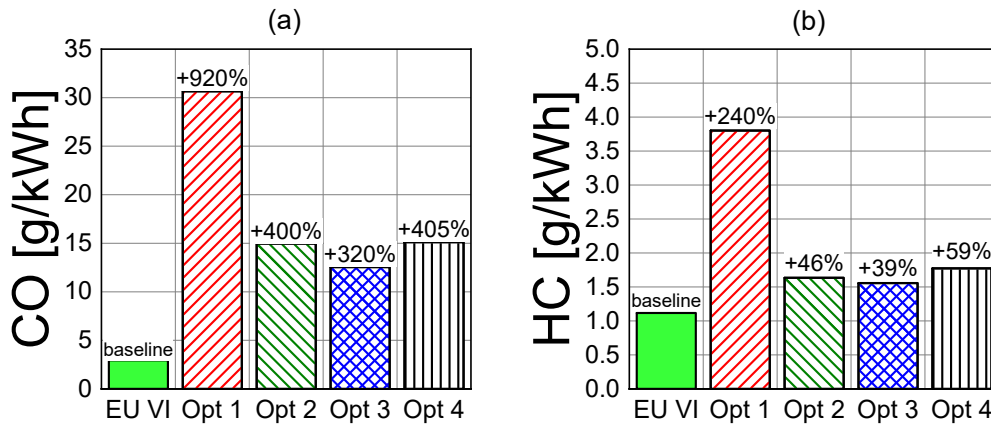


Figure 2.11. CO (a) and HC (b): comparison between the baseline and the optimized PCCI calibrations.

Therefore, the third optimization has been computed in order to minimize the *bsfc* (with proper constraints on NO_x , CO and HC) and results to be probably the best trade-off achieved for the tested conditions: in this case it is possible to reduce NO_x emissions of 89% and soot of 88%, while the *bsfc* penalty is lower than 10%, the increase in CO is contained to around 3 times the baseline CDC values and the HC emissions are only +39% higher.

Finally, the fourth model-based optimization point has the aim to minimize simultaneously NO_x emissions and *bsfc*, while limiting CO, HC and soot emissions to constrained levels. As a matter of fact, no particular convenience seems to be brought by this multi-objective optimization, if compared to Opt #3.

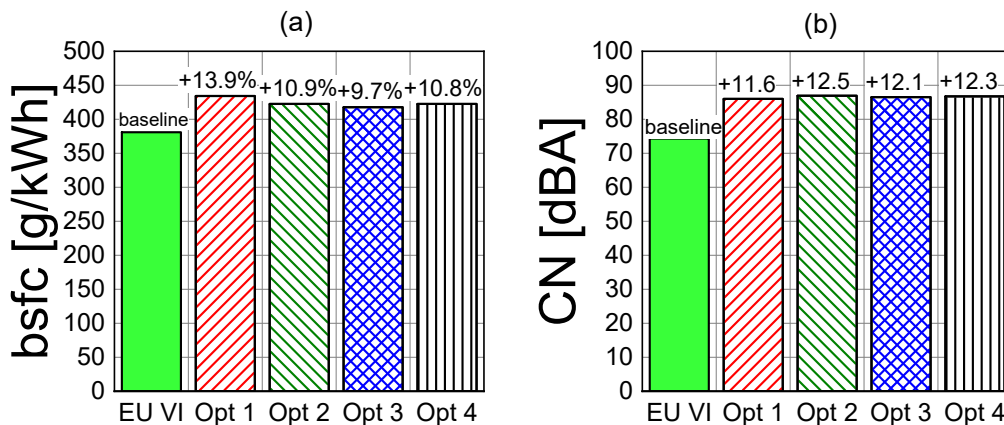


Figure 2.12. *bsfc* (a) and CN (b): comparison between the baseline and the optimized PCCI calibrations.

In all the tested optimizations, the CN is considerably higher than in the reference CDC condition, with an increase ranging between 11.6 and 12.5 dBA (cf. Figure 2.12(b)). This is in part due to the fact that the PCCI tests have been performed with a single fuel injection strategy, while the Euro VI calibration features a double-pilot injection strategy in the considered engine operating point. Moreover, the considerably advanced injection pattern (and consequently, combustion event) and the high premixed degree have all to be accounted for as additional causes for the deteriorated CN levels.

Chapter 3

3. PCCI combustion in an optimized engine hardware

3.1 Engine hardware modifications

Starting from the baseline version of the engine (F1C Euro VI) previously dealt with, a modified engine (which will be referred to as F1C PCCI) has been derived by means of purposely designed hardware modifications to run in PCCI combustion mode. In particular, some engine components were redesigned using 3D CFD combustion models, with the aim to allow the application of the early PCCI combustion mode up to medium loads and medium-high speeds. The details of the hardware modifications are listed hereinafter, and summarized in Table 3.1:

- the CR was reduced from 17.5:1 to 14.6:1, in order to reduce the in-cylinder pressure and temperature conditions before the onset of the combustion event and, consequently, to achieve lower flame peak combustion temperatures, which are the main responsible for in-cylinder NO_x formation mechanisms;

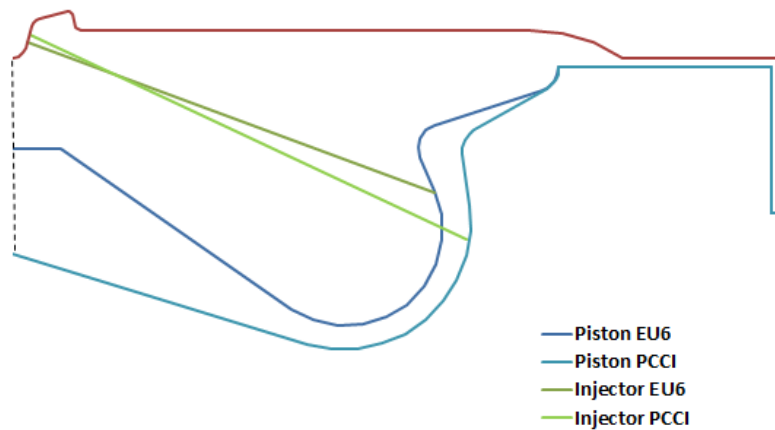


Figure 3.1. Section view of the piston bowl and injector spray edge of the F1C Euro VI and the F1C PCCI engines.

- the piston bowl shape was redesigned to be more suitable for the fuel spray-air mixing with advanced injection timings (Figure 3.1);
- new fuel injectors, featuring reduced cone angles (from 139.8° to 130° , as schematically shown in Figure 3.1) and static flowrate (from 990 cm^3 to 750 cm^3 in 30 s, when fueled at 100 bar), were installed to limit the risk of cylinder

wall impingement, as the simultaneous reduction of the CR tends to increase the liquid penetration of the fuel spray inside the combustion chamber;

- the original EGR cooler (nominal maximum thermal power around 6 kW) was replaced by a larger one (nominal maximum thermal power around 32 kW) taken from a production 11-liter displacement engine, to allow suitable cooling power for the high EGR mass flowrates usually involved during PCCI operations. Moreover, the EGR cooling circuit for the F1C PCCI was completely decoupled from its engine cooling loop, with the aim of providing a precise control of the exhaust gas temperature downstream the EGR cooler (in particular, the tests on the F1C PCCI were carried out keeping this gas temperature at around 85°C);
- the EGR poppet valve, installed on the F1C Euro VI, was replaced by a throttle valve, with the aim of increasing the maximum cross-section passage area and, thus, the maximum possible EGR mass flowrate towards the intake manifold;
- a smaller turbo-group, specifically designed to achieve higher boost levels at the lowest engine loads, was installed.

Table 3.1. Comparison of the main technical specifications of the conventional F1C Euro VI diesel engine and of the PCCI version of the engine.

Engine type	FPT F1C Euro VI	FPT F1C PCCI
Number of cylinders	4	
Displacement	2998 cm ³	
Bore / stroke	95.8 mm / 104 mm	
Rod length	160 mm	
Compression ratio	17.5 : 1	14.6 : 1
Valves per cylinder	4	
Turbocharger	Single-stage VGT	Single-stage VGT (smaller turbine with respect to the F1C Euro VI)
Fuel injection system	Common rail injection system	
Injector static flowrate	990 cm ³ in 30 s at 100 bar upstream pressure	750 cm ³ in 30 s at 100 bar upstream pressure
Injector cone angle	139.8°	130°
EGR circuit type	Short-route, high pressure, cooled	
EGR valve type	poppet	throttle
EGR cooler	Max thermal power: 6kW Cooling water circuit integrated with block coolant circuit	Max thermal power: 32kW Dedicated external circuit for the cooling water

3.2 Low load PCCI: comparison between standard (F1C Euro VI) and prototype (F1C PCCI) engines

In order to show a direct comparison, in terms of engine performance and exhaust emissions, between the standard F1C Euro VI and the optimized F1C PCCI, DoE techniques and a model-based optimization procedure (similar to what described in Section 2.2.3) were carried out implementing an early single injection

PCCI strategy on the F1C PCCI, at the same engine operating point previously considered, i.e. 1800×1.

In this case, in addition to SOI, EGR rate and rail pressure, also the VGT rack position was considered as an input factor for the statistical models. In fact, progressively closing the vanes of this smaller VGT, at such a low speed and load engine operating point, led to small increase in boost pressure but appreciable backpressure rise, thus significantly influencing the amount of EGR which comes back to the intake. As output responses for the models, engine-out brake specific emissions (NO_x, soot, HC and CO), *bsfc* and CN were selected.

Once built the response models, they were used to generate the optimal PCCI calibration at 1800×1. As previously done, four different optimizations have been obtained, with the main focus set on the minimization of the NO_x emissions and/or of the *bsfc*, meanwhile setting some upper boundaries to other output parameters. Details on the settings used for the various optimizations are reported in Table 3.2.

Table 3.2. PCCI optimization parameters, at 1800×1 (F1C PCCI).

Point	Exh. flap [%]	SOI [°CA bTDC]	VGT pos. [%]	Rail p. [bar]	Minimization parameters	Constraints (-)
Opt #1	80.6	18	25.0	600	NO _x	none
Opt #2	75.2	20	25.0	500	NO _x	<i>bsfc</i> < 425 g/kWh CO < 45 g/kWh HC < 6.0 g/kWh
Opt #3	74.5	19	35.1	500	<i>bsfc</i>	NO _x < 0.8 g/kWh CO < 40 g/kWh HC < 5.5 g/kWh
Opt #4	75.7	20	44.9	510	NO _x <i>bsfc</i>	Soot < 0.01 g/kWh CO < 40 g/kWh HC < 6.0 g/kWh

Figures 3.2-3.5 show a comparison of the main outcomes between the baseline engine calibration on the standard F1C Euro VI (featuring the CDC mode) and the four different optimizations featuring the early single injection PCCI mode, one for each engine configuration (standard F1C Euro VI and optimized F1C PCCI).

NO_x emissions are always reduced of more than 86% with respect to the baseline CDC engine calibration for all the considered optimizations, but they do not seem to be appreciably influenced by the different CR values between the two engine versions, likely being mainly dependent on the EGR rate (cf. Figure 3.2(a)). This is also in line with the outcomes presented in [Laguitton, et al., 2007] and [Beatrice, et al., 2009].

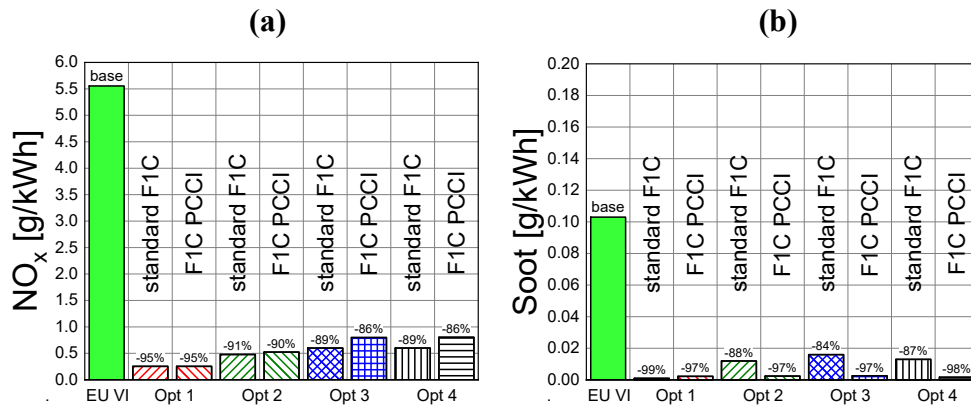


Figure 3.2. NO_x (a) and soot (b): comparison between the baseline CDC and the optimized PCCI calibrations for the two engine configurations (F1C Euro VI and F1C PCCI).

As far as soot emissions are concerned (cf. Figure 3.2(b)), all the optimizations achieved with the F1C PCCI bring to massive reductions, not less than 97%. A slightly lower soot reduction is observable for the PCCI optimizations in the standard F1C Euro VI: in those conditions a little amount of soot is formed during combustion, but the in-cylinder temperatures are too low to promote its post-combustion oxidation. In the case of the F1C PCCI, it is possible that the enhanced mixing associated with the reduced CR is able to further suppress soot formation mechanisms, eliminating the need for high thermal levels for the post-combustion oxidation process.

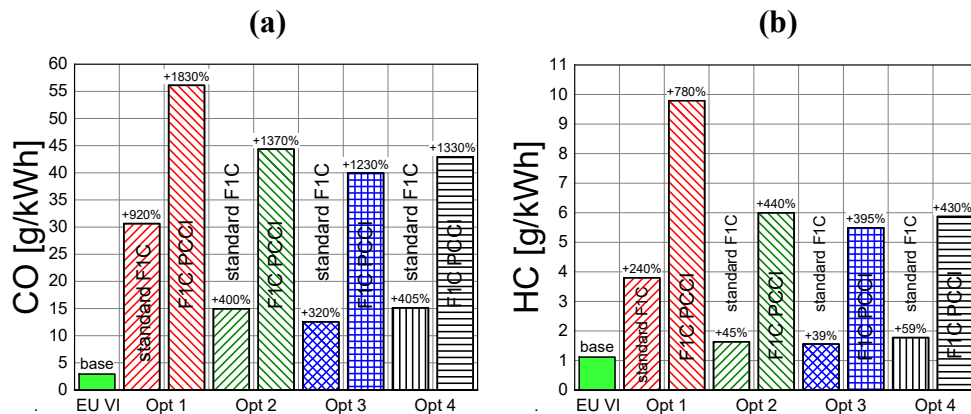


Figure 3.3. CO (a) and HC (b): comparison between the baseline CDC and the optimized PCCI calibrations for the two engine configurations (F1C Euro VI and F1C PCCI).

If reference is made to Figure 3.3, there is a negative impact of the reduced CR, and this is linked to CO and HC engine-out emissions: all the PCCI optimizations achieved with the F1C PCCI give CO and HC levels nearly or more than doubled if compared to what obtained with the F1C Euro VI. Besides the general increase in incomplete combustion species due to the adoption of the early PCCI strategy, compared to the baseline HC and CO levels of the CDC calibration, the further increase in CO and HC emissions due to the reduced CR follows a similar reasoning as for soot. The lower CR causes reduced temperature and pressure conditions at the start of injection and an increased penetration of the liquid fuel spray into the combustion chamber. This leads to excessive fuel dilution with

the intake charge, especially at the boundary of the mixture (over-mixing phenomena) and at the low load condition examined (1800×1).

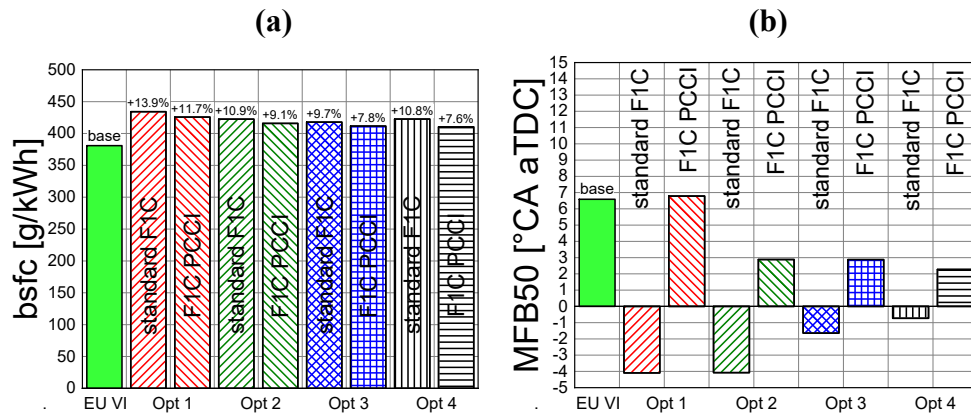


Figure 3.4. *bsfc* (a) and MFB50 (b): comparison between the baseline CDC and the optimized PCCI calibrations for the two engine configurations (F1C Euro VI and F1C PCCI).

Figure 3.4(a) shows the impact of reducing the engine CR on *bsfc*. Unexpectedly, the PCCI optimization achieved with the reduced CR engine gives slightly better results in terms of fuel consumption if compared to the PCCI tests on the standard F1C Euro VI engine, even if well above the baseline values pertaining to the CDC calibration. Even if the lower CR exacerbates the over-mixing phenomena, as previously stated (thus giving rise to a worse combustion efficiency, η_c), it also allows the heat release to take place later during the compression stroke, minimizing the negative work on the piston moving towards the TDC (i.e., higher work conversion efficiency, η_{wc}). As a matter of fact, Figure 3.4(b) shows the positive (i.e., taking place after the TDC) MFB50 values of the different PCCI optimizations with the F1C PCCI, compared with the negative (i.e., taking place before the TDC) MFB50 values of those achieved with the standard F1C Euro VI. Furthermore, as reducing the CR tends to decrease the peak flame temperatures, heat transfer losses are mitigated and less time is available for the heat transfer to occur, as well, due to the more retarded combustion phasing (i.e., better heat-loss efficiency, η_{hl}).

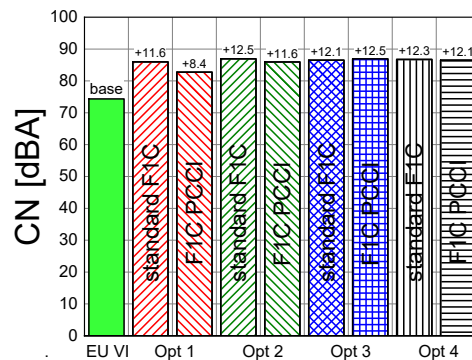


Figure 3.5. CN comparison between the baseline CDC and the optimized PCCI calibrations for the two engine configurations (F1C Euro VI and F1C PCCI).

Finally, in all the tested optimizations the CN is considerably stronger than in the baseline CDC calibration (cf. Figure 3.5), due to the fact that all the PCCI tests have been performed with a single fuel injection strategy, while the Euro VI CDC

calibration features a double-pilot injection strategy. Moreover, the considerably advanced injection pattern (and consequently, combustion event) and the high premixed degree have all to be accounted for as additional causes for the deteriorated CN levels. The reduction of CR only brings slight CN reduction, mainly ascribed to the shift of the combustion event towards the expansion stroke.

3.3 PCCI application on the prototype (F1C PCCI) engine³

Besides the application of the early-PCCI strategy to the F1C PCCI did not allow major benefits at low load, if compared with the results obtained with the baseline F1C Euro VI (cf. the previous Section 3.2), the main aim of the engine hardware modifications was to extend the applicability of this early PCCI combustion mode up to medium loads and medium-high speeds, which were impossible to be reached with the baseline engine hardware. The present Section will show the results of a steady-state testing activity carried out on the prototype F1C PCCI engine to highlight the potentialities of this early single injection PCCI strategy up to $b_{mep} = 8.5$ bar. These results will be shown in terms of pollutant emissions and engine performance parameters and compared with those pertaining to the conventional F1C Euro VI engine (CDC mode), taken as a baseline reference.

As far as the conventional F1C Euro VI engine is concerned, the reference experimental tests were performed by running the engine with the original OEM calibration (whose details are not reported here, for confidentiality reasons), i.e. a CDC calibration featuring a triple fuel injection strategy (two pilot and one main injections), over the complete engine map.

As previously clarified in Section 2.1.2, the PCCI combustion mode implemented on the conventional F1C Euro VI engine showed that it was not possible to exceed 2 bar of b_{mep} . To overcome this limitation, the engine hardware modifications reported in Section 3.1 were implemented, being able to explore the suitability of PCCI operations up to medium loads and medium-high speeds. Specifically, it was possible to perform proper PCCI operations inside a restricted area of the whole engine map, with the maximum engine load explored reaching about $b_{mep} = 8.5$ bar. Inside this area, the following engine operating points were tested, in terms of speed $\times b_{mep}$ (expressed in rpm \times bar): 1000 \times 3.9, 1400 \times 3.0, 1400 \times 4.4, 2000 \times 2.3, 2000 \times 5.0, 2000 \times 6.7, 2000 \times 7.5, 2000 \times 8.4, 2500 \times 2.3, 2500 \times 5.0, 2500 \times 6.7, 2500 \times 7.5, 2500 \times 8.4, 3000 \times 2.3, 3000 \times 5.0, 3000 \times 6.4, 3000 \times 7.5. For each of them, preliminary experimental tests were carried out to explore the PCCI combustion mode according to a “one-factor-at-a-time” (OFAT) approach [Montgomery, 2000], varying the following engine control variables:

³ Most of the contents of this Section have been previously published in [d'Ambrosio, S., Gaia, F., Iemmolo, D., Mancarella, A., Salamone, N., & Vitolo, R. (2018). “Performance and Emission Comparison between a Conventional Euro VI Diesel Engine and an Optimized PCCI Version and Effect of EGR Cooler Fouling on PCCI Combustion”. SAE Technical Paper, 2018-01-0221. doi:10.4271/2018-01-0221].

electric start of injection (SOI) of the single injection pulse, exhaust flap position, VGT rack position and rail pressure (p_{rail}). It is worth pointing out that, again, in order to obtain high EGR rates, the EGR valve was always kept in the completely open position. Then, for each explored engine operating point, an optimum PCCI calibration was selected through the use of a proper objective function, meant to point out the best compromise in terms of simultaneous reduction of soot and NO_x without excessive penalties on $bsfc$, tailpipe CO and HC, and CN.

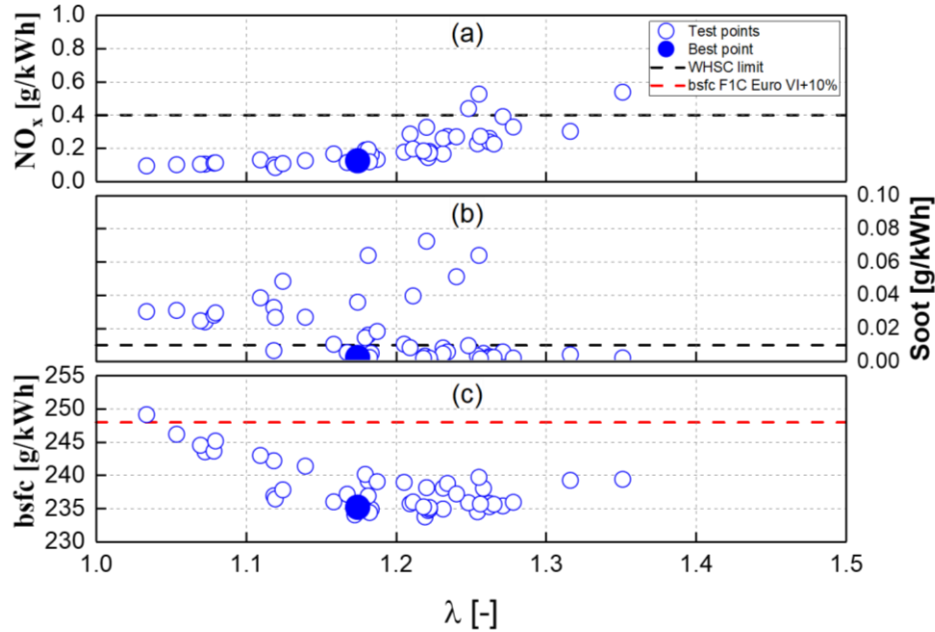


Figure 3.6. NO_x , soot and $bsfc$ as a function of λ at 2000×5 , for different values of the input variables.

In order to provide information on how the optimum PCCI calibration has been achieved, Figure 3.6 depicts NO_x , soot and $bsfc$ as a function of the relative air-fuel ratio (λ), at the 2000×5 working point. The tests have been carried out according to the OFAT approach and therefore involve different values of the abovementioned inputs. As soot was quite low at 2000×5 , due to the high premixing, the aim of the calibration was mainly related to reduce the engine-out NO_x , while limiting the $bsfc$ penalty. Furthermore, at $b_{mep} = 5$ bar, exhaust temperatures were high enough to allow the DOC to properly abate engine-out CO and HC, so they were not considered as a priority for the PCCI optimum choice at 2000×5 .

A suitable objective function, in the form $K_1 \cdot \left(\frac{NO_x}{reference\ NO_x}\right)^2 + K_2 \cdot \left(\frac{PM}{reference\ PM}\right)^2 + K_3 \cdot \left(\frac{bsfc}{reference\ bsfc}\right)$, was defined in order to find the best combination of inputs that result in a simultaneous minimization of NO_x , soot and $bsfc$ (K_1 , K_2 and K_3 coefficients allow a calibration of the relative weights of the different terms making up the objective function, but where left equal to 1 in the present analysis, according to reference found in [Montgomery & Reitz, 2000]). The black dashed horizontal lines in Figure 3.6 refer to the Euro VI emission limits of the World Harmonized Stationary Cycle (WHSC) [EC, 2011], reported in Table 3.3 and taken as a reference, whereas the dashed red line represents the 10%

increase in the *bsfc* experimentally measured for the baseline CDC calibration (on the F1C Euro VI). These references are the same used for the definition of the previously reported objective function.

Table 3.3. Euro VI emission standards for heavy-duty diesel engines for the World Harmonized Stationary Cycle (WHSC).

	NO _x [g/kWh]	PM [g/kWh]	HC [g/kWh]	CO [g/kWh]
WHSC limit	0.40	0.01	0.13	1.5

As Figure 3.6 highlights, the optimum PCCI calibration at 2000×5 is achieved over a narrow range of λ values, i.e. around 1.1÷1.2, due to the simultaneous optimization of the three considered output.

A similar methodology was adopted for the other tested PCCI points. It was generally found that the input variables had to be selected so that the corresponding λ value is in the 1.1÷1.8 range. The λ values for each PCCI optimum calibration are reported in Figure 3.7. It can be seen how the air-fuel ratio increases, i.e. moving towards globally leaner mixtures, when the engine load decreases, because it is not possible to further increase the EGR rate (and hence to reduce the λ values), due to the onset of combustion instabilities (higher cylinder-to-cylinder and cycle-to-cycle variations, till the occurrence of misfiring events) and a dramatic increase in engine-out CO and HC emissions. This was ascribed to the air handling system, which was optimized for medium loads, since NO_x and soot emissions at low loads do not represent a major issue.

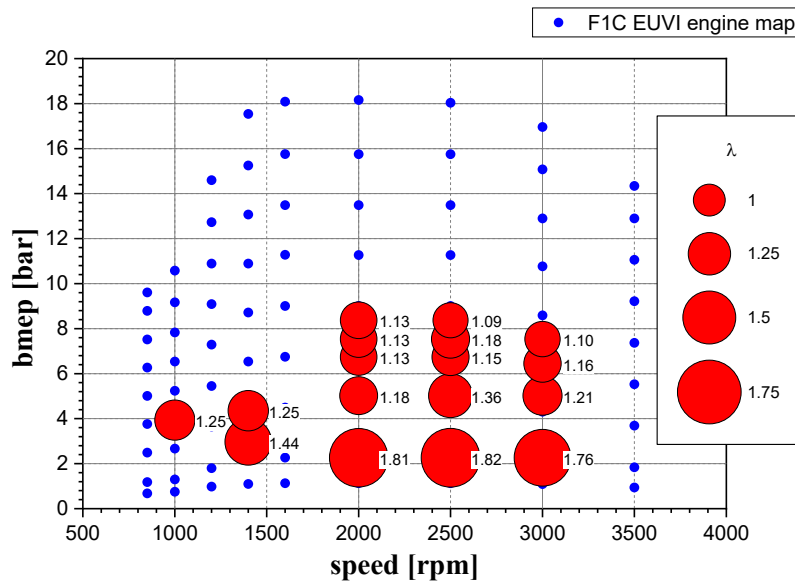


Figure 3.7. Air-fuel ratio (λ) for the F1C PCCI engine.

The values of SOI in the considered PCCI calibrations range from 22 to 46 °CA bTDC, and they are generally more advanced with increasing engine speed and load. The advanced SOI values also determine advanced MFB50 values, which occur before TDC at the highest PCCI loads. The considered p_{rail} is about 150-450 bar higher than that of the F1C Euro VI featuring the baseline CDC calibration,

with the greatest differences generally measured at the lowest loads. The exhaust flap position is generally more throttled than in the F1C Euro VI, especially at highest loads, and this determines, together with the advanced MFB50, an expected increase in *bsfc*.

Figures 3.8-3.11 and 3.14-3.15 show, for all the PCCI working points, the percentage variation of exhaust pollutant emissions, *bsfc*, CN and maximum in-cylinder pressure derivatives of the optimum PCCI points on the F1C PCCI engine, compared to the results of the baseline CDC calibration on the corresponding points, obtained on the F1C Euro VI engine. The green or red filled circles, with their size being proportional to the percentage variation value, highlight a reduction or an increase, respectively, of the considered y-axis value in the F1C PCCI engine, compared to corresponding result achieved with the baseline CDC calibration on the F1C Euro VI one.

Specific emissions, fuel consumption and combustion noise

Figure 3.8 depicts the percentage reduction, compared to the CDC calibration values, of engine-out NO_x and soot emissions achievable with the early-PCCI strategy implemented on the F1C PCCI engine. Again, a massive reduction (that is, ranging from 85% to 97%, cf. Figure 3.8(a)) in NO_x emissions is clear for the whole portion of engine map explored with PCCI strategies. The current SCR system technology manufactured for heavy-duty diesel applications usually ensure a conversion efficiency that ranges from 90% to 92%, when a cooled EGR strategy is employed [Jiao, 2015]. Therefore, on this whole portion of engine map where PCCI has been explored, engine-out NO_x emissions can reach values comparable with the corresponding tailpipe emissions achievable with the use of an SCR after-treatment device, possibly guaranteeing a remarkable urea consumption reduction.

As soot emissions are considered, Figure 3.8(b) shows that an average reduction of more than 90% is obtained, compared to the CDC calibration values, with peaks of nearly 100% (which means an ultra-low soot combustion) at the lowest loads, thanks to the advanced fuel injection pattern featured during the PCCI operations.

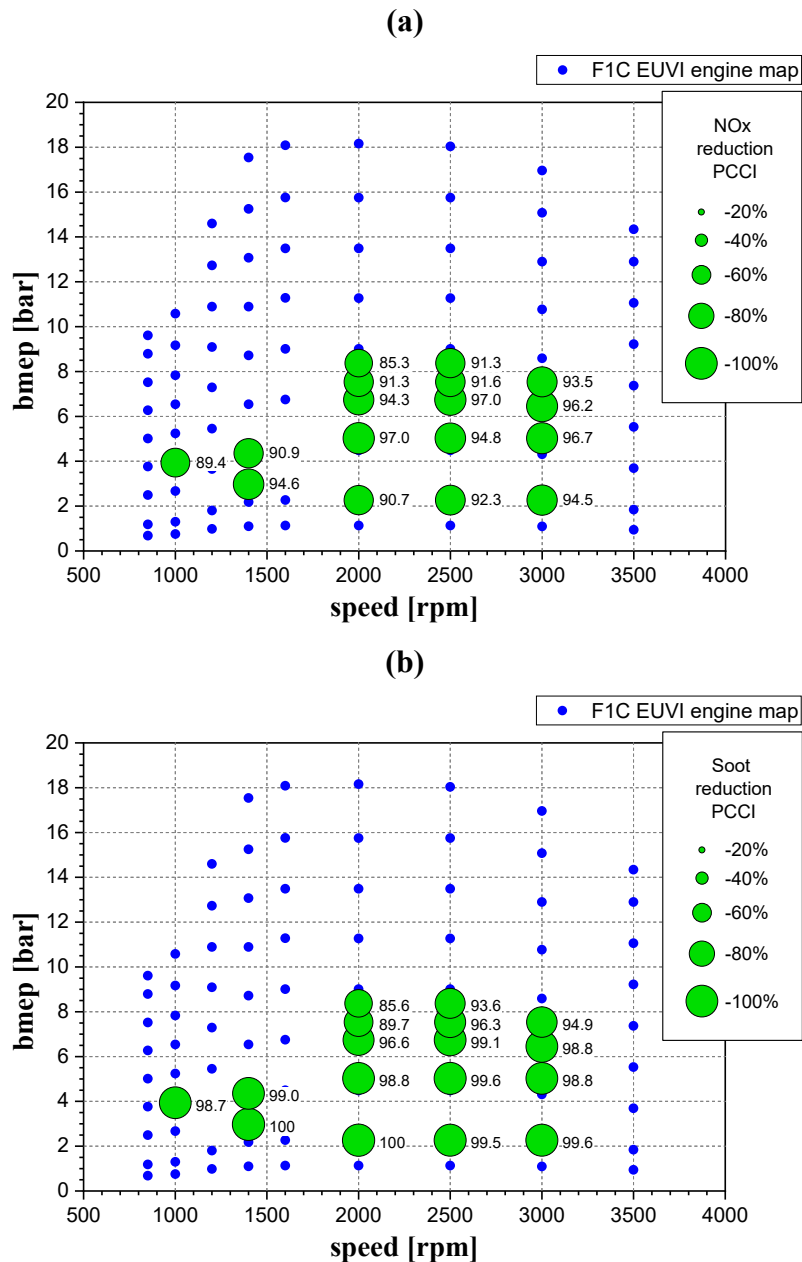


Figure 3.8. Percentage variations in engine-out NO_x (a) and soot (b) emissions between the F1C PCCI and the corresponding CDC values on the F1C Euro VI engine.

It is then confirmed that both engine-out CO and HC emission levels, reported in Figure 3.9, go through dramatic increase compared to the values of the baseline CDC on the Euro VI engine. At low load and speed conditions, as previously explained for the 1800×1 case, the enlarged ID values obtained with the PCCI operations tend to exacerbate over-mixing phenomena, hindering a complete combustion process and producing high amounts of unburned HC and CO. Conversely, when the load increases, it can be seen how engine-out CO tend to dramatically reach huge concentrations, up to 20 times the values of the baseline CDC on the Euro VI engine, while the worsening of the engine-out HC emissions is more limited. This is because HC emissions are generally closely correlated with the ID, with a longer ID (typical of low load and speed conditions) causing higher HC emissions (due to enhanced liquid fuel penetration length and consequent wall

wetting) and global λ values only playing a secondary role [Han, et al., 2012]. Differently, at high load conditions, CO emissions are primarily influenced by mixing (i.e., by the lack of oxygen due to low global λ) rather than by the in-cylinder temperature [Peterson, et al., 2010]: even if a high thermal level could be still available during the latest stages of the combustion, enhancing the chemical kinetics, the final oxidation of the CO molecules into CO₂ is primarily prevented by the lack of oxygen.

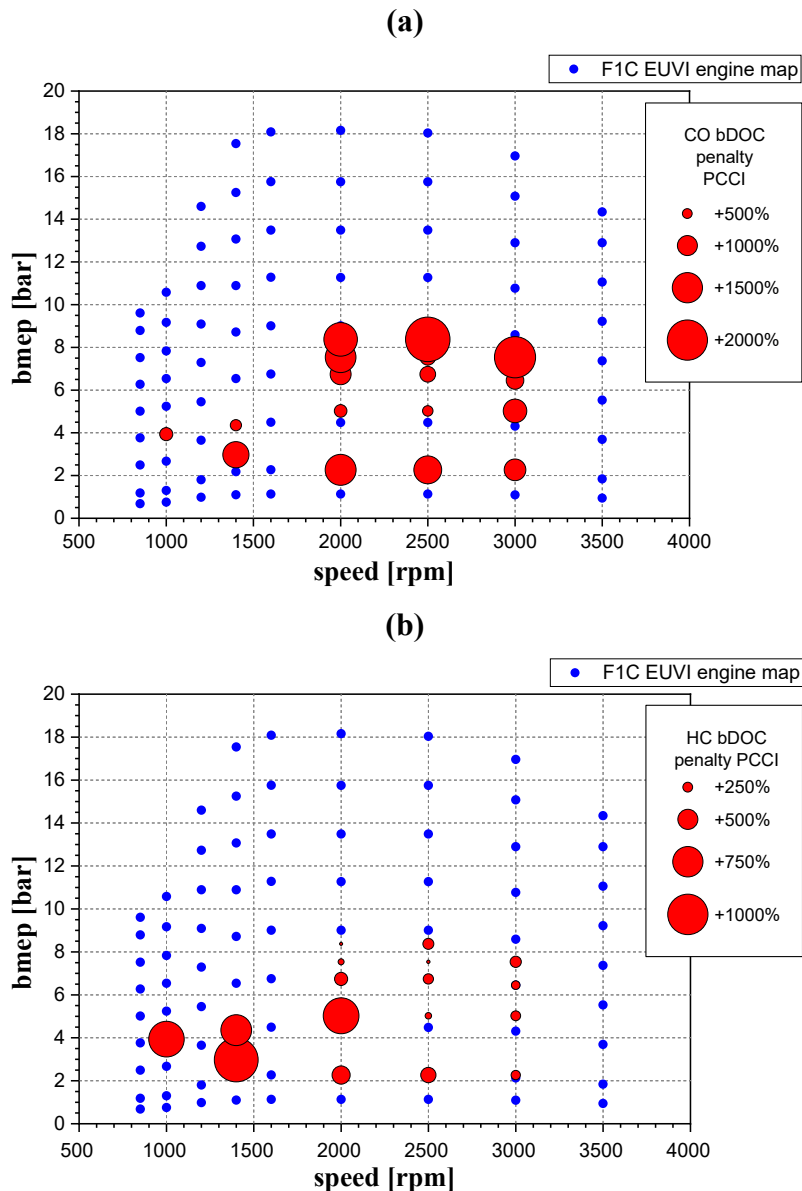
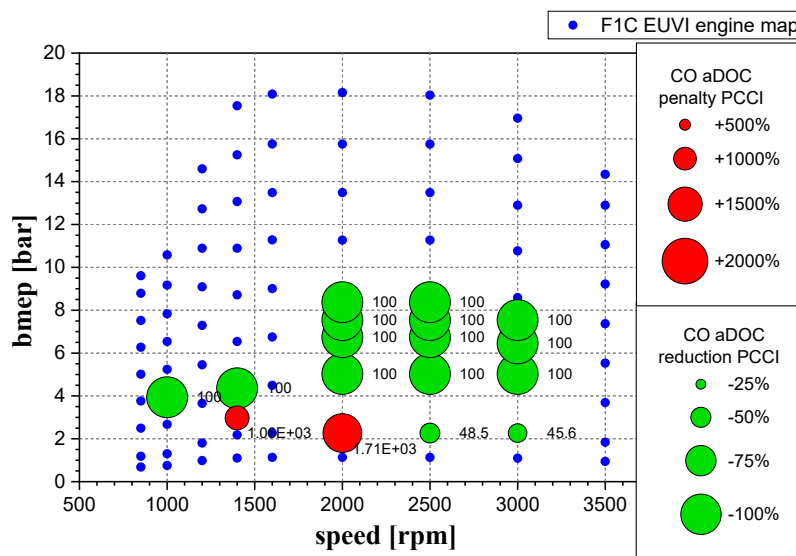


Figure 3.9. Percentage variations in engine-out CO (a) and HC (b) emissions between the F1C PCCI and the corresponding CDC values on the F1C Euro VI engine.

The DOC performance requirements for PCCI strategies are expected to be more stringent than in CDC operations. At this regard, Figure 3.10 reports the percentage variations of the tailpipe CO (Figure 3.10(a)) and HC (Figure 3.10(b)) emissions, measured downstream the DOC, with respect to the WHSC limit. The comparison with the CDC values on the F1C Euro VI was not possible because no ATS system was installed on that engine in its original configuration at the test bench. The tests were performed in steady-state conditions, waiting for a proper

stabilization of the engine conditions (i.e., until the exhaust gas temperature upstream the DOC kept almost steady) and then measuring the tailpipe emissions downstream the catalytic converter. It is evident how the DOC is effective at properly abating engine-out CO and HC emissions only above a certain load (about $b_{mep} = 3\div 4$ bar), i.e. at conditions which feature exhaust gas temperatures hot enough to make the DOC work sufficiently above its light-off temperature, thus being able to achieve a CO conversion efficiency of nearly 100% and to stay well below the WHSC limits of tailpipe HC. Unfortunately, the DOC light-off temperature appears not to be reached below this engine load conditions (with a partial exclusion of high speed and low load points, for which the DOC conversion efficiency, even though not the highest, is still able to reduce tailpipe CO emissions by about 45%, with respect to the WHSC limit), making engine-out CO and HC emissions problematic.

(a)



(b)

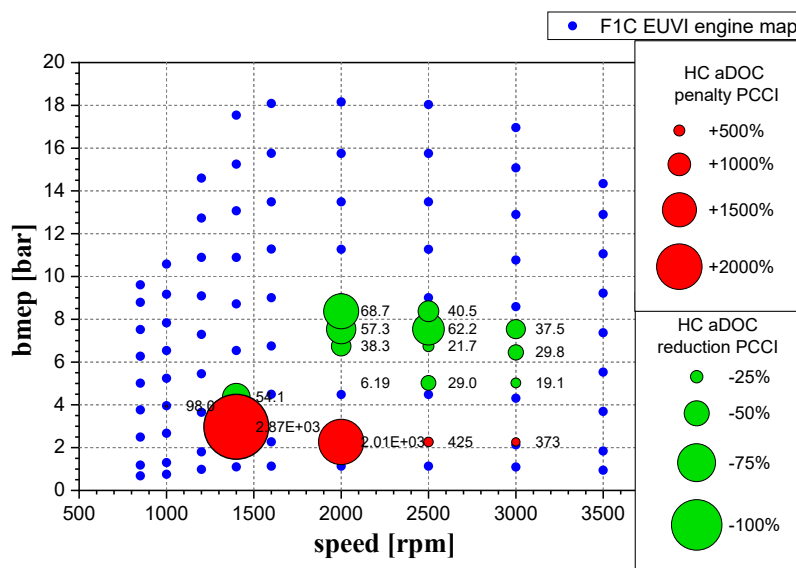


Figure 3.10. Percentage variations of tailpipe CO (a) and HC (b) emissions between the F1C PCCI engine and the WHSC limit.

Figure 3.11 shows how the early PCCI operations lead to a fuel consumption penalty ranging from about 3% to 11%, if compared to the corresponding *bsfc* values obtained with CDC operations with the baseline F1C Euro VI. The adverse effects, in terms of fuel consumption penalties, found with the F1C PCCI engine are partly due to the lower CR (which accounts for about 2.5% reduction on the ideal air-standard cycle efficiency [d'Ambrosio, et al., 2018]) and to the decrease in combustion efficiency (over the 0.5-3% range [d'Ambrosio, et al., 2018]). Furthermore, as previously explained, *bsfc* is also negatively affected by the very early values of SOI (an early SOI advances MFB50, i.e. the combustion event occurs mainly during the last part of the compression stroke) and the highly throttled exhaust flap positions (a throttled exhaust flap position determines an increase in engine backpressure and in EGR rate, which in turn reduces the ideal cycle efficiency due to its influence on the heat capacity ratio of the inducted charge). On the other hand, the F1C Euro VI engine equipped with an SCR system, tested by the OEM, features a urea consumption ranging from 0.5% to 4.5% of the fuel consumption, within the same portion of engine map tested for the F1C PCCI. In addition, according to literature results [Singh, et al., 2009], the fuel consumption penalty associated with DPF backpressure and regeneration strategies ranges from 4.5% to 7.0%, depending on the frequency of the regeneration events. When PCCI combustion strategies are implemented, the very low engine-out NO_x and soot emissions would allow the urea consumption for the SCR system to be minimized, especially when the engine is working within the area of the engine map where suitable PCCI operations are attainable. Furthermore, also the frequency of DPF regeneration events would be minimized. Thus, if analyzing a comprehensive fluid (fuel + urea) operating cost, some fuel penalties deriving from the implementation of the PCCI strategy may be tolerated. For instance, to evaluate the objective function needed to find the optimum PCCI points in our analysis, a 10% *bsfc* increase (compared to the *bsfc* measured for the baseline CDC calibration on the F1C Euro VI) was considered.

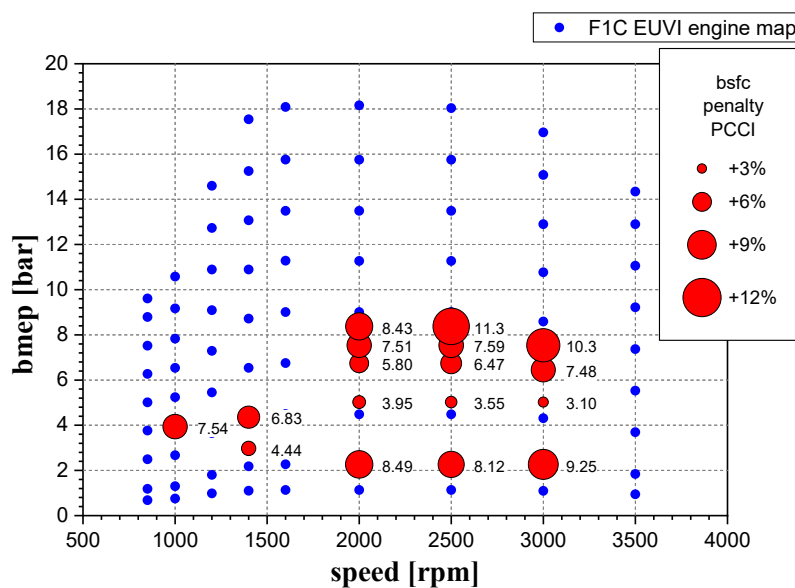


Figure 3.11. Percentage variations of *bsfc* between the F1C PCCI and the corresponding CDC values on the F1C Euro VI engine.

As expected, significant differences are found if the in-cylinder pressure traces of the baseline CDC points on the F1C Euro VI and the PCCI optimum points on the F1C PCCI are compared.

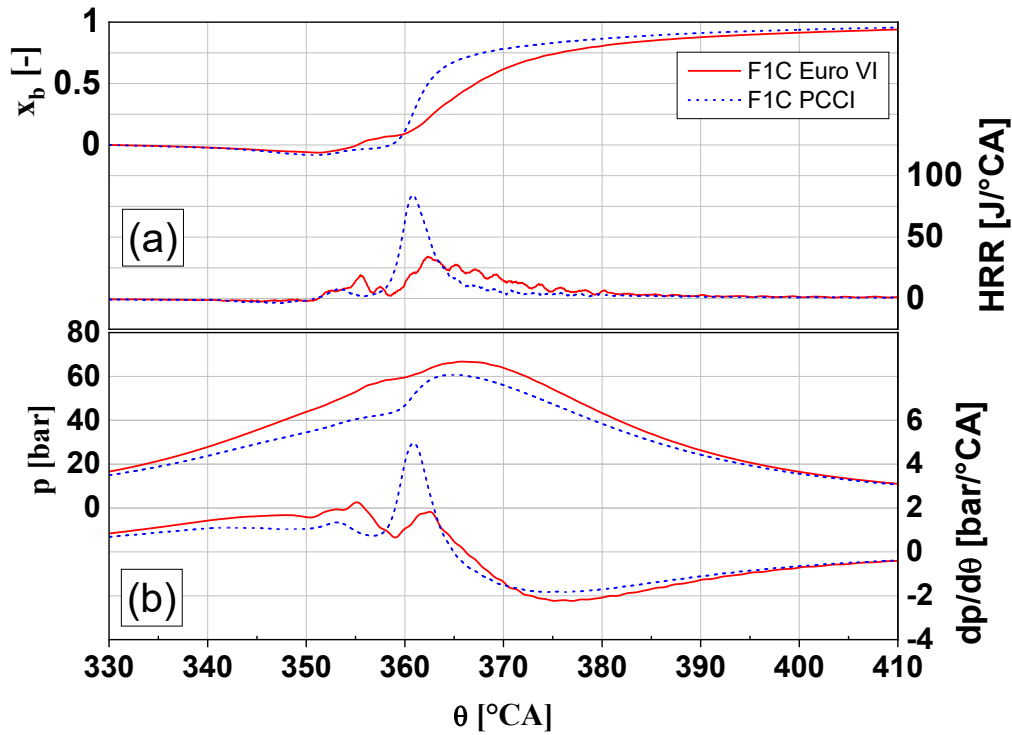


Figure 3.12. Mass fraction burned x_b (a - left axis), HRR (a - right axis), in-cylinder pressure (b - left axis), and its derivative (b - right axis) versus crank angle position at the 2000×2.3 point for both the F1C PCCI (blue dotted line) and the corresponding CDC calibration on the F1C Euro VI engine (red solid line).

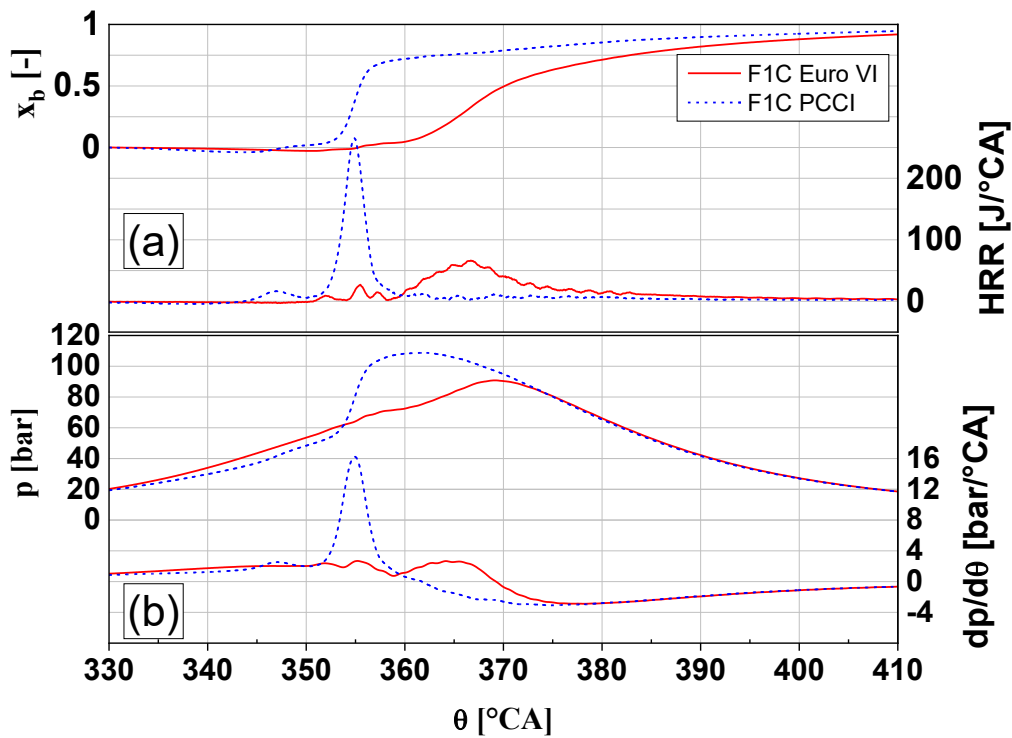


Figure 3.13. Mass fraction burned x_b (a - left axis), HRR (a - right axis), in-cylinder pressure (b - left axis), and its derivative (b - right axis) versus crank angle position at the 2000×7.5 point for both the F1C PCCI (blue dotted line) and the corresponding CDC calibration on the F1C Euro VI engine (red solid line).

Figures 3.12 and 3.13, respectively related to the 2000×2.3 and to 2000×7.5 engine operating points, show, in the bottom part, the p_{cyl} trace and its derivative (measured inside the cylinder #1) and, in the upper part, the corresponding HRR and mass fraction burned (X_b). The PFP values for the F1C PCCI are smaller than the corresponding CDC calibration values at low loads, while they are larger at higher loads. At low loads, e.g. at 2000×2.3 (Figure 3.12), the very large ID, due to the large EGR dilution the engine can tolerate, makes the PFP occur during the expansion stroke and, consequently, the maximum pressure derivative is dampened (below 5 bar/°CA). At higher loads, e.g. at 2000×7.5 (Figure 3.13), the combustion process develops well before the TDC, i.e. during the compression stroke, with a consequent large increase in the PFP and in the maximum pressure derivative (which reaches up to 16 bar/°CA). As shown in Figure 3.14, the maximum values of the in-cylinder pressure derivatives within the explored PCCI area range between 5-20 bar/°CA. These values are much bigger than those achieved with the CDC calibration on the F1C Euro VI, which ranged between 1.5-5 bar/°CA. This result may be used to set a further limit to the maximum explored *bme_p* in PCCI combustion mode. However, the PFP values of all the PCCI working points on the F1C PCCI engine never exceeded the PFP values achieved at full-load with the F1C Euro VI engine.

The major issue related to the large values of in-cylinder pressure derivatives during PCCI operations is the high CN levels [Torregrossa, et al., 2017], as also seen in previous Sections. Figure 3.15 shows the CN increment experienced during the PCCI tests with respect to the baseline CDC calibration. As the increment in CN is huge (up to +18.7 dBA), appropriate countermeasures should be taken into account to limit the increase in the acoustic noise, such as splitting the fuel injection strategy, as it will be detailed in the following Chapter.

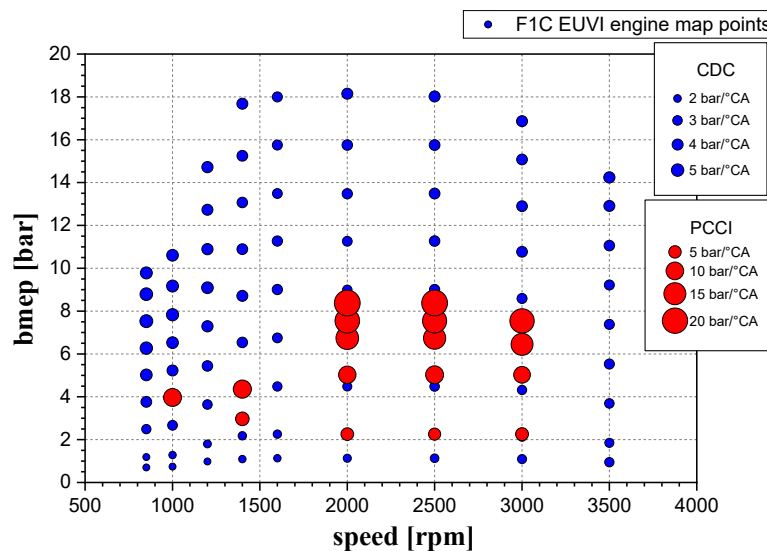


Figure 3.14. Maximum in-cylinder pressure derivatives during PCCI operations on the F1C PCCI and during CDC operations on the F1C Euro VI engine.

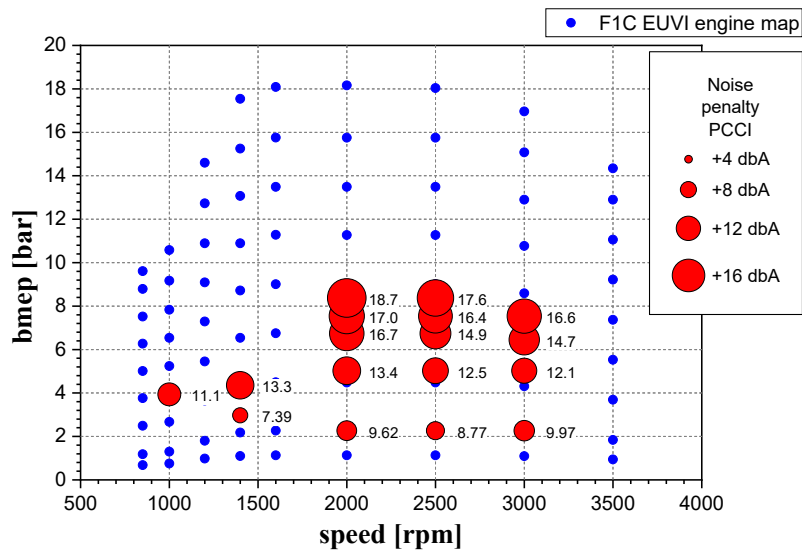


Figure 3.15. Increment of CN levels (in dB) between the F1C PCCI and the corresponding CDC values on the F1C Euro VI engine.

3.4 “Uncooled” EGR strategy at low load⁴

One of the main issues, characteristic of all LTC concepts, has been pointed out to be the harmful increase in incomplete combustion species emissions, due to the relatively low in-cylinder temperatures during the combustion process, the increased ID period (which sharpens the occurrence of over-mixing phenomena) and the wall-wetting by the early injected fuel. Nevertheless, great attention has been put on this theme, especially focusing on CO and HC emissions during vehicle cold starts or when operating at the lowest engine loads, i.e. during conditions featuring the lowest in-cylinder and exhaust temperatures. In these circumstances, for instance during a given type approval driving cycle, the managing of the after-treatment systems could be troublesome and represent a key theme, as high engine-out CO and HC levels cannot be mitigated until the catalytic system reaches its light-off temperature [Boot, et al., 2009; Ye, et al., 2012]. Several countermeasures may be adopted to mitigate these issues, such as limiting the early injection wall-wetting through injectors with narrower spray cone angles [Walter & Gatellier, 2002; Genzale, et al., 2009], using alternative fuels featuring lower boiling points [Shimazaki, et al., 1999] or recirculating “uncooled” EGR [Zeraati-Rezaei, et al., 2017].

As previously highlighted, the F1C PCCI engine was endowed with injectors featuring reduced cone angles (from 139.8° to 130°) and lower static flowrate (from 990 cm^3 to 750 cm^3 in 30 s, when fueled at 100 bar) than those mounted on the baseline F1C Euro VI version. This is to limit the risk of cylinder wall impingement. Nevertheless, the simultaneous reduction of the engine CR (from 17.5:1 to 14.6:1),

⁴ Most of the contents of this Section have been previously published in [d'Ambrosio, S., Mancarella, A., Manelli, A., & Salamone, N. (2019). "Effect of the application of an uncooled high-pressure EGR strategy in low-load diesel PCCI operation". AIP Conference Proceedings, 2191(1), 020055. doi:10.1063/1.5138788].

mainly thought to achieve lower flame peak combustion temperatures, responsible for the in-cylinder NO_x formation mechanisms, tends to dramatically increase the liquid penetration of the fuel spray inside the combustion chamber, exacerbating the over-mixing phenomena responsible of worsened engine-out HC and CO emissions. As a result, the low-load PCCI region calibrated on the F1C PCCI engine was previously pointed out to dramatically suffer of too high tailpipe incomplete combustion species emissions. Therefore, the application of an “uncooled” EGR strategy within the lowest load PCCI operating region was experimentally tested as a way to limit them [d’Ambrosio, et al., 2019].

3.4.1 “Hot” and “cold” EGR system layout configurations

So far, it has been clear how the recirculation of high quantity of cooled exhaust gas back to the intake manifold is almost mandatory for the early PCCI strategies, as they help to reduce the peak combustion temperatures. Cooling the EGR is beneficial, as the increment in density of the burned gases downstream the EGR cooler increases the recirculated mass of inert gases and therefore reflects in a further reduction of in-cylinder NO_x production. On the other hand, the lower EGR temperatures may enhance the risk of over-mixing phenomena, raising in-cylinder formation of HC and CO, as well as they may negatively affect the exhaust gas temperature upstream the after-treatment line. Therefore, a comparison between regularly “cooled” and “uncooled” EGR strategies (featuring the short-route EGR configuration, as previously highlighted in the engine experimental setup) has been performed to point out possible benefits coming from avoiding the EGR cool down, especially at the lowest loads. Starting from the already discussed F1C PCCI prototype engine configuration, two different EGR system layouts were tested. The first layout (which will be called “cold”, or “cooled”, EGR system) consists in the regular installation on the F1C PCCI engine of the 32 kW thermal cooling power EGR cooler, i.e. a water-to-gas heat exchanger, whose aim is to cool down the exhaust gases sent back to the intake manifold. The cooling water required, in turn, is cooled down by means of a second water-to-water heat exchanger, decoupled from the engine cooling loop, with the possibility to control the cooling water flowrate through this second heat exchanger by regulating a PID-controlled electrovalve. With this secondary cooling circuit, independent from the engine main cooling system, it is possible to control the temperature of the recirculated gases downstream the EGR cooler. In particular, the target temperature set was kept equal to 85°C throughout the experimental campaign. The second layout (which will be called “hot”, or “uncooled”, EGR system) is then obtained by removing the EGR cooler, replacing it with a straight duct. Obviously, in this way, no cooling and no control of the EGR temperature is performed. Thus, the temperature of the exhaust gases sent back to the intake manifold will depend on the combustion characteristics of each engine working point, with some influence of the heat transfer through the straight duct due to unavoidable conduction and convection mechanisms.

For these tests, the ATS only consisted of a DOC for the HC and CO oxidation. Thermocouples and pick-up streams for the gaseous pollutant emissions

measurement were placed both upstream and downstream the DOC, to evaluate its working temperatures and the related HC and CO conversion efficiency.

3.4.2 Experimental comparison between hot and cold EGR system layouts

The comparison tests between hot and cold EGR layouts were performed on the following steady-state engine working points (expressed in terms of speed n [rpm] \times torque Trq [Nm]), using early single injection PCCI calibrations: 1000 \times 27, 1400 \times 27, 2000 \times 27, 2500 \times 27, 3000 \times 27 ($b_{mep} \approx 1$ bar), 2000 \times 54, 2500 \times 54, 3000 \times 54 ($b_{mep} \approx 2$ bar), 1000 \times 71, 1400 \times 71, 2000 \times 71, 2500 \times 71, 3000 \times 71 ($b_{mep} \approx 3$ bar) and 1000 \times 94 ($b_{mep} \approx 4$ bar). The portion of the engine map considered has been load-limited to guarantee stable PCCI operations, especially with the hot EGR configuration. In fact, when no EGR cooling is performed, the increase in load leads to recirculate hotter and hotter gases, thus rapidly approaching quasi-stoichiometric inlet charges due to the worsened volumetric efficiency (λ_v) and rapidly rising soot emissions, not in line with the aim of this study.

For each of the considered working points, preliminary tests were performed, again, by exploring several combinations of the most relevant calibration parameters (i.e., the position of the VGT to control the boost pressure, the position of the exhaust flap to control the EGR rate, the SOI and the rail pressure), with the “one-factor-at-a-time” approach [Montgomery, 2000]. Then, these selected variables have been varied among variation ranges suitable to the realization of PCCI combustion events, for both hot and cold EGR configurations.

Table 3.4. Relevant engine parameters for the “optimal” calibrations, with cold and hot EGR configurations.

Speed [rpm]	Torque [Nm]	Cold EGR				Hot EGR			
		SOI [°bTDC]	p_{rail} [bar]	T_{int} [°C]	EGR rate [%]	SOI [°bTDC]	p_{rail} [bar]	T_{int} [°C]	EGR rate [%]
1000	27	16	600	53	63.5	16	600	92	53.6
1000	71	22	1200	59	47.8	14	1600	98	39.3
1000	94	22	1000	61	50.2	14	1600	93	43.4
1400	27	18	600	55	58.8	18	600	99	40.7
1400	71	28	650	62	58.8	24	1600	111	41.7
2000	27	20	600	59	57.4	26	800	111	43.8
2000	54	22	1000	60	55.7	26	1400	128	58.6
2000	71	34	1000	55	46.9	34	1400	150	55.9
2500	27	24	600	57	53.9	30	800	116	37.0
2500	54	26	1000	58	53.3	34	1200	136	44.8
2500	71	34	1200	54	47.6	38	1200	170	57.3
3000	27	28	600	52	54.4	36	1200	128	41.5
3000	54	26	1400	60	56.0	38	1400	150	50.2
3000	71	34	1600	51	53.7	40	1600	176	51.5

Starting from these preliminary tests, “optimal” calibrations (reported in Table 3.4) were selected for each engine operating point, both with hot and cold EGR configuration, minimizing an objective function which considered the main engine-out emissions and performance parameters with different weighting factors. Results

in terms of engine-out (labelled as bDOC, i.e. before the DOC converter) and tailpipe emissions (labelled as aDOC, i.e. after the DOC converter), as well as exhaust gas temperature upstream the after-treatment DOC and *bsfc*, are presented in the following Figures 3.16-3.24. In each of these figures, the blue and orange circles respectively refer to the cold and hot EGR configurations, while their dimensions are proportional to the value of the parameter reported on the y-axis (arranged on the graphs in different speed/torque coordinates throughout the portion of the engine map under investigation). The comparison has been performed keeping the engine stationary at every engine operating point, waiting enough time to let the conditions reach a proper thermal equilibrium.

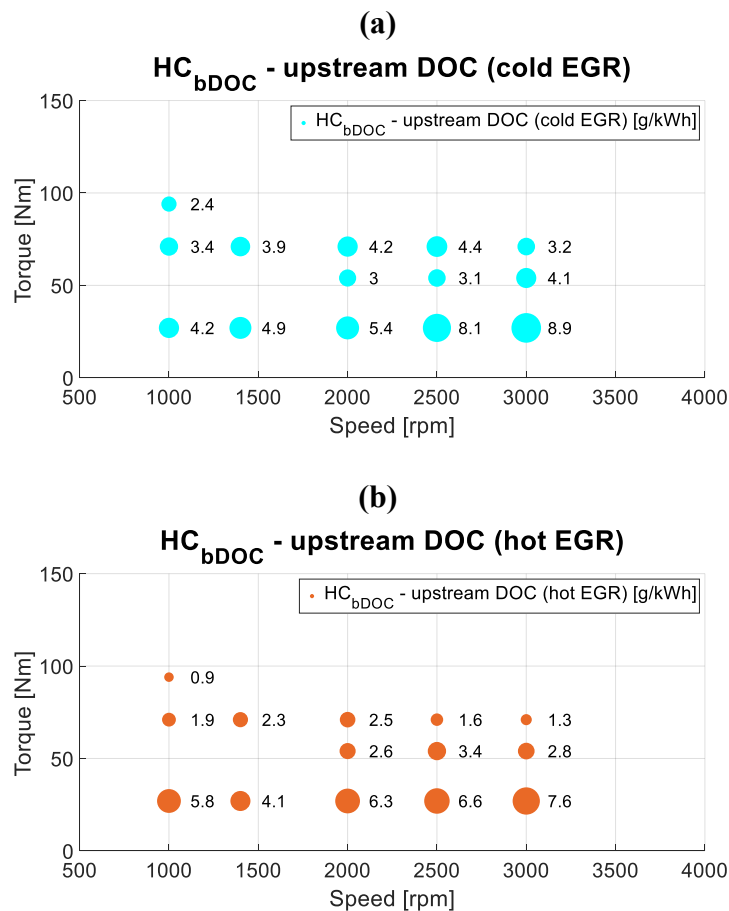


Figure 3.16. Comparison of engine-out HC emissions, with cold (a) and hot (b) EGR strategies.

Figures 3.16-3.17 compare respectively the engine-out unburned HC and CO emissions when using either cold or hot EGR strategies. High levels of HC (Figure 3.16) and CO (Figure 3.17) emissions are confirmed in both the considered EGR layouts and throughout all the considered low-load portion of the engine map.

(a)

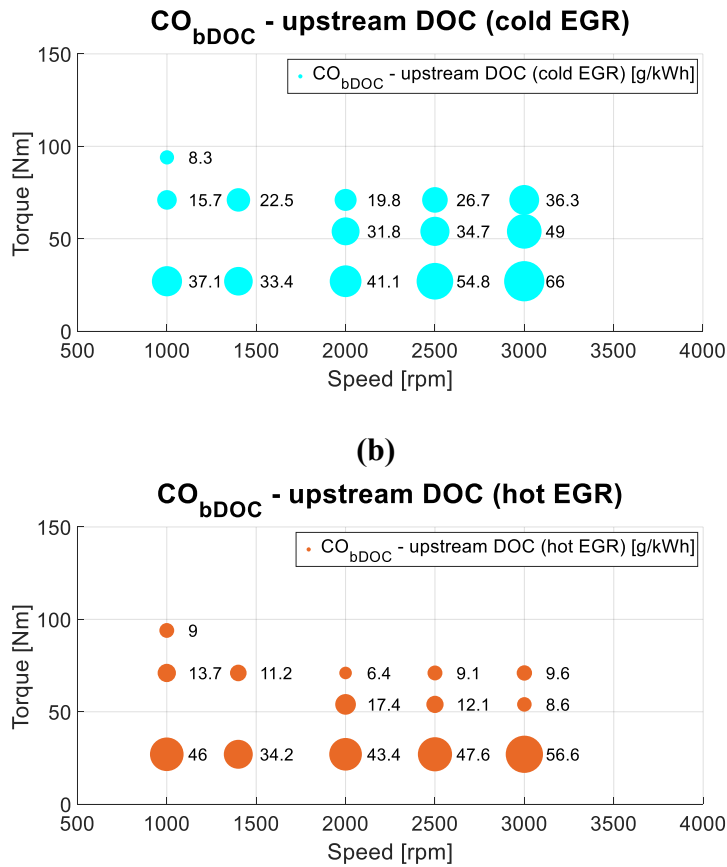


Figure 3.17. Comparison of engine-out CO emissions, with cold (a) and hot (b) EGR strategies.

Comparing Figure 3.16(a) and Figure 3.17(a) (referring to cold EGR) with, respectively, Figure 3.16(b) and Figure 3.17(b) (referring to hot EGR), it may be pointed out how the application of the uncooled EGR strategy, at the lowest considered load (i.e., $b_{mep} = 1$ bar and $Trq = 27$ Nm), tends to slightly worsen the incomplete combustion processes from PCCI operations. In this condition, the additional thermal energy the hot EGR gases are able to give to the intake charge (which might promote HC and CO oxidation) may be not enough to balance the negative effect coming from the reduction in the charge density and in the in-cylinder trapped mass obtained as the EGR temperature grows (which generate a further reduction in the in-cylinder oxygen availability and an increased difficulty to oxidize HC and CO molecules [d'Ambrosio & Ferrari, 2015a]). Conversely, at $b_{mep} \geq 2$ bar (i.e., $Trq \geq 54$ Nm), the balance between the abovementioned two effects overturn, thus making the uncooled EGR strategy slightly beneficial to reduce engine-out HC and CO emissions.

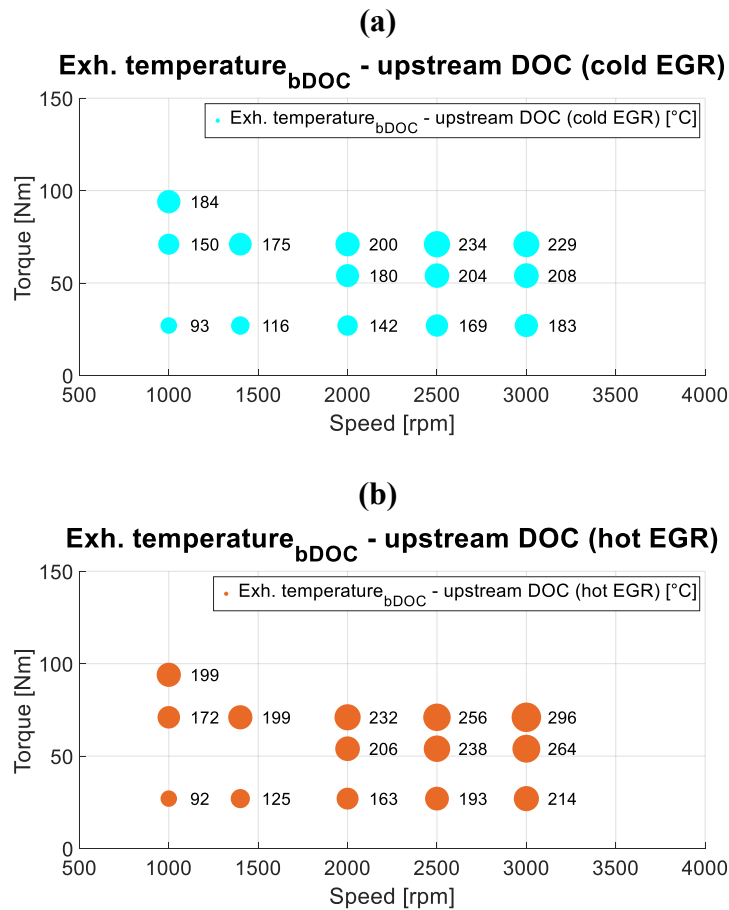


Figure 3.18 Comparison of the exh. gas temp. upstream the DOC, with cold (a) and hot (b) EGR strategies.

Figure 3.18 shows the exhaust gas temperature measured upstream the DOC, for both cold (Figure 3.18(a)) and hot (Figure 3.18(b)) EGR configurations. In all the investigated engine working points but the lowest load and speed case (1000×1 [rpm×bar]), recirculating uncooled EGR leads to higher intake gas temperatures (cf. Figure 3.19) and higher exhaust gas temperatures as well, with the exhaust temperature gains ranging from around 10 to 60°C. The main advantage of this extra thermal energy upstream the DOC is that it may be effectively exploited to let the DOC reach its light-off temperature [Ye, et al., 2012], which has been verified not to be reached in the majority of the analyzed points, if a conventional cold EGR strategy is adopted (this will be detailed hereinafter, in the following Figures) and whose importance is crucial, considering the very high level of engine-out HC and CO emissions given by the engine and highlighted in Figures 3.16-3.17.

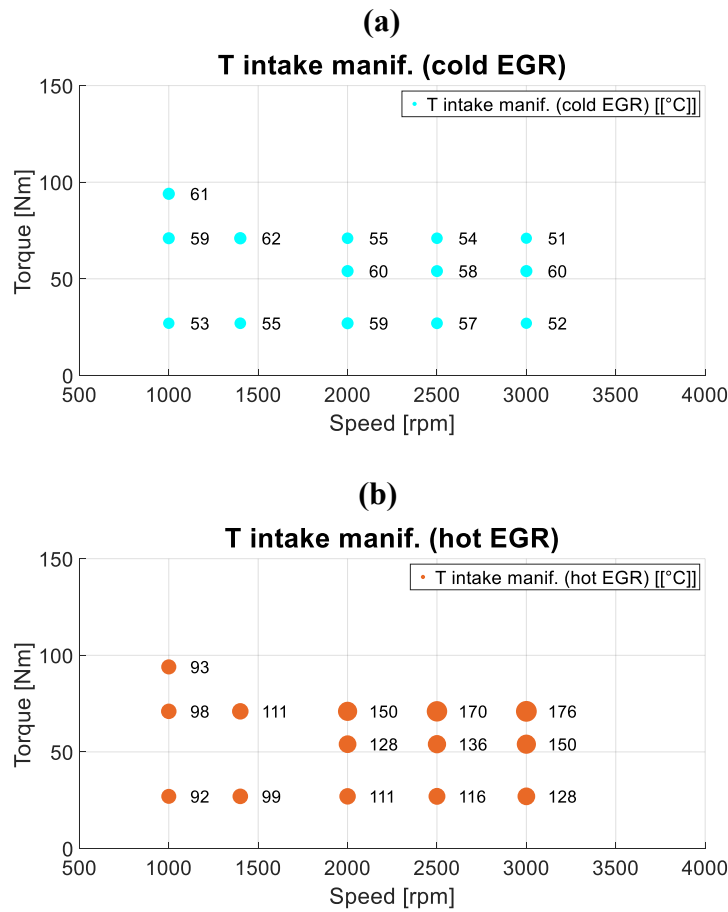


Figure 3.19 Comparison of the intake gas temperature, with cold (a) and hot (b) EGR strategies.

The following Figures 3.20-3.21 show respectively a comparison of the tailpipe (i.e., downstream the DOC) unburned HC and CO emissions when using cold or hot EGR strategies. The main advantage which can be highlighted by comparing Figure 3.20(a) and Figure 3.21(a) (referring to cold EGR) with, respectively, Figure 3.20(b) and Figure 3.21(b) (referring to hot EGR), is an enlargement of the area of the engine map where unburned HC and CO tailpipe emissions are cut almost up to zero by the DOC activity, when implementing the uncooled EGR layout. This is due to the already mentioned increase in exhaust gas temperature upstream the after-treatment system, which makes the DOC light-off temperature to be overcome. Still, at low speed and load conditions, uncooled EGR is not able to provide appreciable advantages with respect to the cold EGR case. Actually, it even provides slightly worse results at $b_{mep} = 1$ bar, when ranging from $n = 1000$ rpm to $n = 2000$ rpm, due to a too small increase in the exhaust temperatures which does not balance the already pointed out increase in engine-out HC and CO emissions.

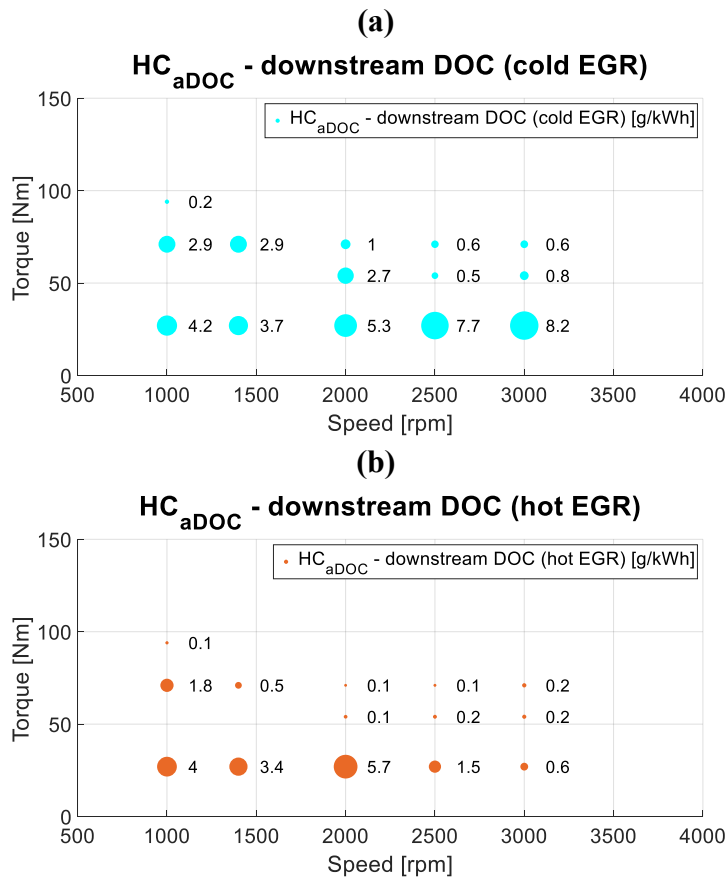


Figure 3.20 Comparison of tailpipe HC emissions, with cold (a) and hot (b) EGR strategies.

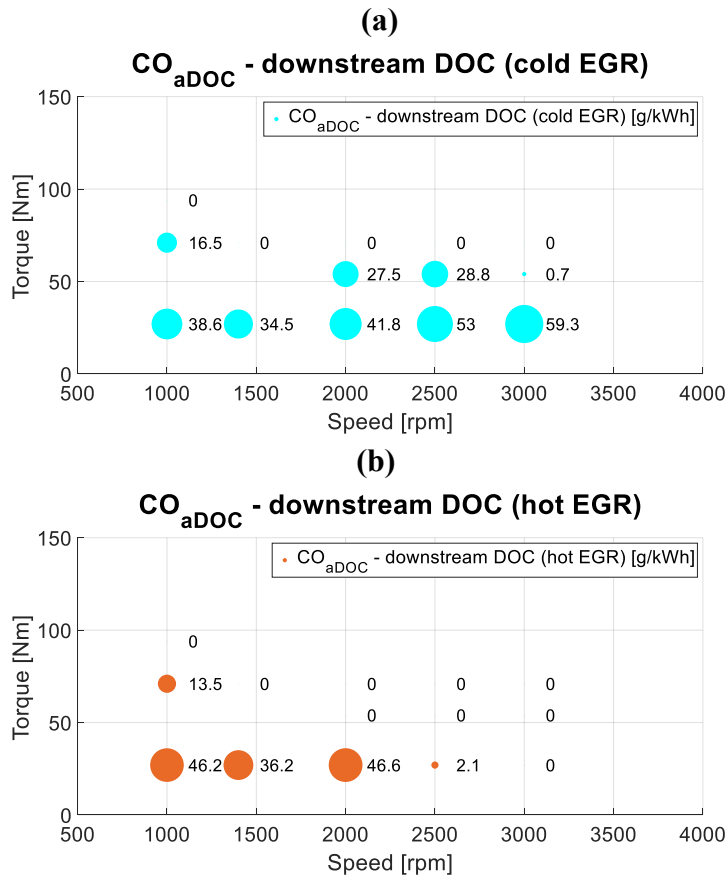


Figure 3.21 Comparison of tailpipe CO emissions, with cold (a) and hot (b) EGR strategies.

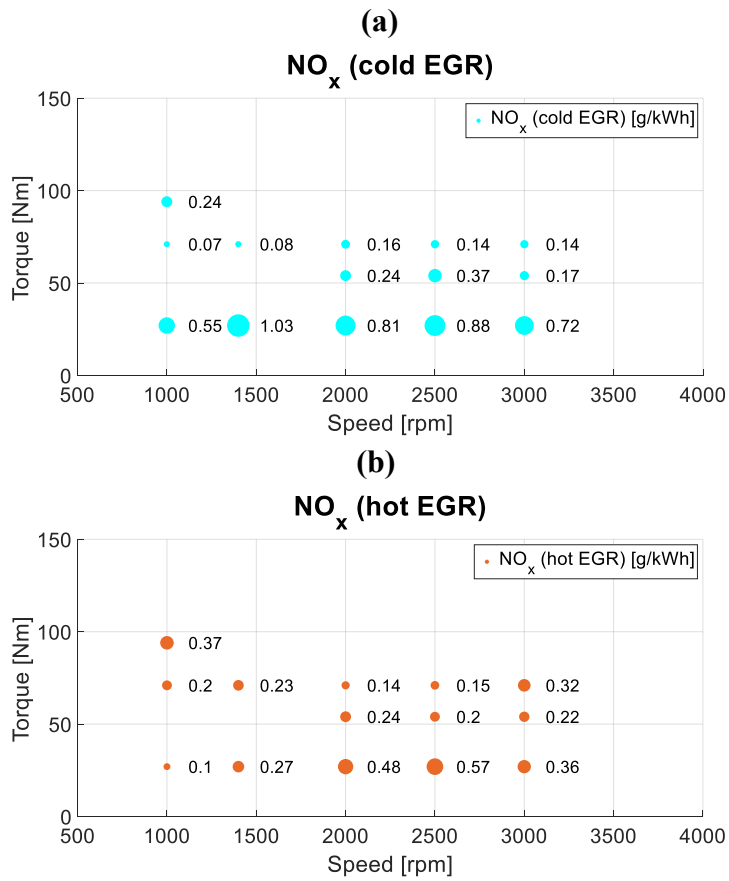


Figure 3.22 Comparison of exhaust NO_x emissions, with cold (a) and hot (b) EGR strategies.

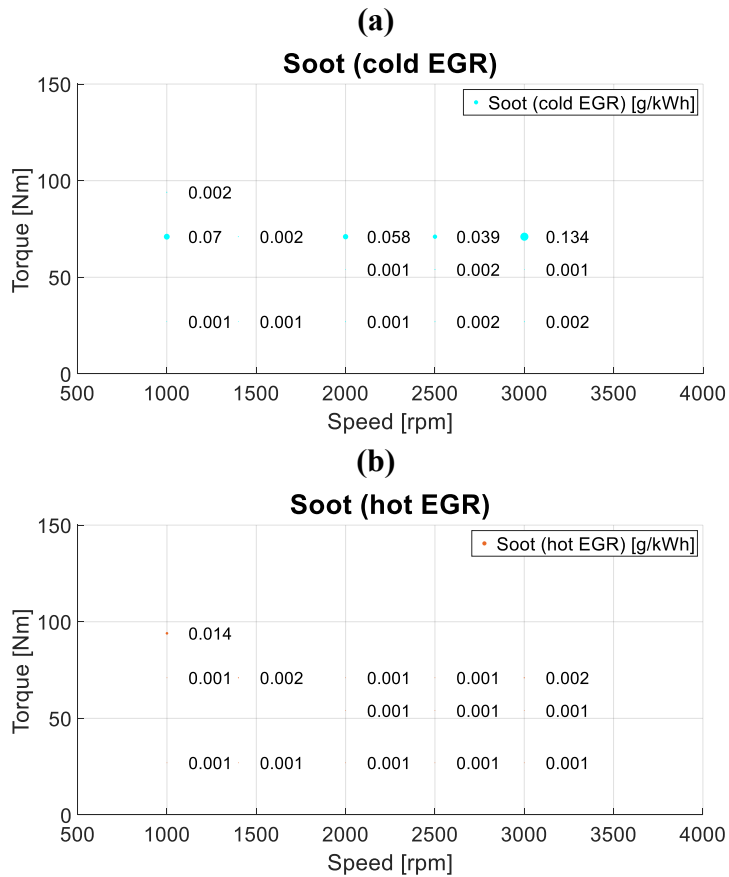


Figure 3.23 Comparison of exhaust soot emissions, with cold (a) and hot (b) EGR strategies.

Due to the low load PCCI conditions, the absence of the EGR cooler does not affect remarkably NO_x and soot emissions (cf. Figures 3.22-3.23), which keep at the outstandingly low levels typical of all early-PCCI operations.

On the other hand, *bsfc* (cf. Figure 3.24) seems to be slightly reduced when using uncooled EGR at $b_{mep} = 1$ bar, while at the higher loads considered it slightly worsens, especially at low speed. Anyway, with both the analyzed EGR layouts, the fuel consumption is higher with respect to the CDC operations run on the original version of the engine.

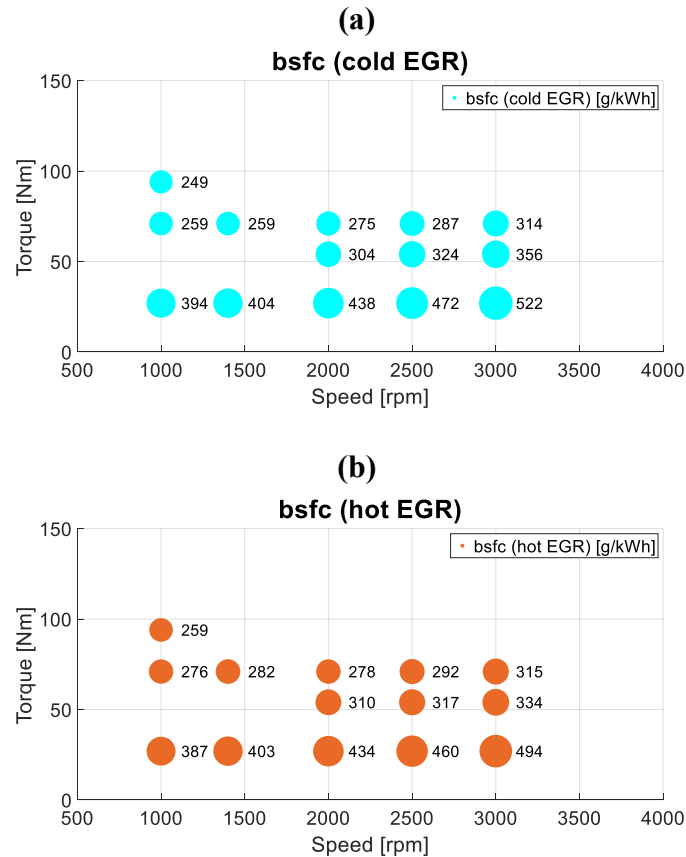


Figure 3.24 Comparison of *bsfc*, with cold (a) and hot (b) EGR strategies.

Summarizing, it is clear that the use of uncooled EGR may be favorable in the low load PCCI regime and, in practical applications, this could be implemented by installing a bypass valve upstream the EGR cooler, with a bypass pipe in parallel. However, from the thermal perspective (i.e. higher temperature possible), it would be certainly better to use some sort of variable valve control (VVC) (e.g., negative a valve overlap) in order to achieve high levels of internal EGR [Boot, et al., 2009].

Chapter 4

4. Noise and emissions reduction by multiple injection PCCI strategies

4.1 Double fuel injection PCCI strategy

In the following, a double fuel injection strategy, with a proper calibration of the timing and of the amount of fuel injected per each fuel shot, will be investigated. This solution exhibited a major potential to reduce incomplete combustion engine-out emissions, *bsfc* and CN over a wide range of engine operating conditions, if compared with single fuel injection PCCI, relying on the combination of the highly premixed combustion of the first fuel injection and on the acceleration of the oxidation rate due to the second one.

4.1.1 Results and discussion

A comparison between single and double injection patterns with the early-PCCI concept was performed on the following steady-state engine working points (expressed in terms of speed n [rpm] \times torque Trq [Nm]): 1400 \times 27 ($bmeP \approx 1$ bar), 1000 \times 94 ($bmeP \approx 4$ bar), 2000 \times 120 ($bmeP \approx 5$ bar), 2000 \times 161 ($bmeP \approx 6.5$ bar) and 2000 \times 200 ($bmeP \approx 8.5$ bar).

Starting from an early single fuel injection pattern, part of the fuel was moved into a postponed second fuel injection shot. Introducing a second fuel injection, additional parameters (i.e., fuel quantity and timing of the second injection pulse) have to be calibrated, while the parameters which were found to be relevant in the case of the early single injection PCCI (i.e., rail pressure, timing of the first injection pulse, EGR rate, etc.) may need to be recalibrated, rising the difficulty to interpret the results of a comparison between single and double injection patterns. Consequently, to understand the effects of these additional influential parameters and to check which further improvements may be achieved by the introduction of a double fuel injection pattern, the following Sections look into the effects of proper single-variable sweeps of first and second pulse injection timing, as well as into the influence of the fuel split ratio, on exhaust pollutant emissions, *bsfc* and CN. Each single-variable sweep highlights the effect of a single parameter, keeping all the other parameters fixed, thus isolating which is the effect of each parameter on emissions and performance. Unfortunately, besides the simplicity of this approach,

its weakness is that possible important interactions between variables may not be identified, and this should be kept in mind when interpreting the results.

The double injection PCCI calibration was derived starting from the baseline single injection optimum calibration previously presented, but variations on several calibration parameters were necessary in order to find a good compromise between the different “requirements” of the two separate injection events. For instance, it was generally found beneficial to slightly reduce the EGR rate (especially at higher loads) and to vary the rail pressure (depending on the engine operating point) from what calibrated for the single injection case. In fact, the tolerance to the EGR rate with the introduction of the second fuel shot was found to decrease, due to excessive emissions of soot and incomplete combustion species, especially when relatively late second injection shots were dealt with. Moreover, while the earlier (first) part of the injection seemed to tolerate low rail pressure, with possible advantages by using low pressures coming from reduced spray wall impingement, the second injection can generally give better results when a high rail pressure is implemented, in order to promote air entrainment and fuel droplet break-up, avoiding excessive soot formation.

Second injection timing (SOI_{2nd}) sweeps

In order to look into the effects of the second injection timing on the combustion characteristics, DT sweeps were performed by progressively retarding the SOI of the second injection (SOI_{2nd}), while keeping the SOI of the first pulse (SOI_{1st}) fixed. The DT sweeps were performed twice, once per each ratio of the first/second injection quantities q_{1st}/q_{2nd} (namely 75%/25% and 50%/50%), as outlined in Figure 4.5..

In the following Figures 4.2, 4.5-4.6 and 4.8-4.9, several y-axes, which report engine-out NO_x, soot, CO and HC emissions, *bsfc*, CN and MFB50 (for the 1400×1 case) or EGR rate (for all the other cases), are stacked in function of the DT for the five engine operating points previously reported (i.e., 1400×1, 1000×4, 2000×5, 2000×6.5 and 2000×8.5). In each graph, the light green (with triangular symbols) and the dark green (with square symbols) solid lines refer, respectively, to the results of the 75%/25% and 50%/50% double injection PCCI strategies. They are both compared with the results pertaining to the single injection PCCI strategy (i.e., the calibration whose results are reported in Section 3.3), outlined as a horizontal red solid line, and with those of the baseline CDC calibration obtained in the conventional F1C Euro VI, outlined as a horizontal dashed violet line.

(a)

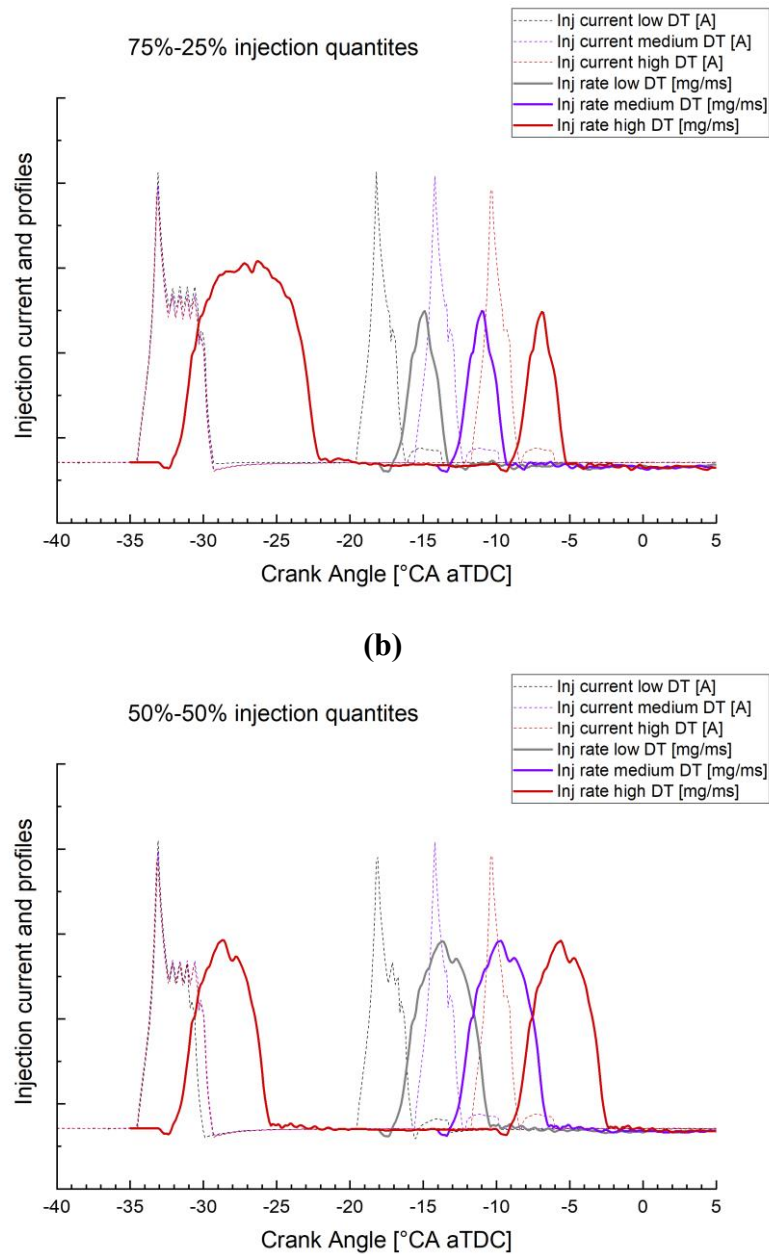


Figure 4.1. Example of 2nd injection timing sweeps: fuel injection rate and current profiles for a 75%-25% (a) and 50%-50% (b) fuel split.

Second injection timing (SOI_{2nd}) sweeps at low loads

The experimental analysis started from a low-load condition, corresponding to the engine operating point 1400×1 . Starting from the early single fuel injection calibration, which featured a SOI of $18^\circ CA$ bTDC, the fuel injection event was divided into two separate shots, varying the SOI_{2nd} and the ratio of the first- and second-injection quantities (i.e., the fuel split ratio q_{1st}/q_{2nd}). In this case, the minimum DT was restricted to $740 \mu s$, corresponding to about $6^\circ CA$, since lower DT values did not give appreciable differences from the single injection case, due to the relevant fuel premixing.

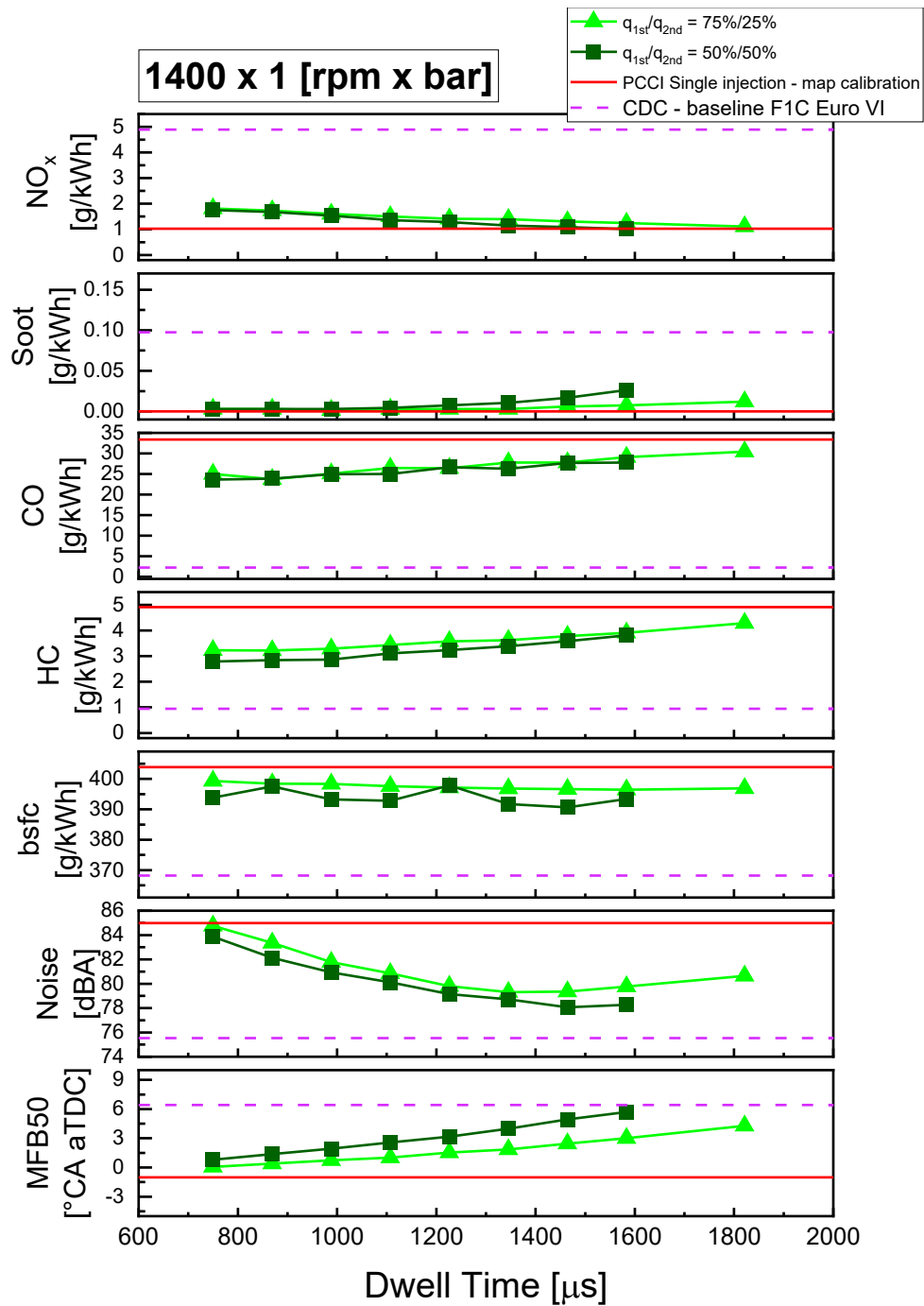


Figure 4.2. Results of a 2nd injection timing sweep at 1400×1, for a 75%-25% (light green and triangular symbols) and 50%-50% (dark green and square symbols) fuel split. Comparison with the PCCI single injection (red solid line) and the CDC baseline (violet dashed line) calibrations.

Progressively delaying the SOI_{2nd} , the combustion event tends to be delayed, as can be seen by the monotonically increasing trend of the MFB50 reported in Figure 4.2, and the corresponding variation of $bsfc$ as a function of the DT mainly depends on how much the combustion event is shifted towards the TDC. In fact, the more the combustion is delayed towards the TDC, the more the heat release takes place later during the compression stroke, minimizing the negative work on the piston moving upwards (that is to say, higher work conversion efficiency η_{wc}). Furthermore, the more the fuel is injected during the second injection event (i.e.,

passing from $q_{1st}/q_{2nd} = 75\%/25\%$ to $q_{1st}/q_{2nd} = 50\%/50\%$, the more pronounced is this positive effect on $bsfc$, which is then the lowest when $q_{1st}/q_{2nd} = 50\%/50\%$ and the most delayed SOI_{2nd} are featured. Nevertheless, introducing a double-pulse injection strategy at low load brings to $bsfc$ values which are not too far from those obtained with the single-pulse injection pattern (reductions range from about -2% to -4%), keeping still quite worse than the fuel consumption values of the reference CDC calibration (ranging from the worst case of +8%, when implementing the double pulse strategy with the minimum DT and $q_{1st}/q_{2nd} = 75\%/25\%$, to the best case of +5.5% when implementing the double pulse strategy with high DT and $q_{1st}/q_{2nd} = 50\%/50\%$). The lower CR (as a result of the piston bowl design modifications brought on the F1C PCCI), the lower η_c related to appreciable wall impingement phenomena and the need of extensive EGR rates, all contribute to this detrimental fuel consumption.

As far as engine-out CO and HC emissions are concerned, double injection PCCI strategies at this low load seem to give appreciable benefits if compared to the single-stage injection pattern, whichever DT and fuel split ratio are implemented. The second injection has the potential to increase the in-cylinder temperature in the last part of the combustion phase, causing accelerated oxidation of HC and CO and, as a consequence, also some benefit on the thermal efficiency. In particular, Figure 4.2 witnesses how the best results are achieved when the two injection events are close, with reductions of about 25% CO and 40% HC, while progressively delaying the SOI_{2nd} shows monotonically increasing trend of both these incomplete combustion species. Indeed, a more delayed SOI_{2nd} might cause its fuel spray to target in proximity of the dome of the piston bowl (whose design has been optimized for the largely advanced timings of the first injection, in the F1C PCCI version). This can cause a liquid film deposition that is able to combust only partially, thus possibly increasing the emissions of incomplete combustion species [Lee & Reitz, 2006]. Moreover, delaying part of the heat release after the TDC might cause substantial reductions of the time available before temperature drops (due to the downward motion of the piston) and burnout mechanisms freeze the oxidation rates of any residual CO and HC molecule prior to the exhaust phase.

For both engine-out CO and HC emissions, the $q_{1st}/q_{2nd} = 50\%/50\%$ seems to be the most convenient strategy. In fact, injecting more fuel during the first early injection ($q_{1st}/q_{2nd} = 75\%/25\%$) lets a larger amount of fuel to burn in a highly premixed way (as can be perceived from the HRR traces depicted in Figure 4.3). Again, higher premixing means a bigger risk of over-mixing phenomena, thus hindering a complete combustion process and producing greater amounts of HC and CO.

Progressively retarding the SOI_{2nd} , keeping the SOI_{1st} fixed, causes a monotonically decreasing trend of engine-out NO_x emissions. The highly premixed combustion of the first early injection rises the in-cylinder pressure and temperature conditions before the occurrence of the second injection event, shortening its ID [Maiboom, et al., 2008]. Consequently, the combustion of the second injection develops at a larger extent in the mixing-controlled phase. Lower peak temperature and pressure values are achieved in correspondence of the diffusive flames when the SOI_{2nd} is

the most delayed, thus leading to reduced NO_x production. Comparing single against multi-pulse PCCI strategies with high DT values (cf. Figure 4.2), it turns out that the two strategies offer similar results in terms of NO_x emissions, when high DT split injections are dealt with, leading to massive reductions compared to the baseline CDC calibration (up to -80%). Nevertheless, low DT values make NO_x grow above the single injection PCCI level (up to +80%), even if keeping much lower than the CDC level (-60%).

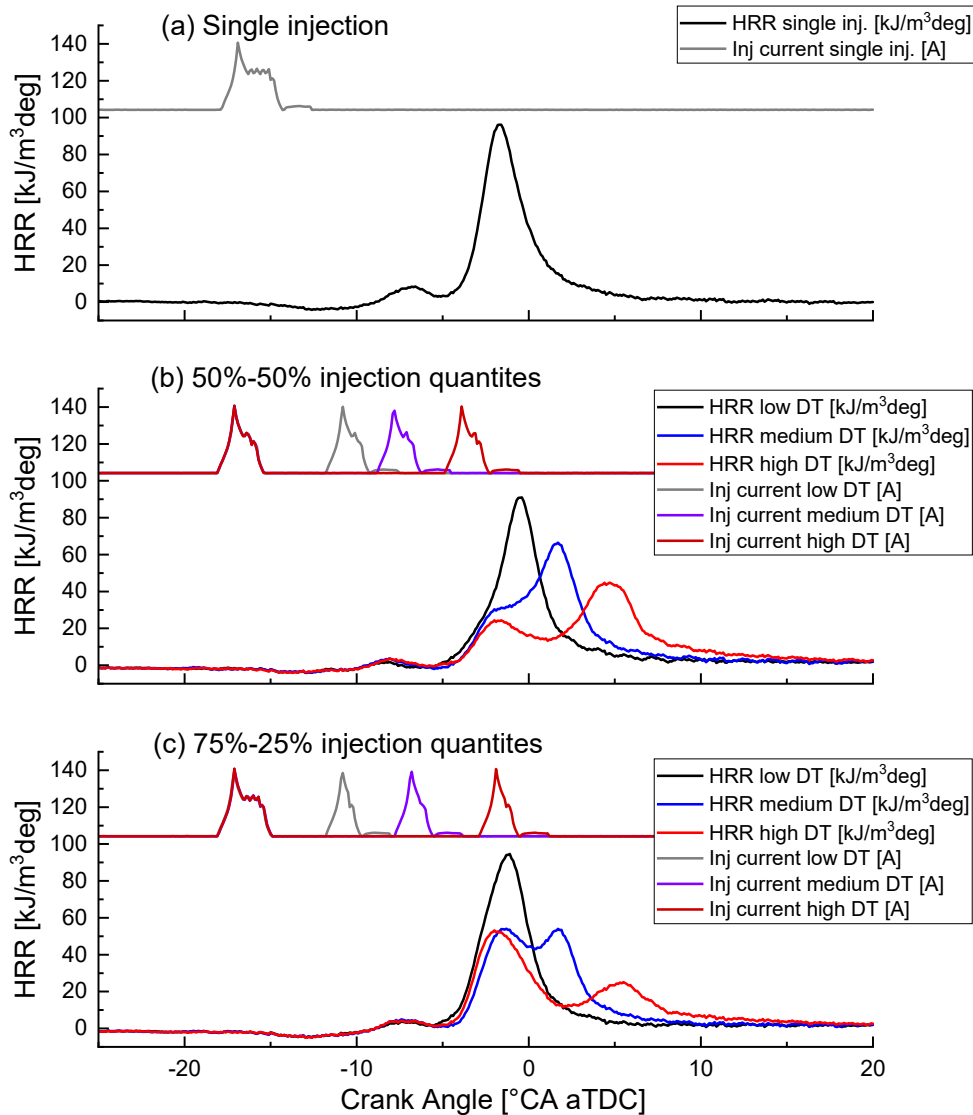


Figure 4.3. Comparison of the HRR traces at 1400×1 , between the PCCI single injection (a) and the 50%-50% (b) and 75%-25% (c) fuel split with double injection (2nd injection timing sweep).

As regards soot emissions, the progressive delay of $\text{SOI}_{2\text{nd}}$ causes slightly worsening soot increases (therefore, the trend in function of the DT is the opposite of what highlighted for NO_x), since the injected fuel quantity is relatively small and the intake in-cylinder O_2 concentrations are quite high. If the DT between the injections is small, soot emissions are extremely low, as those featured by the single-stage injection pattern. In fact, referring to Figure 4.3, with the lowest DT values the second injections start prior to the onset of the HTHR of the first early injection, allowing a longer premixing time, which results in lower smoke

emissions. Conversely, if the DT is enlarged too much, by delaying the second pulse, soot emissions start to increase, especially when the fuel split ratio is increased in favor of the second pulse ($q_{1st}/q_{2nd} = 50\%/50\%$), likely because in these conditions there is no sufficient time to oxidize all the soot particles produced during the combustion process of this larger and delayed second injection. Nevertheless, even in this case, soot emission levels keep much lower than those of the CDC baseline calibration, with a soot reduction not lower than 70%.

Finally, Figure 4.2 shows rapid CN reductions when SOI_{2nd} is progressively delayed, even if this decreasing trend flattens out with the highest DT implemented. This dependence of CN was expected, since retarding SOI_{2nd} generally results in a smoother combustion: moving the second pulse towards the TDC, the in-cylinder pressure and temperature conditions at the time of its SOI become increasingly favorable to autoignition and thus shorten the ID, reducing the duration and intensity of the premixed burn and, as a consequence, causing lower rates of pressure rise, which are strongly linked to CN generation. In fact, Figure 4.3 displays how, as previously seen talking about soot, when the timing of the second injection is close to the SOI_{1st} (minimum DT), a single high peak of HRR can be detected, after the onset of the LTHR. Therefore, the two injection pulses burn together under a premixed phase, and this explains the intense noise experienced in these cases, which approaches the CN featured by the single injection pattern (around 85 dBA), as shown in Figure 4.2. Conversely, excluding the case of the lowest DT between injections, two distinct peaks can be observed in the HRR profiles after the LTHR (cf. Figure 4.3(b) and Figure 4.3(c)). The first peaks of heat release are due to premixed combustion of the first injection, and are heavily reduced by the two-stage injection patterns featuring medium-to-high DT. Then, if the second peak of heat release (linked to the combustion of the second injection) is phased so that its evaporation smoothens the ongoing combustion process by absorbing heat, destructive interference of the in-cylinder pressure waves are triggered (i.e., destructive interference of a “spike” in the in-cylinder pressure increase with the preceding peak), attenuating the energy content of p_{cyl} in the 1–3 kHz range [Fuyuto, et al., 2014; d'Ambrosio, et al., 2018]. This CN dampening mechanism is evident as long as a noise spectrum analysis is performed. Therefore, the ensemble average p_{cyl} signals (obtained from 100 consecutive cycles, featuring low, medium and high DT values) were filtered by means of a low-pass filter with a cut-off frequency of 5 kHz, useful to remove the contributions resulting from the glow plug adapters in which the piezoelectric in-cylinder pressure transducers are fitted. Then, a fast Fourier transform (FFT) was applied to estimate the acoustic pressure levels (measured in dB) of the p_{cyl} signals, dividing their frequency contributions into one-third octave band intervals and summing the power spectral values within each of them. The resulting quantities were then assigned to the middle frequencies of each one-third octave band interval. The third-octave spectrum was then filtered through a structural frequency filter, which simulates the acoustic attenuation through the engine block (CAV filter), and by the so-called A-scale correction, which takes into account human acoustic perception.

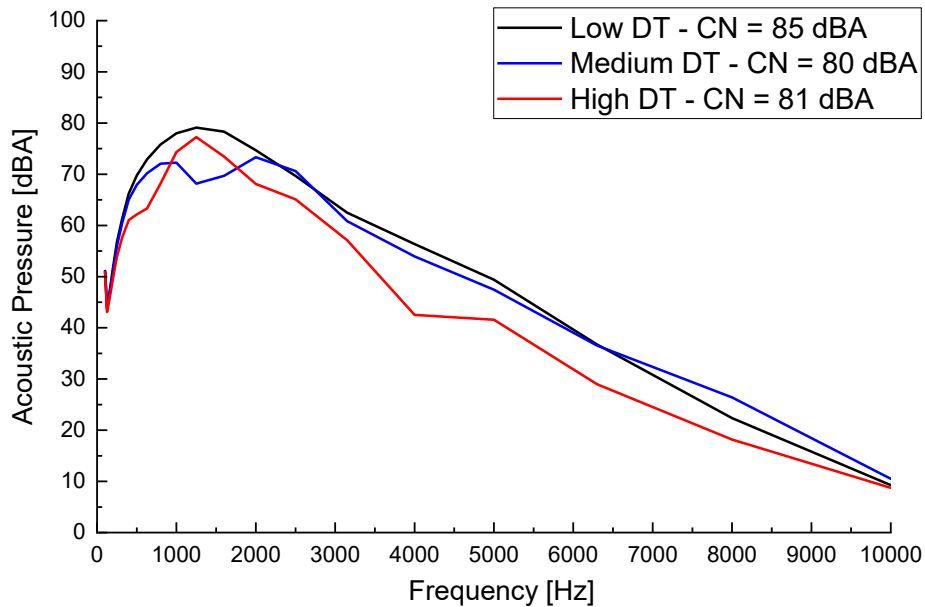


Figure 4.4. One-third octave frequency bands at 1400×1 , for the 75%-25% fuel split with double injection strategies (2nd injection timing sweep, with low, medium and high DT values).

The results are showed in Figure 4.4, which reports the frequency (in Hz) in the horizontal x-axis and the acoustic pressure (in dBA) in the vertical y-axis. A frequency range (around 500–3000 Hz) in which the spectral CN highlights the highest values, exists in each of the three Fourier spectra (low, medium and high DT). Within a narrower frequency band (around 1000-2000 Hz), the presence of a pronounced valley zone is evident only for the medium DT value (blue curve in Figure 4.4), while it tends to disappear as the DT value is increased (red curve) or decreased (black curve). The presence of valley zone in the medium DT case suggests that there is not an overly dominant frequency in the signal, which can give tonality to the noise. In fact, the higher the peak intensity and the smaller the extension of the peak zone, the more recognizable the CN as a specific noise by the human ear [d’Ambrosio & Ferrari, 2015b]. Therefore, a strong reduction of CN with respect to the single injection PCCI pattern can be achieved (about 4÷5 dBA lower), although some penalties are still present if the comparison is made with the CDC calibration (about 3÷4 dBA higher).

Second injection timing (SOI_{2nd}) sweeps at medium-to-high loads

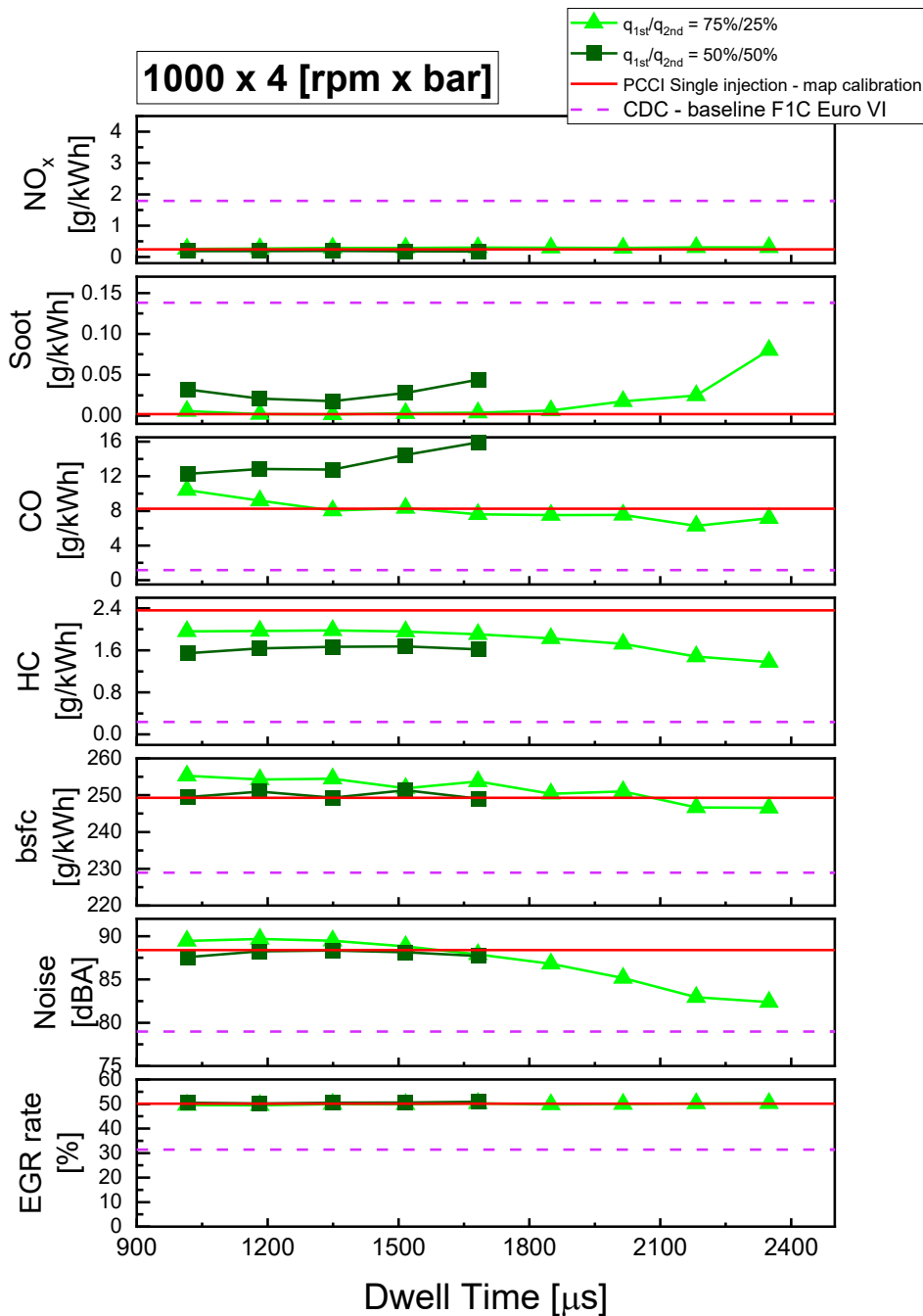


Figure 4.5. Results of a 2nd injection timing sweep at 1000×4, for a 75%-25% (light green and triangular symbols) and 50%-50% (dark green and square symbols) fuel split. Comparison with the PCCI single injection (red solid line) and the CDC baseline (violet dashed line) calibrations.

Second injection timing sweeps were performed also at medium-to-high load conditions, corresponding to the engine operating points 1000×4, 2000×5, 2000×6.5 and 2000×8.5. Again, the analysis started from the early single fuel injection calibrations and then dividing the fuel injection event into two separate shots, varying SOI_{2nd} and q_{1st}/q_{2nd} . The tolerance to the EGR rate with the introduction of the second fuel shot was found to decrease at this higher engine loads, due to excessive emissions of soot and unburned combustion species,

especially when relatively late second injection shots were dealt with. Therefore, the EGR rates were reduced (except for the 1000×4 point, for which this reduction was not necessary and a slight advance of the SOI of the first injection was enough) if compared to the single-stage injection case, and the following Figures 4.6 and 4.8-4.9 will include a graph to highlight these differences.

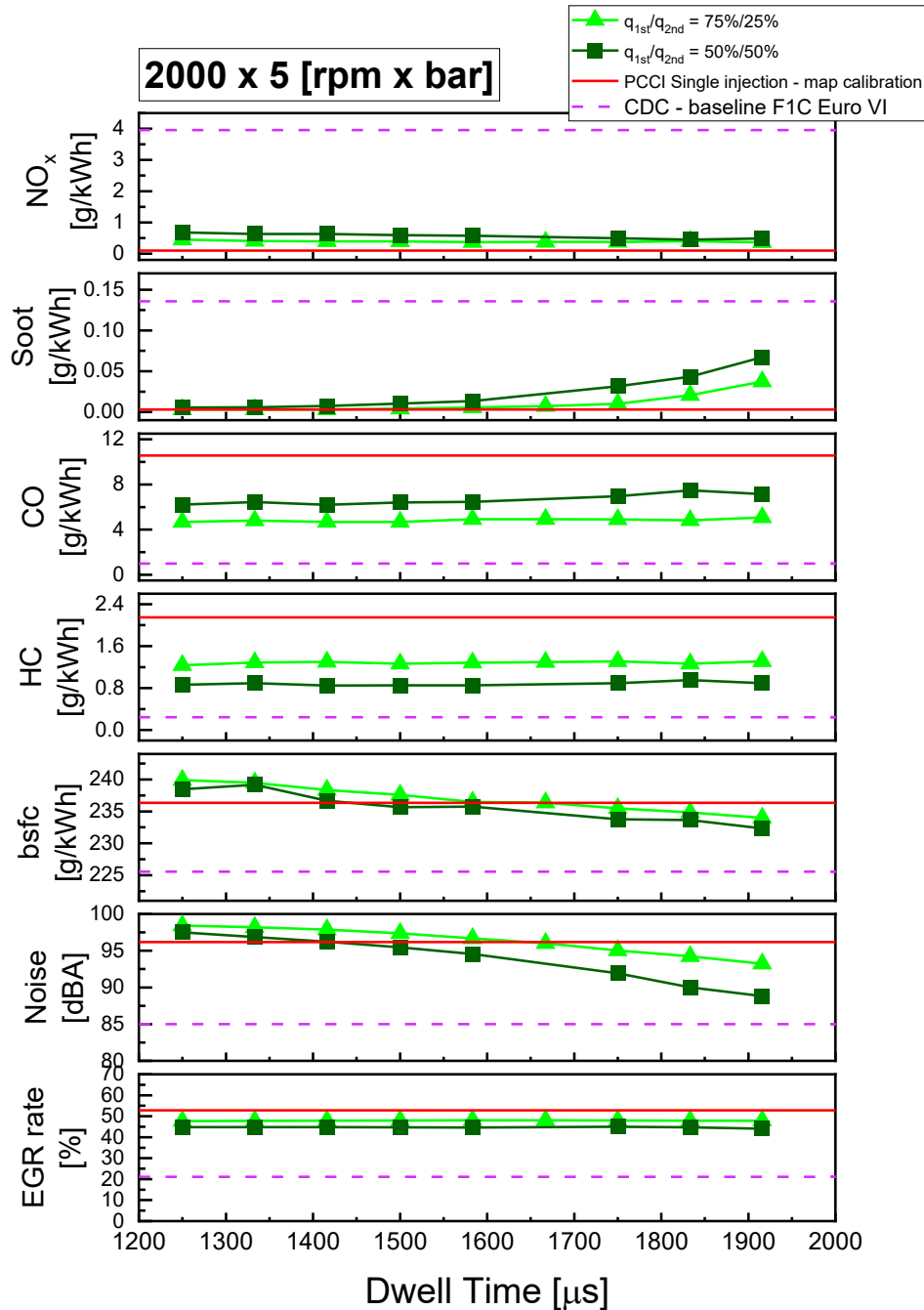


Figure 4.6. Results of a 2nd injection timing sweep at 2000×5, for a 75%-25% (light green and triangular symbols) and 50%-50% (dark green and square symbols) fuel split. Comparison with the PCCI single injection (red solid line) and the CDC baseline (violet dashed line) calibrations.

The results shown in Figures 4.5-4.6 and 4.8-4.9 highlight tendencies which are somewhat similar to those reported in the lower load case, i.e. 1400×1. Progressively delaying the SOI_{2nd}, the *bsfc* keeps showing a monotonic tendency to

decrease, as a function of the DT. As previously stated for the 1400×1 case, this is due to a higher work conversion efficiency (η_{wc}), thanks to the reduced negative work on the piston moving upward when the combustion is shifted later, and this is linked, again, to the fact that the 50%/50% fuel split ratio curves (dark green) give lower fuel consumption values than the 75%/25% ones (light green). Actually, this latter statement is true in all the considered higher load engine operating points, apart from the 2000×6.5 (cf. Figure 4.8), where the 50%/50% fuel split ratio curve even overcomes the engine-out CO and HC levels of the single injection PCCI, especially when $DT \geq 1300 \mu s$ are implemented. This witnesses a poor combustion efficiency (η_c), which counterbalances any possible benefit on *bsfc*.

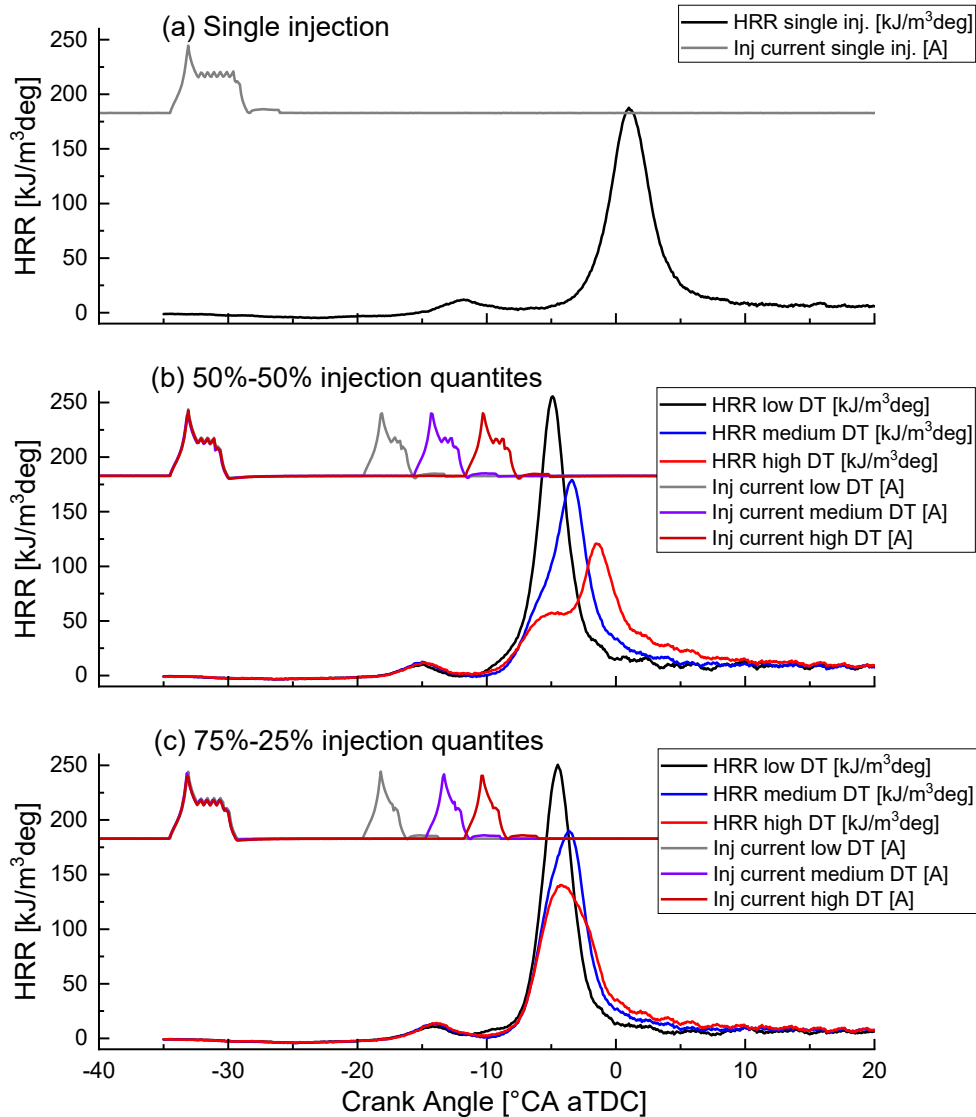


Figure 4.7. Comparison of the HRR traces at 2000×5 , between the PCCI single injection (a) and the 50%-50% (b) and 75%-25% (c) fuel split with double injection (2nd injection timing sweep).

The introduction of a double-pulse PCCI strategy at higher load brings to *bsfc* values not too far from those obtained with the single-pulse injection pattern, and in some cases slightly worse (cf. Figure 4.5 and Figure 4.8, referring to, respectively, 1000×4 and 2000×6.5 engine operating points), if low DT values are implemented. As previously stated, in order to dampen excessive soot emissions,

the double-pulse pattern needs a lower EGR rate than the early single injection case, thus advancing the SOC of the early injected fuel (as can be seen in Figure 4.7, in the case of 2000×5) and causing a lower η_{wc} due to this earlier combustion phasing, only partially mitigated by the positive effect on fuel consumption given by the later injection of the second fuel shot. Overall, the *b_{sfc}* values still keep quite higher than those pertaining to the reference CDC calibration (ranging from the worst case of about +11%, when implementing the double pulse strategy with the minimum DT and $q_{1st}/q_{2nd} = 75\%/25\%$, at 1000×4, to the best case of just +2.5% when implementing the double pulse strategy with the maximum DT and $q_{1st}/q_{2nd} = 50\%/50\%$, at 2000 ×5).

As far as CO and HC emissions are concerned, progressively retarding the SOI_{2nd} , keeping the SOI_{1st} fixed, does not seem to bring substantial variations. Unlike the low load case, trends in function of the DT are flat, clearly showing the marginal control exerted by the second injection timing on these pollutant species when the load increases, likely due to the raised in-cylinder temperature and pressure conditions linked to the higher engine load. As a consequence, since relatively small ID values are expected, even with the most delayed SOI_{2nd} , the majority of the heat release occur shortly before the TDC, avoiding substantial reductions of the time available before temperature drops (due to the downward motion of the piston) and burnout mechanisms freeze the oxidation rates of any residual CO and HC molecule prior to the exhaust phase, as it happens at lower load. Exception is made for the 50%/50% fuel split ratio curves at 1000×4 and 2000×6.5 (cf. Figure 4.5 and Figure 4.8, respectively), which show increasing trends when the DT values are enlarged. This might be avoided if slightly lower values of EGR were implemented, giving additional oxygen availability for the late oxidation of the previously produced CO. In general, the double injection PCCI strategy seems potentially able to mitigate engine-out CO and HC emissions with respect to the single pulse strategy (up to -50%) also at higher load, but marginal control can be exerted by the second injection timing on these pollutant species.

A slightly decreasing trend of engine-out NO_x emissions is observable with the progressive delay of the SOI_{2nd} (keeping the SOI_{1st} fixed), as it was detected (and explained) also at low loads. Comparing single against double-pulse PCCI strategies, it turns out that both strategies offer the opportunity of massive NO_x reductions compared to the baseline CDC calibration (from -65% to -95%), with an overall better performance given by the single injection PCCI in all the tested engine points but the 1000×4, that is the only one for which the same EGR rate between the two strategies was implemented. This suggests a much more robust dependence of NO_x emissions from the EGR rate than from the particular fuel injection pattern.

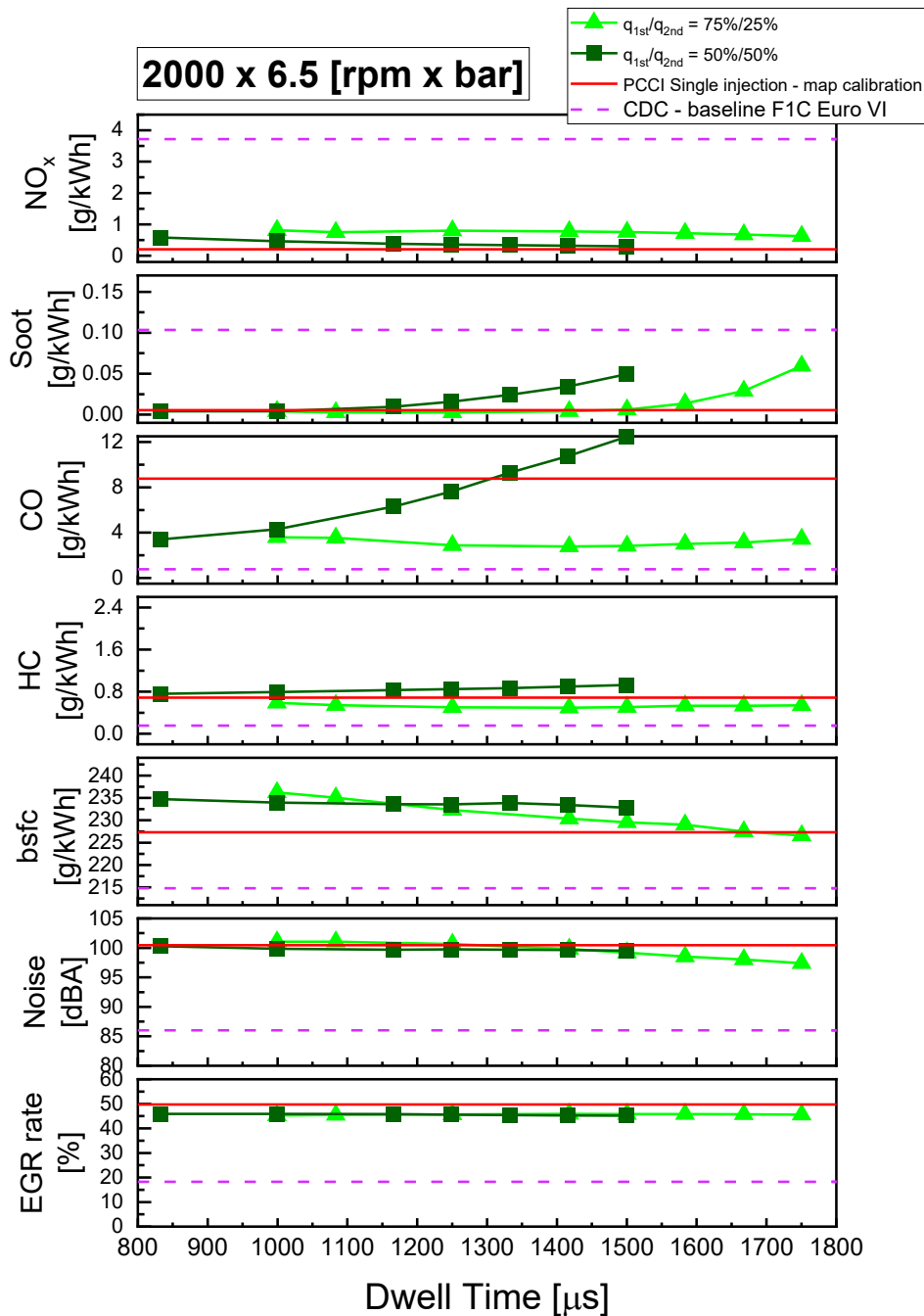


Figure 4.8. Results of a 2nd injection timing sweep at 2000×6.5, for a 75%-25% (light green and triangular symbols) and 50%-50% (dark green and square symbols) fuel split. Comparison with the PCCI single injection (red solid line) and the CDC baseline (violet dashed line) calibrations.

As far as soot emissions are concerned, unlike the low load case, a sharply worsening soot trend is clear, with non-negligible peaks when medium-to-high DT values are reached, especially at the highest load engine point considered, i.e. 2000×8.5 (cf. Figure 4.9). Whereas, soot emissions keep extremely low (at the levels featured by the single-stage injection pattern) when the DT between the injection is small. With medium-to-high DT values, especially when $q_{1st}/q_{2nd} = 50\%/50\%$ (largest second pulse fuel quantity), the second fuel injection occurs after the ignition and the luminous flame formation of the first one (as can be perceived

from Figure 4.7(b), in the case of 2000×5 , where the HRR shows two distinct peaks with the most delayed and largest second injection event).

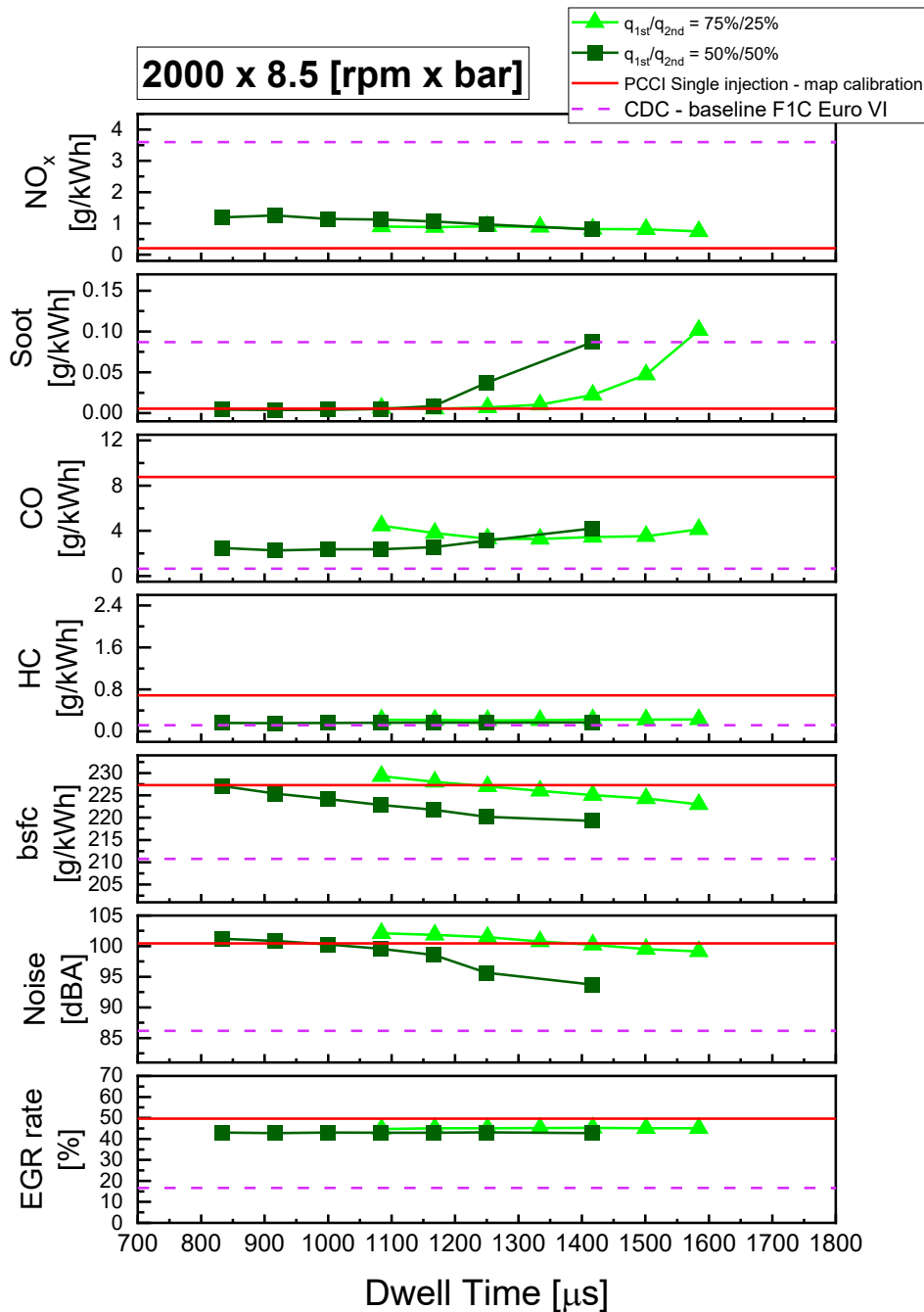


Figure 4.9. Results of a 2nd injection timing sweep at 2000×8.5 , for a 75%-25% (light green and triangular symbols) and 50%-50% (dark green and square symbols) fuel split. Comparison with the PCCI single injection (red solid line) and the CDC baseline (violet dashed line) calibrations.

Therefore, a rich mixture is still present in the near-nozzle region whilst the first injection combustion is ongoing, and therefore the luminous flames of the first injection combustion can propagate towards this rich mixture zone, increasing soot formation [Fuyuto, et al., 2014]. Then, being the second fuel pulse so large and delayed, there is not enough time to oxidize all the soot particles previously produced, also taking into account the reduced in-cylinder oxygen concentration linked to the higher loads considered. Conversely, with the lowest DT values, the

second injection starts before the onset of the HTHR of the first early injection (as can be perceived from Figure 4.7(c), in the case of 2000×5, where the HRR shows a single peak even with the most delayed second injection event), allowing a longer premixing time which results in reduced smoke emissions. In general, the double injection PCCI strategy might potentially introduce issues as regards soot emissions, primarily linked to interference phenomena between the second fuel shot and the luminous flames generated by the combustion of the previous first injection event, but an adequate control can be exerted by a proper calibration of the second injection timing and quantity.

Finally, monotonic CN reductions are still detectable at higher loads when the SOI_{2nd} is progressively delayed, since this generally results in a milder combustion event, as can be seen in Figure 4.7(b) and Figure 4.7(c), in the case of 2000×5. It can also be pointed out how a single peak of HRR is present (after the onset of the LTHR) in all the cases but when $q_{1st}/q_{2nd} = 50\%/50\%$ and the DT values are the highest (i.e., most delayed SOI_{2nd}). When a unified premixed burning of the two pulses occurs, the CN levels experienced are not too far from the CN featured by the single injection pattern, i.e. much larger than the acceptable CDC calibration performance. Conversely, it is still better to realize a combustion event featuring two distinct HRR peaks, i.e. implementing medium-to-high DT and delayed SOI_{2nd} , in order to achieve CN reductions up to 5÷6 dBA compared to the single-stage PCCI calibration.

First injection timing (SOI_{1st}) sweeps

In order to look into the effects of the first injection timing on the combustion characteristics, DT sweeps were performed by progressively advancing the SOI_{1st} , while keeping the SOI_{2nd} fixed. Again, the DT sweeps were performed twice, once per each ratio of the first/second injection quantities q_{1st}/q_{2nd} (namely 75%/25% and 50%/50%), as outlined in Figure 4.10.

In Figure 4.12, several y-axes, which report engine-out NO_x , soot, CO and HC emissions, *bsfc*, CN and EGR rate for the 2000×5 engine operating point, are stacked in function of the DT. Similarly to what done in the previous sub-section, the light blue (with triangular symbols) and the dark blue (with square symbols) solid lines refers, respectively, to the results of the 75%/25% and 50%/50% double injection PCCI strategies. They are both compared with the results pertaining to the single injection PCCI strategy (i.e., the calibration whose results are reported in Section 3.3), outlined as a horizontal red solid line, and with those of the baseline CDC calibration obtained in the conventional F1C Euro VI, outlined as a horizontal dashed violet line.

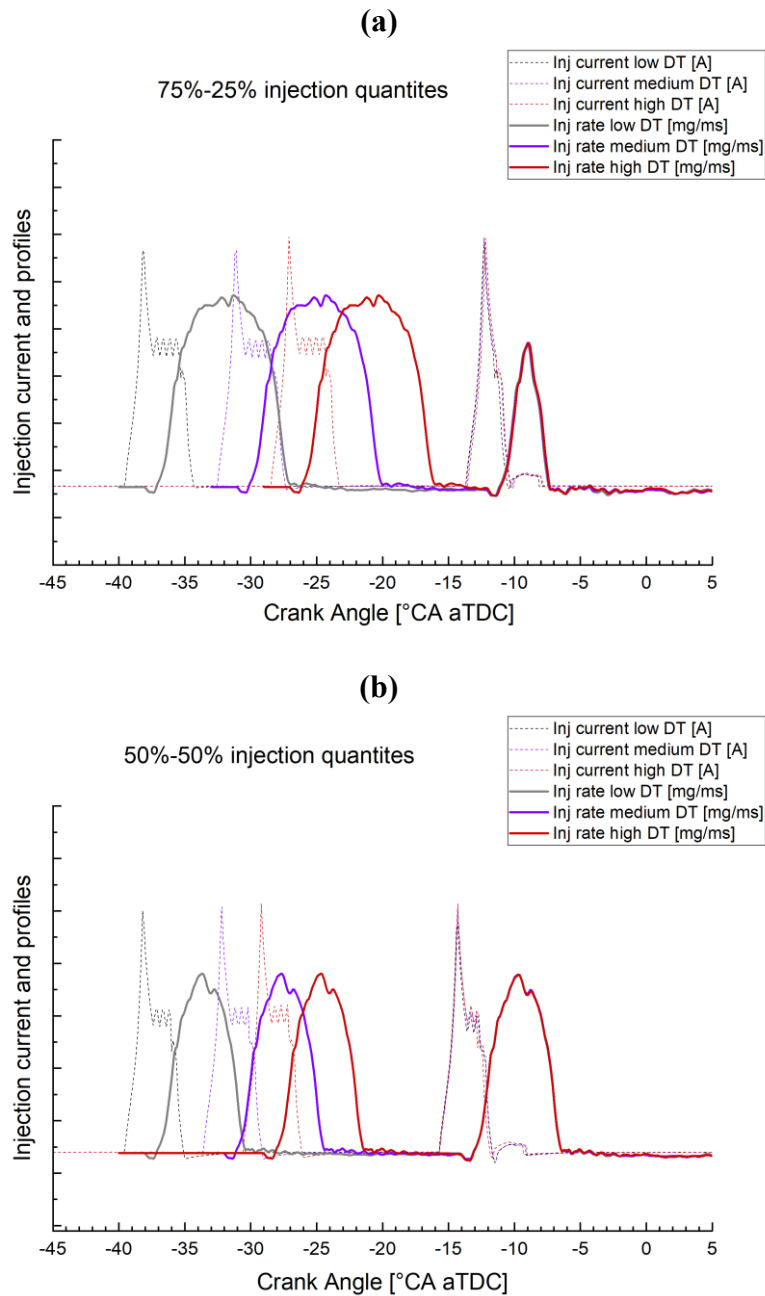


Figure 4.10 1st injection timing sweeps: fuel injection rate and current profiles for a 75%-25% (a) and 50%-50% (b) fuel split, at 2000 \times 5.

The analysis, carried out at 2000 \times 5, started from the results of the second injection timing sweeps previously reported in Figure 4.6 and Figure 4.7. First of all, the “best” DT value and the corresponding SOI_{2nd} angle, meant to be the best compromise between the analyzed pollutant emissions and engine performance during the considered sweeps, were selected. Then, this SOI_{2nd} angle was kept fixed, while sweeps of SOI_{1st} (in both the case of $q_{1st}/q_{2nd} = 75\%/25\%$ and 50%/50%) were performed, by progressively advancing or delaying the first injection pulse from this selected SOI_{2nd}. During the tests, SOI_{1st} was varied between 40 to 28 °CA bTDC, while the start of injection timing for the second fuel shot was kept constant at SOI_{2nd} = 16 °CA bTDC.

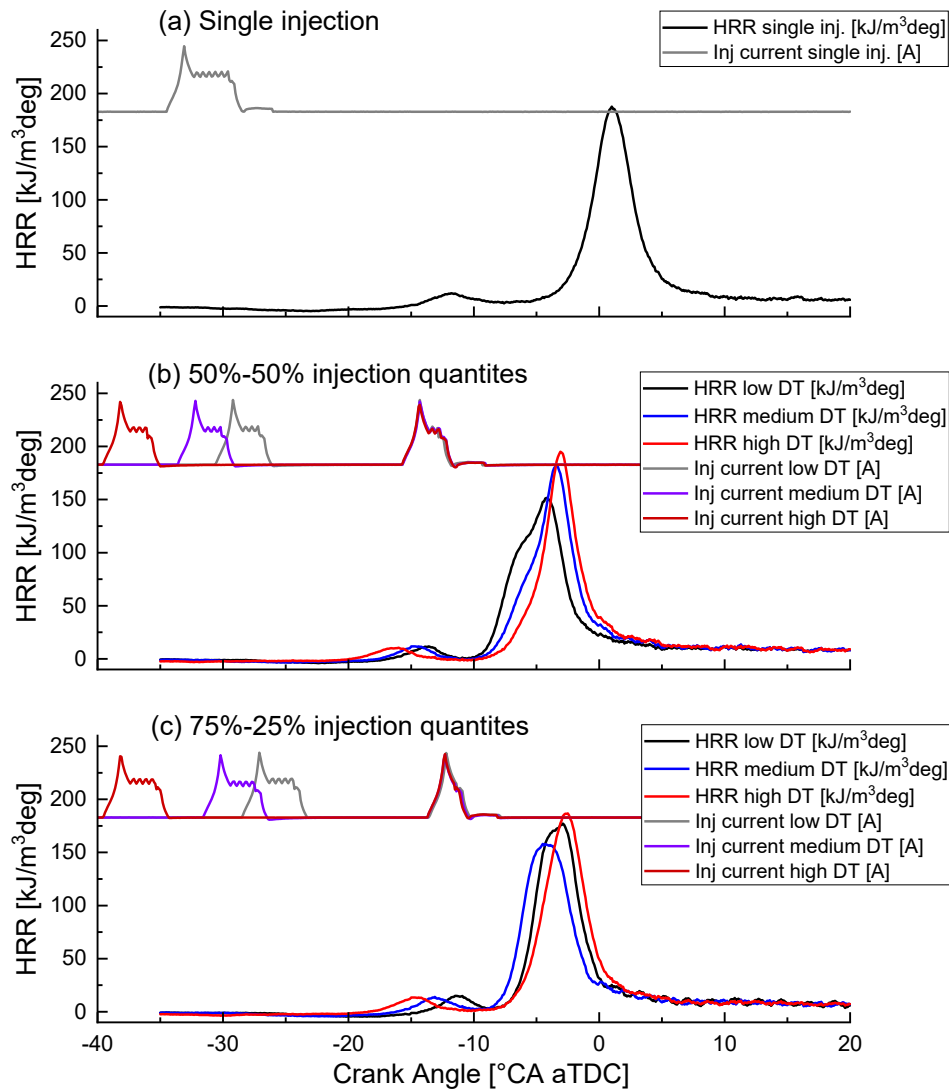


Figure 4.11. Comparison of the HRR traces at 2000x5, between the PCCI single injection (a) and the 50%-50% (b) and 75%-25% (c) fuel split with double injection (1st injection timing sweep).

Figure 4.11 shows the HRR traces obtained during the SOI_{1st} sweep tests at 2000x5 for the 50%/50% (Figure 4.11(b)) and 75%/25% (Figure 4.11(c)) fuel split strategies with double injection, comparing them with the HRR pertaining to the corresponding single injection PCCI calibration (Figure 4.11(a)). When the SOI_{1st} is progressively advanced (i.e., passing from the black (low DT) curves to the red (high DT) ones) depicted in Figure 4.11(b) and Figure 4.11(c), while the LTHR simply seems to shift towards earlier timings, the HTHR profile tends to be stretched towards the TDC, at later timings.

A more advanced SOI_{1st} value is responsible for the advance of the LTHR onset since an earlier injection gives more time to the fuel to vaporize and mix, with a consequent earlier start (and consequently end) of its low temperature oxidation reactions. As a consequence, the second injection event, whose timing (SOI_{2nd}) is kept fixed, is injected around the onset of the LTHR, in the case of low DT (i.e., black curves and least advanced first injection), and during the NTC period, when the LTHR is already finished, in the case of high DT (i.e., red curves and most advanced first injection). As pointed out in [Nishi, et al., 2015], the change of

intermediate species concentration in time may have different tendencies whether the second injection occurs prior to or after the LTHR. For instance, Nishi et al. report that HCHO concentration decreases faster and H₂O₂ concentration increases faster when the second injection occurs prior to the LTHR (i.e., in the case of low DT in our case, corresponding to the least advanced first injection and more delayed LTHR) and, being the production and consumption rate of H₂O₂ and HCHO, respectively, indications of acceleration in chemical reactions, this finally causes and advancing in the start timing of the HTHR.

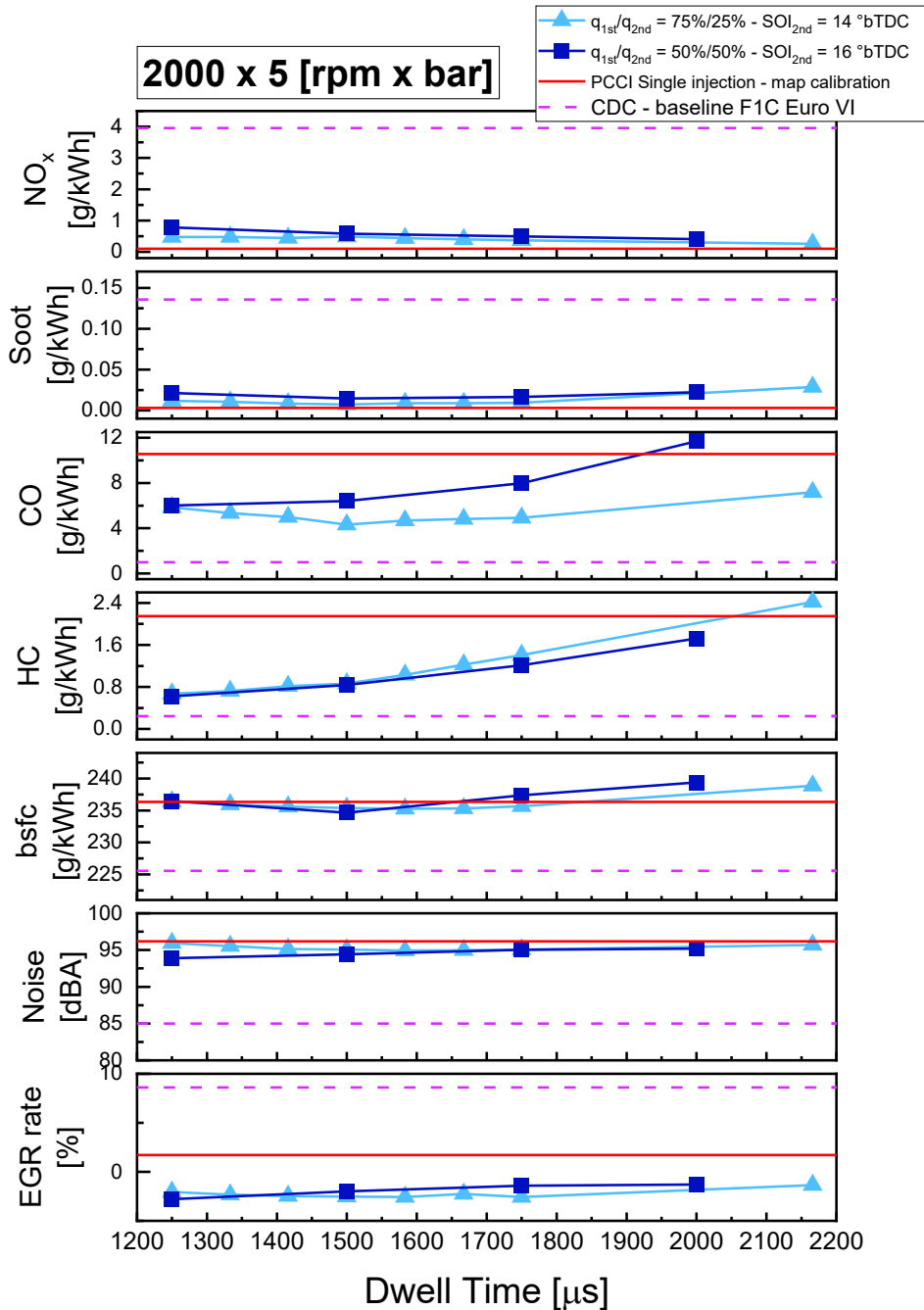


Figure 4.12. Results of a 1st injection timing sweep at 2000×5, for a 75%-25% (light blue and triangular symbols) and 50%-50% (dark blue and square symbols) fuel split. Comparison with the PCCI single injection (red solid line) and the CDC baseline (violet dashed line) calibrations.

Progressively advancing the SOI_{1st} does not bring to a well-defined trend of $bsfc$, whose values keep in proximity of the red horizontal line referring to what obtained with the single-pulse injection pattern, as can be seen in Figure 4.12. Apparently, the progressive advance of the SOI_{1st} seems only to slightly increase fuel consumption when the earliest SOI_{1st} are reached, likely being correlated to the sharp increase in CO and HC emissions (which will be discussed hereinafter) and to the consequent lower combustion efficiency. Nonetheless, as previously stated, the double-pulse PCCI strategy at 2000×5 needs a lower EGR rate than the early single injection case, in order to dampen excessive soot emissions. Therefore, a lower η_{wc} may also be expected, due the consequent earlier combustion phasing (which is also highlighted by the HRR traces reported in Figure 4.11), even if the delayed injection of the second fuel shot may have a positive effect on fuel consumption, due to the increased thermal energy made available for late oxidation of HC and CO molecules

As far as engine-out CO and HC emissions are concerned, the progressive advance of the SOI_{1st} yields to severe increase in both these incomplete combustion species emissions. The 75%/25% fuel split and earliest timing (largest DT values) combination seems to be the worst for HC emissions. This is likely due to a too high proportion of early injected fuel during the 1st injection event, which tends to impinge the cylinder walls and the piston head near the squish region (due to the distant position of the piston at the instant of the SOI_{1st}), making poor usage of the oxygen present inside the piston bowl volume [Opat, et al., 2007]. Although part of this fuel may properly oxidize later, during the mixing-controlled or late cycle burn-out phases, part of it may reside for too long in the crevice volumes and other parts of the squish region, escaping a complete combustion process and contributing to higher HC engine-out emissions. On the other hand, it is the 50%/50% fuel split (always at the earliest timing) case to bring to the worst CO emissions. This is thought to be primarily due to a too high proportion of late injected fuel during the 2nd injection event, which may have not enough time to properly mix with the inducted oxygen, thus being unable to complete the late oxidation stages which have to oxidize CO into CO₂. Moreover, in these conditions, a more advanced SOI_{1st} (coupled with a lower fuel mass to the first injection) may increase the chance of creating over-lean mixtures, increasing the CO levels due to chemical kinetic effects.

The results shown in Figure 4.12 suggest that both soot and NO_x emissions are not heavily influenced by the SOI_{1st} sweep. The premixing time available to the first injected fuel mass is large enough in all the tested conditions to suppress soot formation mechanisms, and EGR rates are still sufficiently high to limit NO_x formation. However, both their levels are slightly higher than what obtained with the single injection pattern, due to the presence of the second delayed injection event which tends to burn under a mixing-controlled combustion phase.

Finally, as far as CN levels are dealt with, SOI_{1st} sweeps do not make them change evidently. In fact, all the SOI_{1st} values implemented enable a strong intensity of the premixed phase burn and, as a consequence, steep rates of pressure rise, which are strongly linked to CN generation. Figure 4.11 highlights how a single

high peak of HRR can be detected after the onset of the LTHR, in all the considered conditions.

Selection of a suitable compromise with double injection PCCI

The first (SOI_{1st}) and second (SOI_{2nd}) injection timing sweeps, as well as the different ratios between first and second injection fuel quantities q_{1st}/q_{2nd} , have shown that improvements can be achieved, in terms of exhaust pollutant emissions and engine performance, by the introduction of a double injection PCCI pattern, if reference is made to the issues shown by the early single PCCI calibration.

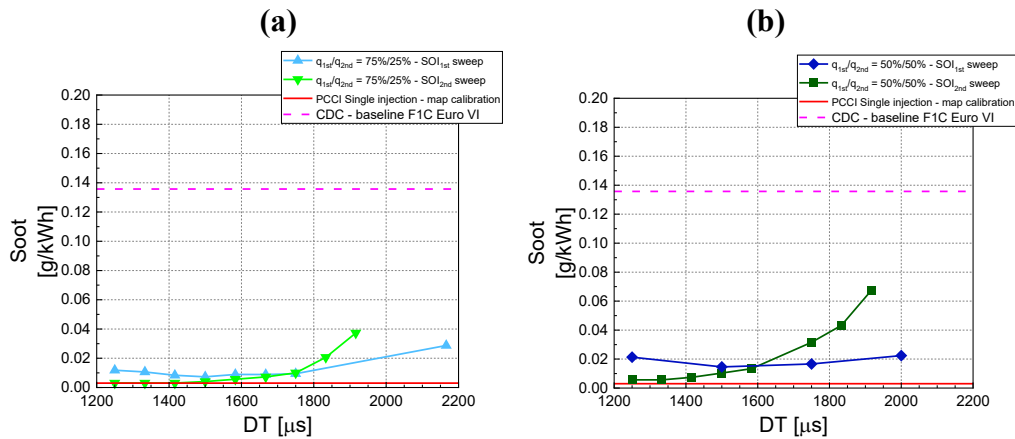


Figure 4.13. Soot emissions comparison of 1st (light and dark blue) and 2nd (light and dark green) injection timing sweeps at 2000×5 , for a 75%-25% (a) and 50%-50% (b) fuel split. Comparison with the PCCI single injection (red solid line) and the CDC baseline (violet dashed line) calibrations.

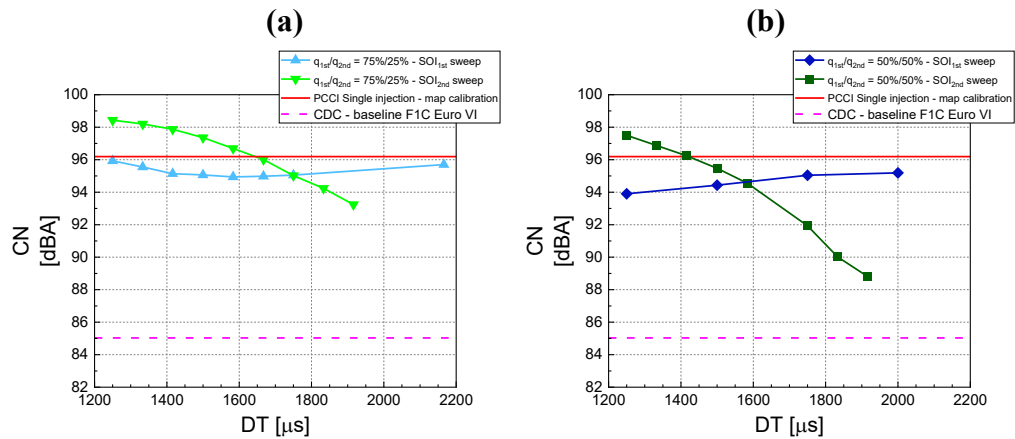


Figure 4.14. CN comparison of 1st (light and dark blue) and 2nd (light and dark green) injection timing sweeps at 2000×5 , for a 75%-25% (a) and 50%-50% (b) fuel split. Comparison with the PCCI single injection (red solid line) and the CDC baseline (violet dashed line) calibrations.

The second pulse injection timing sweeps showed that soot and CN trends in function of the DT are the opposite (cf. the light and dark green lines in Figure 4.13 and Figure 4.14), thus establishing a clear soot-CN trade-off behaviour. Therefore, the adoption of a properly delayed second injection event, especially if $q_{1st}/q_{2nd} = 50\%/50\%$ (larger second pulse fuel quantity) is implemented, is able to allow CN reductions up to $5 \div 6$ dBA compared to the single-stage PCCI calibration, accepting a certain reduction on engine-out soot mitigation brought by PCCI, depending on

the engine operating point. At this regard, the SOI_{1st} does not affect substantially this soot-CN trade-off outcome (cf. the light and dark blue lines in Figure 4.13 and Figure 4.14, which retain almost flat).

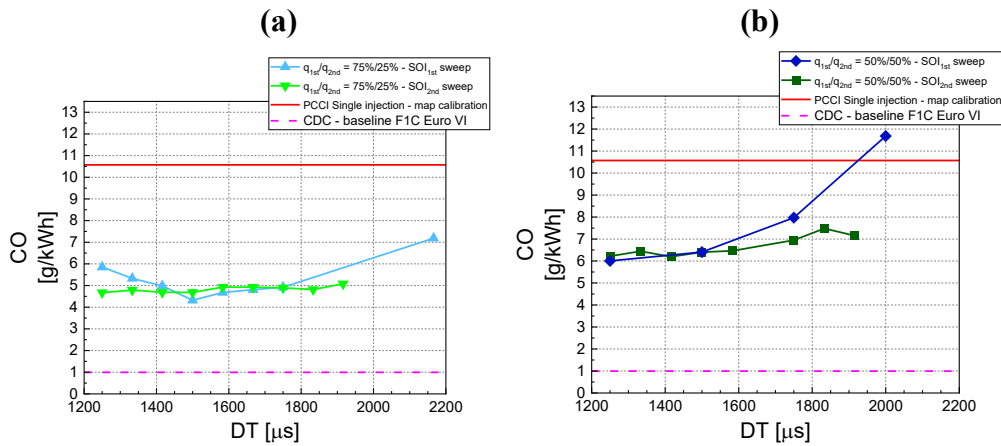


Figure 4.15. CO emissions comparison of 1st (light and dark blue) and 2nd (light and dark green) injection timing sweeps at 2000×5 , for a 75%-25% (a) and 50%-50% (b) fuel split. Comparison with the PCCI single injection (red solid line) and the CDC baseline (violet dashed line) calibrations.

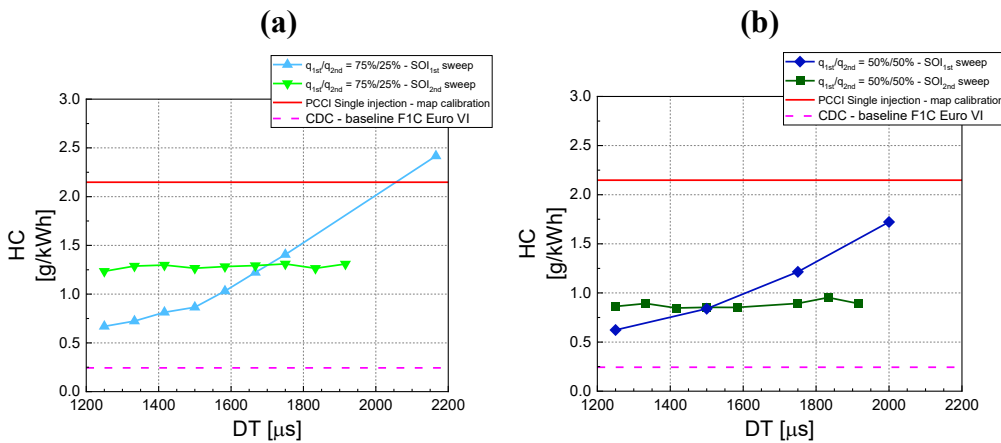


Figure 4.16. HC emissions comparison of 1st (light and dark blue) and 2nd (light and dark green) injection timing sweeps at 2000×5 , for a 75%-25% (a) and 50%-50% (b) fuel split. Comparison with the PCCI single injection (red solid line) and the CDC baseline (violet dashed line) calibrations.

On the contrary, the control of engine-out CO and HC emissions seems to be relatively insensitive to any SOI_{2nd} sweep, while a much heavier impact is evident when variations of SOI_{1st} are dealt with (cf. the light and dark green lines, which are almost flat, and the light and dark blue lines, which show sharply increasing trends, in Figure 4.15 and Figure 4.16). At this regard, reducing the advance of the first injection event and preferring a 50%/50% fuel split may lead to a limitation of engine-out HC and CO emissions, as this improves mixture preparation and reduces the spray interaction with the cylinder walls. However, it is still unfeasible to reach the lowest HC and CO levels pertaining to the CDC calibration, due to the relatively high premixing and EGR rate needed to implement such a double injection PCCI pattern.

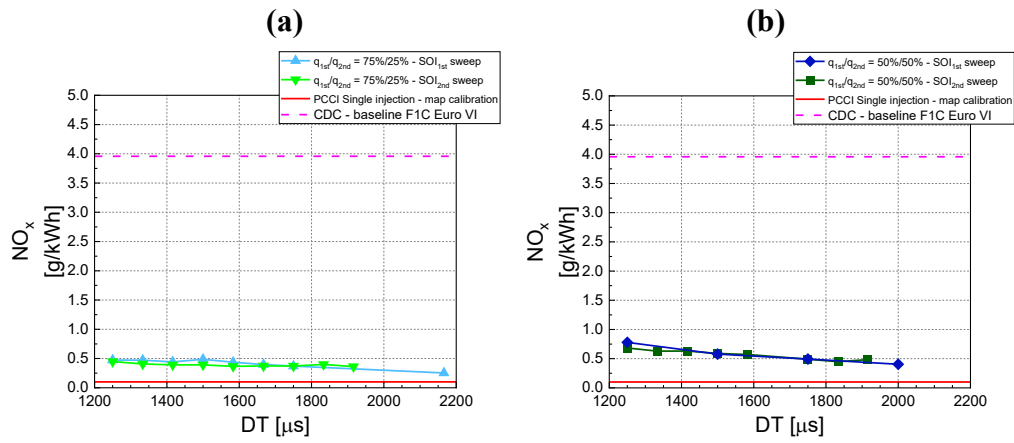


Figure 4.17. NO_x emissions comparison of 1st (light and dark blue) and 2nd (light and dark green) injection timing sweeps at 2000×5 , for a 75%-25% (a) and 50%-50% (b) fuel split. Comparison with the PCCI single injection (red solid line) and the CDC baseline (violet dashed line) calibrations.

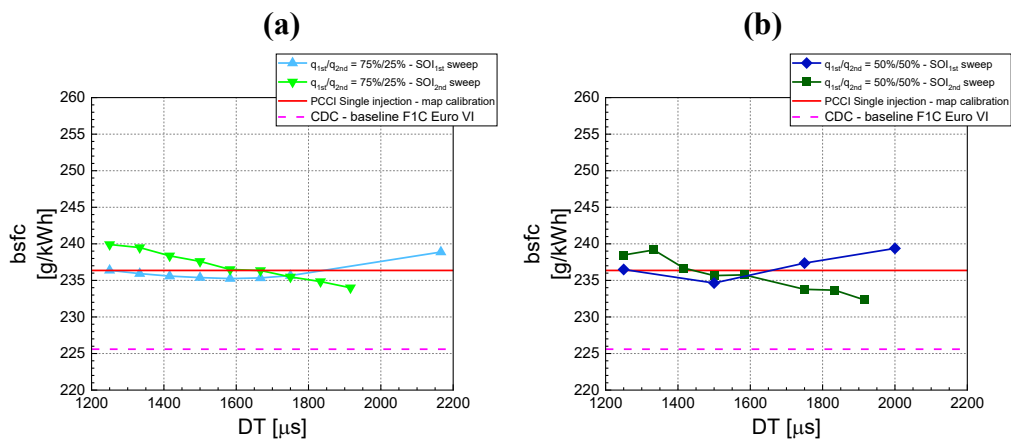


Figure 4.18. $bsfc$ comparison of 1st (light and dark blue) and 2nd (light and dark green) injection timing sweeps at 2000×5 , for a 75%-25% (a) and 50%-50% (b) fuel split. Comparison with the PCCI single injection (red solid line) and the CDC baseline (violet dashed line) calibrations.

The results shown in Figure 4.17 and Figure 4.18 suggest that both NO_x emissions and $bsfc$ are not heavily influenced by either SOI_{1st} or SOI_{2nd} sweeps. The EGR rates are sufficiently high in all the tested conditions to limit NO_x formation, ensuring at least (in the worst case) an 80% NO_x reduction compared to the CDC calibration levels. The fuel consumption penalty associated with the double injection PCCI pattern is still quite high (with slight benefits, compared to what obtained with the early single PCCI pattern, depending on the engine operating point) due to the already mentioned lower CR of the engine, the decrease in combustion efficiency, the relatively early values of SOI_{1st} and the highly throttled exhaust flap positions (needed to guarantee a sufficient rate of EGR). Nevertheless, the possibility to cut the urea consumption of the SCR and the fuel consumption penalty associated with the DPF backpressure and its regeneration strategies, if compared to what needed by the baseline F1C Euro VI engine, may again make this higher $bsfc$ tolerable, in a comprehensive fluid (fuel + urea) operating cost analysis.

4.2 Triple fuel injection PCCI strategy

As previous Sections have pointed out, the benefits coming from the adoption of a double injection PCCI strategy (compared to an early single PCCI pattern) may be summarized in the possibility to reduce engine-out CO and HC emissions, *bsfc* and CN, while suffering of acceptable increase in NO_x and soot, which in any case retain at levels far below the typical values pertaining to CDC. To explore further the potentialities of multiple injection PCCI strategies, a triple injection PCCI pattern was investigated, and the results are reported hereinafter.

4.2.1 Results and discussion

Preliminary tests were performed at two steady-state engine working points (expressed in terms of speed n [rpm] \times torque Trq [Nm]), i.e. 1400 \times 27 (*bme_p* \approx 1 bar) and 2000 \times 120 (*bme_p* \approx 5 bar), by splitting the injection pattern into three different fuel shots. Several combinations of the most relevant calibration parameters (i.e., timings and relative fuel quantities of each injection event, position of the VGT, position of the exhaust flap, rail pressure) were explored within proper limits, in order to find a good compromise between low exhaust pollutant emissions, *bsfc* and CN. Once a proper triple injection PCCI pattern was found, to carry out a consistence comparison with it, the first two injection shots were merged at the same (most advanced) SOI_{1st}, obtaining a corresponding double injection pattern. Similarly, by merging all the three injection shots at the same (most advanced) SOI_{1st}, a corresponding single PCCI pattern was obtained. A schematic drawing of the injection patterns taken into account at these two engine operating points is given in Figure 4.19 and Figure 4.20.

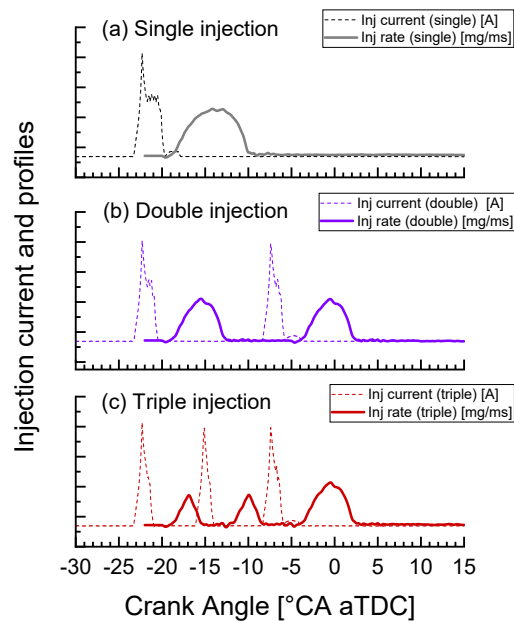


Figure 4.19. Fuel injection rate and current profiles for the single (a), double (b) and triple (c) PCCI injection patterns, at 1400 \times 1.

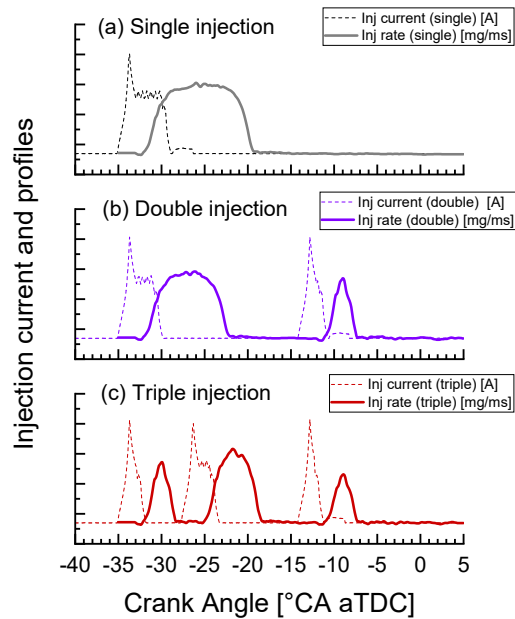


Figure 4.20. Fuel injection rate and current profiles for the single (a), double (b) and triple (c) PCCI injection patterns, at 2000×5 .

EGR rate sweeps

The previously cited single, double and triple injection PCCI strategies are compared along an EGR sweep, achieved by progressively throttling the exhaust flap in order to increase the exhaust backpressure and, consequently, the EGR mass flowrate recirculated back into the intake manifold.

In the following Figures 4.21-4.22, several y-axes, which report engine-out soot, CO and HC emissions, *bsfc* and CN, are stacked in function of the engine-out NO_x emissions (with increasing NO_x values corresponding to reducing EGR values) for the two engine operating points previously reported (i.e., 1400×1 and 2000×5). In each graph, the red (with circular symbols), green (with square symbols) and blue (with triangular symbols) lines refer, respectively, to the results of the single, double and triple injection PCCI strategies along the EGR sweep carried out. As a reference, the results pertaining to the baseline CDC calibration obtained in the conventional FIC Euro VI are outlined as a horizontal (for y-axes variables) and a vertical (for NO_x) dashed violet lines.

The fuel consumption values for all the three injection PCCI patterns are not greatly affected by the EGR rate, except when very high dilution levels are dealt with, for which increasing trends are highlighted. Multiple (i.e. both double and triple) injection PCCI patterns give generally better results than the single-stage one, with *bsfc* reductions up to 7÷8%, if dilution levels are not step up to the maximum. This is linked to the reduced tolerance to the EGR rate which is experienced with the introduction of a second and/or third fuel shots, due to their reduced premixing time and to their consequent rising tendency towards the emission of soot and incomplete combustion species, when a low in-cylinder oxygen concentration is available.

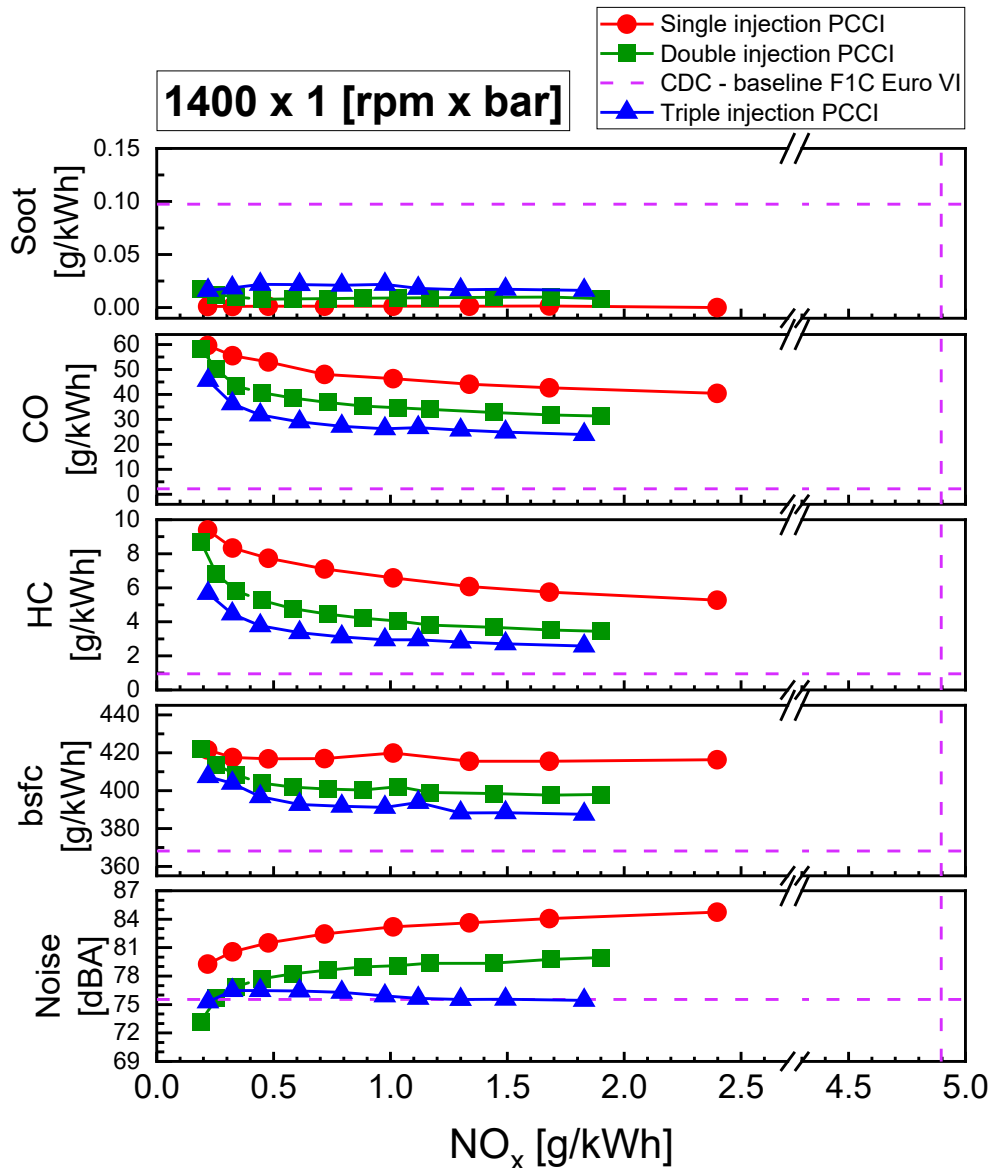


Figure 4.21. Results of an EGR sweep at 1400×1 . Comparison between PCCI single (red line), double (green line), triple (blue line) injections and the CDC baseline (violet dashed lines) calibration.

However, it is still impossible to reach the fuel consumption values of the reference CDC calibration, with the minimum penalty settled slightly over +4%.

As far as engine-out CO and HC emissions are concerned, all the trends shown with different colors in Figure 4.21 and Figure 4.22 display steeply worsening behaviors when high dilution levels are reached, due to rising difficulty to reach an optimal in-cylinder oxygen utilization.

Benefits seem to be achievable by means of the triple injection PCCI strategy along all the EGR sweep at 1400×1 (cf. Figure 4.21), since it mitigates both CO and HC emissions even further than what achievable with the double injection pattern. The presence of a delayed fuel shot (in both the double and the triple injection schedules) has the potential to increase the in-cylinder temperature in the last part of the combustion phase, producing accelerated oxidation of the previously formed HC and CO molecules. Nevertheless, splitting the injection pattern in more

than two events may have the advantage of reducing the fuel quantity per each shot and, consequently, the liquid penetration length, thus possibly reducing the occurrence of spray impingements against the cylinder wall and/or the piston surface.

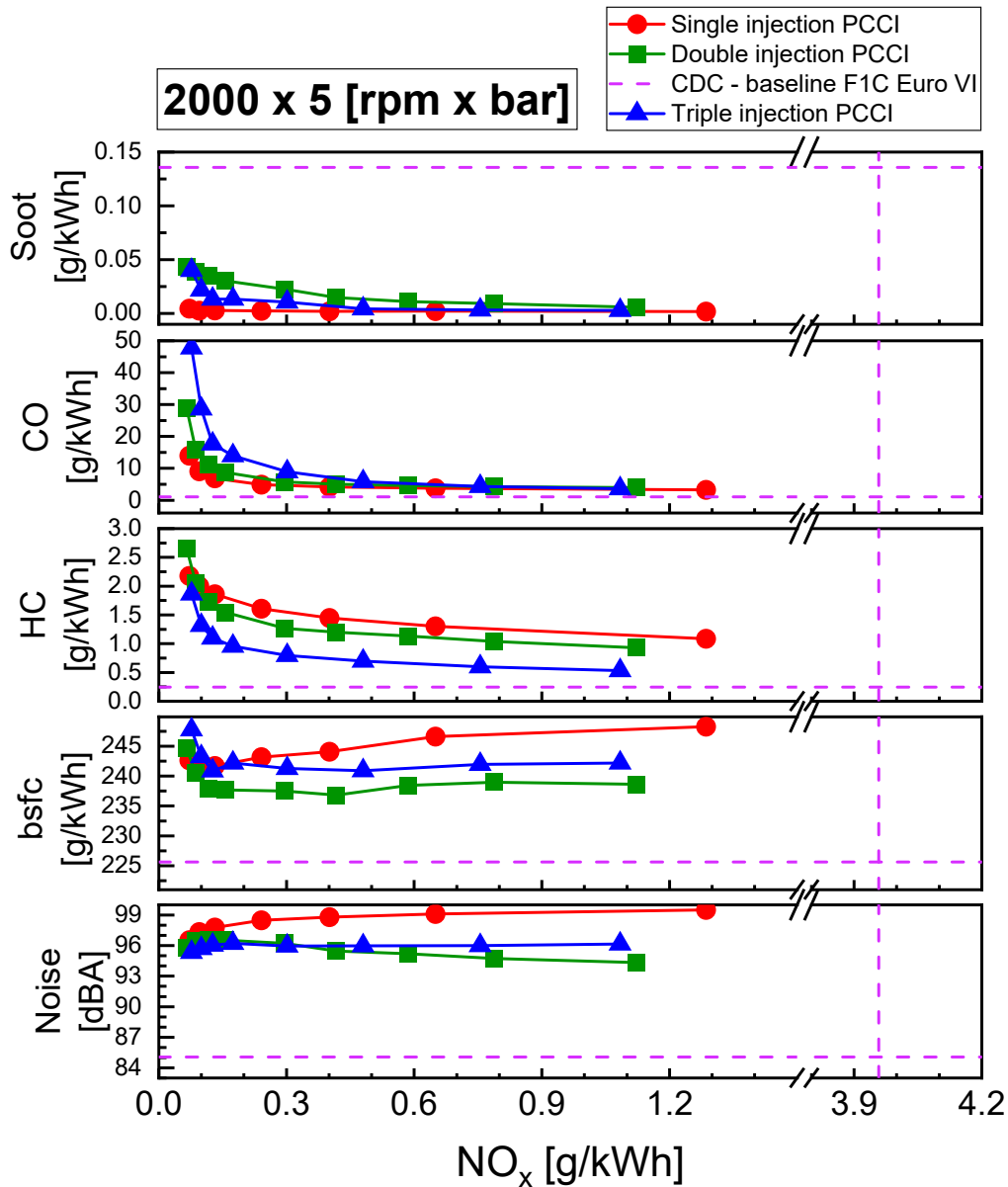


Figure 4.22. Results of an EGR sweep at 2000×5 . Comparison between PCCI single (red line), double (green line), triple (blue line) injections and the CDC baseline (violet dashed lines) calibration.

At higher load, i.e. at 2000×5 , the triple injection pattern is still the best in terms of engine-out HC emission reduction, due to its potential to limit the injected fuel quantity that impinges the walls and the piston head, but it seems to suffer of worse engine-out CO emissions, especially when the largest EGR rates are implemented. This could be due to the fact that a largest portion of fuel is injected at later instants (and, hence, with lower premixing) when the triple injection schedule is applied: this may cause a lack of time for part of the fuel to properly mix with the in-cylinder oxygen, thus being unable to complete the late oxidation stages which bring the CO molecules to oxidize into CO_2 .

Soot emissions for the single injection strategy are negligible, while for both the multiple injection strategies an increase is observed, especially at 2000×5 with the highest EGR rates. The combination of relatively higher load and large EGR rate makes the in-cylinder oxygen concentration drop, raising the possibility of soot generation. While the highly advanced timing of the single injection event gives enough premixing time to prevent soot formation, the introduction of relatively delayed separate fuel shots (with double and triple patterns) promotes the possibility of interference phenomena between the different fuel sprays and subtracts time available to oxidize all the soot particles previously produced. Nevertheless, even in the worst case, soot emissions are decreased of more than 60% if compared to the CDC calibration.

Finally, intense CN reductions are possible with the introduction of a triple injection strategy, even better than what achievable with a double injection pattern. At 1400×1, it is even possible to reduce CN down to the levels pertaining to CDC calibration, while it is still impossible to accomplish the same result at 2000×5, with reductions up to 5÷6 dBA compared to the single-stage PCCI calibration but penalties of more than 8 dBA compared to the CDC levels.

Chapter 5

5. Control-oriented models for EGR and MFB50 estimation

5.1 EGR mass flowrate estimation⁵

From what highlighted in the previous Sections, EGR is one of the crucial parameters involved in early-PCCI combustion, and its rate should be optimized inside a narrow interval to achieve a reasonable compromise in terms of engine-out pollutant emissions, fuel consumption and CN level. Excessive recirculation back into the cylinders may lead to insufficient oxygen to properly burn the fuel, generating enormous amount of CO and HC and unacceptable fuel penalties, up to the occurrence of misfire events. Too low recirculation, on the other hand, may not be sufficient to simultaneously abate NO_x and soot emissions, which is definitely the main goal of all LTC strategies. Unfortunately, the harsh conditions of the EGR path make it tough to directly measure the EGR mass flowrate by using dedicated sensors [Lee, et al., 2014; Griffin, et al., 2003]. Therefore, the needed precision on the control of the EGR system, which may be essential for the enhancement of all the LTC advanced combustion controls, should rely on accurate estimation of the EGR rate [d'Ambrosio et al., 2017].

Many different types of models have been suggested in the literature for the estimation of the EGR flowrate, each characterized by different spatial and time resolutions [Diop, et al., 1999; Wahlström & Eriksson, 2011; Castillo, et al., 2013; Yang, et al., 2016]. Zero-dimensional models, in particular, may feature as main asset low computational effort, as previously pointed out. This, potentially, makes them particularly suitable for on-board ECU applications, especially if they require, for calculations, only input signals from conventional sensors connected to the ECU.

5.1.1 Setting up the models

In the following, four different approaches to estimate the EGR mass flowrate recirculated back into the intake manifold through the EGR system are exposed and compared in steady-state applications. All of them were developed and tested on

⁵ Most of the contents of this Section have been previously published in [d'Ambrosio, S., Iemmolo, D., Mancarella, A., Salamone, N., Vitolo, R., & Hardy, G. (2017). "Zero Dimensional Models for EGR Mass-Rate and EGR Unbalance Estimation in Diesel Engines". SAE Technical Paper, 2017-24-0070. doi:10.4271/2017-24-0070].

the F1C Euro VI complete engine map, made up of 120 key-points at different engine speed and load values. The four approaches are reported below:

- Physical-chemical method. This procedure, discussed in details in [d'Ambrosio et al., 2011] and not further reported here, starts from the combustion chemical reaction of the fuel with air and requires as inputs the gaseous emission concentration (HC, NO, NO₂, CO, CO₂ and O₂) and the smoke level measurements in the exhaust raw gases, as well as the CO₂ concentration measurement in the intake manifold;
- Fluid dynamics model. It is based on the EGR valve geometric dimensions and on the application of the nozzle equation for compressible flows [Heywood, 1988; d'Ambrosio et al., 2013], and requires as inputs the measured values of temperature and pressure measured upstream and downstream of the EGR valve;
- Semi-physical model. It is based on the application of the nozzle equation for compressible flows and on the estimation of the temperature and pressure conditions of the gases in the exhaust manifold (i.e., upstream of the EGR valve) as a function of relevant engine parameters by means of statistical models;
- Purely statistical model. It is obtained by modeling the EGR flowrate as a second-order polynomial function and requires as inputs a proper set of engine parameters.

The first approach for EGR estimation, i.e. the physical-chemical method, is sufficiently accurate if provided with low-uncertainty measurements of the concentrations of the different intake and exhaust chemical species, and its results will be taken as reference for the steady-state assessment of the other analyzed models. It could also be observed that this approach may also be applied to transient working conditions, if the measuring instruments are capable of achieving suitably fast dynamic responses [d'Ambrosio et al., 2011]. However, only testbed applications are feasible with this method, due to the need of dedicated gas analyzers.

The fluid dynamics model, too, requires as inputs data that can be easily collected at the testbed, but generally not available for on-board applications, such as the measurements of temperature and pressure of the gases upstream of the EGR valve.

Therefore, both the semi-physical and statistical models, which require as inputs only variables that are commonly available in the engine ECU, have been considered to estimate the EGR flowrate with possible on-board implementations.

Fluid dynamics model

The fluid dynamics model, as previously stated, needs the knowledge of the EGR poppet valve geometric dimensions (cf. Figure 5.1, which reports the geometric profiles of the valve and of its seat) to determine the EGR flow passage area to be used in the nozzle equation for compressible flows. In particular, the

geometric passage area through the EGR valve was computed as a function of the EGR poppet valve lift and of its command duty-cycle.

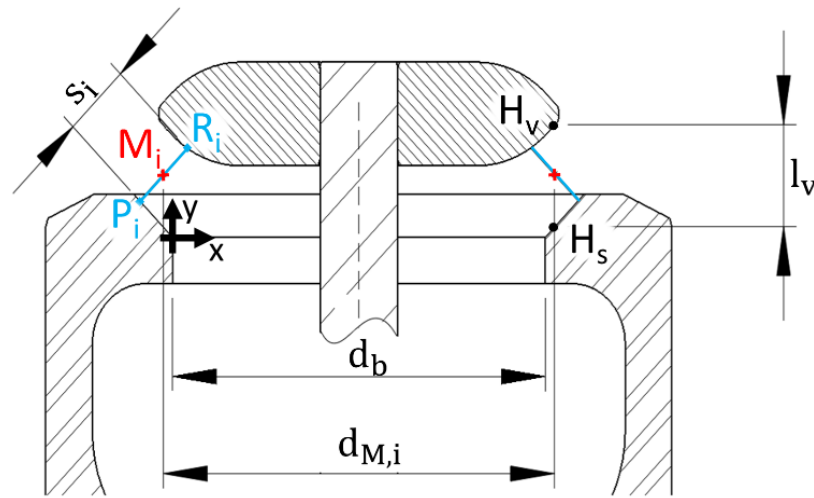


Figure 5.1. Geometric profiles of the EGR poppet valve and of its seat.

The two profiles, of the EGR valve and of its seat, and their relative position were parametrically represented making reference to a cross-section plane (x,y), as the one represented in Figure 5.1. The letters H_v and H_s indicate the contact surface in which the two conjugated profiles overlap when the valve is closed. Therefore, the distance l_v , along the y-axis, between these two points represents the valve lift.

As long as the valve profile is curve, it is not obvious to determine which is the geometric passage area between the valve and the seat for every possible j^{th} value of the valve lift. Thus, once the equations to describe parametrically the two profiles were set, an algorithm was used to calculate, for each considered j^{th} value of the valve lift $l_{v,j}$, the minimum distance s_i between the poppet valve and the seat among the set of all the possible segments that connect the two profiles. In this way, for each considered j^{th} value of the valve lift $l_{v,j}$, the geometric passage area $A_v(l_{v,j})$ between the poppet valve and seat profiles was calculated as the minimum among the areas of the surfaces of revolution generated by a 360° rotation of these segments, around the valve axis, according to:

$$A_v(l_{v,j}) = [\min(\pi \cdot d_{M,i} \cdot s_i)]_j \quad (2)$$

$$d_{M,i,j} = d_b - 2 \cdot x_{M,i,j} \quad (3)$$

$$s_{ij} = \left[\sqrt{(x_{P,i} - x_{R,i})^2 + (y_{P,i} - y_{R,i})^2} \right]_j \quad (4)$$

where $d_{M,i,j}$ is the diameter of the circular area corresponding to the barycenter M_{ij} of the segment s_{ij} , d_b is the minimum seat diameter (which is in correspondence of the origin of the considered (x,y) plane), $x_{M,i,j}$ is the abscissa of the point M_{ij} , while $x_{R,i}$, $x_{P,i}$, $y_{R,i}$, $y_{P,i}$ are the coordinates of the couple of points $R_{,i}$ and $P_{,i}$ connected by the j^{th} segment s_{ij} .

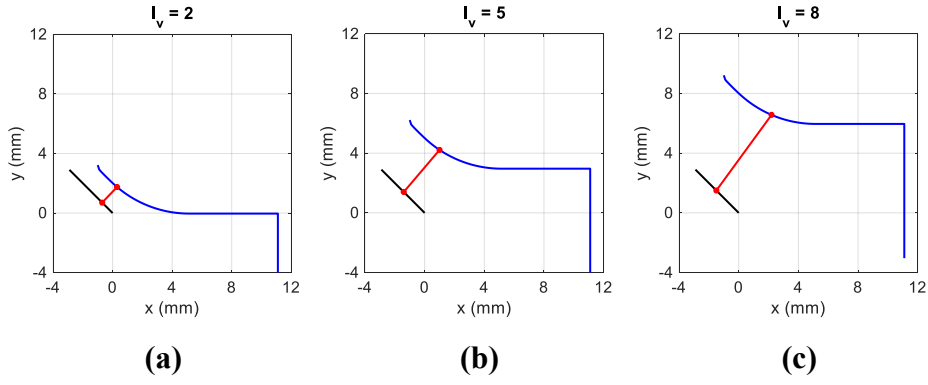


Figure 5.2. Geometric passage area at different poppet valve lifts l_v : 2 mm (a), 5 mm (b) and 8 mm (c).

As a further clarification, Figure 5.2 reports the section of the geometric passage area determined for three different valve lift values l_v (i.e. 2, 5 and 8 mm), while Figure 5.3(a) shows the variation of the geometric passage area as a function of the lift, according to the performed calculations. Moreover, tests were performed to characterize the EGR valve lift as a function of the duty-cycle of the electric signal provided to the valve actuator (Figure 5.3(b)). As a matter of fact, the maximum lift achievable through the electric actuation of the valve (slightly lower than 6 mm, cf. Figure 5.3(b)) is much lower than the maximum one which could be obtained if operating the valve manually (around 9 mm, cf. Figure 5.3(a)).

At this point, it was possible to estimate the EGR mass flowrate (\dot{m}_{EGR}) studying the system as a convergent nozzle under subsonic compressible flow conditions (taking into account that the Mach number, for the considered experimental tests, reaches values up to 0.55), according to the well-known relation:

$$\hat{m}_{EGR,fd} = A_{EGR} \frac{p_{exh}}{\sqrt{RT_{exh}}} \sqrt{\frac{2k}{k-1} \left[\left(\frac{p_{co}}{p_{exh}} \right)^{\frac{2}{m}} - \left(\frac{p_{co}}{p_{exh}} \right)^{\frac{m+1}{m}} \right]} \quad (5)$$

where $\hat{m}_{EGR,fd}$ represents the EGR mass flowrate estimation obtained by the fluid-dynamics model, A_{EGR} is the EGR gas flow passage area, p_{exh} and T_{exh} represent, respectively, the pressure and temperature of the gas in the exhaust manifold (i.e., upstream of the EGR valve) measured at the test bench, R is the elastic constant of the exhaust gas calculated from the concentration of chemical species in the raw exhaust gas flow, p_{co} is the pressure measured downstream of the EGR cooler and m (polytropic index) was assumed equal to 1.5 [d'Ambrosio et al., 2013] (higher than the isentropic exponent equal to 1.4, as the EGR valve is cooled).

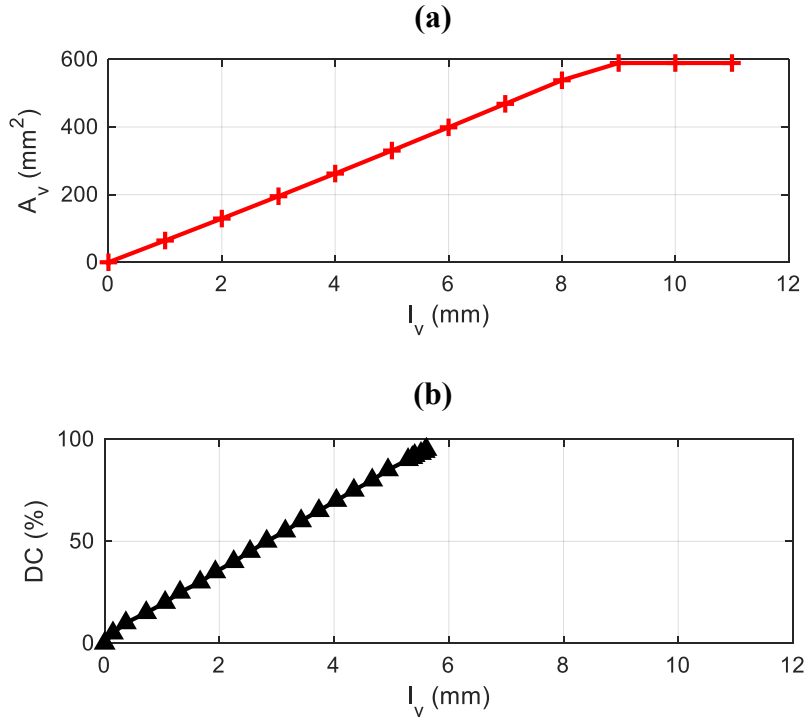


Figure 5.3. EGR valve geometric passage area (a) and electric duty-cycle (b) as function of the lift.

In Eq. (5) the pressure p_{co} is used, instead of a more appropriate pressure measurement downstream of the EGR valve, because of the compact layout of the EGR system, which could not allow the installation of any sensor between the valve and the cooler. As a consequence, p_{co} was the nearest available measurement point and could be considered almost equal to the pressure downstream the EGR valve, if the pressure drop along the EGR cooler was neglected.

Then, Eq. (5) was applied to a large set of experimental working conditions in which \dot{m}_{EGR} was known (i.e., estimated by means of the reference physical-chemical method) so that the effective EGR flow area A_{EGR} could be figured out and compared to the geometric passage area A_v . A discharge coefficient μ_v could be defined as the ratio between the regression functions of A_{EGR} and A_v , respectively:

$$\mu_v = \frac{A_{EGR}}{A_v} \quad (6)$$

The trend of the discharge coefficient μ_v as a function of the valve lift is reported in Figure 5.4(b), while the different experimental values of A_{EGR} and A_v (and their respective regression functions) are reported in Figure 5.4(a). From Figure 5.4(b), it can be observed how μ_v keeps constant, at a value slightly under 0.9, when l_v is small, while it decreases when l_v goes beyond a critical value $l_{v,e}$. Therefore, the characterization of the function $\mu_v(l_v)$ is possible through a proper piecewise-defined regression function, defined by a second-order polynomial function for $l_v > l_{v,e}$ and a constant value for $l_v \leq l_{v,e}$. With such a definition of μ_v , the \dot{m}_{EGR} estimation provided in Eq. (5) could be modified by replacing $A_{EGR}(l_v)$ with its approximation $\hat{A}_{EGR} = A_v(l_v) \mu_v(l_v)$.

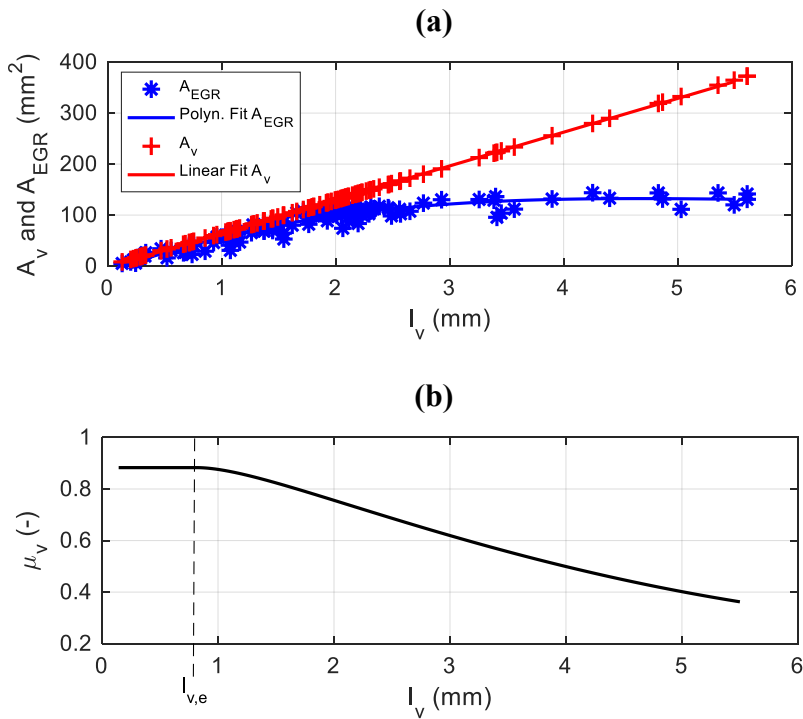


Figure 5.4. Effective EGR flow area and geometric flow area (a) and flow coefficient (b) as a function of the valve lift.

The discharge coefficient μ_v mainly accounts for the effects of flow detachment from the valve-seat profiles, which causes a vena contracta region smaller than the geometric cross-section area.

Some CFD simulations were performed using the software tool “SolidWorks Flow Simulation” to visualize how the flow becomes detached from the geometric surfaces. Appropriate boundary conditions were set according to the data available in some experimental tests. The simulation results are depicted in Figure 5.5, in terms of flow velocity fields for three l_v values: 2 mm, 5 mm and 8 mm. The flow detachment phenomenon becomes increasingly evident as the lift of the valve steps up, while the EGR flow keeps more attached to the geometric surfaces when the smallest l_v value is implemented.

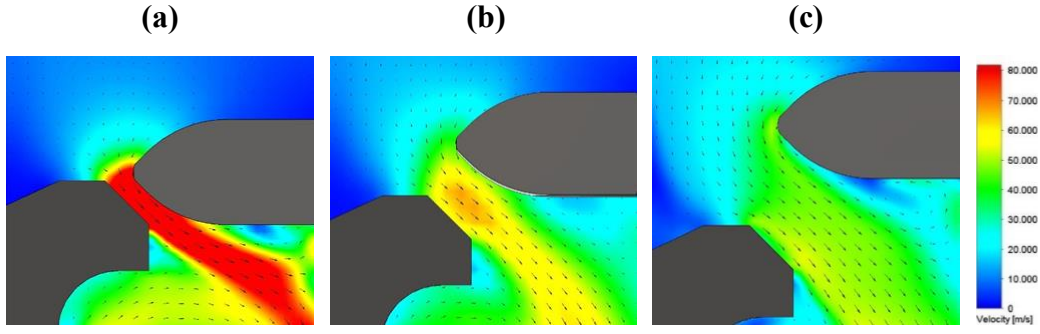


Figure 5.5. CFD flow velocity fields for three different l_v values: 2 mm (a), 5 mm (b) and 8 mm (c).

Semi-physical model

From Eq. (5), it is clear how the above described fluid-dynamics model, to correctly predict \dot{m}_{EGR} , requires the measurement of the exhaust pressure (p_{exh}) and temperature (T_{exh}). However, standard ECUs are usually not provided with dedicated measurement devices. Thus, as long as these models are developed for possible real-time control purposes, their implementation would need suitable estimations of p_{exh} and T_{exh} , i.e. the thermodynamic conditions upstream of the EGR valve. For this purpose, the semi-physical model exploits two different sub-models (namely \hat{p}_{exh} and \hat{T}_{exh}), developed through statistical techniques, to perform these two estimations as a function of a proper set of engine parameters commonly available in standard ECUs.

As far as p_{exh} estimation is concerned, the exhaust gas pressure turned out to be well correlated with the following engine parameters: the intake boost pressure p_{boost} , the relative air-fuel ratio λ , the inlet air mass flowrate \dot{m}_{air} and the engine speed n . Also other variables, such as the injected fuel mass and the SOI, were considered as potential inputs for the \hat{p}_{exh} sub-model, but they were found to affect only marginally the results. Thus, once chosen p_{boost} , λ , \dot{m}_{air} and n as proper input variables, minimizing the number of regressors as far as the smallest statistically significant set (6 terms) was found, the following second-order polynomial sub-model was obtained:

$$\hat{p}_{exh} = \beta_0 + \beta_1 n + \beta_2 p_{boost} + \beta_3 p_{boost}^2 + \beta_4 \dot{m}_{air}^2 + \beta_5 \lambda^2 \quad (7)$$

which featured a coefficient of determination $R^2 = 0.99$ and a root mean square error $RMSE = 14.11$ mbar (while the modeled variable ranged from around 1 to 3 bar, over the complete experimental engine map considered).

As far as T_{exh} estimation is concerned, a linear function of the relative air-fuel ratio (λ), intake manifold pressure p_{boost} and temperature T_{MAN} was chosen:

$$\hat{T}_{exh} = \alpha_0 + \alpha_1 p_{boost} + \alpha_2 T_{MAN} + \alpha_3 \lambda \quad (8)$$

which gives $R^2 = 0.98$ and $RMSE = 20.45$ °C, (while the modeled variable ranged from around 140 to 600 °C, over the complete experimental engine map considered).

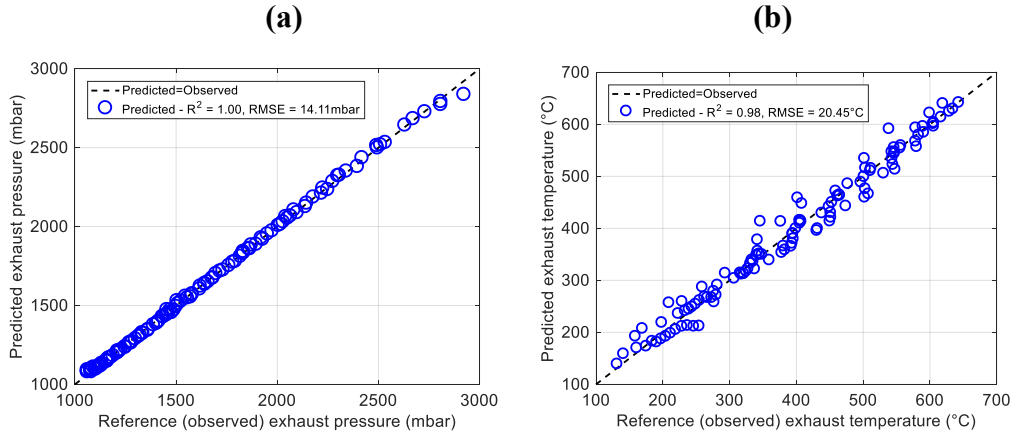


Figure 5.6. Predicted vs. experimental correlation for p_{exh} (a) and T_{exh} (b).

As a visualization, Figure 5.6 shows the correlation between predicted (modeled) and experimental (measured) values for p_{exh} and T_{exh} .

Exploiting these sub-models, the estimation of \hat{m}_{EGR} can be achieved as follows:

$$\hat{m}_{EGR,sp} = A_v(l_v) \mu_{v,sp}(l_v) \frac{\hat{p}_{exh}}{\sqrt{R\hat{T}_{exh}}} \sqrt{\frac{2k}{k-1} \left[\left(\frac{p_{boost}}{\hat{p}_{exh}} \right)^{\frac{2}{m}} - \left(\frac{p_{boost}}{\hat{p}_{exh}} \right)^{\frac{m+1}{m}} \right]} \quad (9)$$

where, $\hat{m}_{EGR,sp}$ represents the EGR mass flowrate estimation obtained by the semi-physical model, the coefficient $\mu_{v,sp}$ is the discharge coefficient re-calculated comparing the result obtained by Eq. (9) with the reference EGR mass flowrate calculated by means of the physical-chemical model, \hat{p}_{exh} and \hat{T}_{exh} represent, respectively, the pressure and temperature of the gas in the exhaust manifold (i.e., upstream of the EGR valve) estimated by the above described sub-models, R is the elastic constant of the exhaust gas calculated from the concentration of chemical species in the raw exhaust gas flow, p_{boost} is the boost pressure measured in the intake manifold and m (polytropic index) was assumed equal to 1.5, as previously done in Eq. (5). The re-calculation of μ_v was performed considering it as a fitting coefficient that accounts not only for the flow detachment phenomena, previously described, but also for other non-idealities, including modeling uncertainties. At this regard, Figure 5.7 compares the discharge coefficient μ_v expressed in Eq. (5) with the coefficient $\mu_{v,sp}$ expressed in Eq. (9). Furthermore, the pressure in the manifold p_{boost} , measured by the ECU, was considered as a suitable approximation of the pressure at the EGR cooler output p_{CO} , used in Eq. (5).

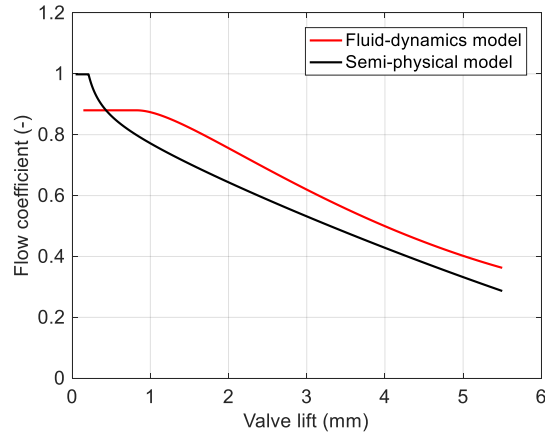


Figure 5.7. Discharge coefficients comparison for the fluid-dynamics and the semi-physical model.

Purely statistical model

The last approach applied to model \dot{m}_{EGR} is purely statistical. This means that, unlike the previously reported models, in this case the relationship between the input data and the output \dot{m}_{EGR} estimation is obtained without considering any particular physical law or underlying process, but using only statistical techniques. In particular, \dot{m}_{EGR} can be described through polynomial functions which receive, as inputs, some or all of the following variables, selected among those commonly available in standard ECUs and assessed to have an influence on the EGR mass flowrate: engine speed (n), injected fuel mass (q_b), intake boost pressure (p_{boost}), EGR valve position (EGR_{pos}), exhaust flap position ($ExhFlp_{pos}$), SOI of the main injection (SOI_{main}), position of the blades of the variable geometry turbine (VGT_{pos}). As a matter of fact, this set of variables is supposed to be the one which mostly affects the required inputs of the equation for convergent nozzle under subsonic compressible flow conditions (cf. Eq. (5)), i.e. the gas pressure at the intake and exhaust manifolds, the temperature of the exhaust gases as well as the EGR valve flow area.

As a starting point, the model was originally built as a second-order polynomial function which included all the regressors related to the interactions of the inputs. Then, other models were built, choosing several sub-sets from all the regressors of the starting model and comparing their performances. The best performance (on the experimental engine map dataset, which was used to fit the model coefficients) was achieved with the simplest linear model, as follows:

$$\hat{m}_{EGR,s1} = \gamma_{01} + \gamma_{11}n + \gamma_{21}q_b + \gamma_{31}p_{boost} + \gamma_{41}VGT_{pos} \quad (10)$$

Other models were set and tested, too, all providing similar outcomes on the same experimental dataset. For instance, another model will be considered for comparison:

$$\hat{m}_{EGR,s2} = \gamma_{02} + \gamma_{12}n + \gamma_{22}q_b + \gamma_{32}p_{boost} + \gamma_{42}VGT_{pos} + \gamma_{52}EGR_{pos} + \gamma_{62}ExhFlp_{pos} + \gamma_{72}SOI_{main} + \gamma_{82}VGT_{pos}^2 \quad (11)$$

The first model, expressed in Eq. (10), gives $R^2 = 0.966$ and $RMSE = 1.11$ g/s, while the latter, expressed in Eq. (11), gives $R^2 = 0.91$ and $RMSE = 1.77$ g/s.

5.1.2 Assessment and validation of the models

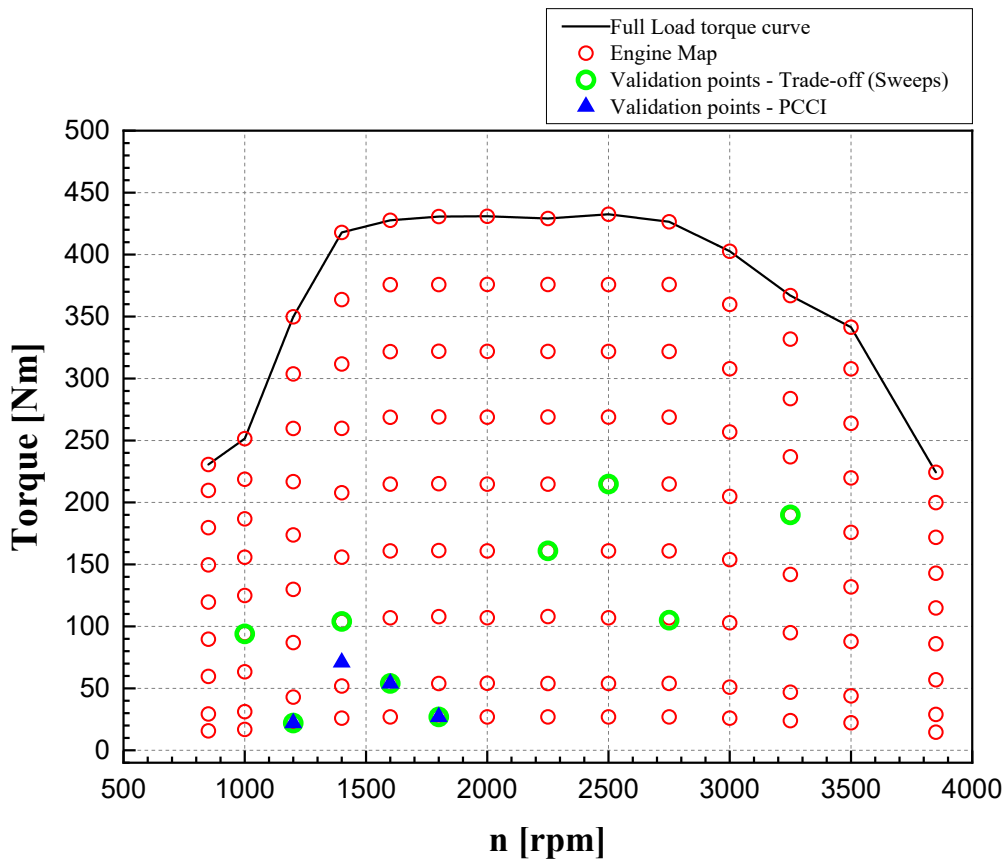


Figure 5.8. Engine operating points carried out at the test bench on the F1C Euro VI engine (red circles: Engine map; green circles: Trade-off validation tests; blue triangles: PCCI validation tests).

All the previously described models were developed and set up using an experimental complete engine map, performed at the test bench on the F1C Euro VI engine under CDC mode, as depicted in Figure 5.8 (red circles). As an additional step, a model validation procedure was carried out through the assessment of the predicting performances of these models on other experimental datasets, including a full replication of the same engine map, several air quantity sweeps at different engine operating points as well as some tests in PCCI combustion mode. The purpose was to assess if these models were able to perform a reliable estimation even when the operating conditions move away from the calibration dataset, used to tune the model coefficients, as long as this feature would be essential for any model-based control application.

Figures 5.9-5.11 show the results of this validation procedure, for each experimental validation dataset taken into consideration. The \dot{m}_{EGR} estimations pertaining to all the previously described models are reported on the y-axis, with different colors and symbol shapes (red plus signs for the fluid-dynamics model, black squares for the semi-physical model, blue circles for the first pure statistical model, violet diamonds for the second pure statistical model). Instead, the x-axis

reports the reference \dot{m}_{EGR} value, obtained by means of the baseline physical-chemical method. The values of R^2 and RMSE, for each considered model, are also reported inside the legend box.

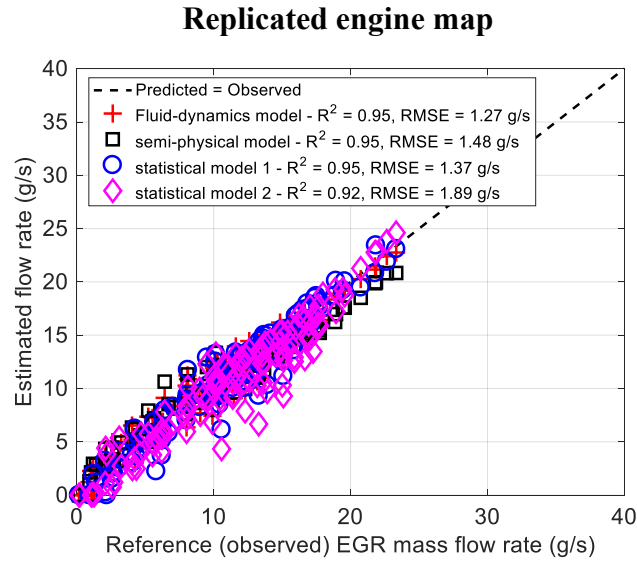


Figure 5.9. Validation of the models for the prediction of \dot{m}_{EGR} on the replicated engine map dataset.

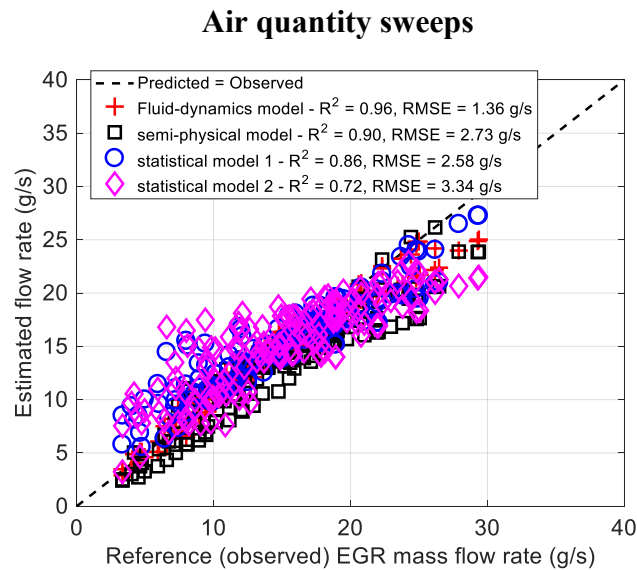


Figure 5.10. Validation of the models for the prediction of \dot{m}_{EGR} on the air quantity sweeps dataset.

Figure 5.9 shows the validation of the analyzed models on a fully replicated engine map. The dispersion of the all the symbols around the 45° bisecting line (where estimation and reference coincide) shows that, on this experimental dataset, which is nominally equivalent to the calibration engine map, all the models are comparable in terms of R^2 , ranging between 0.92 and 0.95, and RMSE, ranging between 1.27 and 1.89 g/s (while the prediction variable \dot{m}_{EGR} ranges from 0 to around 23 g/s).

Figure 5.10 shows the validation of the analyzed models on air quantity sweep tests realized at 9 different engine working points (cf. green circles depicted in Figure 5.8), varying on the whole speed range and bounded inside a low-to-medium load area of the engine map. Each air quantity sweep is achieved starting from the

baseline calibration and making the air quantity varying from the highest value (i.e., without EGR) to the lowest (i.e., with the maximum EGR rate tolerated, before the occurrence of too high cycle-to-cycle and cylinder-to-cylinder instability), while keeping constant all the other calibration parameters. Therefore, these tests cover a high variety of working conditions, from slightly to extremely outside the baseline engine calibration. The dispersion of all the symbols around the 45° bisecting line, if compared to the previous case, is generally wider, and this highlights a general degradation of the outcomes of the models. The fluid-dynamics model (cf. the red plus signs in Figure 5.10) turns out to have the highest accuracy, with its estimation outcomes virtually comparable with those obtained on the replicated engine map dataset, even if a weak decline in the model performance appears for \dot{m}_{EGR} higher than 23÷25 g/s, which are the maximum values reached on the baseline engine map. The semi-physical model (cf. the black squares in Figure 5.10) provides an R^2 value slightly smaller than that featured by the fluid-dynamics one, along with a higher RMSE, up to 2.73 g/s, which is around 9% of the maximum \dot{m}_{EGR} . Conversely, both the purely statistical models under investigation exhibit a significant deterioration of the estimation capability: the first one (cf. the blue circles in Figure 5.10), i.e. the simplest linear function, displays a wide dispersion for the smallest \dot{m}_{EGR} values, while the second (cf. the violet diamonds in Figure 5.10) shows critical fitting errors for all the low-to-medium range of \dot{m}_{EGR} , with a broadly poor correlation between the physical phenomenon and its forecast. Comparable results were also obtained by validating the models on a set of experimental EGR valve sweeps and exhaust flap sweeps, performed at the same 9 engine working points highlighted by green circles in Figure 5.8.

Finally, the four models previously analyzed were validated on some experimental datasets under PCCI combustion mode, at 4 different engine operating points which featured low-to-medium speed and low load: 1200×1, 1400×3, 1600×2, 1800×1 (all expressed in terms of speed n [rpm] × $bmeP$ [bar], and depicted with blue triangles in Figure 5.8). For each of them, statistical DoE test plans were available, as they were carried out to perform model-based calibration procedures (under PCCI combustion mode), similarly to what explained in the previous Sections.

PCCI tests

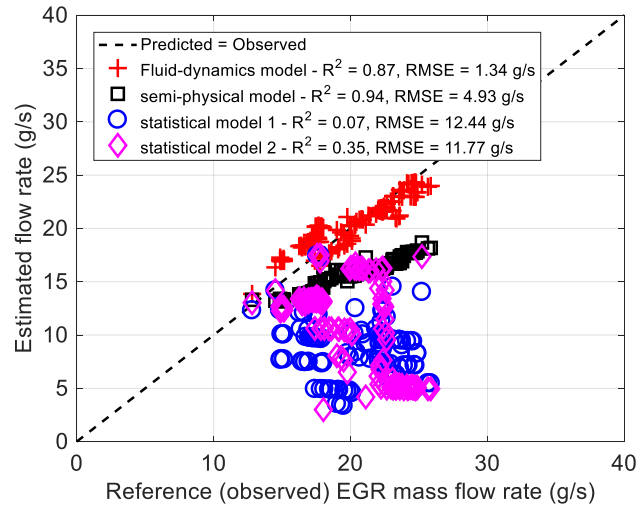


Figure 5.11. Validation of the models for the prediction of \dot{m}_{EGR} on the PCCI dataset.

Figure 5.11 reveals how the fluid-dynamics model (cf. the red plus signs in Figure 5.11) is almost the only one which provides reliable \dot{m}_{EGR} estimations, in these high-EGR working conditions. Indeed, its statistical indicators R^2 (0.87) and RMSE (1.34 g/s) are not far from those obtained with the same model on the other kind of validation tests previously reported. The semi-physical model (cf. the black squares in Figure 5.11) features a high R^2 of 0.94, nevertheless its RMSE (4.93 g/s) is nearly doubled if compared to the previous validation datasets. This points out the presence of a systematic bias, which raises as the EGR mass flowrate increases. Then, both the purely statistical models under investigation proved to have extremely poor predictive capabilities on these PCCI tests: the first model (cf. the blue circles in Figure 5.11) seems to be totally uncorrelated with the described phenomena (indeed, its R^2 tends to zero), while the second one (cf. the violet diamonds in Figure 5.11) displays evident worsening correlations for \dot{m}_{EGR} values close to or bigger than the maximum \dot{m}_{EGR} value featured in the calibration map.

This analysis shows that the fluid-dynamics model is the only one able to properly describe the phenomena, providing a robust \dot{m}_{EGR} estimation in every working condition, even if not explored in the model calibration phase. Also the semi-physical approach generally provides satisfactory outcomes, although a systematic bias is evident when PCCI tests are considered. This could be due to the dependance of the model-estimated exhaust temperature and pressure on some engine parameters that may have negligible effects on the model calibration with the original engine map dataset. In particular, a systematic underestimation of the exhaust pressure was detected on the PCCI dataset working conditions. It could be worth highlighting that these PCCI tests have been carried out keeping the EGR valve in fully open position, while varying the EGR flowrate by throttling at the exhaust by means of the exhaust flap, but these consequently high exhaust backpressure values were not thoroughly explored in the calibration dataset. Finally, the purely statistical polynomial models, built without a background knowledge of the physics

of the phenomena, proved to be unable to properly predict the EGR mass flowrate in working conditions different from the calibration dataset, although they showed satisfactory estimation capabilities on the original calibration map.

5.2 Real-time combustion control techniques⁶

A possible application of the above described EGR models could be related to the realization of airpath system controllers. In fact, an accurate control of the EGR rate is possible through a complete control of the whole airpath system, thus including both the EGR and fresh air loops as well as the intake and exhaust manifolds [Chauvin, et al., 2007]. However, when implementing PCCI combustion concepts with high amount of EGR, the implementation of just an airpath controller is often not sufficient. In fact, one of the main issues in PCCI operations is that the onset of the combustion event is highly sensitive to small variations of the in-cylinder initial conditions (i.e., temperature, pressure and EGR rate). Thus, slight retardation of the combustion phasing (e.g., due to excessive EGR in one of the cylinders) may lead to wide cylinder-to-cylinder and/or cycle-to-cycle variations in terms of *imep* and/or MFB50, up to the occurrence of misfiring events, in the worst cases. Conversely, slight advance of the combustion phasing (e.g., due to lack of EGR in one of the cylinders) may lead to a sharp increase in p_{cyl} , deteriorating the acoustic comfort up to potential damage to the engine if peak firing pressure limits are exceeded [Hillion, et al., 2008; Spessa, et al., 2017]. Further complications are expected when speed and load transient operations are dealt with. Because of the different time constants characteristic of the response of the airpath with respect to the fuelpath, deviations from steady-state calibrated setpoints are likely [Carlucci, et al., 2014], and a control on just the airpath actuators is not able to provide fast enough adjustment to transient changes. Therefore, stable and efficient PCCI operations need accurate real-time combustion controls, which cannot be managed without a suitable control of the fuel injection parameters.

The conventional control architecture for standard ECUs is map-based, i.e. relies on quantities which need to be interpolated from purposely calibrated look-up tables (“maps”), generally featuring, as index values, estimated or measured parameters such as the estimated fuel injected mass, the intake air mass, the engine speed, and/or the boost pressure. In particular, as regards the fuelpath control, maps related to SOI_{main} (i.e., the SOI of the main injection) depend on the total injected fuel mass and on the engine speed, but different maps are also calibrated to take into account the different possible number of pilot injections. When transient operations are detected, standard ECUs apply suitable dynamic corrections to address the different time constants of the fuel injection pressure, boost pressure

⁶ Most of the contents of this Section have been previously published in [Spessa, E., d'Ambrosio, S., Iemmolo, D., Mancarella, A., Vitolo, R., & Hardy, G. (2017). “Steady-State and Transient Operations of a Euro VI 3.0L HD Diesel Engine with Innovative Model-Based and Pressure-Based Combustion Control Techniques”. SAE International Journal of Engines, 10(3), 1080-1092. doi:10.4271/2017-01-0695].

and EGR rate variations. As a matter of fact, the experimental calibration procedure of these maps, also taking into account the determination of all their possible corrections in function of the different engine working conditions (e.g. transient corrections, multiple maps when varying the number of fuel injections, etc.), is highly time-consuming and expensive. Moreover, the SOI_{main} is not a robust control parameter, as it is not straightforwardly correlated to the engine combustion efficiency and/or to the in-cylinder pollutant formation [Finesso, et al., 2017a], meaning that it would be nearly impossible to create reliable SOI maps for PCCI applications. As a consequence, when real-time combustion control are implemented, MFB50 (or SOC) is the most commonly exploited monitoring parameter, being the combustion process phasing acknowledged to be one of the features that mostly affect both CDC and PCCI combustion modes. Also $imep$ and the peak value of HRR may be considered in some applications [Chung, et al., 2016].

Real-time combustion control algorithms may offer several benefits over conventional map-based approaches. First of all, they require lower experimental efforts in the calibration phase. Secondly, they give the possibility of optimizing, in real-time, the engine operating parameters to achieve the required targets in terms of performance (e.g., combustion stability, acoustic comfort and/or fuel consumption) or exhaust pollutant emissions, by monitoring closely correlated parameters such as the MFB50. In this way, they manage to be robust to deviations from the baseline calibration dataset, caused by either internal or external factors (such as intake conditions, EGR unbalance, coolant temperature, engine component aging, turbo-lag effects during transients, etc.), as they are able to detect these variations, to predict their effects on the combustion process outcomes and finally to compensate for them [Spessa, et al., 2017].

There are two different ways to monitor MFB50 and SOC in real-time: the pressure-based and the model-based approaches. The pressure-based approach [Yu, et al., 2013; Carlucci, et al., 2014; Chung, et al., 2016] is based on in-cylinder pressure measurements (carried out by dedicated pressure transducers) from which direct information about the mass fraction burned profile (X_b) and the actual MFB50/SOC values are retrieved. Conversely, the model-based approach generally collects the information linked to MFB50/SOC from semi-empirical models of the in-cylinder combustion phenomenon. For instance, the SOC detection may be achieved by modeling and estimating the ID value, i.e. the time interval between the SOI and the SOC [Hillion, et al., 2008]. Instead, an improved accumulated fuel mass approach may be exploited for the estimation of the heat release rate (and, consequently, of the MFB50) by a low-throughput model, which needs as inputs a set of engine parameters commonly measured (or estimated) by standard ECUs [Catania, et al., 2011; Baratta, et al., 2015; Finesso, et al., 2015].

In the following, an application of pressure-based and model-based approaches for MFB50 control will be discussed.

5.2.1 Real-time combustion controls for the MFB50 monitoring

Pressure-based approach

The real-time pressure-based control of the MFB50 is performed starting from the measurement signals of the in-cylinder pressure time-histories acquired by dedicated transducers, fitted to the glow-plug seats of each cylinder. The actual MFB50 value, for each cylinder, is calculated starting from the estimation of the net energy release Q_{net} , evaluated through a single-zone modeling approach [Heywood, 2018], as follows:

$$dQ_{net} = \frac{\gamma}{\gamma-1} p dV + \frac{1}{\gamma-1} V dp \quad (12)$$

where $\gamma = c_p/c_v$, p is the instantaneous in-cylinder pressure and V the instantaneous chamber volume. The value of γ is kept constant (a reference value can be 1.37) in order to have a short computational time, although γ would depend on the chemical compositions of the burned gases which, in general, vary depending on the engine operating conditions [Catania, et al., 2011]. The net heat release profile Q_{net} , integrated from Eq. (12), is then normalized to its maximum to obtain the mass fraction burned curve (X_b), monotonically rising from 0 to 1. The MFB50 value is obtained, by definition, as the crank angle at which X_b becomes equal to 0.5, that is the instant when the 50% of the injected fuel mass has burnt.

In this way, the actual MFB50 (i.e., $MFB50_{act}$) is evaluated, on a cycle-to-cycle and cylinder-to-cylinder basis, and it is then compared with a target MFB50 value (i.e., $MFB50_{tgt}$), specifically calibrated to achieve desired goals in terms of engine performance and pollutant emissions. The difference between the target and the actual MFB50 values, for each cylinder j and cycle i , represents the error on combustion barycenter the real-time control has to compensate:

$$ERR_j(i) = MFB50_{tgt,j}(i) - MFB50_{act,j}(i) \quad (13)$$

In order to minimize $ERR_j(i)$, the SOI of the main pulse in the following cycle $i+1$ is corrected as follows:

$$SOI_{main,j}(i+1) = SOI_{main,j}(i) + K_{mod,j}(i) \cdot ERR_j(i) \quad (14)$$

where $K_{mod,j}(i)$ is a modulating coefficient, limited in the range $[0.1, 1]$, introduced to ensure the stability of the control and varied at each cycle as a function of the sign of the error between two consecutive cycles [Finesso, et al., 2017b].

Model-based approach

The real-time model-based control of the MFB50 is performed inverting a predictive heat release model, which is based on a refined version of the accumulated fuel mass (AFM) approach, one of the most widely used for diesel

engines [Finesso, et al., 2015; Finesso, et al., 2017]. For this approach, the starting assumption is that the rate of chemical energy released by the fuel $\left(\frac{dQ_{ch}}{dt}(t)\right)$ is proportional to the energy associated with the in-cylinder accumulated fuel mass, i.e. the fuel quantity available for the combustion at any considered time instant. This energy, at any time t , is calculated as the difference between the chemical energy $\left(Q_{fuel}(t - \tau)\right)$ associated with all the fuel quantity injected up to that time t and all the energy already released by the fuel at the same time $\left(Q_{ch}(t)\right)$ [Chmela & Orthaber, 1999; Finesso, et al., 2015]. Eq. (15) shows how the rate of chemical energy release was computed, with accurate results, for pilot injections [Finesso, et al., 2017]:

$$\frac{dQ_{ch}}{dt}(t) = K \cdot [Q_{fuel}(t - \tau) - Q_{ch}(t)] \quad (15)$$

where K and τ are model calibration parameters related, respectively, to the combustion rate and the ID. Conversely, the chemical energy release of the main injection was computed by means of a modified formulation, which had been proposed in [Finesso, et al., 2015] to take into account the turbulence induced by the main fuel injection on the heat release, which may not be neglected in diesel sprays:

$$\frac{dQ_{ch}}{dt}(t) = K_1 \cdot [Q_{fuel}(t - \tau) - Q_{ch}(t)] + K_2 \frac{dQ_{fuel}}{dt}(t - \tau) \quad (16)$$

where K_2 is an additional model calibration parameter. Proper correlations were identified for the abovementioned model calibration parameters, as functions of the in-cylinder pressure and temperature values at SOI/SOC and of other engine variables (including rail pressure, estimated intake oxygen concentration and engine speed).

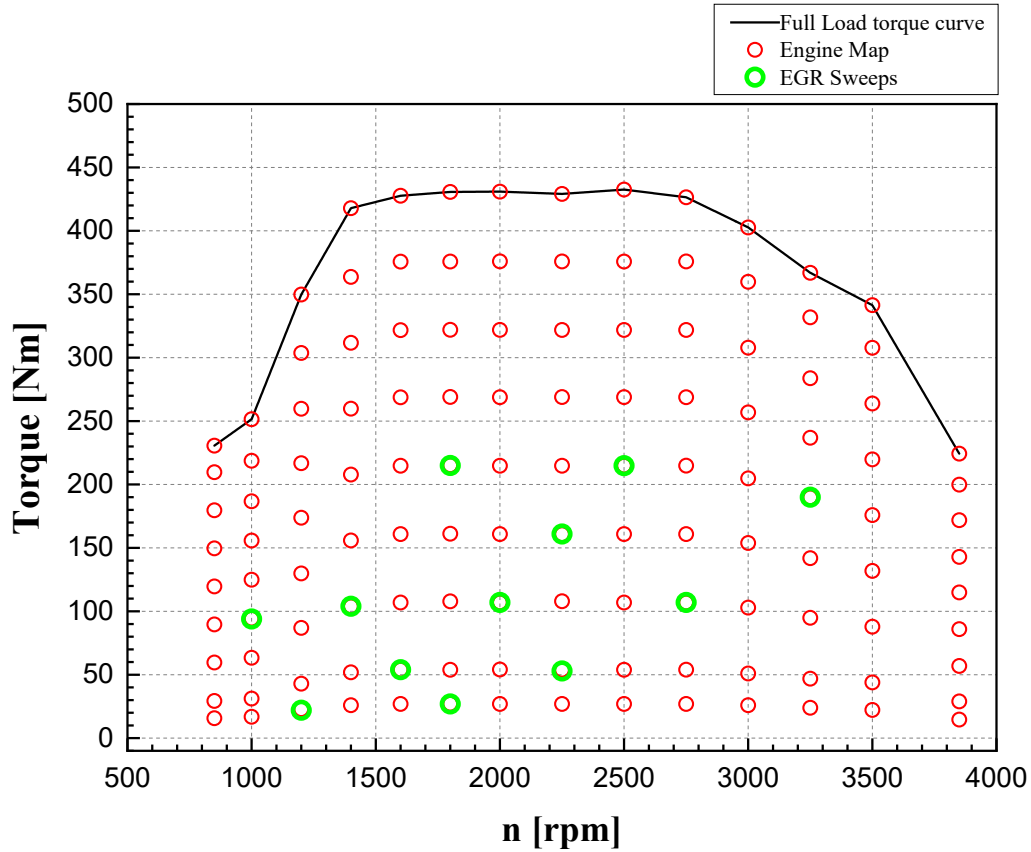
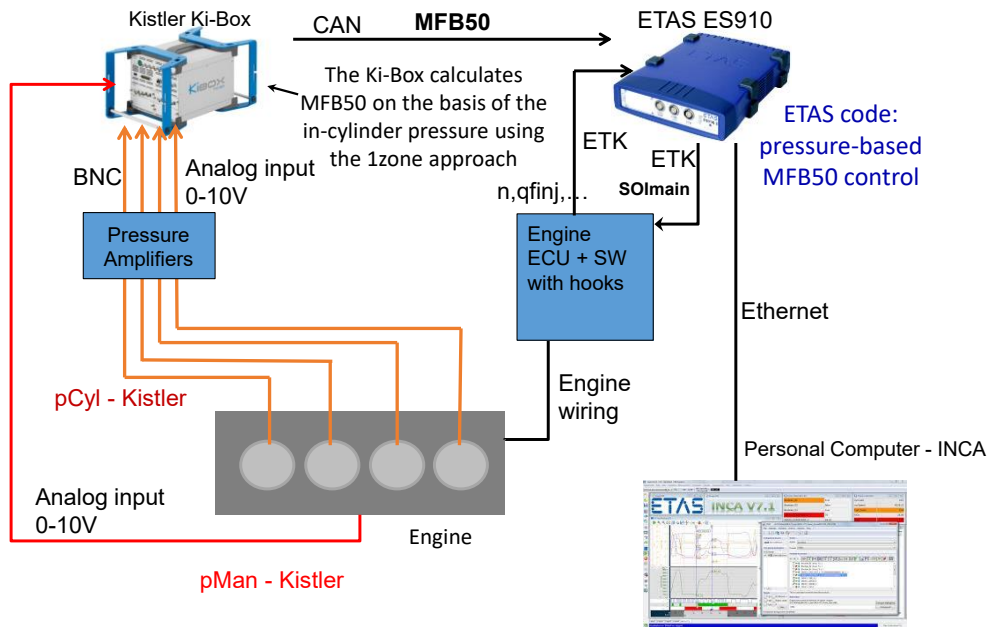


Figure 5.12. Engine operating points carried out at the test bench on the FIC Euro VI engine under CDC mode (red circles: Engine map; green circles: EGR sweeps).

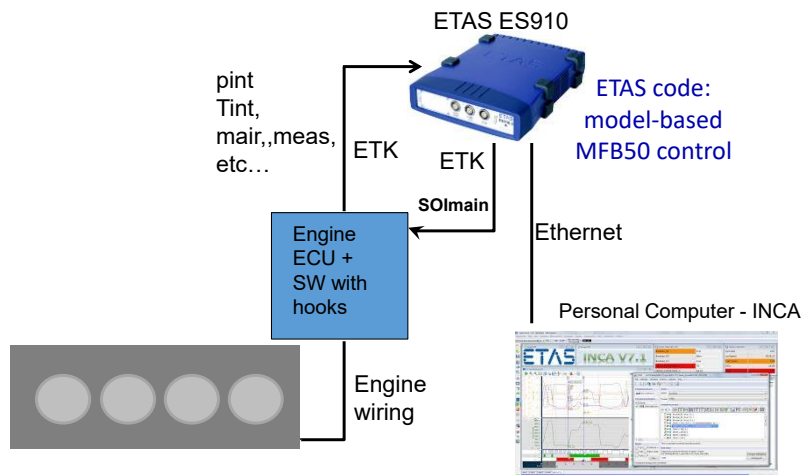
The heat release model, properly inverted, is able to predict which is the SOI_{main} value needed to reach the desired $MFB_{50_{tgt}}$, adjusting it on a cycle-to-cycle basis. This is done adopting an iterative procedure able to provide the desired SOI_{main} command with an uncertainty lower than $0.2\text{ }^{\circ}CA$ [Finesso, et al., 2017]. Clearly, unlike the pressure-based approach, no cylinder-to-cylinder control of the SOI is possible, as the model receives as inputs a set of ECU variables (e.g., intake temperature and pressure, engine speed, intake air mass flowrate, etc.) which are related to the whole engine, and not to the specific cylinder, unlike the information given by the in-cylinder pressure transducers. The predictive model was assessed on a complete engine map (cf. red circles depicted in Figure 5.12) and on 12 EGR sweeps (cf. green circles depicted in Figure 5.12), featuring an RMSE between experimental and predicted around $0.8\text{ }^{\circ}CA$.

The model-based control, relying on this inverted heat release model, uses an estimation of the actual MFB_{50} , and is therefore an open-loop control.

Rapid prototyping setup



(a): RP setup for testing the pressure-based technique



(b): RP setup for testing the model-based technique

Figure 5.13. Schematics of the RP setup for the pressure-based (a) and model-based (b) MFB50 controls

Both the previously described real-time combustion algorithms for MFB50 were developed in MATLAB/Simulink. First, they were assessed and tested in a Model-in-the-Loop (MiL) phase, i.e. coupling the Simulink tool to an engine emulator model running in GT-Power. Then, they were deployed on an ETAS ES910 RP device by means of the ETAS Intecrio software tool, in order to test the functionalities of the controls in a Hardware-in-the-Loop (HiL) configuration (i.e., coupling the RP device to a NI PXI real-time engine emulator). Finally, both the controls were tested in a Rapid Prototyping (RP) phase, to check their potentialities directly on the real engine at the test bench. The RP setup shown in Figure 5.13 had the aim of running the new control strategies bypassing only the standard controls

of the ECU involved in the new setup, avoiding the need of completely reprogramming the ECU [Finesso, et al., 2017; Spessa, et al., 2017].

The RP setup for the pressure-based approach (cf. Figure 5.13(a)) mainly relies on a Kistler Kibox indicating device, which is used to measure the in-cylinder pressure signals from the four cylinders and to evaluate, from them, the cycle-to-cycle real-time MFB50 values, by means of a single-zone combustion model. These MFB50 values are provided (via CAN communication protocol), in real-time, to the RP device, which gives them as inputs to the pressure-based control model. As previously explained, the pressure-based control algorithm is then able to determine which are the cycle-to-cycle SOI_{main} values needed to match the measured MFB50 of each of the four cylinders to the $MFB50_{tgt}$ target value. These updated SOI_{main} values are finally sent back to the ECU (via ETK communication protocol), thus bypassing the SOI_{main} values determined by the standard map-based control of the ECU.

Conversely, the RP setup for the model-based approach (cf. Figure 5.13(b)) does not need any indicating device, as the input signals required by the low-throughput heat release model are only a set of commonly available data from the standard ECU. The control algorithm determines which is the SOI_{main} value, the same for all the cylinders, needed to reach the $MFB50_{tgt}$ value and sends it to the ECU (via ETK communication protocol), thus bypassing the SOI_{main} values determined by the ECU through its standard map-based control.

5.2.2 Experimental tests: results and discussion

An experimental activity on the F1C Euro VI engine at the test bench was performed to compare the performances between the pressure-based and the model-based MFB50 controls, taking as baseline references the results of the standard ECU map-based approach. Tests under both steady-state and transient conditions were analyzed. In particular, the steady-state tests included a full engine map (with the three controls), $SOI/MFB50$ sweeps at two engine operating points (with the map-based and the pressure-based controls), EGR sweeps under PCCI combustion mode (with the map-based and the pressure-based controls), tests with different fuels (i.e. conventional diesel oil, JetA1 fuel and a 50%/50% blend diesel/JetA1). Conversely, the transient tests included a World Harmonized Transient Cycle (WHTC) as well as fast speed and load ramps.

For every experimental test, results in terms of $bsfc$, CN and engine-out pollutant emissions (NO_x , soot, CO and HC) were available. Furthermore, analyses in terms of engine combustion stability were carried out taking into account the coefficient of variation (CoV) of $imep$ (CoV_{imep}) and PFP (CoV_{PFP}). These parameters were computed (for every steady-state test) in two different ways. First, by taking into account 100 consecutive engine cycles for each of the four cylinders of the engine, thus encompassing the cyclic variability of each cylinder ($CoV_{imep,cyl}$ and $CoV_{PFP,cyl}$). Secondly, by considering 400 in-cylinder pressure cycles, 100 consecutive per cylinder, thus encompassing both the cycle-to-cycle and the cylinder-to-cylinder variability of the whole engine ($CoV_{imep,eng}$ and $CoV_{PFP,eng}$).

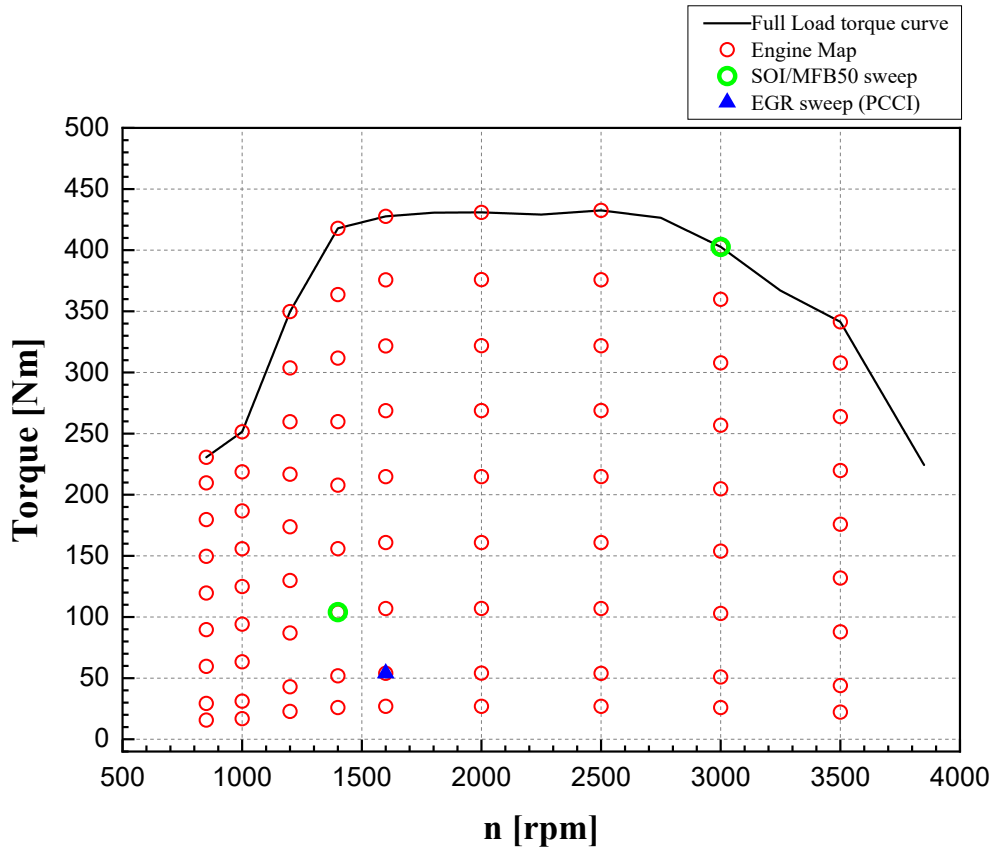


Figure 5.14. Engine operating points selected for the engine map (red circles), for the SOI/MFB50 sweeps (green circles) and for the EGR sweep under PCCI mode (blue triangle).

Figure 5.14 reports, with different colors and symbol shapes, the engine operating points selected for the following steady-state tests.

Steady-state analysis: engine map

The steady-state engine map was carried out once for each of the three controls (i.e., map-based, pressure-based and model-based) and was made up of about 85 engine operating points, featuring the following engine speed values n (in rpm): 850, 1000, 1200, 1400, 1600, 2000, 2500, 3000, 3500 rpm and the following load values (expressed in percentage of the maximum torque achievable at each speed): 7%, 12%, 25%, 37%, 50%, 62%, 75%, 87% and 100% (cf. the red circles depicted in Figure 5.14).

The three considered controls showed negligible differences in terms of $bsfc$, CN and exhaust pollutant emissions (NO_x , soot, CO and HC) on the whole engine map. At the same time, the three controls highlighted slight differences as well, when considering the engine combustion stability. In terms of CoV_{imep} , the conventional ECU map-based approach showed CoV_{imep} peak values which do not go beyond 4% at the lowest loads, either if taking into account separately each cylinder ($CoV_{imep,cyl}$) or the whole engine ($CoV_{imep,eng}$). Conversely, CoV_{imep} values become even lower than 1% when the load increases, thus highlighting a really stable combustion process of the engine in all the examined working conditions.

a) $CoV_{PPF,eng}$ at 850 rpm

b) $CoV_{PPF,eng}$ at 2000 rpm

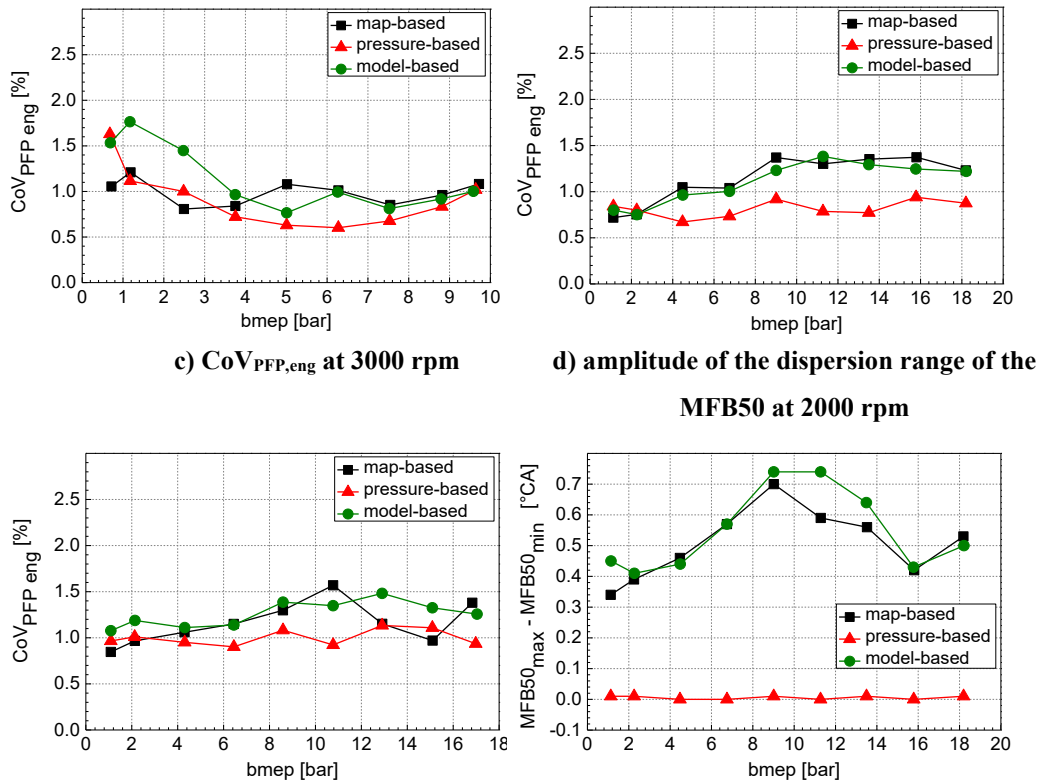


Figure 5.15. Coefficient of variation of the peak firing pressure evaluated for the whole engine $CoV_{PFP,eng}$ (a, b and c) and amplitude of the dispersion range of the MFB50 (d) on engine mapping tests: comparison between the map-based, the pressure-based and the model-based controls. $CoV_{PFP,eng}$ is shown on tests for various engine loads at three different engine speeds: a) 850 rpm; b) 2000 rpm; c) 3000 rpm. The dispersion of the MFB50 (d) is reported at 2000 rpm for various engine loads.

Also the $CoV_{PFP,cyl}$ values showed values that were similar for all the three control approaches. However, when implementing the pressure-based control, an appreciable decrease in the $CoV_{PFP,eng}$ was generally found, especially at medium-high loads and speeds. More in detail, Figure 5.15 shows the $CoV_{PFP,eng}$ as a function of the engine load (expressed in $bmep$), comparing the three controls at three different engine speeds n (i.e., 850, 2000 and 3000 rpm). For medium-to-high load, it can be noted that the pressure-based control allows to achieve a $CoV_{PFP,eng}$ reduction ranging from 0.2 to 0.7 %. As far as the cycle-to-cycle variability was low and similar for all the controls, a reduction of $CoV_{PFP,eng}$ can be mainly ascribed to a lower dispersion of the PFP values between the four cylinders. Hence, the pressure-based model is able to provide reduced cylinder-to-cylinder variations in terms of PFP, primarily due to its potentiality of keeping very precisely the same MFB50 target for each cylinder. This latter effect can be clearly observed with reference to Figure 5.15(d), which reports the difference between the maximum and the minimum MFB50 values (averaged on 100 consecutive engine cycles) occurring within the four cylinders, as a function of $bmep$, comparing the baseline ECU map-based strategy to the pressure-based and model-based control techniques. The graph reports the results obtained for various engine loads at 2000 rpm, but similar trends (here not reported) are obtained for the other engine speeds. A certain cylinder-to-cylinder dispersion of the MFB50 is observable both with the map-based and the model-based controls, with a difference of about 0.8 °CA between

the cylinder which shows the most advanced combustion event and the one featuring the most delayed phasing. On the other hand, the pressure-based control technique shows practically no MFB50 cylinder-to-cylinder fluctuations, providing consequently a slightly more uniform distribution of CN levels between the cylinders, as it is detectable from Figure 5.16(a), which again shows the results at 2000 rpm and different loads. However, this potentiality from the pressure-based control did not give appreciable benefits in terms of engine-out pollutant emissions, as it can be seen considering the engine-out NO_x and soot emissions of the three controls at 2000 rpm, reported in Figure 5.16(b).

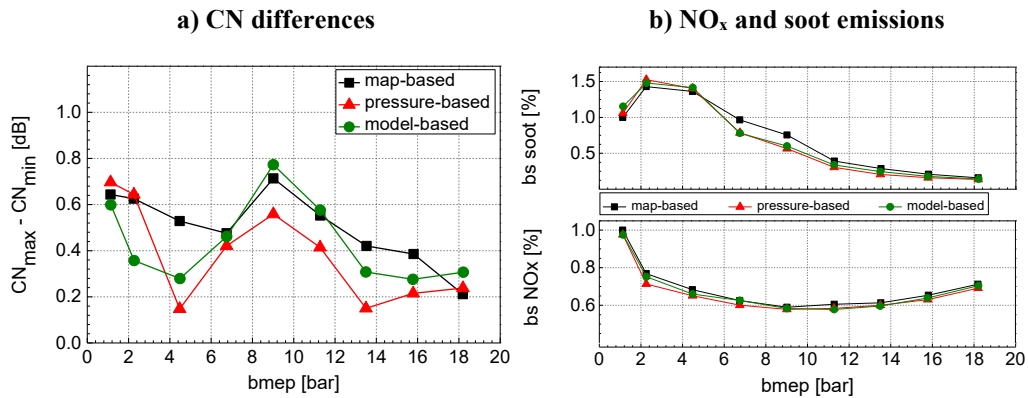


Figure 5.16. Amplitude of the dispersion range of the CN (a) and NO_x and soot emissions (b) vs. *bmep* at 2000 rpm: comparison between the map-based, the pressure-based and the model-based controls. The values are reported in adimensional units, referring all the values to those measured at *bmep* = 1 bar for the map-based control

Steady-state analysis: SOI/MFB50 sweep tests

A further comparison between the baseline ECU map-based control and the pressure-based control technique was carried out considering some steady-state SOI/MFB50 sweep tests. At two different engine working points, namely 1400×104 (referring to the number before the × symbol as the engine speed *n*, in rpm, and to the following number as the engine torque *Trq*, in Nm) and 3000 rpm at full load (cf. the green circles depicted in Figure 5.14), a sweep of SOI values was considered for a single fuel injection pattern (i.e. the pilot injections were disabled) featuring the baseline ECU map-based control. For each of these tests, the corresponding values of MFB50, averaged on 100 cycles, were calculated per each cylinder. Then, the average of these four values of MFB50 (one per each cylinder) was set as a target for the tests featuring the pressure-based control. For these SOI/MFB50 sweep tests, the model-based method was not considered because the MFB50 estimating model was developed considering the baseline engine calibration, featuring conventional SOI values and multiple fuel injection patterns. A model-based control could be applied in such tests only after a proper recalibration of the model under these different working conditions.

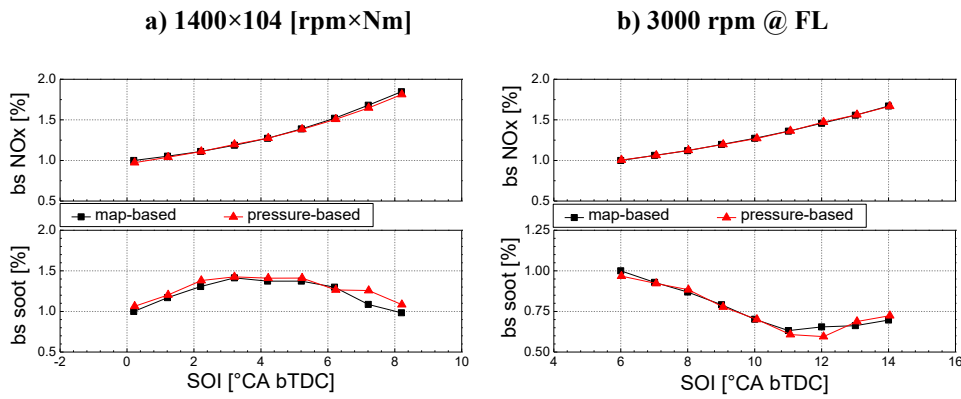


Figure 5.17. Engine-out soot and NO_x emissions vs. SOI at 1400 rpm × 104 Nm (a) and 3000 rpm × full load (b): comparison between the map-based and the pressure-based controls during SOI sweeps. The values are reported in adimensional units, referring all the values to those measured with the baseline SOI (the lowest value in the x-axes) for the map-based control.

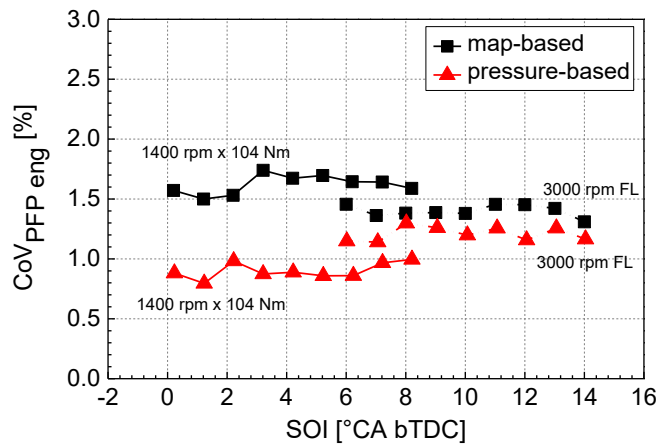


Figure 5.18. Coefficient of variation of the peak firing pressure evaluated for the whole engine $CoV_{PFP,eng}$ VS SOI on the SOI/MFB50 sweep tests, at 1400×104 and 3000×FL: comparison between the map-based and the pressure-based controls.

As in the case of the engine map tests, the results obtained with the conventional ECU map-based and the pressure-based controls, in terms of *bsfc* and exhaust pollutant emissions, do not show appreciable differences, as can be seen in Figure 5.17, which reports engine-out soot and NO_x emissions as a function of the SOI values. Nevertheless, also these SOI/MFB50 sweep tests highlighted a reduction of the $CoV_{PFP,eng}$ values when implementing the pressure-based control with respect to the baseline map-based one, as shown in Figure 5.18. On the other hand, similar dispersions in terms of CN were found applying the two controls, which cannot be compared to the results shown on the engine map tests since these latter were performed with a triple fuel injection pattern, while the SOI/MFB50 tests were carried out featuring a single fuel injection strategy.

Steady-state analysis: EGR sweep tests under PCCI combustion mode

Further steady-state tests were carried out under PCCI combustion mode to further assess the newly developed MFB50 controls. In particular, the comparison

involved the original baseline map-based control and pressure-based technique. The tests were performed at 1600×54 (rpm × Nm, cf. the blue triangle depicted in Figure 5.14) with a high EGR ratio (>60%) and an advanced single fuel injection strategy. The EGR poppet valve was kept fully open, while a sweep of EGR mass flowrate was carried out by progressively raising the engine backpressure (and, consequently, the pressure difference between the exhaust and the intake manifolds) by means of the actuation of the already mentioned exhaust flap, placed downstream of the turbine. More in detail, the EGR sweep tests were performed in the following way: first, with the original ECU map-based control, the SOI was kept fixed at 23 °CA bTDC, while the EGR ratio was progressively increased until combustion instability was reached. Then, implementing the pressure-based control, MFB50 target values were set equal to the average value from the four cylinders obtained during EGR sweep tests with map-based control. Table 5.1 summarizes the main test conditions of the performed EGR sweep tests, where the SOI values in the case of the pressure-based control are the result output measured once the target MFB50 was set (notice that a 100% exhaust flap position corresponds to a full closure position).

Table 5.1. Test conditions for the EGR sweep tests under PCCI combustion mode.

Exhaust flap position	EGR rate	Map-based.	Pressure-based				
		SOI [°CA bTDC]	target MFB50 [°CA aTDC]	SOI [°CA bTDC]			
				Cyl. #1	Cyl. #2	Cyl. #3	Cyl. #4
94.5%	62.4%	23	0.1	23.5	23.2	23.1	21.6
95.0%	64.1%	23	1.8	23.7	23.2	23.1	21.2
95.2%	65.0%	23	3.2	23.8	23.1	23.0	20.9
95.3%	65.5%	23	4.3	23.6	22.8	22.7	20.5
95.4%	65.9%	23	5.1	23.5	22.6	22.6	20.3
95.45%	66.3%	23	6.6	23.9	22.7	22.6	20.3
95.5%	66.7%	unstable	7.5	23.4	22.3	22.2	19.9
95.6%	67.0%	unstable	7.5	27.4	25.1	25.1	22.3

Thanks to the PCCI combustion mode implemented, engine-out soot and NO_x emissions were very low in every test condition, while similar values of *bsfc*, CO and HC were obtained for both the tested controls, in analogy with the previous tests. In this case, both the CoV_{imep,eng} and CoV_{PPF,eng} values were lower for the pressure-based technique, with a lower CN dispersion among the cylinders. With reference to Figure 5.19(a) and Figure 5.19(b), small differences are obtained with the two controls for the lower-end of the considered working range (in terms of exhaust flap position), while significant reductions are obtained for the most throttled flap positions, i.e. in conditions which tend to make the combustion more unstable. Consequently, the pressure-based control allows to operate the engine with the flap in a more throttled position, i.e. with higher average EGR rates, reducing the penalties on combustion stability. This increases the chance of application of the PCCI combustion mode, possibly increasing the engine tolerance to transient cycle-to-cycle and cylinder-to-cylinder unbalance on the EGR rate.

Moreover, a significant reduction on the dispersion in the CN is observed, as depicted in Figure 5.19(c), which reports, for each test, the difference between the maximum and the minimum CN levels of the four cylinders.

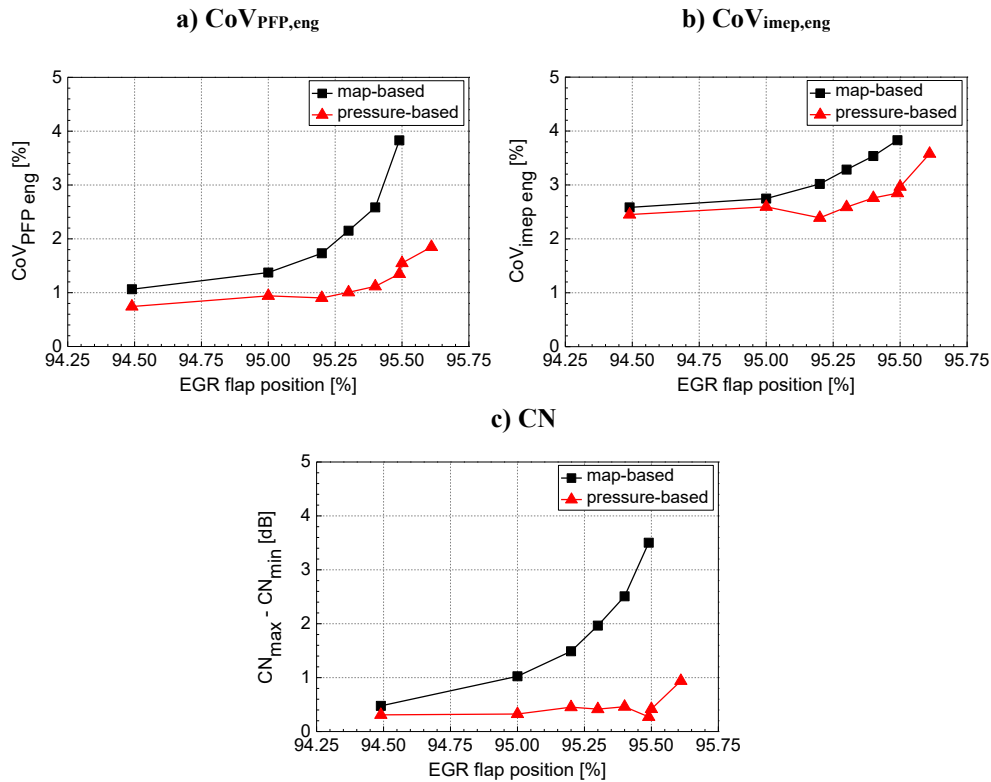


Figure 5.19. Coefficient of variation of the peak firing pressure $CoV_{PFP,eng}$ (a) and of the indicated mean effective pressure $CoV_{imep,eng}$ (b) evaluated for the whole engine, and amplitude of the dispersion range of the CN (c) on the EGR sweep tests under PCCI combustion mode: comparison between the map-based and the pressure-based controls.

Steady-state analysis: tests with different fuel blends

Blends of Jet A1 fuel and conventional diesel oil (according to EN 590 regulations), whose main properties are listed in Table 5.2, have been fed to the engine to evaluate the robustness of the real-time MFB50 controls and their possible benefits if compared to the baseline map-based approach. Engine map tests have been performed using a 50%/50% blend JetA1/diesel and a 100% JetA1 fuel, implementing the three different controls. In addition, a SOI/MFB50 sweep was performed at 1400×104 (rpm \times Nm), comparing the baseline map-based control with the pressure-based technique.

In terms of engine performance and emissions, these tests did not provide appreciable differences among the considered controls, but the different fuel compositions did introduce slight variations in MFB50, when the engine was run without real-time MFB50 controls. This means that injecting different fuels with a map-based calibration may bring to variations in the combustion process, which may affect the combustion stability, possibly exacerbated during transient operations. On the other hand, the MFB50 real-time controls, by keeping the MFB50 at a desired target value, would allow to maintain the same evolution of the

combustion process whichever are the boundary conditions, e.g. the fuel properties/composition.

Table 5.2. Main properties of Jet A1 and diesel EN590 fuels.

Property	Jet A1	Diesel EN590
Cetane Number [-]	-	53.1
Flash Point [°C]	55	70
Density at 15°C [kg/m ³]	797	844
Viscosity at 40°C [mm ² /s]	1241	2860
Lower Heating Value [MJ/kg]	43.3	43.4

Transient analysis

The transient analysis hereby reported is based on the results obtained on some engine load ramps (at two different engine speed levels, namely 1400 rpm and 2000 rpm), and on a WHTC type-approval cycle (cf. Figure 5.20).

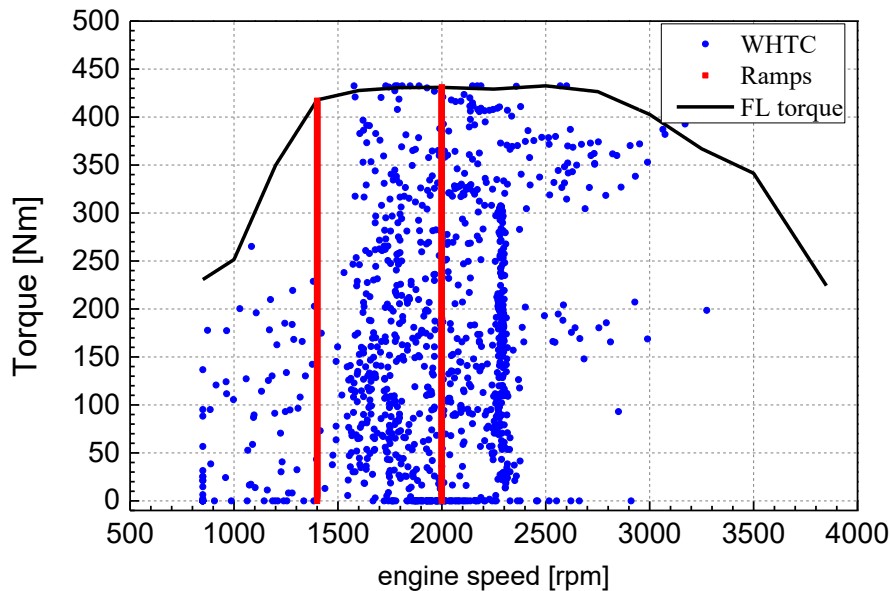


Figure 5.20. Engine operating points during the WHTC (blue markers) and the load ramps (red markers). The black solid line represents the full load curve.

As a preliminary analysis, some transient ramps varying only speed, only load and a combination of them (performed in 10 s variation time intervals) were tested to check their influence on SOI_{main} and MFB50. Then, the same ramps were also performed progressively reducing the variation time intervals, i.e. from 10 s to 5 s and 3 s. Since the MFB50 values did not change significantly with the engine speed (cf. Figure 5.21), the following steps of the analysis only selected the fastest load ramps, at the two different speed values previously reported. The slope of these load ramps was comparable with a fast transient cycle, as the WHTC is.

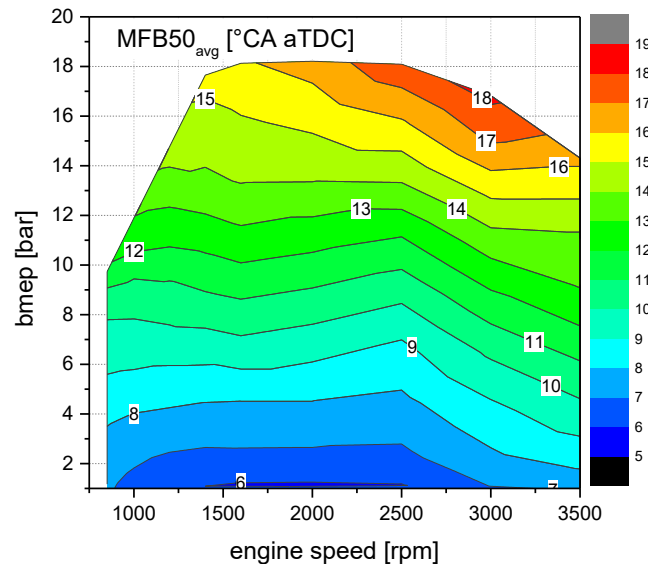


Figure 5.21. MFB50 values, averaged between the four cylinders, as a function of engine speed and $bmep$ on the engine map tests.

As previously stated, the baseline ECU map-based control sets the SOI_{main} through purposely calibrated look-up tables, function of engine speed and injected fuel per cycle. If a load-increasing transient maneuver is detected, a transient correction on SOI_{main} is applied, taking into account the actual p_{rail} and boost pressure values, with the aim to avoid excessive increase in smoke at the exhaust and too high in-cylinder PFP. Considering the performed transient tests, this correction also produces a significant reduction of NO_x . In order to provide a coherent comparison between the map-based control and the newly developed MFB50-based ones, this transient SOI_{main} correction on the original calibration was bypassed (by setting the SOI_{main} referring to the steady-state map by means of the RP device), because at the current development status the pressure-based and model-based controls did not perform any dynamic correction based on other engine variables (e.g. p_{rail} and boost pressure). Therefore, when the map-based calibration results will be shown in this Section, they will refer to the map-based calibration without any transient correction.

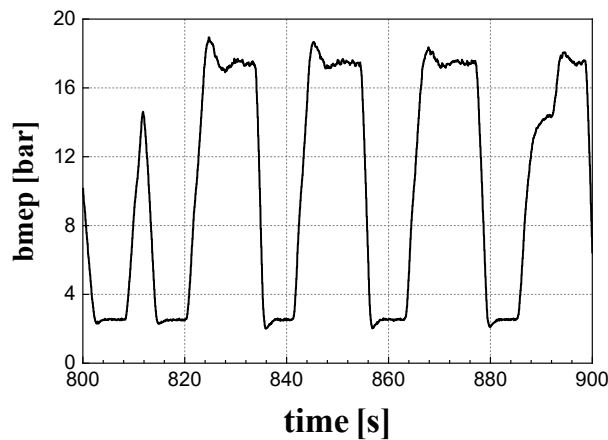


Figure 5.22. Portion of the reference load variation transient profile, at 1400 rpm.

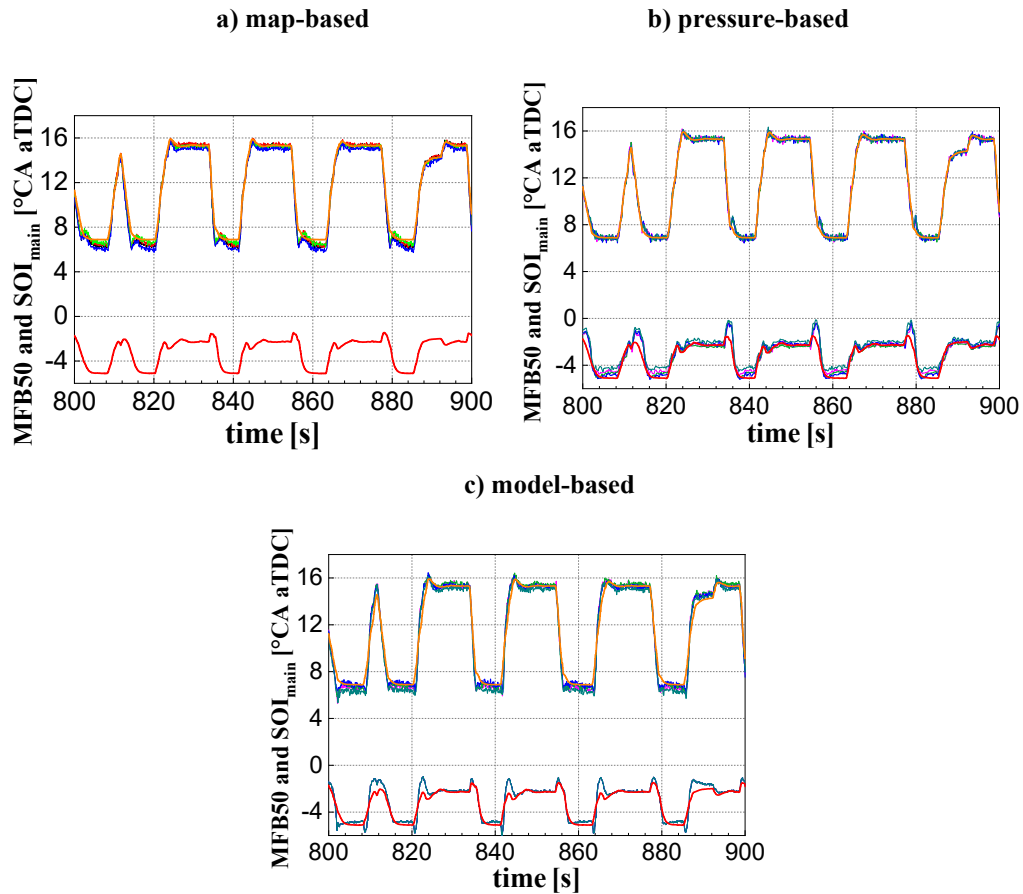


Figure 5.23. Transient load variation profile at 1400 rpm - MFB50 and SOI_{main} values: comparison between the map-based (a, without SOI correction), the pressure-based (b) and the model-based (c) controls.

A portion of the performed load ramp, at 1400 rpm, is depicted in Figure 5.22, while the corresponding SOI_{main} and MFB50 values during the tests are reported in Figure 5.23 for the map-based control (Figure 5.23(a)) the pressure-based control (Figure 5.23(b)) and the model-based control (Figure 5.23(c)). In all the graphs of Figure 5.23, the orange thick line (in the upper part of the graphs) represents the MFB50 target relative to the pressure-based control, whereas the thin colored lines close to it represent the actual MFB50 values for the different cylinders. The SOI_{main} (in the lower part of the graphs) indicated with the thick red line represents the SOI of the main injection evaluated interpolating the steady-state map. For the map-based control (Figure 5.23(a)), this corresponds to the SOI_{main} actuated in all the cylinders, while when the pressure-based control (Figure 5.23(b)) is applied, the actual cylinder-to-cylinder SOI_{main} varies with respect to the map-based one (as indicated by the different colored lines close to the thick red one) in order to match the MFB50 target. For the model-based control (Figure 5.23 (c)), the SOI_{main} , reported with a green thin line, is calculated (and implemented in all the cylinders) based on the estimated MFB50. It can be observed that the pressure-based model allows to limit the cylinder-to-cylinder dispersion of the MFB50 with respect to the target. However, unlike what has been highlighted from the steady-state tests, the MFB50 target is not perfectly matched in this case, due to the highly dynamic nature

of the transient operations. To further analyze this effect, Figure 5.24 shows the amplitude of the cylinder-to-cylinder variation of the MFB50 during the considered transient operations: with the pressure-based control, the MFB50 dispersion is less spread around a lower mean value, if compared to the conventional map-based control. Still concerning the MFB50, the model-based control showed a cylinder-to-cylinder variation bandwidth similar to the map-based control, mostly due to the absence of a cylinder-to-cylinder SOI_{main} control. Moreover, the SOI_{main} set during the test shows an undershoot behavior at the beginning of the load ramp and an overshoot after it (cf. Figure 5.23(c)), possibly due to uncertainties in the real-time estimation of the intake oxygen needed for the control model [Finesso, et al., 2017] during highly transient operations.

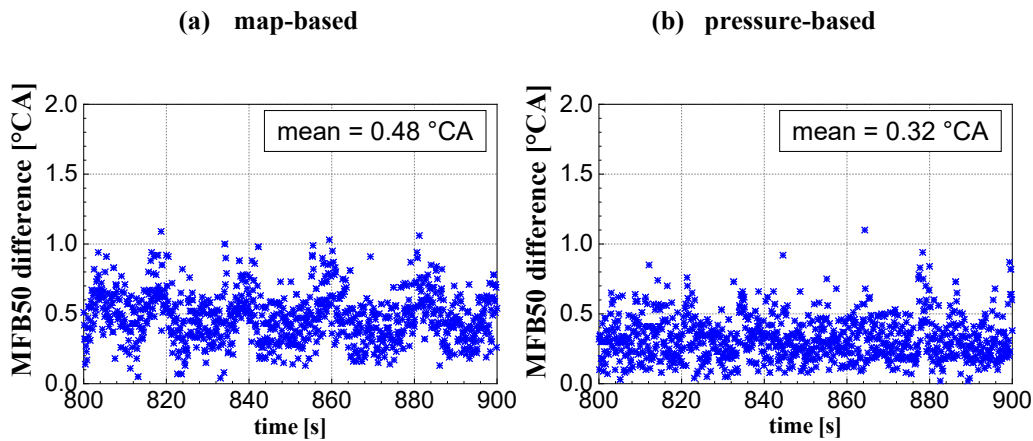


Figure 5.24. Amplitude of the variation range of the MFB50 and related mean MFB50 variations during transient operations: comparison between the map-based (a, without SOI correction) and the pressure-based (b) controls.

As regards the WHTC cycle tests, the complete type-approval cycle was performed once per each of the considered controls. The results showed that the values of fuel consumption were virtually unaffected by the considered control, while possible variations in terms of engine-out HC were difficult to be estimated as their value was quite low (around 0.5 g per WHTC cycle). Values of CO showed some dispersion among different repetitions, however pressure-based and model-based controls showed lower values up to 6% with respect to the map-based control. As far as NO_x are concerned, the pressure-based control generally showed an improvement around 1.5% with respect to the map-based one, whereas a not completely definite trend was found for the model-based control. All of these pollutant emission results were evaluated averaging each cumulated emission value along several repetitions of the considered maneuver.

In general, these results confirm that the proposed MFB50 real-time controls are always comparable to the standard map-based one in terms of fuel consumption and exhaust pollutant emissions, without producing any detrimental effect when operating the engine under CDC combustion mode. Moreover, in some cases, some minor positive effects have been shown. This encourages the research in this field towards the application of this methodology to transient operation in PCCI combustion mode, where larger benefits are expected due to the significant improvements achievable on combustion stability. Furthermore, the pressure-based

control technique could give the possibility to reduce the time needed for engine calibration and to improve the combustion quality with engine ageing, thanks to its ability to auto-compensate for time drifts or for other random or systematic variations in the boundary conditions with respect to reference calibrated ones: therefore, it could be considered of interest for CDC combustion modes as well.

Chapter 6

6 Preliminary assessment of a dual-mode operation strategy

6.1 Dual-mode operation strategy

Although the benefits of simultaneous reduction of NO_x and soot emissions given by early PCCI strategies would be desired across the whole engine map, this type of combustion features a limited practicable operating range, as thoroughly proved in the previous Sections, being expected to replace the CDC only at low-to-medium loads. In fact, as load increases, the heat release rate grows excessively (due to lack of dilution), resulting basically in a noisier than desired combustion and approaching operating and structural constraints such as the maximum in-cylinder pressure derivatives (linked to CN) and the PFP values.

When the load increases beyond the limits of the early PCCI strategies, a late PCCI concept may become more advantageous. CN dampens more within an acceptable range, owing to the late injection timings, while emissions may be lowered. However, even in this case, an upper operating limit is present, dictated again by CN, knocking, and particulate emissions becoming excessive [Ickes, et al., 2009]. When this occurs, a transition to CDC strategies for high load operation is needed. In this way, a dual-mode combustion system, which combines PCCI concepts up to medium loads and then switches to CDC up to full load operation, would be adopted.

The major hurdle of such a dual-mode combustion system would be the complexity (and the related costs) associated with the development of a suitable engine control, which could adjust the engine operating combustion mode based on the prevailing engine operating conditions and manage the transition from PCCI to CDC (and vice-versa) whenever required [Agarwal, et al., 2017]. Nevertheless, it has been pointed out how CR is one of the most influential parameters on the premixed charge and, as a consequence, on combustion characteristics of PCCI in the diesel engines. In particular, a dual-mode combustion engine featuring a too low CR value would allow a long ID period and, therefore, high air-fuel premixing levels, but it would be problematic as far as cold engine startability and engine efficiency at high load (in CDC mode) are dealt with. On the other hand, a too high CR value would give minor problems during engine cold starts and high load CDC operations, but would limit the air-fuel premixing levels and the EGR tolerance, thus reducing the possible benefits of PCCI combustion at milder loads [Beatrice, et al., 2008]. Therefore, in order to optimize a dual-mode combustion system, the

CR should be chosen carefully or, more conveniently, the realization of a variable compression ratio engine could be considered. Several variable compression ratio solutions, featuring either a continuous or a two-stage CR variation technology, have been investigated in literature [Takalkar & Khan, 2017], each with pros and cons. A continuously variable CR would allow more flexibility towards the engine combustion optimization, while a two-stage CR variation system would guarantee less impact on the engine design as well as on the production process. An example (and further details) of two-stage variable compression ratio solution with eccentric piston pin can be found in [Wittek, et al., 2009]. Other works, such as [Nevin, et al., 2007], have also shown the potentiality of VVT technology as a mean to achieve lower CR during PCCI operations, through LIVC without fuel penalties (cf. the Introduction Section). In fact, by delaying the intake valve closure, the effective compression stroke of the engine and, consequently, the compression work made by the piston, can be reduced. Therefore, VVT may be a viable alternative to VCR systems, allowing also the possibility of different effective CR values in different areas of the engine map.

6.2 Preliminary assessment of the performance of a simulated dual-mode operation engine along NEDC and WHTC cycles

The aim of this Section is to perform a preliminary assessment of the performance of a simulated dual-mode operation engine when operated to fulfil driving mission profiles, and to compare it with what achievable by the reference F1C Euro VI engine, in terms of fuel consumption, exhaust pollutant emissions and urea consumption (as the reference engine/vehicle is endowed with the SCR system for the reduction of NO_x emissions).

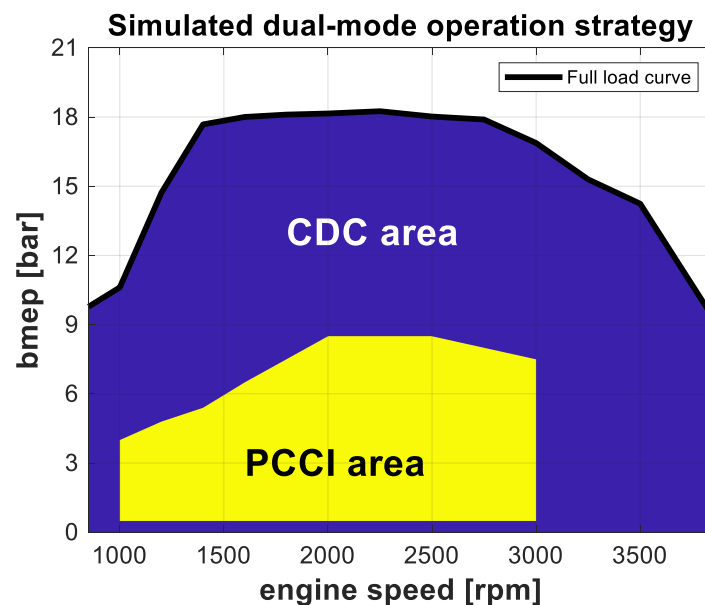


Figure 6.1. Combination of CDC and PCCI calibration for the simulation of a dual-mode operation strategy.

A complete engine map calibration was not available for the F1C PCCI engine, which was only calibrated in the area of interest for early PCCI combustion, as discussed in Chapter 3, and a dedicated CDC calibration was not performed in the rest of the engine map. Moreover, no suitable engine control was developed to manage the transition from PCCI to CDC (and vice-versa) whenever required by the engine operating conditions. Since “real” transient operations were not possible with the F1C PCCI engine, a dual-mode operation engine (i.e. an engine calibrated with a PCCI/CDC “hybrid” combustion mode) was simulated with the following assumptions:

- within the area calibrated on the F1C PCCI engine (cf. yellow area in Figure 6.1), the simulated engine runs under PCCI combustion mode, and its performance is reproduced from the fuel consumption and exhaust pollutant emissions measured on the F1C PCCI engine;
- outside the PCCI area (cf. purple area in Figure 6.1), the simulated engine runs under CDC combustion mode, and its performance is reproduced from the fuel consumption, urea consumption and exhaust pollutant emissions measured on the baseline F1C Euro VI engine;
- transition from PCCI to CDC combustion modes (and vice-versa) are considered instantaneous;
- engine response during transients is simulated by interpolating steady-state maps.

It is worth highlighting how this “ideal” combination of PCCI and CDC combustion modes is retrieved from two engines with different hardware specifications (cf. Table 3.1), including different CR values and turbo-group size. Therefore, it should not be rigorous to consider a simulated dual-mode operation engine able to perform similarly to both the F1C PCCI within the PCCI area and to the F1C Euro VI in the rest of the engine map. Nevertheless, starting from the design of the F1C PCCI engine and hypothesizing the implementation of technical solutions such as the previously mentioned VCR [Wittek, et al., 2009] or VVT [Nevin, et al., 2007] systems, as well as a two-stage turbocharging, with a larger low-pressure turbo-group in series with a smaller high-pressure one, this latter endowed with by-pass valves [Buchwald, et al., 2006], good performance may be expected in both the PCCI and CDC areas. Under the hypothesis that, in such a “fully-upgraded” PCCI engine, it would be possible to obtain a calibration giving performance similar to those of the F1C Euro VI engine, within the CDC area, and similar to the F1C PCCI, within the PCCI area, the differences between the two hardware configurations of the engines are considered virtually not affecting the current analysis. Although this assumption, along with that of instantaneous transition from PCCI to CDC combustion modes, are not rigorous and not validated by experimental evidence, they allow to perform this preliminary assessment and to provide a first feedback on the potentialities of a dual-mode operation diesel engine along driving mission profiles.

Another source of simplification stems from the simulation of the engine response during transients by means of interpolation of measurement outputs from steady-state (and warmed-up) points carried out during the experimental campaign, thus neglecting real effects the engine could undergo during transient operations, including the engine warm-up and its effects on the after-treatment devices. For each time instant along the driving cycles, the engine working point is estimated in terms of engine speed and load. Then, fuel consumption, urea consumption and exhaust pollutant emission maps are interpolated to get the instantaneous results. For this purpose, the following engine configurations have been considered for comparison:

- reference CDC engine: baseline CDC calibration on the F1C Euro VI engine, tested across the whole (steady-state) engine map;
- simulated PCCI/CDC “hybrid” combustion mode engine (referred to as “simulated PCCI engine” in the following): baseline CDC calibration on the F1C Euro VI engine (the same as the previous point), replaced by either a single- or a multiple-injection PCCI calibration within the area where PCCI was calibrated on the F1C PCCI engine.

The CDC calibration of the reference F1C Euro VI engine, as previously stated, is compliant with the Euro VI Heavy-Duty standards. Nonetheless, the F1C engines are also available, from the OEM, for light-commercial vehicles applications, compliant with the Euro 5 Light-Duty standards. Therefore, World Harmonized Transient Cycle (WHTC) and the New European Driving Cycle (NEDC) type-approval profiles were selected as reference driving mission profiles.

The WHTC, included in the Euro VI type-approval procedures, is a transient test of 1800 s duration, with several motoring segments. It requires the engine to be tested rather than the whole vehicle and, consequently, it directly consists of a second-by-second sequence of normalized engine speed and torque values, which shall be converted (i.e., “denormalized”) to the actual values for the engine under test based on some engine-mapping curve characteristics (for instance idle speed, speed where maximum torque is obtained, maximum torque, etc.). The actual engine speed and torque values over the WHTC cycle are schematically shown below, in Figure 6.2.

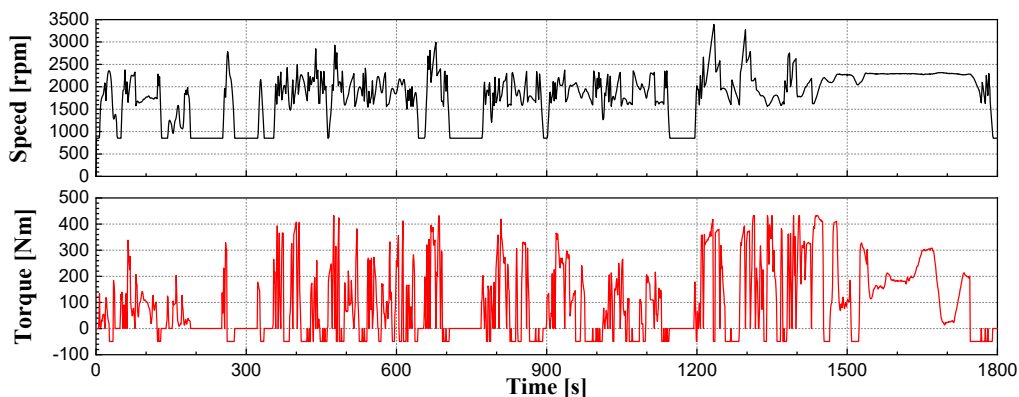


Figure 6.2. Engine speed and torque sequence over the WHTC cycle.

The NEDC, conversely, was the chassis dynamometer test used for emission testing and certification in Europe, until September 2017 (i.e., also for Euro 5 type-approval). It was used to test the whole vehicle rather than the engine, for passenger cars and Light-Duty vehicles (vehicle classes M1, M2, N1 and N2 up to a reference mass of 2,610 kg), thus being defined as a second-by-second sequence of vehicle speed (in km/h) and engaged gear, as shown in Figure 6.3.

Table 6.1. Main technical specifications of the reference light-duty commercial vehicle.

Total vehicle curb mass	2271 kg	
Axles	1 steering, 2 wheels/axle 1 drive, 2 wheels/axle	
Gearbox	Gear	Ratio ($\tau_{g,i}$) Efficiency ($\eta_{g,i}$)
	I	5.375 0.965
	II	3.154 0.965
	III	2.041 0.965
	IV	1.365 0.965
	V	1 0.965
Final drive	Ratio (τ_{fd})	Efficiency (η_{fd})
	2.917	0.98
Engine displacement - iV_e	2.998 dm ³	
Engine inertia - J_e	0.36 kg·m ²	
Wheel inertia (single) - J_w	2.255 kg·m ²	
Rolling radius - R_{roll}	0.34 m	
Vehicle curb mass - m	2271 kg	
Coast-down coefficients	$F_0 = 108.98$ N	
	$F_1 = 4.4311$ N/(km/h)	
	$F_2 = 0.0589$ N/(km/h) ²	

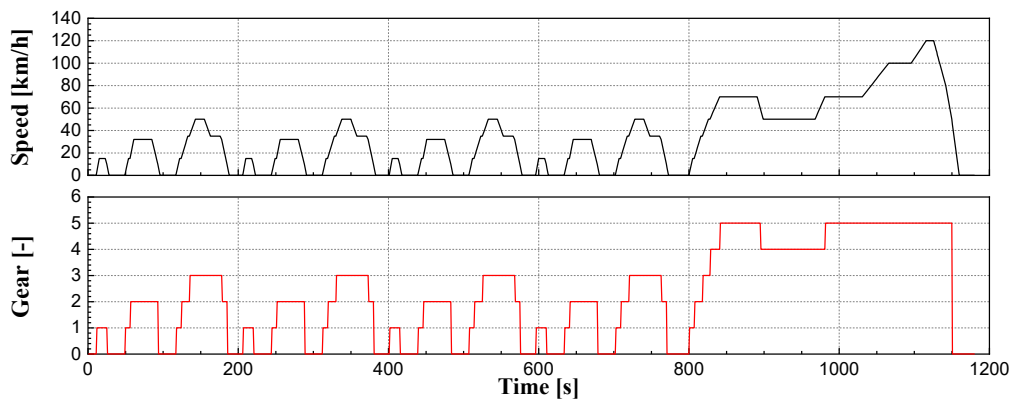


Figure 6.3. Vehicle speed and gear sequence over the NEDC cycle.

To translate these data into a sequence of engine speed and torque values, the whole vehicle characteristics have to be taken into account (cf. Table 6.1) and properly modeled. First of all, considering a model with a kinematic approach in which the vehicle is exactly realizing the cycle profile, engine speed $n(t)$ at any time instant t can be calculated as follows:

$$n(t) = \frac{v(t)}{2\pi R_{roll}} \cdot \tau_{g,i}(t) \cdot \tau_{fd} \quad (17)$$

where $v(t)$ is the instantaneous vehicle speed at time t (cf. the speed sequence displayed in Figure 6.3), R_{roll} is the wheel rolling radius, $\tau_{g,i}(t)$ is the gear ratio of the i^{th} gear engaged at time t and τ_{fd} is the final drive ratio. Then, to compute the engine torque $T(t)$, the engine power $P_e(t)$ has to be calculated first. This can be estimated considering the resistant forces that oppose to the vehicle motion and the power required to accelerate the vehicle:

$$\eta_{g,i}(t) \cdot P_e(t) = F_{res}(t) \cdot v(t) + m_{eq}(t) \frac{d}{dt}(v(t)) \cdot v(t) \quad (18)$$

where $\eta_{g,i}(t)$ is the gear efficiency of the i^{th} gear engaged at time t , $F_{res}(t)$ stands for the total resistant forces opposing to the vehicle motion and $m_{eq}(t)$ is the equivalent (apparent) mass of the vehicle. In particular, $F_{res}(t)$ is calculated from the coast-down coefficients F_0 , F_1 and F_2 (experimentally measured during deceleration tests with the gearbox in the neutral position and the clutch engaged, without using the brakes) as follows:

$$F_{res}(t) = F_0 + F_1 \cdot v(t) + F_2 \cdot v^2(t) \quad (19)$$

Therefore, the coast-down coefficients already take into account power dissipation downstream of the gearbox and $\eta_{f,d}$ (efficiency of the final drive) is not considered in the first term of Eq. (18). Moreover, $m_{eq}(t)$ is defined as an equivalent mass moving at the same speed of the vehicle and having the same kinetic energy:

$$\frac{1}{2} m_{eq}(t) \cdot v^2(t) = \frac{1}{2} m \cdot v^2(t) + \frac{1}{2} \sum_k J_k \cdot \omega_k^2(t) \quad (20)$$

where m is the standard vehicle mass (curb mass of the vehicle + 100 kg) and J_k is the inertia of the k^{th} rotating (at the speed $\omega_k(t)$) part, including the engine and the wheels. However, the NEDC procedure (for the homologation of different vehicles) would require the roller test bench to be equipped with a set of several flywheels of different masses (each corresponding to a particular range of reference mass of the vehicle) to simulate the resistant force to motion, neglecting the contribution of the rotating masses. Therefore, the term $\frac{1}{2} m_{eq} \cdot v^2(t)$ in Eq. (20) would have to be replaced by the kinetic energy related to the inertia of the flywheel mounted at the roller test bench and corresponding to the range of the standard mass of the considered vehicle, whose curb mass is defined in Table 6.1. However, Eq. (20) has been used as it is, since the presented approach is not intended to give exact calculations of the homologation procedure.

Finally, the engine torque $Trq(t)$ is calculated as:

$$Trq(t) = \frac{P_e(t)}{n(t)} \quad (21)$$

The engine speed and torque values over the NEDC cycle, resulting from the abovementioned calculation procedure, are schematically shown below, in Figure 6.4.

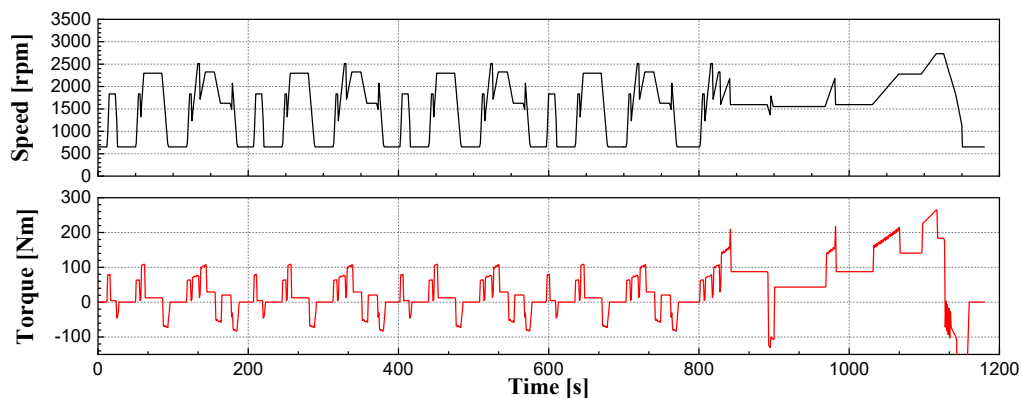


Figure 6.4. Engine speed and torque sequence over the NEDC cycle.

In the following, the comparative results of the performance of both the reference F1C Euro VI and the simulated PCCI engine, running with either a single- or a multiple-injection PCCI calibration in the PCCI area, are presented along the NEDC and the WHTC driving mission profiles.

From Figure 6.5 on, adimensional quantities for pollutant emissions, fuel and urea consumptions will be reported. In particular, they will be normalized by the final cumulated value achieved at the end of the respective simulated cycles with the CDC calibration.

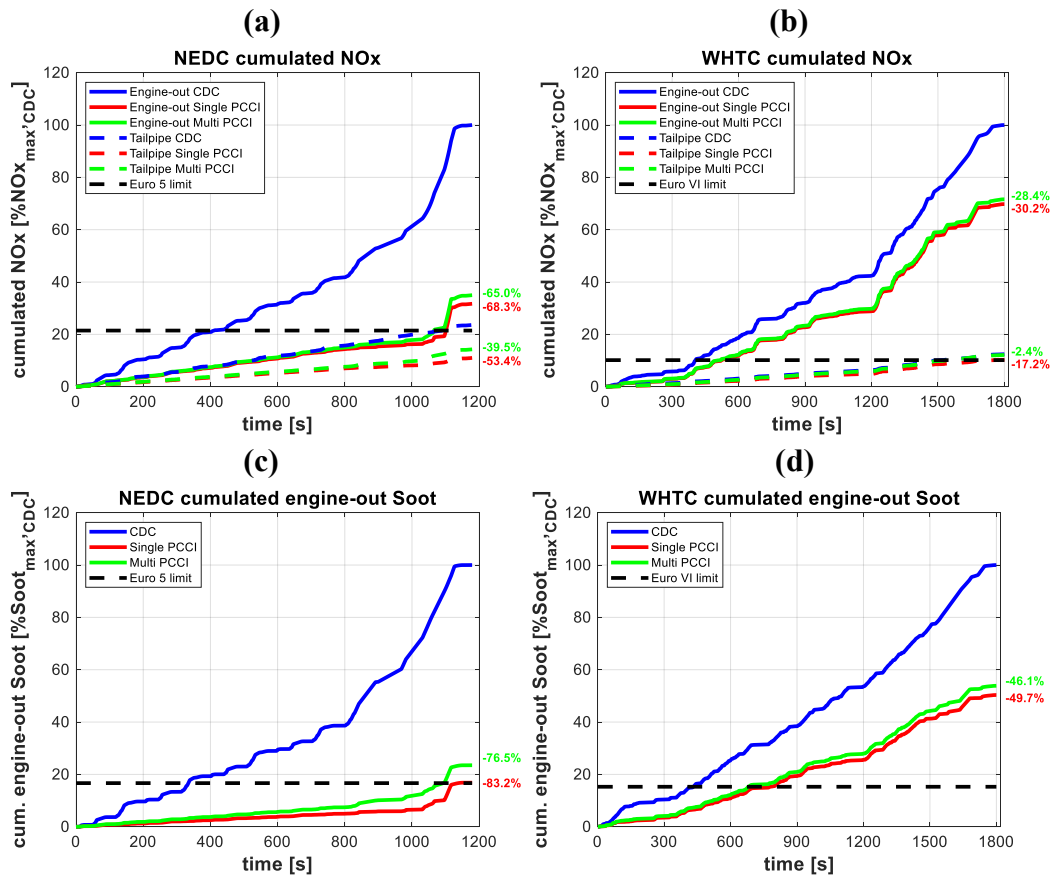


Figure 6.5. Cumulated NO_x (a and b) and Soot (c and d) emissions over the simulated NEDC (a and c) and WHTC (b and d) cycles, with CDC (blue lines), single-injection PCCI (red lines) and multiple-injection PCCI (green lines). The black dashed horizontal lines represent reference Euro 5/Euro VI limits.

Figure 6.5 shows the cumulated trends of NO_x and soot emissions over the simulated NEDC (Figure 6.5(a) and Figure 6.5(c)) and WHTC (Figure 6.5(b) and Figure 6.5(d)) cycles, in function of time t . The solid monotonically rising lines represent engine-out emissions while the dashed ones stand for tailpipe levels. The blue color corresponds to the CDC calibration running on the conventional FIC Euro VI, the red color to the dual mode operation strategy, made by single-injection PCCI and CDC, running on the simulated PCCI engine, while the green color to the dual mode operation strategy, made by multiple-injection PCCI and CDC, running again on the simulated PCCI engine. The black dashed horizontal line gives a reference of either the Euro 5 or the Euro VI emission limits, respectively for NEDC or WHTC cycles. It is worth to underline that Euro 5/Euro VI limits are reported only for reference, either in Figure 6.5 or in all of the following Figures. None of these simulations, with all the simplification hypotheses previously clarified, are intended to be representative of a homologation procedure. Therefore, although in some of the graphs Euro 5/Euro VI limits may be overcome, it has to be considered that all the simulations here discussed are based on interpolation of steady-state tests performed on a warmed-up engine and, for instance, no thermal or transient behaviors may be taken into account.

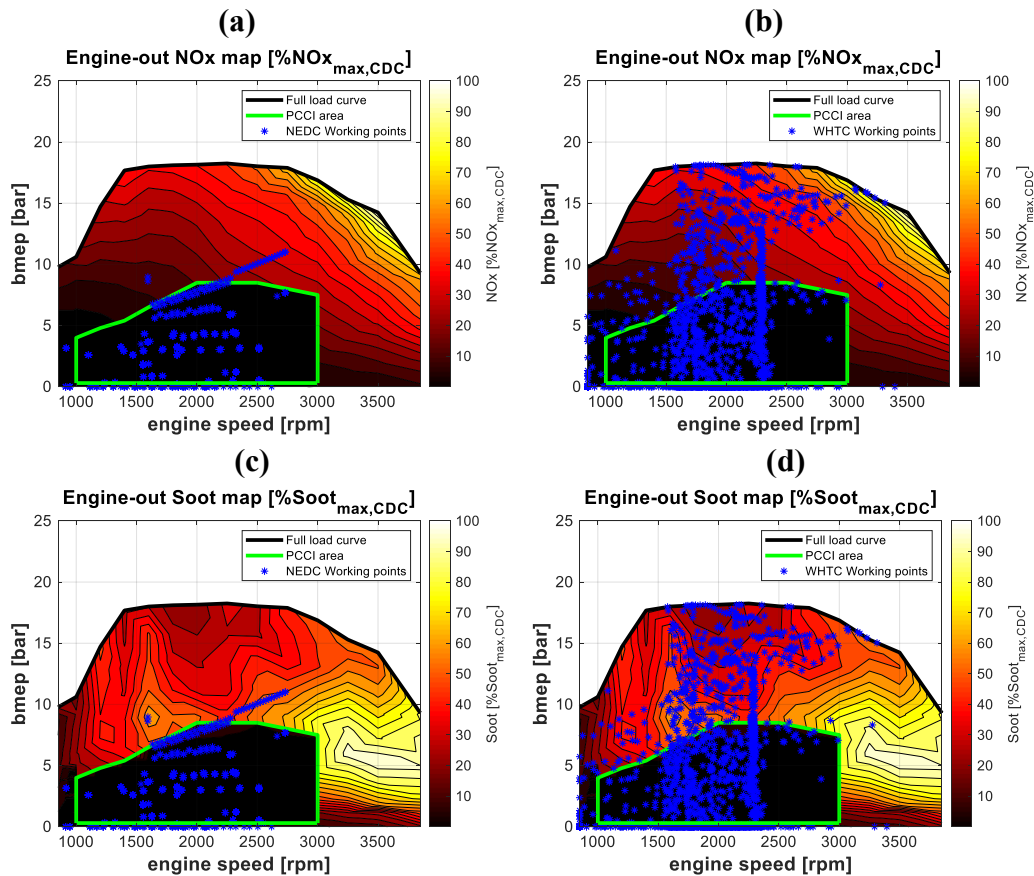


Figure 6.6. Engine-out NO_x (a and b) and Soot (c and d) maps for the simulated PCCI engine. The second-by-second engine operating points over the simulated NEDC (a and c) and WHTC (b and d) cycles are overlapped as blue stars.

Figure 6.6 show a visualization of the engine-out NO_x and soot maps for the simulated PCCI engine, running with the combination of single-injection PCCI and CDC, as well as of the engine operating points (blue stars) relative to the simulated NEDC (Figure 6.6(a) and Figure 6.6(c)) and WHTC (Figure 6.6(b) and Figure 6.6(d)) cycles. This can quickly point out how the WHTC cycle exploits the engine for a relevant part of the time in the medium-high load region, where CDC must be used, while almost the whole NEDC cycle (but its very last part) makes the engine be run within the PCCI area.

Engine-out soot emissions decrease of more than 80% (compared to what achievable with the CDC) with the application of the single-injection PCCI combustion over the NEDC cycle (cf. Figure 6.5(c)), while a slightly lower reduction (of up to 76%) is achievable if multiple-injection PCCI strategies are implemented. This reduction is obtained thanks to the ultra-low soot within the PCCI area (cf. Figure 6.6(c)) and due to the majority of the NEDC cycle requiring engine operating points inside this area: virtually, at the end of the NEDC cycle, engine-out soot emissions with the single-injection PCCI match the Euro 5 limit, which is supposed to consider the presence of a DPF. Anyway, in this analysis, soot was only measured at the engine-out position, as no DPF was installed during the experimental testbed campaign, nor with the Euro VI nor with the PCCI versions of the F1C engine. When switching to the WHTC cycle, the engine-out soot reduction achievable with PCCI strategies keeps being meaningful, but shrinks,

with single-injection PCCI able to achieve a reduction of slightly under 50%, and multiple-injection PCCI of about 45%. In both the cases, the need of a DPF (due to the need to switch to CDC mode, whenever higher loads are required) seems to be unavoidable, as the Euro VI limit is far from being met, just considering engine-out performance. Therefore, the introduction of PCCI strategies should be intended as able to considerably decrease the need of DPF regeneration, rather than to avoid its installation, also taking into account that a limit on the number of particles is present in the Euro 6/Euro VI regulations.

As far as NO_x emissions are concerned (cf. Figure 6.5(a) and Figure 6.5(b)), the application of either single- or multiple-injection PCCI modes allows to reduce significantly engine-out NO_x emissions along both the NEDC and the WHTC cycles, if compared to CDC levels. Again, this reduction is much more evident along the NEDC (up to about -65%, against about -30% along the WHTC) and slightly higher when the single-injection PCCI calibration is implemented. Conversely, if tailpipe NO_x (dashed lines in Figure 6.5(a) and Figure 6.5(b)) are dealt with, a preliminary consideration has to be mentioned. Since no SCR was installed during the experimental testbed campaign, nor with the Euro VI nor with the PCCI versions of the F1C engine, in order to point out a comparison on NO_x tailpipe emissions, the set of exhaust emission maps, available for the F1C Euro VI engine from the experimental campaign and used to create the interpolation along the driving mission profiles, was expanded with some results coming from steady-state tests performed by FPT Industrial in their research center in Arbon (Switzerland). These results, indeed, provided measurements about tailpipe NO_x and urea consumption, since this testbed installation included an SCR for NO_x reduction, not available at Politecnico. Therefore, the tailpipe NO_x dashed lines in Figure 6.5(a) and Figure 6.5(b) are obtained interpolating this additional set of data for the CDC case (blue dashed line), while for both the single- and multiple-injection PCCI cases (red and green dashed lines), the interpolation is made on this NO_x tailpipe CDC data (outside the PCCI area) and on the NO_x engine-out PCCI data (inside the PCCI area), basically hypothesizing that the urea consumption of the SCR is null whenever the engine runs inside the PCCI area (cf. Figure 6.7).

As a result, along both the NEDC and the WHTC cycles, tailpipe NO_x emissions are reduced by the introduction of PCCI, meaning that inside the PCCI area engine-out NO_x are even lower than tailpipe NO_x achieved by a CDC calibration and an SCR after-treatment system. This reduction varies from the -53%, resulting from the application of a single-injection PCCI calibration along the NEDC, to the tiny -2.4% achievable by multiple-injection PCCI along the WHTC. As a reference, the 53% reduction over the NEDC settles well below the Euro 5 limit, while the 2.4% reduction over the WHTC settles slightly above the Euro VI limit. Also in this case, it is reasonable that the introduction of a PCCI calibration may not be able to avoid an after-treatment management of NO_x emissions, but may substantially contribute to urea economy, if SCR applications are considered. In particular, the estimated urea consumption reduction (cf. Figure 6.8) over the NEDC cycle is around -73% (no difference is made between single- and multiple-injection PCCI, in this case), while this reduction shrinks till around -37% when the WHTC cycle is dealt with,

due to the frequency of high-load requests and, therefore, to the expected more frequent switches to CDC.

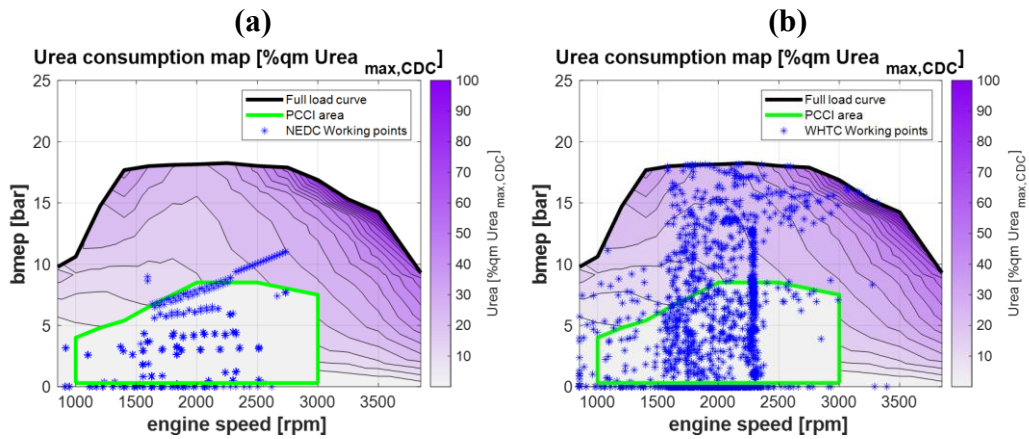


Figure 6.7. Urea consumption maps for the simulated PCCI engine. The second-by-second engine operating points over the simulated NEDC (a) and WHTC (b) cycles are overlapped as blue stars. Urea consumption inside the PCCI area is null.

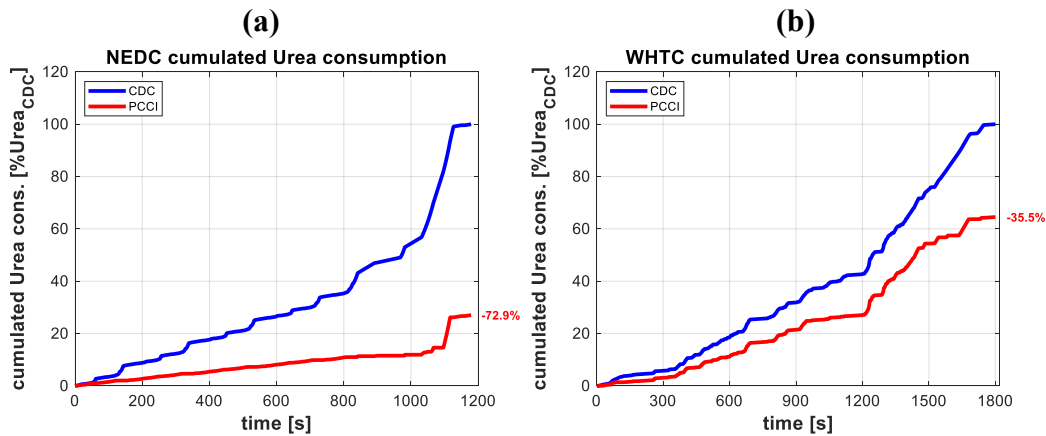


Figure 6.8. Cumulated urea consumption over the simulated NEDC (a) and WHTC (b) cycles, with CDC (blue lines) and single-injection PCCI (red lines).

With reference to Figure 6.9, which show CO and HC emissions along the simulated NEDC and WHTC cycles, the abrupt increase of these incomplete combustion species, already highlighted for steady-state applications in the previous Chapters, is confirmed. Both engine-out CO and HC emissions with single-injection PCCI reach values well beyond the CDC engine-out levels (more than +800% for CO and +340% for HC along the NEDC). The multiple-injection PCCI calibration can give slightly better results from this point of view, but CDC engine-out levels keep inaccessible (more than +700% for CO and +260% for HC, along the NEDC). The fact the WHTC cycle requires, for a longer time (cf. Figure 6.10), the switch to CDC mode, which generates less incomplete combustion species, produces lower penalties on the final cumulated values of engine-out CO and HC, but again way too larger than CDC values, which may result to be even below the Euro 5/Euro VI limits in some cases, without taking into account the DOC activity.

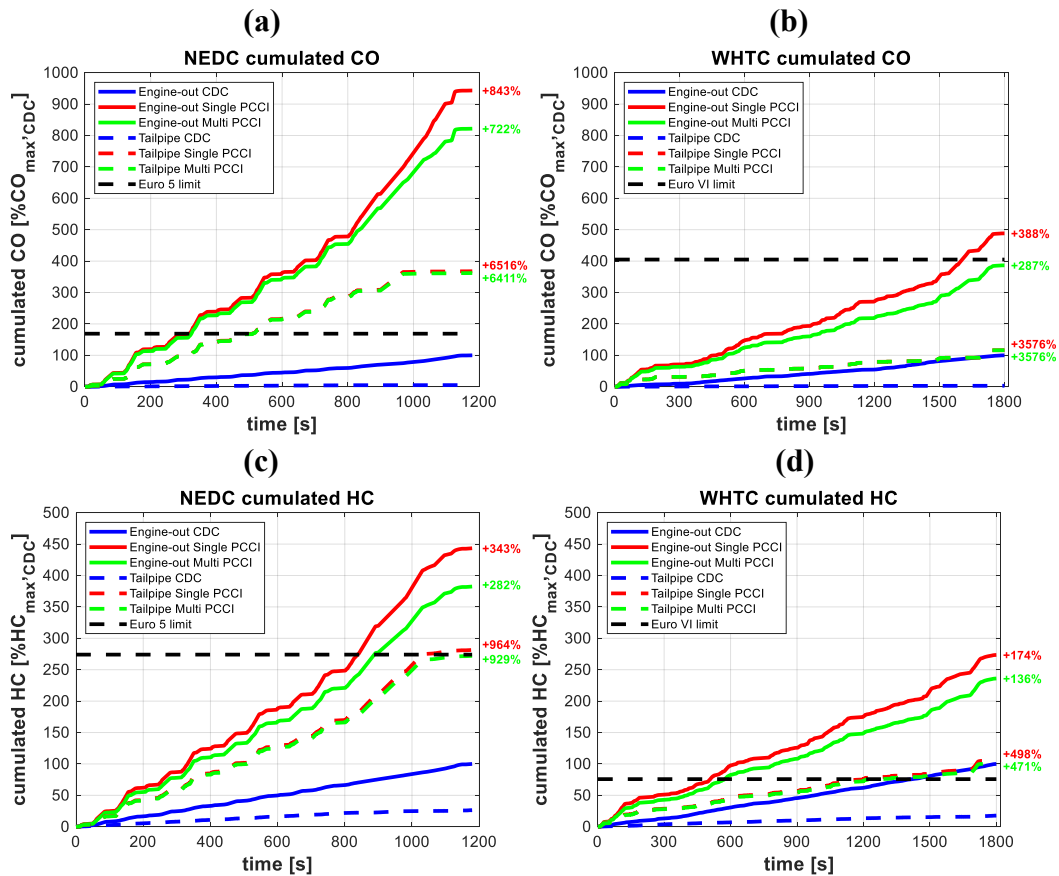


Figure 6.9. Cumulated CO (a and b) and HC (c and d) emissions over the simulated NEDC (a and c) and WHTC (b and d) cycles, with CDC (blue lines), single-injection PCCI (red lines) and multiple-injection PCCI (green lines). The black dashed horizontal lines represent reference Euro 5/Euro VI limits.

Tailpipe HC and CO emissions are cut almost to zero when the CDC calibration is dealt with (cf. Figure 6.9), while the presence of the DOC results to be crucial in the case of PCCI. Most of the engine-out emissions of CO and HC can be treated effectively by the DOC activity, and therefore also in the PCCI case tailpipe emissions significantly drop with respect to the engine-out ones. Nevertheless, a non-negligible amount of cumulated tailpipe incomplete combustion species is detected for the simulated PCCI engine, along both the considered cycles. Tailpipe CO emissions are well above the Euro 5 limit (around +100%) when the NEDC cycle is considered, while they keep well below the Euro VI limit when the WHTC is dealt with. Tailpipe HC emissions are, conversely, in line or slightly above the Euro 5/Euro VI limits (notice that Euro 5 limit is actually an HC+NO_x limit), along both the considered cycles. Negligible benefits derive from the implementation of multiple-injection PCCI strategies.

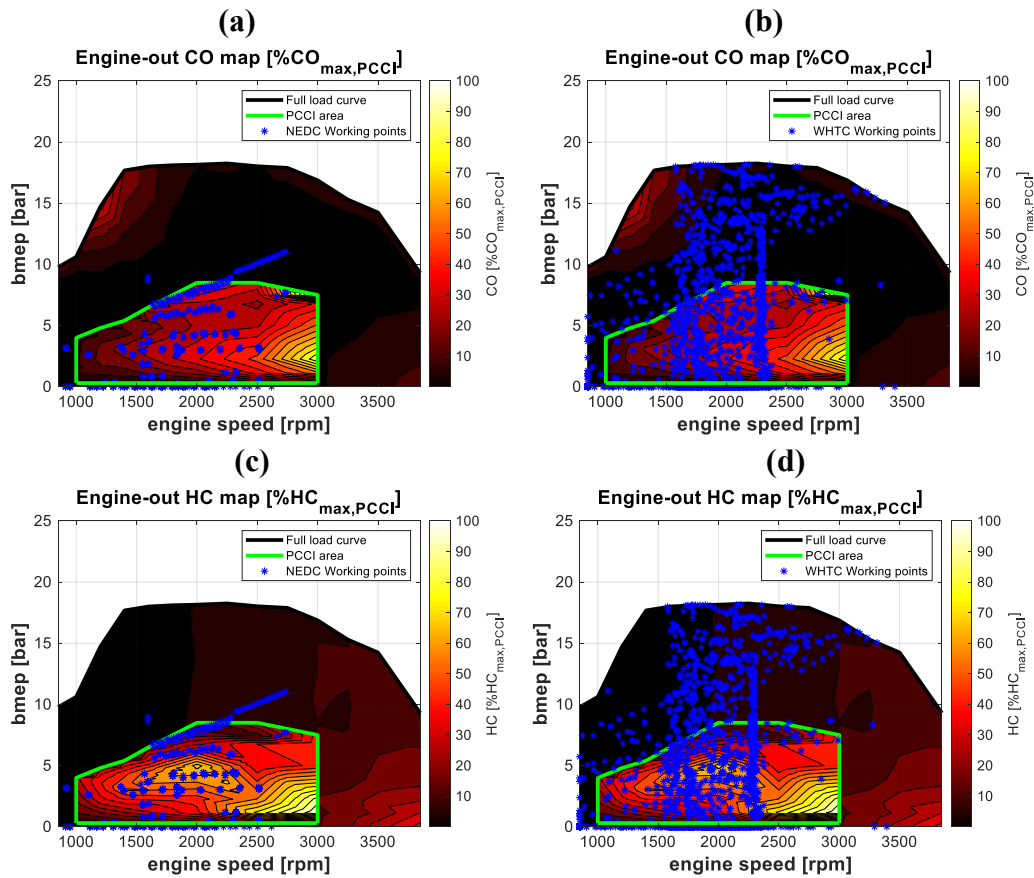


Figure 6.10. Engine-out CO (a and b) and HC (c and d) maps for the simulated PCCI engine. The second-by-second engine operating points over the simulated NEDC (a and c) and WHTC (b and d) cycles are overlapped as blue stars.

As can be seen in Figure 6.11, while tailpipe CO and HC are almost cut to zero nearly everywhere outside the PCCI area, a wide portion of the lowest-load PCCI area shows non-negligible values. This is due to the low exhaust gas temperature featured by the engine, when operated with early PCCI strategies at the lowest loads, as pointed out in Section 3.4. This causes insufficient thermal energy to keep the DOC at a temperature high enough to properly oxidize HC and CO molecules. At this regard, as previously clarified, the approach of interpolating the results of steady-state (and warmed-up) engine points leads to the impossibility of properly characterize the thermal issues during cold-starts, likely underestimating the cumulated tailpipe HC and CO emissions in the first part of the considered cycles. On the other hand, it is equally likely that, after the initial heat-up period, once the DOC has overcome its light-off temperature, a certain thermal inertia would prevent its instantaneous cool-down when very low load engine points are run. Consequently, especially along a WHTC (which features several working portions close to full load, i.e. with high exhaust gas temperature), it is likely that the after-treatment line temperature may keep constantly beyond the catalysts light-off temperatures once it has been overcome, allowing the DOC (and similar considerations could be made also for the SCR) to work properly till the end of the cycle [Verbeek, et al., 2008]. This means that flatter tailpipe curves may be expected in the second part of the cycles, especially for the WHTC (cf. Figure 6.9).

(a)

(b)

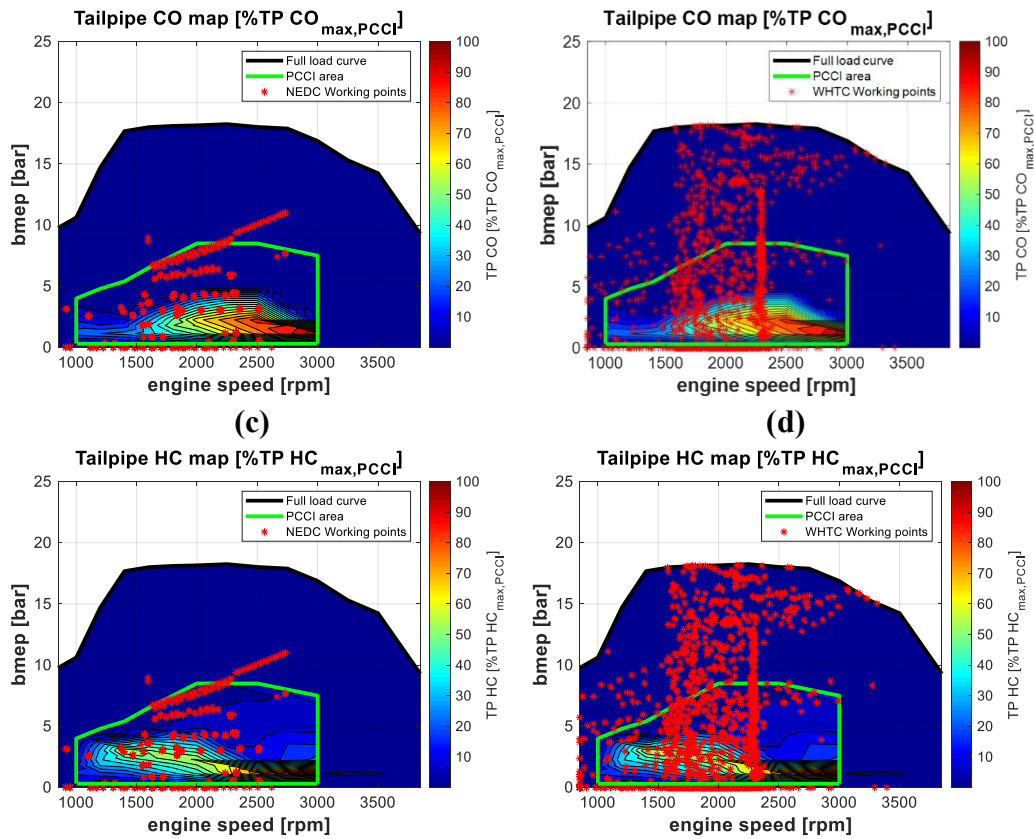


Figure 6.11. Tailpipe CO (a and b) and HC (c and d) maps for the simulated PCCI engine. The second-by-second engine operating points over the simulated NEDC (a and c) and WHTC (b and d) cycles are overlapped as red stars.

Nevertheless, even with the aforementioned inaccuracy, the topics highlighted in the present Section have further remarked as the one of the biggest limits for the implementation of PCCI combustion modes is the considerable rise of tailpipe HC and CO emissions with respect to CDC case. Therefore, one of the main key-points towards an extensive implementation of this kind of combustion (and in general of all the classes of LTC modes) on road engines is to find proper solutions for their treatment. As an example of possible solutions to be implemented, electrically heated catalysts (EHCs) for the after-treatment line have been proved to be able to increase the DOC temperature to about 180°C in 20s idling, while only 50°C can be reached without electrical assistance [Kim, et al., 2012]. Moreover, hot EGR PCCI calibrations at the lowest load, as described in Section 3.4, may effectively increase the exhaust gas thermal energy upstream the catalysts, giving additional benefits if coupled with EHCs.

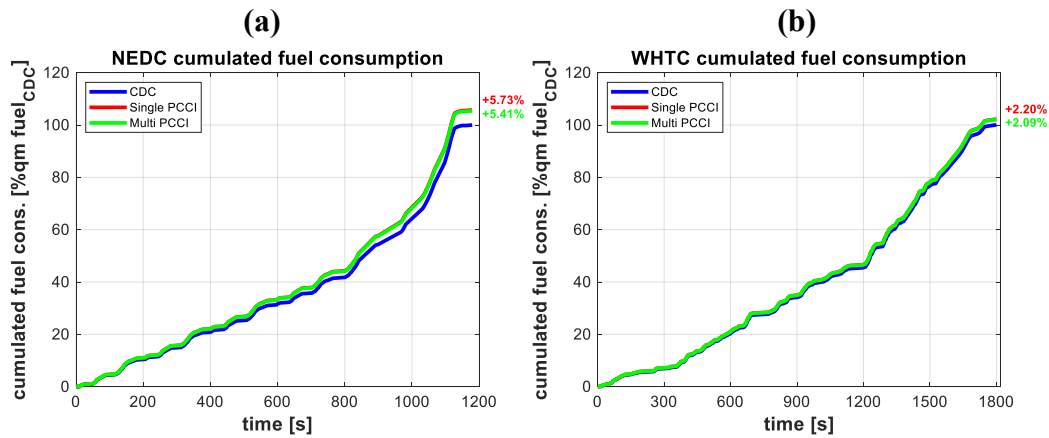


Figure 6.12. Cumulated fuel consumption over the simulated NEDC (a) and WHTC (b) cycles, with CDC (blue lines), single-injection PCCI (red lines) and multiple-injection PCCI (green lines).

Finally, as far as cumulated fuel consumptions are dealt with (cf. Figure 6.12), PCCI strategies introduce non-negligible penalties if compared to the reference CDC case, with only minor benefits achieved with multiple-injection PCCI. In particular, single-injection PCCI highlights fuel consumption penalties up to +5.7% along the NEDC, which reduce to +2.2% along the WHTC, due to its lower average exploitation of the engine under PCCI combustion mode (cf. Figure 6.13). Conversely, multiple-injection PCCI is able to reduce only marginally these penalties, settling around +5.4% along the NEDC and +2.0% along the WHTC.

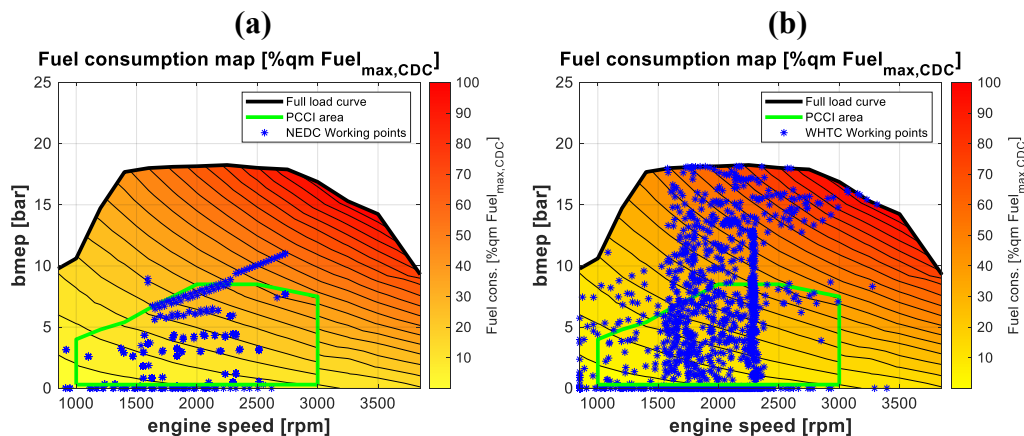


Figure 6.13. Fuel consumption maps for the simulated PCCI engine. The second-by-second engine operating points over the simulated NEDC (a) and WHTC (b) cycles are overlapped as blue stars.

It is worth pointing out how these fuel consumption penalties are estimated without considering the possible benefit deriving from reduced frequency of DPF regeneration required from the PCCI strategies (due to the sharp cut of engine-out soot), which may provide a small but appreciable contribution in real-driving conditions. It has been estimated that an active regeneration event of the DPF should occur whenever the soot load of the catalyst reaches the limit of about 5.5 g/l, as this value gives the lowest estimated fuel penalty (+2.2%, as an average, for CDC applications [Singh, et al., 2009]), taking into account that more frequent regeneration events would cause more fuel consumption due to the need of purposely calibrated post-injections, while less frequent regeneration events would

increase the soot load inside the catalyst, thus making the engine backpressure rise at the expense of thermodynamic efficiency. As a rough estimation, it may be stated that if a PCCI engine cuts the engine-out soot emissions of $N\%$ along a certain mission profile, it might be able to reduce of a similar percentage the frequency of DPF active regeneration events. A Δ fuel penalty (linked to active regeneration of the DPF) can be estimated for a PCCI engine as follows: $(1 - N/100) \cdot 2.2$ [%]. Therefore, if a PCCI engine features a *bsfc* penalty of $X\%$ without considering the influence of DPF regeneration, the overall *bsfc* penalty X_t (compared to CDC) would reduce to $X_t = (X - 2.2 \cdot N/100)$ [%], if considering it. Table 6.2 and Table 6.3 show the results of the abovementioned calculations over the simulated NEDC and WHTC cycles. As a matter of fact, the fuel consumption penalties introduced by PCCI strategies (either single-injection or multiple-injection) compared to CDC are actually lower than what previously reported in Figure 6.12, reducing from around +5.6% to +3.8% along the NEDC and from around +2.1% to 1.1% along the WHTC, just considering the influence of the reduced frequency of the DPF regeneration events.

Table 6.2. Effect of active regeneration strategies of the DPF on fuel penalties from PCCI, along the NEDC.

Strategy along NEDC	Fuel cons. penalty X [%]	Engine-out soot reduction N [%]	Δ Fuel cons. DPF regen. $(1-N/100) \cdot 2.2$ [%]	Overall fuel cons. penalty $(X-2.2 \cdot N/100)$ [%]
CDC	Reference	Reference	+2.2%	Reference
Single-inj. PCCI	+5.73%	-83.2%	+0.37%	+3.90%
Multi-inj. PCCI	+5.41%	-76.5%	+0.52%	+3.73%

Table 6.3. Effect of active regeneration strategies of the DPF on fuel penalties from PCCI, along the WHTC.

Strategy along WHTC	Fuel cons. penalty X [%]	Engine-out soot reduction N [%]	Δ Fuel cons. DPF regen. $(1-N/100) \cdot 2.2$ [%]	Overall fuel cons. penalty $(X-2.2 \cdot N/100)$ [%]
CDC	Reference	Reference	+2.2%	Reference
Single-inj. PCCI	+2.20%	-49.7%	+1.11%	+1.11%
Multi-inj. PCCI	+2.09%	-46.1%	+1.19%	+1.08%

Moreover, as a consequence of the reduced engine-out NO_x emissions from the PCCI engine, the reduction of urea consumption ($Z\%$, cf. Figure 6.8) should be also considered, in an overall analysis of the total fluid (fuel + urea) consumption and related costs. For this purpose, if the cumulated values of fuel (V_{fuel}) and urea (V_{urea}) consumptions (in liter) along a certain mission profile are known, as well as the fuel (C_{fuel}) and urea (C_{urea}) prices (in €/liter), the total fluid cost penalty (*TFCP*) given by PCCI if compared to CDC may be estimated as follows:

$$TFCP = \frac{X_t - Z \cdot \frac{C_{urea} \cdot V_{urea}}{C_{fuel} \cdot V_{fuel}}}{1 + \frac{C_{urea} \cdot V_{urea}}{C_{fuel} \cdot V_{fuel}}} \quad (20)$$

Taking $C_{fuel} = 1.4 \text{ €/l}$ and $C_{urea} = 1.5 \text{ €/l}$ as a reference, and considering that the ratio $\frac{V_{urea}}{V_{fuel}}$ is equal to 0.0187 (along the NEDC) and to 0.0228 (along the WHTC), the results reported in the following Table 6.4 and Table 6.5 may be obtained, along the simulated NEDC and WHTC cycles.

Table 6.4. Total fluid cost penalties from PCCI, along the NEDC.

Strategy along NEDC	Overall fuel cons. penalty X_f [%]	Urea cons. reduction Z [%]	Total fluid cost penalty $TFCP$ [%]
CDC	Reference	Reference	Reference
Single-inj. PCCI	+3.90%	-72.9%	+2.39%
Multi-inj. PCCI	+3.73%	-72.9%	+2.22%

Table 6.5. Total fluid cost penalties from PCCI, along the WHTC.

Strategy along WHTC	Overall fuel cons. penalty X_f [%]	Urea cons. reduction Z [%]	Total fluid cost penalty $TFCP$ [%]
CDC	Reference	Reference	Reference
Single-inj. PCCI	+1.11%	-35.5%	+0.24%
Multi-inj. PCCI	+1.08%	-35.5%	+0.21%

The total fluid cost penalty introduced by PCCI strategies (either single-injection or multiple-injection), compared to CDC, settles around +2.3% along the NEDC, while it goes down to slightly more than +0.2% along the WHTC. This witnesses how, if the analysis of the fuel consumption penalties from PCCI is not just limited to the direct fuel consumption increase, thoroughly pointed out in the previous Chapters, then PCCI combustion may even approach CDC performance in terms of total fluid cost.

Chapter 7

7 EGR cooler fouling⁷

The importance of calibrating the correct EGR rate during PCCI operations to avoid excessive *bsfc* values and/or poor combustion efficiency has been remarked several times, throughout the manuscript. Besides possible application of uncooled EGR schemes at low loads, as described in Section 3.4, high EGR requirement (with the employment of a short-route EGR loop) for PCCI generally means that more heat needs to be rejected into the EGR cooler in order to cool down the exhaust gas. Moreover, the possibility to have relatively high soot at the exhaust, during possible transient operation or during the transition to CDC calibration for high-load operation, is likely to cause fouling issues to the EGR circuit, and to the EGR cooler primarily, adversely affecting the reliability of the system itself. The combination of cooled EGR flowrates containing high concentrations of HC during PCCI operation and high PM when the engine is operated at higher load under CDC mode, promotes a progressive accumulation of an insulating deposit layer on the walls of the heat exchanger [Abarham, et al., 2013; Hong, et al., 2011]. The creation of this deposition layer on the walls of the EGR cooler gradually degrades its heat transfer efficiency [Abd-Elhady & Malayeri, 2013]. Moreover, it can cause an appreciable pressure drop, or even severe clogging [Kim, et al., 2008], thus hindering the EGR to flow through the recirculating system. This could be a major problem when PCCI combustion is implemented, as the EGR quantity is one of the most important parameters that needs to be controlled.

7.1 Experimental outcomes about the EGR cooler fouling

This Section describes the influence of the EGR cooler fouling on the F1C PCCI engine performance. It is worth recalling that the EGR cooler installed on this engine is different and larger than that mounted on the F1C Euro VI, as already clarified in Section 3.1.

Throughout part of the experimental campaign, several repetitions of the same steady-state test point (namely the 2000×5) were acquired, featuring an early single injection PCCI calibration with fixed calibration inputs, in terms of SOI, p_{rail} , VGT and exhaust flap positions, as well as fully open EGR valve. The purpose was to

⁷ Most of the contents of this Section have been previously published in [d'Ambrosio, S., Gaia, F., Iemmolo, D., Mancarella, A., Salamone, N., & Vitolo, R. (2018). "Performance and Emission Comparison between a Conventional Euro VI Diesel Engine and an Optimized PCCI Version and Effect of EGR Cooler Fouling on PCCI Combustion". SAE Technical Paper, 2018-01-0221. doi:10.4271/2018-01-0221].

point out any possible temporal drifts in engine performance and emissions caused by the progressive EGR cooler fouling. Figures 7.1-7.6 are plotted as functions of the working time. As already mentioned, the EGR cooling circuit in the F1C PCCI testbed application is separated from the engine cooling system and is cooled by means of an external conditioning system, so that the exhaust gas temperature at the EGR cooler outlet (T_{EGRco}) can be kept fixed by a PID controller at a value of about 85 °C. Before starting the experimental campaign, a run-in of a few hours was performed to stabilize the EGR cooler performance. The repetition tests at 2000×5 started to be recorded after about 25 hours of working time and continued until about 120 hours. Three points are highlighted with different colours in Figures 7.1-7.6 to highlight the drifted values at about 40, 80 and 120 hours of EGR cooler operating time. During this period, various engine working conditions were explored, but only the points corresponding to the same fixed calibration at 2000×5 are reported in Figures 7.1-7.6. Although the engine was designed to provide an improved PCCI combustion mode, featuring low soot emissions, a refined PCCI calibration was not implemented in the ECU, and this possibly led to relatively high soot working conditions for an appreciable amount of time during the preliminary experimental tests, which were carried out to look for the optimum calibration. Moreover, low EGR coolant water temperatures may have enhanced the HC condensation phenomenon during warm-up operations.

The deposition of fouling layers on the EGR cooler surfaces is the result of different fouling mechanisms undergone by the fine soot particles and unburned hydrocarbon molecules contained in the exhaust gases.

The exhaust soot particles tend to be driven towards the cooler walls as a result of the so-called thermophoresis effect [Kuan, et al., 2017]. Owing to the high temperature gradients between the EGR flow and the heat exchanger surfaces, collisions between the higher kinetic energy particles in the middle of the stream and the colder particles close to the metal generate a net (and slow) motion of particles towards the walls. As a result of their low speed in this slow motion towards the surfaces, these particles can easily stick to them, thus gradually building up a deposition layer [Malayeri, et al., 2013; Kuan, et al., 2017]. The net attraction force established between soot particles and walls is generally thought to be the result of Van der Waals forces, which are strong in proximity of the cold surfaces but weaker when the deposit layer temperature rises [Storey, et al., 2011]. If dry soot particles stick, they tend to create a very porous deposit layer, with a porosity up to 98% [Madler, et al., 2006].

As far as the HC is concerned, the heavy hydrocarbon molecules present in the exhaust gases can either condensate on the EGR cooler surfaces prior to soot deposition (thus helping the solid particles to stick) or diffuse through the already deposited dry porous fouling layer [Storey, et al., 2011]. In both cases, hydrocarbon condensation has a strong influence on the deposit morphology, which changes from a dry porous layer to a sludge-like deposit, depending to a great extent on the coolant water temperature [Hong, et al., 2011].

Besides these build-up mechanisms, which make the deposit layer grow up during time, removal mechanisms are also possible. The removal of soot particles

from the fouling layer can occur as a result of the shear forces between the gas flow and the stuck particles: if these shear forces overcome the adhesion forces, the soot particles can roll out the fouling layer [Abd-Elhady & Malayeri, 2013].

The insulating layer set up by soot deposition and HC condensation mechanisms make the overall thermal performance of the EGR cooler deteriorate, due to its additional thermal resistance. Moreover, the material stuck to the cooler tube walls reduces the cross-section flow area for the EGR flow, thus causing an increase in the pressure drop across the heat exchanger and consequent detrimental effects on engine performance.

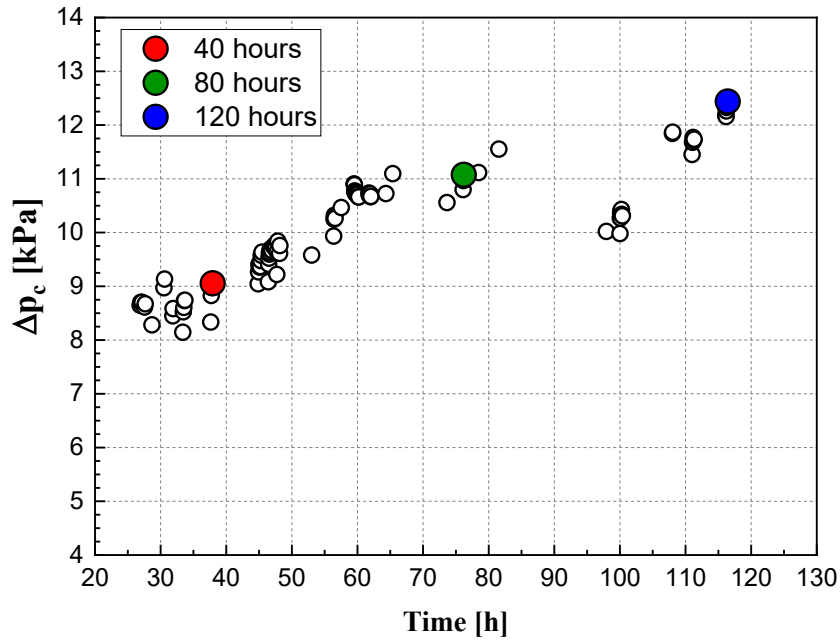


Figure 7.1. Differential pressure across the EGR cooler as a function of the working time in the F1C PCCI engine (repetition of a 2000×5 test over time).

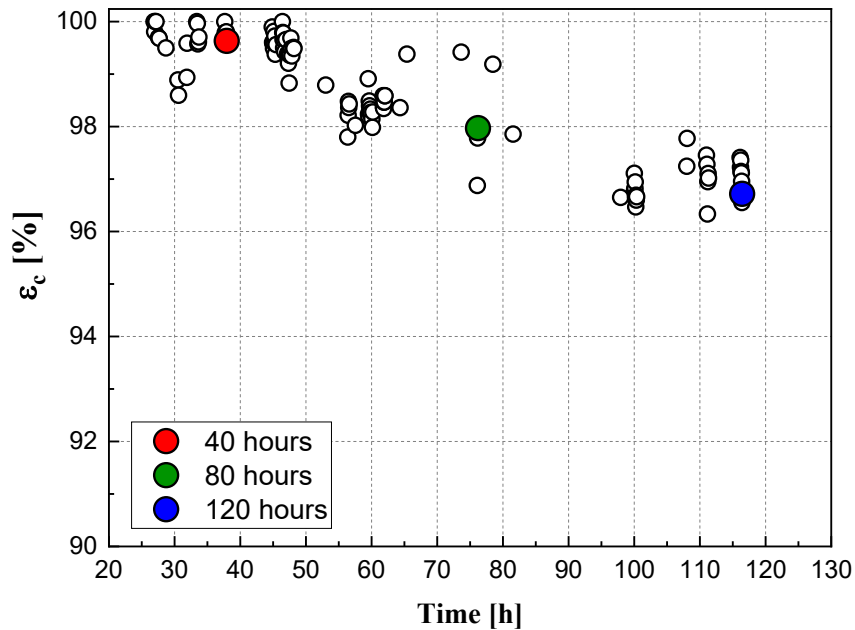


Figure 7.2. EGR cooler effectiveness as a function of the working time in the F1C PCCI engine (repetition of a 2000×5 test over time).

Figure 7.1 and Figure 7.2 show the change in mechanical and thermal performance of the EGR cooler over time. The mechanical performance is expressed in terms of pressure drop across the EGR cooler (Δp_c), whereas the thermal performance is expressed in terms of cooler effectiveness (ε_c) which is, by definition, the actual heat transfer from the EGR flow to the coolant divided by the maximum possible heat transfer. This can be expressed as [d'Ambrosio et al., 2013]:

$$\varepsilon_c = \frac{T_{EGRci} - T_{EGRco}}{T_{EGRci} - T_{H_2Oci}} \quad (21)$$

where T_{EGRci} is the exhaust gas temperature at the EGR cooler inlet, T_{EGRco} is the exhaust gas temperature at the EGR cooler outlet and T_{H_2Oci} is the coolant temperature at the EGR cooler inlet.

Along the engine operation, the pressure drop across the EGR cooler gradually increased of about 4 kPa, from a starting value slightly over 8 kPa (cf. Figure 7.1), whereas the cooler effectiveness decreased from about 100% to 96.5%, as shown in Figure 7.2. These degradations in mechanical and thermal performance of the EGR cooler suggests an appreciable thickening of the fouling layer over time. Despite this, high ε_c values were still detected after 120 h, possibly due to the large size and, consequently, large surface area where the heat transfer takes place, of the EGR cooler installed on the F1C PCCI. For this reason, the increment in thermal resistance, due to the fouling layer, did not determine a massive deterioration of the thermal performance. Therefore, the decrease in thermal effectiveness (which furthermore, in the considered test bench configuration, does not affect the desired EGR gas temperature downstream the cooler, kept fixed around 85 °C owing to the PID controller), was found to be less problematic than the degradation in the mechanical performance. This latter, in fact, caused a progressive reduction in the EGR mass flowrate (Figure 7.3(b)) as well as a simultaneous increase in both the upstream EGR cooler pressure (p_{EGRci}) and the exhaust manifold pressure (p_{exh}), due to the growth thickness of the fouling layer, which partially clogs the cross-section flow area.

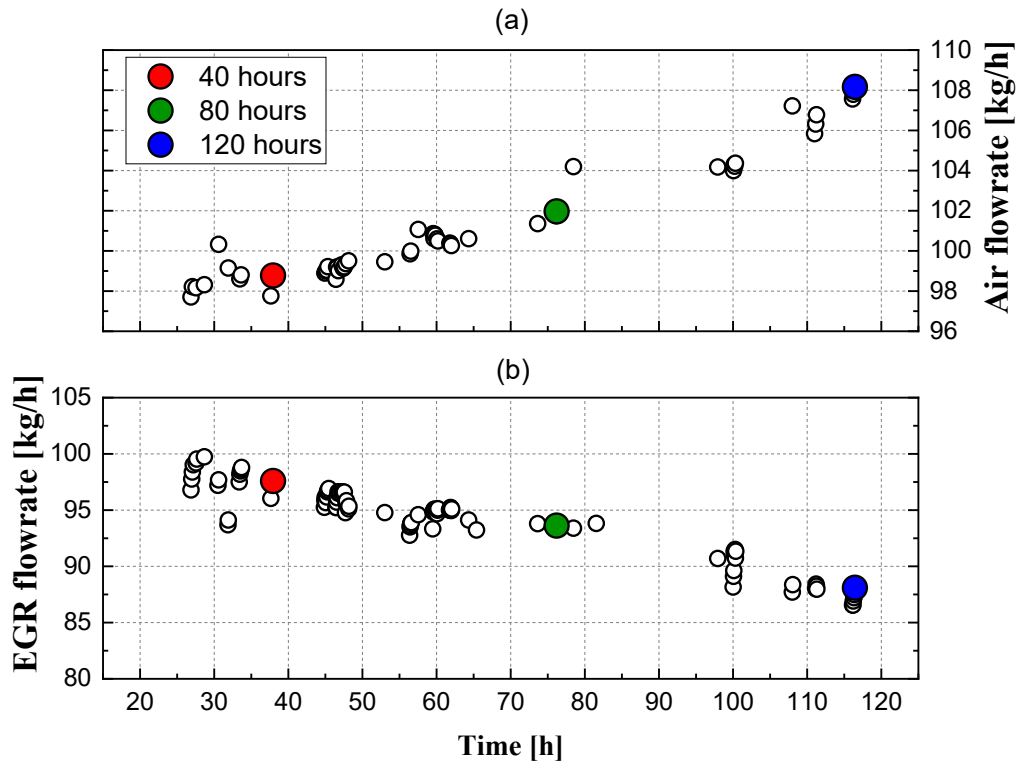


Figure 7.3. Air (a) and EGR (b) mass flowrates as a function of the working time in the FIC PCCI engine (repetition of a 2000×5 test over time).

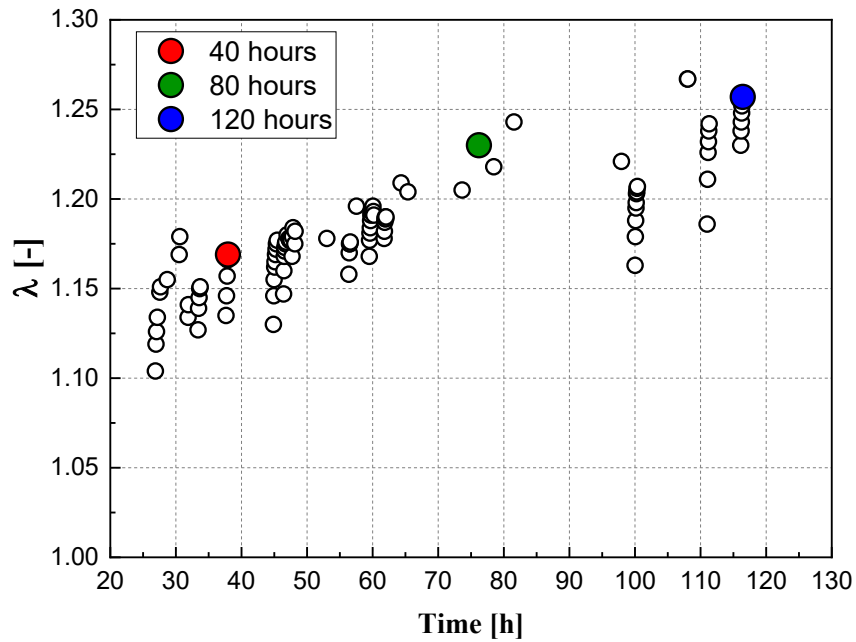


Figure 7.4. Lambda (λ) values as a function of the working time in the FIC PCCI engine (repetition of a 2000×5 test over time).

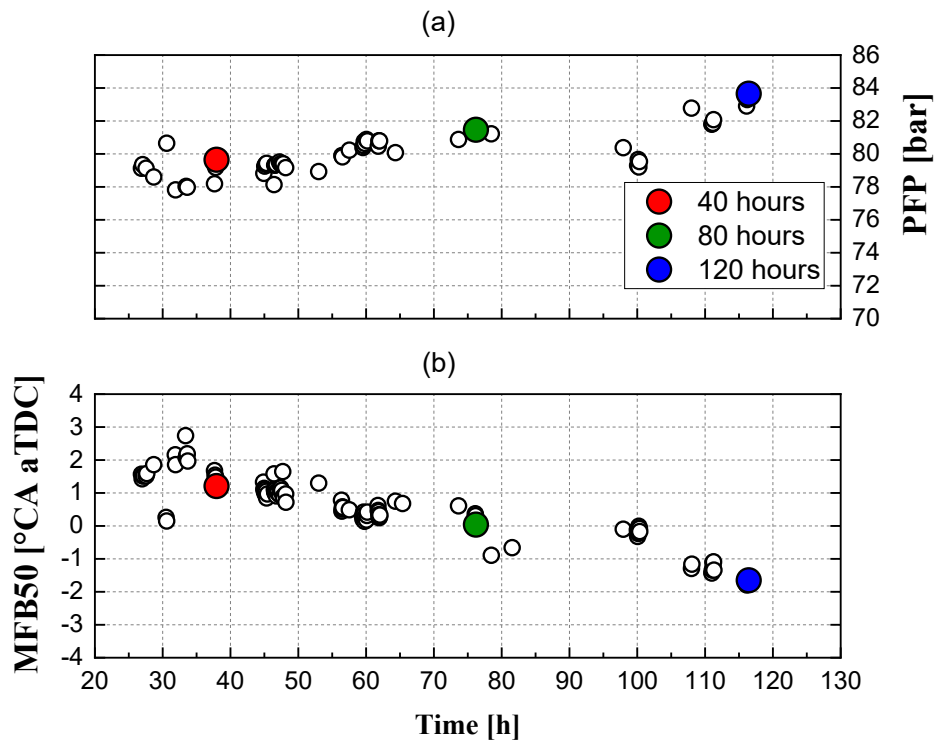


Figure 7.5. PFP (a) and MFB50 (b) values as a function of the working time in the F1C PCCI engine (repetition of a 2000×5 test over time).

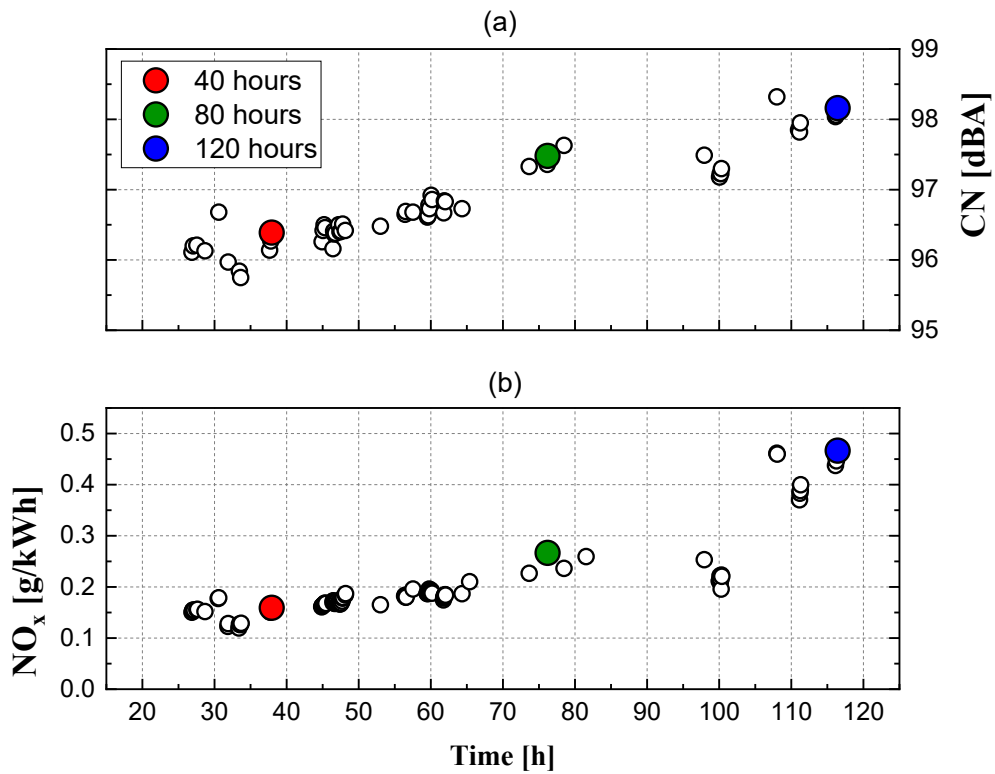


Figure 7.6. CN (a) and NO_x (b) as a function of the working time in the F1C PCCI engine (repetition of a 2000×5 test over time).

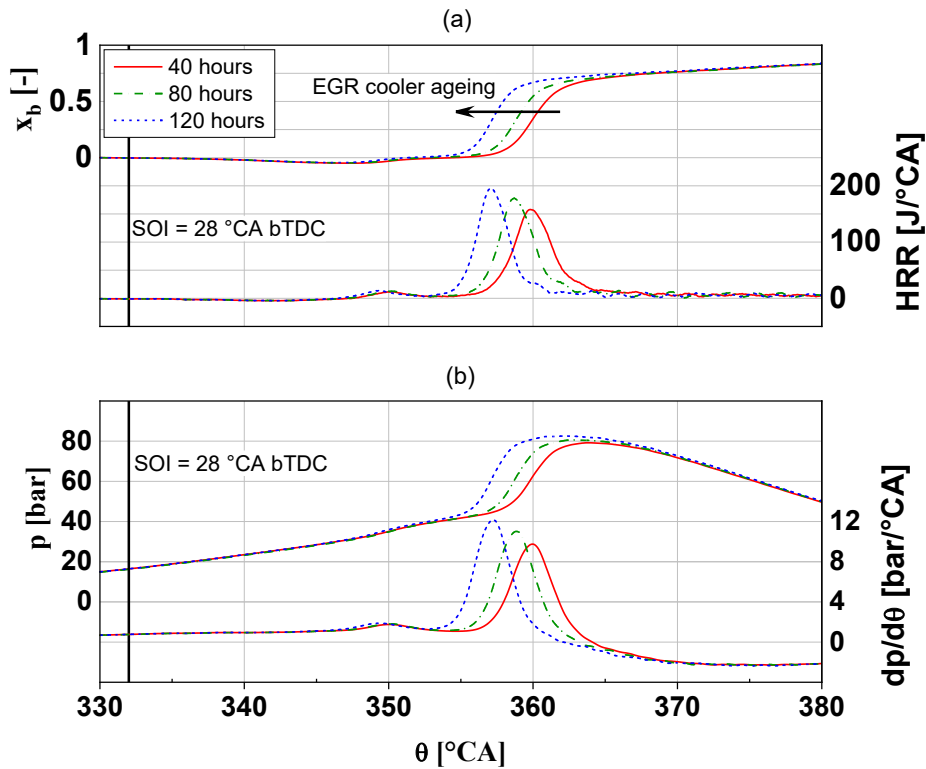


Figure 7.7. Mass fraction burned x_b (a – left axis), HRR (a - right axis), in-cylinder pressure (b – left axis), and its derivative (b - right axis) versus crank angle position for different working times of the EGR cooler (3 repetitions of a 2000×5 test over time).

The decrease in the EGR mass flowrate induced an increment in both the intake air mass flowrate (Figure 7.3(a)) and the value of λ (Figure 7.4), since the fuel flowrate varied to a much lower extent. Therefore, the combustion development became progressively faster, thus resulting in earlier MFB50 values (Figure 7.5(b)), higher peaks of in-cylinder pressure (Figure 7.5(a)) and, consequently, increased NO_x exhaust emissions (Figure 7.6(b)) and CN levels (Figure 7.6(a)).

The effect of the EGR cooler fouling is also visible in Figure 7.7, which illustrates the mass fraction burned x_b , HRR, in-cylinder pressure and its derivative traces versus the crank angle position for different working times of the EGR cooler (corresponding to the three colored points reported in Figures 7.1-7.6). All of them are evaluated from a single zone analysis implemented in the AVL Concerto software for indicating analysis. The progressive cooler fouling, reducing the EGR flowrate, determines an advanced and faster combustion. The LTHR takes place at about 350 °CA and does not seem to be influenced by the EGR rate (even though the average intake temperature of the fouled cooler is slightly lower, due to the higher air level and to the lower EGR flowrate). The HRR peak is more advanced and intense in the case of fouled cooler, as it exploits a higher in-cylinder intake oxygen concentration.

Apart from these “long-term” effects, EGR cooler fouling shows “short-term” effects as well, which are outside the “long-term” trend. For instance, if reference is made to Figure 7.1, an appreciable decrease (of about 1.5 kPa) in Δp_c can be detected after about 93 h of engine running. This is possibly caused by “short-term”

partial depletion of the deposit layer thickness due to temporary stronger shear forces (likely dependent on the particular engine working points explored, at different speed and load values, before the 2000×5 repetition tests) which are able to overcome the particle adhesive forces, causing their rolling out and a consequent partial deposit thinning. However, this fouling layer depletion cannot be complete, likely due to partial sintering mechanisms of the deposits [Abd-Elhady & Malayeri, 2013]. If the deposit layer is exposed to high temperature, soot particles can undergo phenomena of reinforcement of the contact forces, with consequent reduction of the layer porosity: this means that only a low portion of material can be removed with “short-term” recovery phenomena, while the majority of the deposit stay stuck to the walls.

7.2 PCCI performance with the new and aged EGR coolers

A further analysis of the EGR cooler fouling phenomenon on the performance and emissions of PCCI strategy will be detailed in this Section.

As a following step to the activity of the early single injection PCCI calibration (cf. Section 3.3), some “V-optimal” design test plans were set up (taking into account, as input variables, SOI, p_{rail} , flap and VGT positions, like previously done and explained in Sections 2.2 and 3.2) for some of the engine operating points listed in Section 3.3 (including the 2000×5) and then carried out at the test bench. The aim was to use the empirical data, gathered in this way, to build statistical models and compute model-based optimizations to be compared with the results of the “optimum” PCCI calibration achieved by means of the methodology used in Section 3.3, relying on preliminary OFAT tests and objective functions. The results confirmed that the two approaches were able to provide similar results, in terms of optimizations, and, therefore, this topic has not been detailed. Nevertheless, the aim of this Section is to provide details about the effect of EGR cooler, exploiting a comparison of the results between two identical sets of the same “V-optimal” design performed at 2000×5, with both an aged EGR cooler (i.e., with more than 120 h of operation under different working conditions, used after the tests reported in Figures 7.1-7.7) and a new EGR cooler (for which a run-in of a few hours was performed before the tests). The results of the tests employing the fouled EGR cooler are shown, in the following Figures 7.8-7.12, with red squares, while blue circles refer to the tests performed with the new heat exchanger. The colour-filled points highlight the “V-optimal” central test, which was replicated several times during the test-run in order to check for any possible “short-term” drifts.

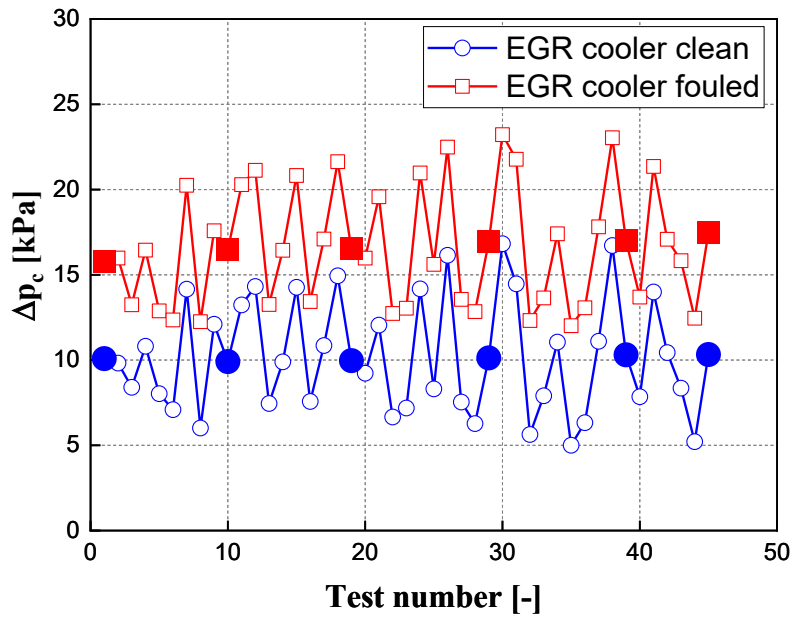


Figure 7.8. Pressure drop across the EGR cooler for the FIC PCCI engine during DoE test plans at 2000×5, with clean (blue) and fouled (red) heat exchanger. The color-filled symbols refer to the central points of the test plans.

The control input variables completely govern the engine air handling, actually excluding the default boost pressure control. Therefore, any drift in the pressure drop across the EGR cooler cannot be compensated for, by the engine air handling system. Figure 7.8 shows that the pressure drop across the cooler is higher for the aged cooler, and a minor drift, highlighted by the DoE central points, can be noted during the tests. It is important to underline that the central point does not correspond to the calibration of the points in Figures 7.1-7.7, and a direct comparison between the Δp_c values reported in Figure 7.1 and Figure 7.8 is therefore not possible.

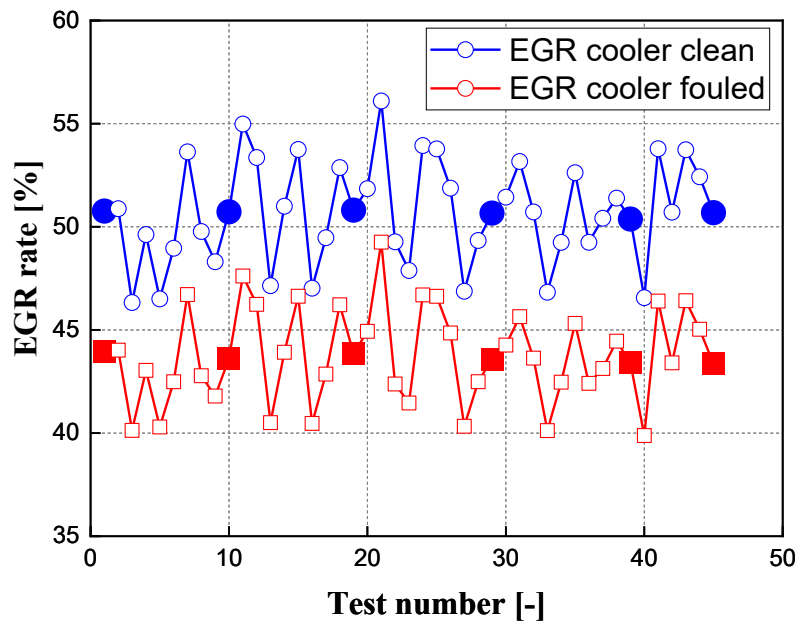


Figure 7.9. EGR rate for the FIC PCCI engine during DoE test plans at 2000×5, with clean (blue) and fouled (red) heat exchanger. The color-filled symbols refer to the central points of the test plans.

Figure 7.9 reports the EGR rate during the DoE test plans execution, further confirming that a clean EGR cooler allows a higher EGR rate to be reached, with the same calibration implemented in the ECU. The different EGR rates also affect MFB50 values (which tend to be more advanced as far as the EGR cooler is clogged) and *bsfc* (which tend to worsen as far as the EGR cooler is clogged), as depicted in Figure 7.10 and Figure 7.11, respectively.

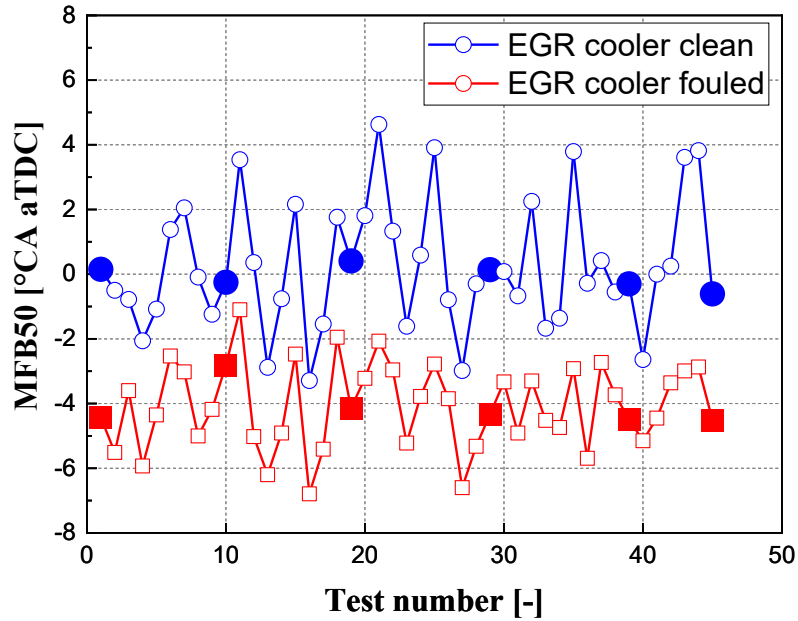


Figure 7.10. MFB50 values for the F1C PCCI engine during DoE test plans at 2000×5, with clean (blue) and fouled (red) heat exchanger. The color-filled symbols refer to the central points of the test plans.

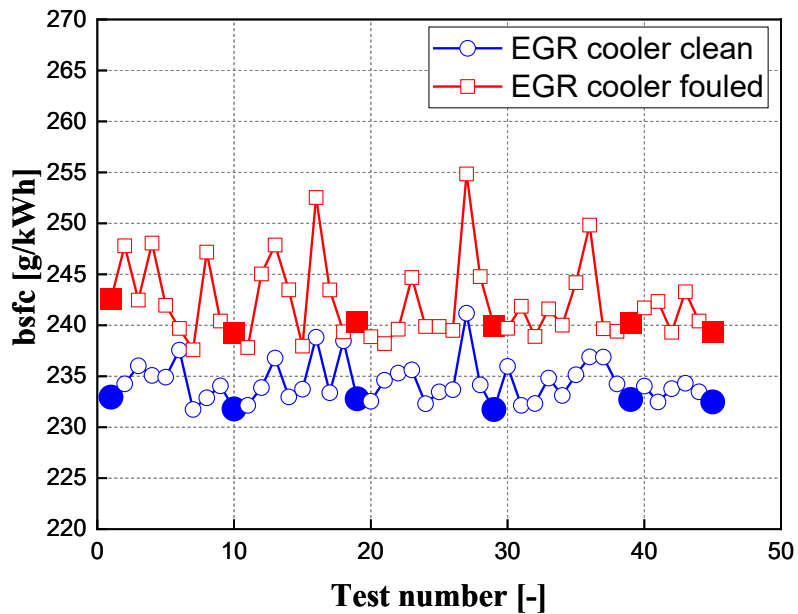


Figure 7.11. *bsfc* values for the F1C PCCI engine during DoE test plans at 2000×5, with clean (blue) and fouled (red) heat exchanger. The color-filled symbols refer to the central points of the test plans.

Figure 7.12 reports the NO_x emissions over the DoE test plans as a function of λ . A dramatic increase in NO_x is clearly visible, as far as the fouled EGR cooler is concerned, mainly due to the reduced dilution levels achievable in this case.

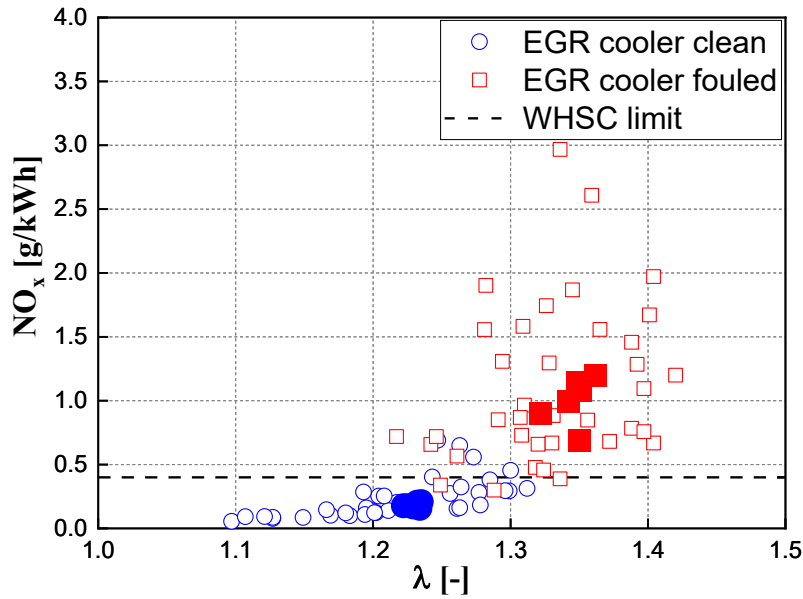


Figure 7.12. NO_x emissions vs. λ for the F1C PCCI engine during DoE test plans at 2000×5, with clean (blue) and fouled (red) heat exchanger. The color-filled symbols refer to the central points of the test plans.

Other exhaust emissions and CN levels are affected by the change in EGR rate, too. This implies that the performance of an optimized calibration can be detrimentally affected in PCCI combustion mode by the level of fouling of the EGR cooler. In order to partially mitigate this effect, an optimized calibration should involve the real-time control of the in-cylinder combustion, for instance with a real-time monitoring of the MFB50 phasing, instead of a conventional map-based SOI control (as described in Chapter 5).

Conclusions

The first part of this investigation examined how far a modern Euro VI, 3.0 l production diesel engine (F1C Euro VI) could be operated under an early PCCI combustion strategy, without changes to the engine hardware. This was possible through a suitable combination of high EGR levels and advanced (single) injection timings, but only inside a very limited (low speed and load) portion of the engine map, up to $b_{mep} = 2\div 3$ bar. Proper optimal calibrations allowed to achieve simultaneous engine-out soot and NO_x reductions (of up to 99% and 95%, respectively, compared to their CDC levels), but with associated severe penalties, such as increased engine-out emission of HC and CO, intense CN, higher fuel consumption and worst combustion stability.

Then, to further investigate the early-PCCI concept and to increase its operating range, several hardware modifications were implemented to the baseline F1C Euro VI engine. These hardware modifications included reduced compression ratio (from 17.5:1 to 14.6:1), modified piston, different fuel injectors with reduced cone angles, a higher volume EGR cooler and a smaller turbo-group.

First, the derived prototype engine (referred to as F1C PCCI) was tested featuring a single fuel injection calibration, and a suitable steady-state calibration with early-PCCI conditions was achieved up to 8.5 bar of b_{mep} . Strong reductions of engine-out NO_x (between -85% and -97%) and soot (between -90% and -99%) emissions were still possible, but too high tailpipe HC and CO emissions at low load, intense CN and fuel consumption penalties ranging from about 3% to 11% (if compared to the corresponding values obtained with CDC operations with the baseline F1C Euro VI engine) still remained major issues.

Secondly, a hot (uncooled) EGR strategy (realized recirculating exhaust gas into the engine without making them flow through the EGR cooler) was tested up to $b_{mep} = 3$ bar. Uncooled EGR proved to be beneficial to increase the exhaust gas temperatures, with gains ranging from +10 to +60°C, compared to the standard cooled EGR strategy in the same engine operating points. Some of this extra thermal energy available upstream the DOC has proven to enhance its conversion efficiency, helping the catalyst to reach its correct operating temperature (and, thus, to be able to cut to almost zero both HC and CO tailpipe emissions) in a wider area of the engine map.

Additional experimental activities on the F1C PCCI engine dealt with multi-pulse (i.e., double and triple) fuel injection PCCI strategies. Splitting the fuel injection pattern proved to have the potential of reducing engine-out HC and CO emissions (up to -50%), with minor penalties in terms of engine-out soot and NO_x (i.e., with reductions compared to CDC values not below around -60%). Multi-pulse injections also allowed to effectively dampen excessive CN levels (of up to 5÷6 dBA, compared to single injection patterns), while slightly improving fuel

economy, especially at lower loads (even if still much higher than CDC levels, up to around +10% in the worst cases).

Several “zero-dimensional” (0D) models for the estimation of the EGR flowrate were developed and experimentally assessed under both conventional and PCCI combustion modes. The most satisfactory results, in terms of predictive capabilities even outside the calibration domain, were pointed out when using EGR models that need dedicated measurement signals, generally not included among the conventional sensors connected to standard ECUs, such as temperature and pressure across the EGR valve. Moreover, both a pressure-based and a model-based real-time combustion control technique, for the evaluation of the MFB50, was presented. Both of these two control approaches were compared to the conventional map-based control of the standard ECU, attaining results always comparable in terms of fuel consumption and exhaust pollutant emissions, without producing any detrimental effect when operating the engine under CDC combustion mode. Moreover, tests performed under early single PCCI combustion regimes with a high EGR rate (>60%) showed the best potentialities of MFB50 control methodologies to improve combustion stability, reducing COV_{imep} and CoV_{PFP} and further extending the tolerable EGR rate.

A preliminary assessment of the potentialities of single- and multiple-injection PCCI, combined with CDC calibration (outside the PCCI area) in order to simulate the functionality of a dual-mode operation strategy engine, have been evaluated along simulated NEDC and WHTC cycles, to give a rough estimation of possible benefits/penalties compared to a reference CDC case. Early single-injection PCCI confirmed its ability to sharply cut engine-out NO_x (of about 68% and 30%, along the NEDC and WHTC, respectively) and soot (of about 83% and 50%, along the NEDC and WHTC, respectively) emissions. Even if the simulated PCCI engine implements a strategy of null urea consumption when it operates inside the PCCI area, tailpipe NO_x emissions still resulted to be lower than in the CDC case, reaching a -53% along the NEDC while shrinking to -17% along the WHTC, since this latter cycle requires the engine to work for a higher amount of time at high load CDC conditions. Urea consumption may be reduced of about 73% along the NEDC and of about 35% along the WHTC, as well. Multiple-injection PCCI introduces only slightly lower benefits in terms of NO_x and soot reduction, but are able to give some benefit in terms of engine-out incomplete combustion species emission, compared to single-injection PCCI patterns (for instance, +722% vs. +843% CO, along the NEDC, and +287% vs. +388%, along the WHTC, if compared to CDC). Fuel consumption penalties range from +2.2% to +5.7% (along the NEDC and the WHTC, respectively) for the single-injection PCCI, while minor benefits may be brought by multiple-injection PCCI. Nevertheless, if these fuel consumption penalties estimations are not just limited to the direct fuel consumption increase, but also take into account the benefits introduced by PCCI due to less frequent regenerations of the DPF and less urea consumption for the SCR, then PCCI combustion may even approach CDC performance in terms of total fluid costs (up to just +0.2% along the simulated WHTC).

Finally, the progressive EGR cooler fouling experienced during the experimental campaign was analysed, and its detrimental effects on PCCI performance and emissions was pointed out. The increased pressure drop across a fouled EGR cooler results in a progressively smaller amount of EGR, thus revealing to be one of the major constraints to the applicability of the PCCI concepts.

Abbreviations and acronyms

aDOC	after (downstream) the Diesel Oxidation Catalyst
AFM	Accumulated Fuel Mass
ANN	Artificial Neural Network
aTDC	after Top Dead Center
ATS	After-Treatment System
BDC	Bottom Dead Center
bDOC	before (upstream) the Diesel Oxidation Catalyst
BEV	Battery Electric Vehicle
<i>bmep</i>	brake mean effective pressure
<i>bsfc</i>	brake specific fuel consumption
bTDC	before Top Dead Center
CA	Crank Angle
CDC	Conventional Diesel Combustion
CFD	Computational Fluid Dynamics
CLD	ChemiLuminescence Detector
CN	Combustion Noise
CoV	Coefficient of Variation
CR	Compression Ratio
DI	Direct Injection
DOC	Diesel Oxidation Catalyst
DoE	Design of Experiments
DPF	Diesel Particulate Filter
DT	Dwell-Time
ECU	Engine Control Unit
EGR	Exhaust Gas Recirculation
EU	European Union

EV	Electric Vehicles
FFT	Fast Fourier Transform
FPT	Fiat Powertrain Technologies
FSN	Filter Smoke Number
GA	Genetic Algorithm
GHG	Green-House Gases
HC	HydroCarbon
HCCI	Homogeneous Charge Compression Ignition
HD	Heavy-Duty
HDV	Heavy-Duty Vehicle
HiL	Hardware in the Loop
HRR	Heat Release Rate
HTHR	High-Temperature Heat Release
ICE	Internal Combustion Engine
ID	Ignition Delay
IFP	Insitut Français du Pétrol
<i>imep</i>	Indicated mean effective pressure
IVC	Intake Valve Closure
LD	Light-Duty
LDV	Light-Duty Vehicle
LIVC	Late Intake Valve Closure
LNT	Lean NO _x Trap
LTC	Low Temperature Combustion
LTHR	Low-Temperature Heat Release
\dot{m}_a	Intake air mass flowrate
\dot{m}_{EGR}	EGR mass flowrate
MFB	Mass Fraction Burned
MFB50	Crank angle location where 50% of the injected fuel mass has burnt
MiL	Model in the Loop

MK	Modulated Kinetics
n	engine rotational speed
NADI	Narrow Angle Direct Injection
NBI	Normal Boundaries Intersection
NDIR	Non-Dispersive InfraRed
NEDC	New European Driving Cycle
NO _x	Nitrogen Oxides
NTC	Negative Temperature Coefficient
OEM	Original Equipment Manufacturer
OFAT	One Factor At a Time
p	pressure
PAH	Polycyclic Aromatic Hydrocarbons
PCCI	Premixed Charge Compression Ignition
p_{cyl}	in-cylinder pressure
PFP	Peak Firing Pressure
PHEV	Plug-in Hybrid Electric Vehicle
PID	Proportional–Integral–Derivative
PM	Particulate Matter
PN	Particulate Number
q	injected fuel quantity
RMSE	Root Mean Square Error
RO ₂	alkylperoxy radicals
RP	Rapid Prototyping
RSM	Response Surface Methodology
SCR	Selective Catalytic Reduction
SOC	Start Of Combustion
SOF	Soluble Organic Fraction
SOI	Start Of Injection
SVM	Support vector machine
t	generic time instant

T	Temperature
TDC	Top Dead Center
<i>TFCP</i>	Total Fluid Cost Penalty
<i>Trq</i>	brake engine Torque
UNIBUS	UNIform Bulky combustion System
V	instantaneous in-cylinder chamber volume
VCR	Variable Compression Ratio
VGT	Variable Geometry Turbine
VVA	Variable Valve Actuation
VVC	Variable Valve Control
VVT	Variable Valve Timing
WHSC	Worldwide Harmonized Stationary Cycle
WHTC	Worldwide Harmonized Transient Cycle
WLTP	Worldwide Light-duty Test Procedure
X_b	fuel mass fraction burnt
X_{EGR}	EGR rate
γ	specific heat capacity ratio
η_c	combustion efficiency
η_{hl}	heat-loss efficiency
η_{wc}	work conversion efficiency
λ	relative air-fuel ratio
ϕ	equivalence ratio

References

- Abarham, M., Zamankhan, P., Hoard, J., Styles, D., Scott Sluder, C., Storey, J., Assanis, D. (2013). "CFD analysis of particle transport in axi-symmetric tube flows under the influence of thermophoretic force". *International Journal of Heat and Mass Transfer*, 61, 94-105. doi:10.1016/j.ijheatmasstransfer.2013.01.071
- Abd-Elhady, M., & Malayeri, M. (2013). "Asymptotic characteristics of particulate deposit formation in exhaust gas recirculation (EGR) coolers". *Applied Thermal Engineering*, 60(1-2), 96-104. doi:10.1016/j.applthermaleng.2013.06.038
- Abdul Karim, Z., & Anwar Bin Sulaiman, S. (2018). *Alternative Fuels for Compression Ignition Engines*. Springer. doi:10.1007/978-981-10-7754-8
- Adomeit, P., Pischinger, S., Becker, M., Rohs, H., & Greis, A. (2004). "Laser Optical Diagnostics and Numerical Analysis of HDSI Combustion". *THIESEL 2004 Conference on Thermo- and Fluid-Dynamic Process in Diesel Engines*, September 8-10, 2004, Valencia, Spain.
- Agarwal, A., Singh, A., & Maurya, R. (2017). "Evolution, challenges and path forward for low temperature combustion engines". *Progress in Energy and Combustion Science*, 61, 1-56. doi:10.1016/j.pecs.2017.02.001
- Akihama, K., Takatori, Y., Inagaki, K., Sasaki, S., & Dean, A. (2001). "Mechanism of the Smokeless Rich Diesel Combustion by Reducing Temperature". *SAE Technical Paper*, 2001-01-0655. doi:10.4271/2001-01-0655
- Anand, K., & Reitz, R. (2016). "Exploring the benefits of multiple injections in low temperature combustion using a diesel surrogate model". *Fuel*, 165, 341-350. doi:10.1016/j.fuel.2015.10.087
- Angrill , O., Geitlinger, H., Streibel, T., Suntz, R., & Bockhorn, H. (2000). "Influence of exhaust gas recirculation on soot formation in diffusion flames". *Proceedings of the Combustion Institute*, 28(2), 2643-2649. doi:10.1016/S0082-0784(00)80683-9
- Asik, J., Peters, J., Meyer, G., & Tang, D. (1997). "Transient A/F Estimation and Control Using a Neural Network". *SAE Technical Paper*, 970619. doi:10.4271/970619
- Baratta, M., Finesso, R., Misul, D., & Spessa, E. (2015). "Comparison between Internal and External EGR Performance on a Heavy Duty Diesel Engine by Means of a Refined 1D Fluid-Dynamic Engine Model". *SAE International Journal of Engines*, 8(5), 1977-1992. doi:10.4271/2015-24-2389
- Beatrice, C., Avolio, G., Del Giacomo, N., Guido, C., & Lazzaro, M. (2008). "The Effect of "Clean and Cold" EGR on the Improvement of Low Temperature Combustion Performance in a Single Cylinder Research Diesel Engine". *SAE Technical Paper*, 2008-01-650. doi:10.4271/2008-01-0650

- Beatrice, C., Del Giacomo, N., & Guido, C. (2009). "Benefits and Drawbacks of Compression Ratio Reduction in PCCI Combustion Application in an Advanced LD Diesel Engine". *SAE International Journal of Engines*, 2(1), 1290-1303. doi:10.4271/2009-01-1447
- Beatrice, C., Guido, C., Del Giacomo, N., & Bertoli, C. (2008). "Study of the compression ratio influence on the performance of an advanced automotive diesel engine operating in conventional and PCCI combustion mode". *THIESEL 2008: Conference on Thermo- and Fluid- Dynamic Processes in Diesel Engines*. Valencia, Spain. doi:10.13140/2.1.4448.8009
- Bendu, H., & Murugan, S. (2014). "Homogeneous charge compression ignition (HCCI) combustion: Mixture preparation and control strategies in diesel engines". *Renewable and Sustainable Energy Reviews*, 38, 732-746. doi:10.1016/j.rser.2014.07.019
- Boot, M., Luijten, C., Somers, L., Eguz, U., van Erp, D., Albrecht, A., & Baert, R. (2009). "Uncooled EGR as a Means of Limiting Wall-Wetting under Early Direct Injection Conditions". *SAE Technical Paper*, 2009-01-0665. doi:10.4271/2009-01-0665
- Boot, M., Rijk, E., Luijten, C., & Somers, B. (2010). "Spray Impingement in the Early Direct Injection Premixed Charge Compression Ignition Regime". *SAE Technical Paper*, 2010-01-1501. doi:10.4271/2010-01-1501
- Box, G., & Cox, D. (1964). "An analysis of transformation". *Journal of the Royal Statistical Society. Series B (Methodological)*, 26(2), 211-252.
- Brooks, T., Lumsden, G., & Blaxill, H. (2005). "Improving Base Engine Calibrations for Diesel Vehicles Through the Use of DoE and Optimization Techniques". *SAE Technical Paper*, 2005-01-3833. doi:10.4271/2005-01-3833
- Buchwald, R., Lautrich, G., Maiwald, O., & Sommer, A. (2006). "Boost and EGR System for the Highly Premixed Diesel Combustion". *SAE Technical Paper*, 2006-01-0204. doi:10.4271/2006-01-0204
- Carlucci, A., Laforgia, D., Motz, S., Saracino, R., & Wenzel, S. (2014). "Advanced closed loop combustion control of a LTC diesel engine based on in-cylinder pressure signals". *Energy Conversion and Management*, 77, 193-207. doi:10.1016/j.enconman.2013.08.054
- Castillo, F., Witrant, E., Talon, V., & Dugard, L. (2013). "Simultaneous Air Fraction and Low-Pressure EGR Mass Flow Rate Estimation for Diesel Engines". *IFAC Proceedings Volumes*, 46(2), 731-736. doi:10.3182/20130204-3-FR-2033.00070
- Catania, A., Finesso, R., & Spessa, E. (2011). "Predictive Zero-Dimensional Combustion Model for DI Diesel Engine Feed-Forward Control". *Energy Conversion and Management*, 52(9), 3459-3175. doi:10.1016/j.enconman.2011.05.003
- Charlton, S. (2005). "Developing diesel engines to meet ultra-low emission standards". *SAE Technical Paper*, 2005-01-3628. doi:10.4271/2005-01-3628

- Chauvin, J., Corde, G., & Petit, N. (2007). "Transient control of a Diesel engine airpath". *2007 American Control Conference*, 4394-4400. doi:10.1109/ACC.2007.4282942
- Chmela, F., & Orthaber, G. (1999). "Rate of Heat Release Prediction for Direct Injection Diesel Engines Based on Purely Mixing Controlled Combustion". *SAE Technical Paper, 1999-01-0186*. doi:10.4271/1999-01-0186
- Chung, J., Min, K., Oh, S., & Sunwoo, M. (2016). "In-cylinder pressure based real-time combustion control for reduction of combustion dispersions in light-duty diesel engines". *Applied Thermal Engineering*, 99, 1183-1189. doi:10.1016/j.applthermaleng.2016.01.012
- Cipolla, G., Vassallo, A., Catania, A. E., Spessa, E., Stan, C., & Drischmann, L. (2007). "Combined application of CFD modeling and pressure-based combustion diagnostics for the development of a low compression ratio high-performance diesel engine". *SAE Technical Paper, 2007-24-0034*. doi:10.4271/2007-24-0034
- Cong, S., McTaggart-Cowan, G., Garner, C., Wahab, E., & Peckham, M. (2011). "Experimental Investigation of Low Temperature Diesel Combustion Processes". *Combustion Science and Technology*, 183(12), 1376-1400. doi:10.1080/00102202.2011.600740
- Curran, H., Gaffuri, P., Pitz, W., & Westbrook, C. (1998). "Comprehensive Modeling Study of n-Heptane Oxidation". *Combustion Flame*, 114, 149-177. doi:10.1016/S0010-2180(97)00282-4
- Dae, S., & Chang, S. (2005). "Effect of n-Heptane Premixing on Combustion Characteristics of Diesel Engine". *Energy & Fuels*, 19, 2240-2246. doi:10.1021/ef050055s
- d'Ambrosio, S., & Ferrari, A. (2015). "Effects of exhaust gas recirculation in diesel engines featuring late PCCI type combustion strategies". *Energy Conversion and Management*, 105, 1269-1280. doi:10.1016/j.enconman.2015.08.001
- d'Ambrosio, S., & Ferrari, A. (2015). "Potential of double pilot injection strategies optimized with the design of experiments procedure to improve diesel engine emissions and performance". *Applied Energy*, 155, 918-932. doi:10.1016/j.apenergy.2015.06.050
- d'Ambrosio, S., & Ferrari, A. (2018). "Exploitation of injection fusion strategies in diesel engines equipped with solenoid injectors". *International Journal of Engine Research*, 19(6), 653-667. doi:10.1177/1468087417728629
- d'Ambrosio, S., Ferrari, A., & Spessa, E. (2013). "Analysis of the exhaust gas recirculation system performance in modern diesel engines". *Journal of Engineering for Gas Turbines and Power*, 135(8), 081601 (13 pages). doi:10.1115/1.4024089
- d'Ambrosio, S., Ferrari, A., Mancarella, A., & Mittica, A. (2020). "Effects of Rate-Shaped and Multiple Injection Strategies on Pollutant Emissions, Combustion Noise and Fuel Consumption in a Low Compression Ratio Diesel Engine". *International Journal of Automotive Technology* volume, 21(1), 197-214. doi:10.1007/s12239-020-0020-0

- d'Ambrosio, S., Finesso, R., & Spessa, E. (2011). "Calculation of mass emissions, oxygen mass fraction and thermal capacity of the inducted charge in SI and diesel engines from exhaust and intake gas analysis". *Fuel*, 90(1), 152-166. doi:10.1016/j.fuel.2010.08.025
- d'Ambrosio, S., Gaia, F., Iemmolo, D., Mancarella, A., Salamone, N., & Vitolo, R. (2018). "Performance and Emission Comparison between a Conventional Euro VI Diesel Engine and an Optimized PCCI Version and Effect of EGR Cooler Fouling on PCCI Combustion". *SAE Technical Paper*, 2018-01-0221. doi:10.4271/2018-01-0221
- d'Ambrosio, S., Iemmolo, D., Mancarella, A., & Vitolo, R. (2016). "Preliminary optimization of the PCCI combustion mode in a diesel engine through a design of experiments". *Energy Procedia*, 909-916. doi:10.1016/j.egypro.2016.11.115
- d'Ambrosio, S., Iemmolo, D., Mancarella, A., Salamone, N., Vitolo, R., & Hardy, G. (2017). "Zero Dimensional Models for EGR Mass-Rate and EGR Unbalance Estimation in Diesel Engines". *SAE Technical Paper*, 2017-24-0070. doi:10.4271/2017-24-0070
- d'Ambrosio, S., Mancarella, A., Manelli, A., & Salamone, N. (2019). "Effect of the application of an uncooled high-pressure EGR strategy in low-load diesel PCCI operation". *AIP Conference Proceedings*, 2191(1), 020055. doi:10.1063/1.5138788
- Dec, J., & Canaan, R. (1998). "PLIF Imaging of NO Formation in a DI Diesel Engine". *SAE Technical Paper*, 980147. doi:10.4271/980147
- Dec, J., & Sjöberg, M. (2004). "Isolating the Effects of Fuel Chemistry on Combustion Phasing in an HCCI Engine and the Potential of Fuel Stratification for Ignition Control". *SAE Technical Paper*, 2004-01-0557. doi:10.4271/2004-01-0557
- Dec, J., & Sjöberg, M. (2007). "Comparing late-cycle autoignition stability for single- and two-stage ignition fuels in HCCI engines". *Proceedings of the Combustion Institute*, 31(2), 2895-2902. doi:10.1016/j.proci.2006.08.010
- DieselNet. (2019). "Emission Standards – Europe: Cars and light trucks". Retrieved September 17, 2019, from <https://www.dieselnets.com/standards/eu/ld.php>
- DieselNet. (2019). "Low Temperature Combustion". Retrieved March 06, 2020, from https://dieselnets.com/tech/engine_ltc.php#ft
- Diop, S., Moraal, P., Kolmanovsky, I., & Van Nieuwstadt, M. (1999). "Intake oxygen concentration estimation for DI diesel engines". *Proceedings of the 1999 IEEE International Conference on Control Applications*, 1, 852-857. doi:10.1109/CCA.1999.807777
- Doosje, E., Willems, F. P., Baert, R., & van Dijk, M. (2012). "Experimental study into a hybrid PCCI/CI concept for next-generation heavy-duty diesel engines". *SAE Technical Paper*, 2012-01-1114. doi:10.4271/2012-01-1114
- EC. (2011). "Commission Regulation (EU) 582/2011". *Official Journal of the European Union*, L 167/1. Retrieved January 07, 2020, from <https://eur-lex.europa.eu/legal-content/EN/TXT/?uri=CELEX:32011R0582>

- EEA. (2016). "Explaining road transport emissions: A non-technical guide". *European Environment Agency*. Retrieved September 17, 2019, from <https://www.eea.europa.eu/publications/explaining-road-transport-emissions>
- EEA. (2018). "Emissions of air pollutants from transport". *European Environment Agency*. Retrieved September 17, 2019, from <https://www.eea.europa.eu/data-and-maps/indicators/transport-emissions-of-air-pollutants-8/transport-emissions-of-air-pollutants-6>
- EEA. (2018). "Greenhouse gas emissions from transport in Europe". *European Environment Agency*. Retrieved September 17, 2019, from <https://www.eea.europa.eu/data-and-maps/indicators/transport-emissions-of-greenhouse-gases/transport-emissions-of-greenhouse-gases-11>
- Finesso, R., Hardy, G., Maino, C., Marello, O., & Spessa, E. (2017). "A New Control-Oriented Semi-Empirical Approach to Predict Engine-Out NOx Emissions in a Euro VI 3.0 L Diesel Engine". *Energies*, 10(12), 1978. doi:10.3390/en10121978
- Finesso, R., Marello, O., Misul, D., Spessa, E., Violante, M., Yang, Y., & Hardy, G. (2017). "Development and Assessment of Pressure-Based and Model-Based Techniques for the MFB50 Control of a Euro VI 3.0L Diesel Engine". *SAE International Journal of Engines*, 10(4), 1538-1555. doi:10.4271/2017-01-0794
- Finesso, R., Spessa, E., Yang, Y., Alfieri, V., & Conte, G. (2015). "HRR and MFB50 Estimation in a Euro 6 Diesel Engine by Means of Control-Oriented Predictive Models". *SAE International Journal of Engines*, 8(3), 1055-1068. doi:10.4271/2015-01-0879
- Fontanesi, F., & Giacomini, P. (2012). "Multiphase CFD-CHT optimization of the cooling jacket and FEM analysis of the engine head of a V6 diesel engine". *Applied Thermal Engineering*, 52, 293-303. doi:10.1016/j.applthermaleng.2012.12.005
- Fuyuto, T., Taki, M., Ueda, R., Hattori, Y., Kuzuyama, H., & Umehara, T. (2014). "Noise and Emissions Reduction by Second Injection in Diesel PCCI Combustion with Split Injection". *SAE International Journal of Engines*, 7(4), 1900-1910. doi:<https://doi.org/10.4271/2014-01-2676>
- Genzale, C., Reitz, R., & Musculus, M. (2009). "Effects of spray targeting on mixture development and emissions formation in late-injection low-temperature heavy-duty diesel combustion". *Proceedings of the Combustion Institute*, 32(2), 2767-2774. doi:10.1016/j.proci.2008.06.072
- Griffin, J., Ganseman, C., Baerts, C., Burkholder, N., Geyer, S., & Smith, D. (2003). "Cooled EGR Rate Measurement with a Thermal Anemometer for EPA02 Heavy Duty Diesel Engine Emission Control". *SAE Technical Paper*, 2003-01-0263. doi:10.4271/2003-01-0263
- Guardiola, C., Gil, A., Pla, B., & Piqueras, P. (2012). "Representation limits of mean value engine models". *Lecture notes in control and information sciences*, 418, 185-206. doi:10.1007/978-1-4471-2221-0_11

- Guzzella, L., & Onder, C. (2010). *"Introduction to modeling and control of internal combustion engines systems"*. Berlin: Springer. doi:10.1007/978-3-642-10775-7
- Hagena, J., Filipi, Z., & Assanis, D. (2006). "Transient diesel emissions: analysis of engine operation during a tip-in". *SAE Technical Paper, 2006-01-1151*. doi:10.4271/2006-01-1151
- Han, D., Ickes, A., Bohac, S., Huang, Z., & Assanis, D. (2012). "HC and CO emissions of premixed low-temperature combustion fueled by blends of diesel and gasoline". *Fuel, 99*, 13-19. doi:10.1016/j.fuel.2012.04.010
- Hardy, W., & Reitz, R. (2006). "A Study of the Effects of High EGR, High Equivalence ratio, and Mixing Time on Emissions Levels in a Heavy-Duty Diesel Engine for PCCI Combustion". *SAE Technical Paper, 2006-01-0026*. doi:10.4271/2006-01-0026
- Hasegawa, R., & Yanagihara, H. (2003). "HCCI Combustion in DI Diesel Engine". *SAE Technical Paper, 003-01-0745*. doi:10.4271/2003-01-0745
- Heywood, J. (2018). *"Internal Combustion Engine Fundamentals"* (Second ed.). McGraw-Hill Intern. Editions.
- Hill, G., Heidrich, O., Creutzig, F., & Blythe, P. (2019). "The role of electric vehicles in near-term mitigation pathways and achieving the UK's carbon budget". *Applied Energy, 251*, 113111. doi:10.1016/j.apenergy.2019.04.107
- Hillion, M., Chauvin, J., Grondin, O., & Petit, N. (2008). "Active Combustion Control of Diesel HCCI Engine: Combustion Timing". *SAE Technical Paper, 2008-01-0984*. doi:10.4271/2008-01-0984
- Hiroyasu, H., Kadota, T., & Arai, M. (1983). "Development and use of a spray combustion modeling to predict diesel engine efficiency and pollutant emissions: part 1 combustion modeling". *Bulletin of JSME, 26(214)*, 569-575. doi:10.1299/jsme1958.26.569
- Hong, K., Lee, K., Song, S., Chun, K., Chung, D., & Min, S. (2011). "Parametric study on particle size and SOF effects on EGR cooler fouling". *Atmospheric Environment, 45*, 5677-5683. doi:10.1016/j.atmosenv.2011.07.036
- Hoofman, N., Messagie, M., Van Mierlo, J., & Coosemans, T. (2018). "A review of the European passenger car regulations – Real driving emissions vs local air quality". *Review and Sustainable Energy Reviews, 86*, 1-21. doi:10.1016/j.rser.2018.01.012
- Ickes, A., Assanis, D., & Bohac, S. (2009). "Load Limits with Fuel Effects of a Premixed Diesel Combustion Mode". *SAE Technical Paper, 2009-01-1972*. doi:10.4271/2009-01-1972
- Iemmolo, D. (2017). "Alternative fuels and combustion modes to lower pollutant emissions from conventional internal combustion engines". *Doctoral Thesis*, Politecnico di Torino, Turin, Italy.
- Jayashankara, B., & Ganesan, V. (2010). "Effect of fuel injection timing and intake pressure on the performance of a DI diesel engine – A parametric study using CFD". *Energy Conversion and Management, 51(10)*, 1835-1848. doi:10.1016/j.enconman.2009.11.006

- Jemni, M., Kantchev, G., & Abid, M. (2011). "Influence of intake manifold design on in-cylinder flow and engine performances in a bus diesel engine converted to LPG gas fuelled, using CFD analyses and experimental investigations". *Energy*, 36, 2701-2715. doi:10.1016/j.energy.2011.02.011
- Jiao, Y. (2015). "Euro VI HDD Engine Technology Overview". *Ricardo presentation, May 2015*.
- Jung, D., & Assanis, D. (2001). "Multi-Zone DI Diesel Spray Combustion Model for Cycle Simulation Studies of Engine Performance and Emissions". *SAE Technical Paper, 2001-01-1246*. doi:10.4271/2001-01-1246
- Kamimoto, T., & Bae, M. (1988). "High Combustion Temperature for the reduction of particulate in diesel engines". *SAE Technical Paper, 880423*. doi:10.4271/880423
- Kawamoto, K., Araki, T., Shinzawa, M., Kimura, S., Koide, S., & Masahiko, S. (2004). "Combination of Combustion Concept and Fuel Property for Ultra-Clean DI Diesel". *SAE Technical Paper, 2004-01-1868*. doi:10.4271/2004-01-1868
- Kim, C., Paratore, M., Gonze, E., Solbrig, G., & Smith, S. (2012). "Electrically Heated Catalysts for Cold-Start Emissions in Diesel Aftertreatment". *SAET Technical Paper, 2012-01-1092*. doi:10.4271/2012-01-1092
- Kim, D., Ekoto, I., Colban, W., & Miles, P. (2009). "In-cylinder CO and UHC Imaging in a Light-Duty Diesel Engine during PPCI Low-Temperature Combustion". *SAE International Journal of Fuels and Lubricants*, 1(1), 933-956. doi:10.4271/2008-01-1602
- Kim, H., Kim, Y., & Lee, K. (2008). "A study of the characteristics of mixture formation and combustion in a PCCI engine using an early multiple injection strategy". *Energy Fuels*, 22(3), 1542-1548. doi:10.1021/ef700568g
- Kim, H., Park, S., Choi, K., & et al. (2008). "Investigation on the flow and heat transfer characteristic of diesel engine EGR cooler". *International Journal of Automotive Technology*, 9(2), 149-153. doi:10.1007/s12239-008-0019-4
- Kimura, S., Aoki, O., Kitahara, Y., & Aiyoshizawa, Y. (2001). "Ultra-Clean Combustion Technology Combining a Low-Temperature and Premixed Combustion Concept for Meeting Future Emission Standards". *SAE Technical Paper, 2001-01-0200*. doi:10.4271/2001-01-0200
- Kimura, S., Ogawa, H., Matsui, Y., & Enomoto, Y. (2002). "An experimental analysis of low-temperature and premixed combustion for simultaneous reduction of NOx and particulate emissions in direct injection diesel engines". *International Journal of Engine Research*, 3(4), 249-259. doi:10.1243/146808702762230932
- Kook, S., Bae, C., Miles, P., Choi, D., & Pickett, L. (2005). "The Influence of Charge Dilution and Injection Timing on Low-Temperature Diesel Combustion and Emissions". *SAE Technical Paper, 2005-01-3837*. doi:10.4271/2005-01-3837
- Kook, S., Park, S., & Bae, C. (2008). "Influence of Early Fuel Injection Timings on Premixing and Combustion in a Diesel Engine". *Energy & Fuels*, 22(1), 331-337. doi:10.1021/ef700521b

- Kuan, C., Styles, D., Bieniek, M., & Hoard, J. (2017). "An EGR Cooler Fouling Model: Experimental Correlation and Model Uses". *SAE International Journal of Engines*, 10(2). doi:10.4271/2017-01-0535
- Kuwahara, K., Furutani, M., Ando, H., & Ohta, Y. (2005). "Impact of Formaldehyde Addition on Auto-Ignition in Internal-Combustion Engines". *JSME International Journal Series B*, 48(4), 708-716. doi:10.1299/jsmeb.48.708
- Lachaux, T., Musculus, M., Singh, S., & Reitz, R. (2008). "Optical Diagnostics of Late-Injection Low-Temperature Combustion in a Heavy-Duty Diesel Engine". *Journal of Engineering for Gas Turbines and Power*, 130(3), 032808 (9 pages). doi:10.1115/1.2830864
- Ladommatos, N., Abdelhalim, S., Zhao, H., & Hu, Z. (1997). "The Dilution, Chemical, and Thermal Effects of Exhaust Gas Recirculation on Diesels Engine Emissions - Part 4: Effects of Carbon Dioxide and Water Vapour". *SAE Technical Paper*, 971660. doi:doi.org/10.4271/971660
- Ladommatos, N., Abdelhalim, S., Zhao, H., & Hu, Z. (1998). "Effects of EGR on Heat Release in Diesel Combustion". *SAE Technical Paper*, 980184. doi:10.4271/980184
- Laguitton, O., Crua, C., Cowell, T., Heikal, M., & Gold, M. (2007). "The effect of compression ratio on exhaust emissions from a PCCIdiesel engine". *Energy Conversion and Management*, 48, 2918-2924. doi:10.1016/j.enconman.2007.07.016
- Lechner, G., Jacobs, T., Chryssakis, C., Assanis, D., & Siewert, R. (2005). "Evaluation of a Narrow Spray Cone Angle, Advanced Injection Timing Strategy to Achieve Partially Premixed Compression Ignition Combustion in a Diesel Engine". *SAE Technical Paper*, 2005-01-0167. doi:10.4271/2005-01-0167
- Lee, H., Park, Y., & Sunwoo, M. (2014). "Observer design for exhaust gas recirculation rate estimation in a variable-geometry turbocharger diesel engine using a model reference identification scheme". *Proceedings of the Institution of Mechanical Engineers Part D: Journal of Automobile Engineering*, 228(14), 1688-1699. doi:10.1177/0954407013511444
- Lee, S., & Reitz, R. (2006). "Spray Targeting to Minimize Soot and CO Formation in Premixed Charge Compression Ignition (PCCI) Combustion with a HSDI Diesel Engine". *SAE Technical Paper*, 2006-01-0918. doi:10.4271/2006-01-0918
- Leermakers, C. A., Luijten, C. C., Somers, L. M., Kalghatgi, G. T., & Albrecht, B. A. (2011). "Experimental Study of Fuel Composition Impact on PCCI Combustion in a Heavy-Duty Diesel Engine". *SAE Technical Paper*, 2011-01-1351. doi:10.4271/2011-01-1351
- Li, T., Suzuki, M., Shudo, T., & Ogawa, H. (2008). "Effect of cetane number on mixture formation and combustion characteristics of ultra-high EGR low temperature diesel combustion". *Review of Automotive Engineering*, 29, 463-470. doi:10.11351/jsaereview.29.463

- Madler, L., Lall, A., & Friedlander, S. (2006). "One-step aerosol synthesis of nanoparticle agglomerate films: simulation of film porosity and thickness". *Nanotechnology*, 17, 4783-4795. doi:10.1088/0957-4484/17/19/001
- Maiboom, A., Tautzia, X., & Hétet, J. (2008). "Experimental study of various effects of exhaust gas recirculation (EGR) on combustion and emissions of an automotive direct injection diesel engine". *Energy*, 33(1), 22-34. doi:10.1016/j.energy.2007.08.010
- Malayeri, M., Zornek, T., Balestrino, S., Warey, A., & Szymkowicz, P. (2013). "Deposition of Nanosized Soot Particles in Various EGR Coolers Under Thermophoretic and Isothermal Conditions". *Heat Transfer Engineering*, 34, 665-673. doi:10.1080/01457632.2012.738320
- Manimaran, R., Thundil, K., & Kumar, S. (2013). "Premixed Charge Compression Ignition in a Direct Injection Diesel Engine using Computational Fluid Dynamics". *WSEAS Transactions on Heat and Mass Transfer*, 8(1), 17-29.
- Mickūnaitis, V., Pikūnas, A., & Mackoit, I. (2007). "Reducing fuel consumption and CO₂ emission in motor cars". *Transport*, 22(3), 160-163. doi:10.1080/16484142.2007.9638119
- Midttun, A., & Witoszek, N. (2016). *Energy and Transport in Green Transition: Perspectives on Ecomodernity*. New York: Routledge.
- Montgomery, D. (2000). *Design and Analysis of Experiments* (5th ed.). Wiley.
- Montgomery, D., & Reitz, R. (2000). "Optimization of Heavy-Duty Diesel Engine Operating Parameters Using a Response Surface Method". *SAE Technical Paper, 2000-01-1962*. doi:10.4271/2000-01-1962
- Murata, Y., Kusaka, J., Daisho, Y., Kawano, D., & et al. (2008). "Miller-PCCI Combustion in an HSDI Diesel Engine with VVT". *SAE International Journal of Engines*, 1(1), 444-456. doi:10.4271/2008-01-0644
- Musculus, M., Lachaux, T., Pickett, L., & Idicheria, C. (2007). "End-of-Injection Over-Mixing and Unburned Hydrocarbon Emissions in Low-Temperature-Combustion Diesel Engines". *SAE Technical Paper, 2007-01-0907*. doi:https://doi.org/10.4271/2007-01-0907
- Musculus, M., Miles, P., & Pickett, L. (2013). "Conceptual models for partially premixed low-temperature diesel combustion". *Progress in Energy and Combustion Science*, 39, 246-283. doi:10.1016/j.pecs.2012.09.001
- National Research Council. (2011). *Assessment of Fuel Economy Technologies for Light-Duty Vehicles*. Washington D.C.: The National Academies Press. doi:10.17226/12924
- Nevin, R., Sun, Y., Gonzalez, D., & Reitz, R. (2007). "PCCI Investigation Using Variable Intake Valve Closing in a Heavy Duty Diesel Engine". *SAE Technical Paper, 2007-01-0903*. doi:10.4271/2007-01-090
- Nishi, M., Ikeda, H., Iida, N., Kuzuyama, H., Umehara, T., & Fuyuto, T. (2015). "Numerical Assessment of Controlling the Interval between Two Heat-Release Peaks for Noise Reduction in Split-injection PCCI Combustion". *SAE Technical Paper, 2015-01-1851*. doi:10.4271/2015-01-1851
- Opat, R., Ra, Y., Gonzalez, D., Krieger, R., Reitz, R., Foster, D., . . . Siewert, R. (2007). "Investigation of Mixing and Temperature Effects on HC/CO

- Emissions for Highly Dilute Low Temperature Combustion in a Light Duty Diesel Engine". *SAE Technical Paper*, 2007-01-0193. doi:10.4271/2007-01-0193
- Park, Y., & Bae, C. (2011). "Influence of EGR and Pilot Injection on PCCI Combustion in a Single-Cylinder Diesel Engine". *SAE Technical Paper*, 2011-01-1823. doi:10.4271/2011-01-1823
- Park, Y., & Bae, C. (2014). "Experimental study on the effects of high/low pressure EGR proportion in a passenger car diesel engine". *Applied Energy*, 133(15), 308-316. doi:10.1016/j.apenergy.2014.08.003
- Parks, J., Prikhodko, V., Storey, J., Barone, T., Lewis, S., Kass, M., & Huff, S. (2010). "Emissions from premixed charge compression ignition (PCCI) combustion and effect on emission control devices". *Catalyst Today*, 151, 278-284. doi:doi.org/10.1016/j.cattod.2010.02.053
- Peterson , B., Ekoto, I., & Miles, P. (2010). "An Investigation into the effects of fuel properties and engine load on UHC and CO emissions from a light-duty optical diesel engine operating in a partially premixed combustion regime". *SAE International Journal of Engines*, 3(2), 38-55. doi:10.4271/2010-01-1470
- Pickett, L., & Siebers, D. (2004). "Non-Sooting, Low Flame Temperature Mixing-Controlled DI Diesel Combustion". *SAE Technical Paper*, 2004-01-1399. doi:10.4271/2004-01-1399
- Pickett, L., & Siebers, D. (2006). "Soot Formation in Diesel Fuel Jets Near the Lift-Off Length". *International Journal of Engine Research*, 7(2), 103-130. doi:10.1243/146808705X57793
- Rakopoulos, C., & Giakoumis, E. (2006). "Review of Thermodynamic Diesel Engine Simulations under Transient Operating Conditions". *SAE Technical Paper*, 2006-01-0884. doi:10.4271/2006-01-0884
- Saxena, S., & Beyoda, I. (2013). "Fundamental phenomena affecting low temperature combustion and HCCI engines, high load limits and strategies for extending these limits". *Progress in Energy and Combustion Science*, 39(5), 457-488. doi:10.1016/j.pecs.2013.05.002
- Schten, K., Ripley, G., Punater, A., & Erickson, C. (2007). "Design of an automotive grade controller for in-cylinder pressure based engine control development". *SAE Technical Paper*, 2007-01-0774. doi:10.4271/2007-01-0774
- Shibata, G., Ogawa, H., Sha, F., & Tashiro, K. (2016). "Impingement and Adhesion on Cylinder Liners with Post Diesel Fuel Injections". *SAE Technical Paper*, 2016-01-2193. doi:10.4271/2016-01-2193
- Shimazaki, N., Akagawa, H., & Tsujimura, K. (1999). "An Experimental Study of Premixed Lean Diesel Combustion". *SAE Technical Paper*, 1999-01-0181. doi:10.4271/1999-01-0181
- Simpson, T., Poplinski, J., Koch, P., & Allen, J. (2001). "Metamodels for computer-based engineering design: survey and recommendations". *Engineering with Computers*, 17(2), 129-150. doi:10.1007/PL00007198

- Singh, N., Rutland, C., Foster, D., Narayanaswamy, K., & He, Y. (2009). "Investigation into Different DPF Regeneration Strategies Based on Fuel Economy Using Integrated System Simulation". *SAE Technical Paper*, 2009-01-1275. doi:10.4271/2009-01-1275
- Soyhan, H., Yasar, H., Walmsley, H., Head, B., Kalghatgi, G., & Sorusbay, C. (2009). "Evaluation of heat transfer correlations for HCCI engine modeling". *Applied Thermal Engineering*, 29(2-3), 541-549. doi:10.1016/j.applthermaleng.2008.03.014
- Spessa, E., d'Ambrosio, S., Iemmolo, D., Mancarella, A., Vitolo, R., & Hardy, G. (2017). "Steady-State and Transient Operations of a Euro VI 3.0L HD Diesel Engine with Innovative Model-Based and Pressure-Based Combustion Control Techniques". *SAE International Journal of Engines*, 10(3), 1080-1092. doi:10.4271/2017-01-0695
- Stanglmaier, R., & Roberts, C. (1999). "Homogeneous Charge Compression Ignition (HCCI): Benefits, Compromises, and Future Engine Applications". *SAE Technical Paper*, 1999-01-3682. doi:10.4271/1999-01-3682
- Storey, J., Sluder, C., Lance, M., Styles, D., & Simko, S. (2011). "Exhaust Gas Recirculation Cooler Fouling in Diesel Applications: Fundamental Studies, Deposit Properties and Microstructure". *Proceedings of International Conference on Heat Exchanger Fouling and Cleaning*. doi:10.1080/01457632.2012.738319
- Styles, D., Giuliano, J., Hoard, S., & Sluder, J. (2008). "Identification and control of factors that affect EGR cooler fouling". *14th Diesel Engine-Efficiency and Emissions Research Conference*. Dearborn (Michigan).
- Takalkar, M., & Khan, I. (2017). "Study of Variable Compression Ratio Engine (VCR) and Different Innovations to Achieve VCR". *International Journal for Research in Applied Science and Engineering Technology*, V, 1473-1478. doi:10.22214/ijraset.2017.11213
- Taylor, A. (2008). "Science review of internal combustion engines". *Energy Policy*, 36(12), 4657-4667. doi:10.1016/j.enpol.2008.09.001
- Tietge, U. (2018). "CO2 emissions from new passenger cars in the EU: Car manufacturers' performance in 2017". Retrieved September 27, 2019, from <https://theicct.org/publications/co2-emissions-new-passenger-cars-eu-car-manufacturers-performance-2017>
- Torregrossa, A., Broatch, A., García, A., & Mònico, L. (2013). "Sensitivity of combustion noise and NOx and soot emissions to pilot injection in PCCI Diesel engines". *Applied Energy*, 104, 149-157. doi:10.1016/j.apenergy.2012.11.040
- Torregrossa, A., Broatch, A., Novella, R., Gomez-Soriano, J., & Mònico, L. (2017). "Impact of gasoline and Diesel blends on combustion noise and pollutant emissions in Premixed Charge Compression Ignition engines". *Energy*, 137, 56-68. doi:10.1016/j.energy.2017.07.010
- Uzun, A. (2012). "A parametric study for specific fuel consumption of an intercooled diesel engine using a neural network". *Fuel*, 93, 189-199. doi:10.1016/j.fuel.2011.11.004

- Verbeek, R., Ligterink, N., & Dekker, H. (2008). "Correlation Factors between European and World Harmonised Test Cycles for heavy-duty engines". *TNO report - EC*. doi:10.13140/RG.2.1.1934.5528
- Wahlström, J., & Eriksson, L. (2011). "Modelling diesel engines with a variable geometry turbocharger and exhaust gas recirculation by optimization of model parameters for capturing non-linear system dynamics". *Proceedings of the Institution of Mechanical Engineers: Part D. Journal of Automobile Engineering*, 225(7), 960-986. doi:10.1177/0954407011398177
- Walter, B., & Gatellier, B. (2002). "Development of the High Power NADI™ Concept Using Dual Mode Diesel Combustion to Achieve Zero NOx and Particulate Emissions". *SAE Technical Paper*, 2002-01-1744. doi:10.4271/2002-01-1744
- Willems, F., Doosje, E., Engels, F., & Seykens, X. (2010). "Cylinder pressure-based control in heavy-duty EGR diesel engines using a virtual heat release and emission sensor". *SAE Technical Paper*, 2010-01-0564. doi:10.4271/2010-01-0564
- Wittek, K., Tienmann, C., & Pischinger, S. (2009). "Two-Stage Variable Compression Ratio with Eccentric Piston Pin and Exploitation of Crank Train Forces". *SAE International Journal of Engines*, 2(1), 1304-1313. doi:10.4271/2009-01-1457.
- Wlodarczyk, M. (2006). "High accuracy glow plug-integrated cylinder pressure sensor for closed loop combustion". *SAE Technical Paper*, 2006-01-0184. doi:10.4271/2006-01-0184
- Yan, F., & Wang, J. (2009). "Enabling Air-Path Systems for Homogeneous Charge Compression Ignition (HCCI) Engine Transient Control". *Proceedings of the ASME 2009 Dynamic Systems and Control Conference*, (pp. 873-880). Hollywood (California).
- Yanagihara, H. (1996). "A simultaneous reduction of NOx and soot in diesel engines under a new combustion system (uniform bulky combustion system UNIBUS)". *17th International Vienna Motor Symposium*. Vienna.
- Yanagihara, H. (2001). "Ignition timing control at TOYOTA 'UNIBUS' Combustion System". *IFP International Congress*.
- Yang, Z., Winward, E., O'Brien, G., Stobart, R., & Zhao, D. (2016). "Modelling the Exhaust Gas Recirculation Mass Flow Rate in Modern Diesel Engines". *SAE Technical Paper*, 2016-01-0550. doi:10.4271/2016-01-0550
- Ye, S., Yap, Y., Kolaczkowski, S., Robinson, K., & Lukyanov, D. (2012). "Catalyst 'light-off' experiments on a diesel oxidation catalyst connected to a diesel engine - Methodology and techniques". *Chemical Engineering Research and Design*, 90(6), 834-845. doi:10.1016/j.cherd.2011.10.003
- Yu, S., Choi, H., Cho, S., Han, K., & Min, K. (2013). "Development of engine control using the in-cylinder pressure signal in a high speed direct injection diesel engine". *International Journal of Automotive Technology*, 14(2), 175-182. doi:10.1007/s12239-013-0019-x

- Zeraati-Rezaei, S., Al-Qahtani, Y., & Xu, H. (2017). "Investigation of hot-EGR and low pressure injection strategy for a Dieseline fuelled PCI engine". *Fuel*, 207, 165-178. doi:10.1016/j.fuel.2017.05.078
- Zhou, X., Liu, E., Sun, D., & Su, W. (2018). "Study on transient emission spikes reduction of a heavy-duty diesel engine equipped with a variable intake valve closing timing mechanism and a two-stage turbocharger". *International Journal of Engine Research*, 20(3), 277-291. doi:10.1177/1468087417748837